UNIVERSITY OF CALIFORNIA, SAN DIEGO

Search for the Standard Model Higgs Boson in the Fully Leptonic WW Decay Channel at CMS

A dissertation submitted in partial satisfaction of the
requirements for the degree
Doctor of Philosophy

in

Physics

by

Matthew LeBourgeois

Committee in charge:

Professor Vivek Sharma, Chair
Professor William Coles
Professor Benjamin Grinstein
Professor Nitu Kitchloo
Professor Avi Yagil

2012

The dissertation of Matthew LeBourgeois is approved, and it is acceptable in quality and form for publication on microfilm and electronically:

_____

_____

_____

_____

_____

Chair

University of California, San Diego

2012

To Mom – I may be the first, but I will not be

the last. Always know that your advice, moral

compass and unending support started the chain.

To Dad – My drive comes only from trying to

be the man I know I might one day be: you.

Mon seul désir est de m'enrichir de nouvelles pensées exaltantes.

All that I desire is to be enriched by intensely exciting new thoughts.

—René Magritte

TABLE OF CONTENTS

Signature Page iii

Dedication iv

Epigraph v

Table of Contents vi

List of Figures ix

List of Tables xii

Acknowledgements xv

Vita and Publications xvii

Abstract of the Dissertation xviii

Chapter 1 Introduction 1

Chapter 2 The Standard Model of Particle Physics 5
2.1 Building the Standard Model 6
2.2 The Gauge Sector 8
2.3 Electroweak Symmetry Breaking 9
2.4 Current Higgs Exclusions Limits 11

Chapter 3 The LHC Accelerator and CMS Experiment 14
3.1 The Large Hadron Collider 14
3.1.1 The Physics of Proton Collisions 16
3.2 The CMS Detector 20
3.2.1 The Superconducting Solenoid 22
3.2.2 The Silicon Detector 24
3.2.3 The Calorimeters 26
3.2.4 The Muon Detectors 31
3.3 Integrated Luminosity Calculation 35
3.4 Data Acquisition and Triggering 37
3.5 Particle Reconstruction and Identification 38
3.5.1 Charged Particle Reconstruction 39
3.5.2 Vertex Reconstruction 40
3.5.3 Electron Reconstruction and Identification 42
3.5.4 Muon Reconstruction and Identification 44
3.5.5 Particle Flow Reconstruction 45

3.5.6 Calculation of Missing Transverse Energy 47
3.5.7 Jet Reconstruction 51
3.5.8 b-Jet Identification 51

Chapter 4 Production of the Higgs Boson and Other Standard Model Processes 55
4.1 Higgs Boson Production 56
4.2 Higgs Boson Decays into two W Bosons 61
4.3 *W* Boson Production 63
4.4 Drell-Yan Production 65
4.5 Top-Quark Production 65
4.6 *WW* Production 68
4.7 Other Di-boson Processes 70
4.8 Summary 70

Chapter 5 Search for the Higgs Boson in the WW Decay Channel 73
5.1 Mass-Independent Selection 74
5.1.1 Suppression of Backgrounds with Fake Leptons . . . 74
5.1.2 Drell-Yan Background Suppression 83
5.1.3 Top Background Suppression 85
5.1.4 Other Background Suppression Selections 86
5.2 Mass-Dependent Selection 87
5.2.1 Zero-jet and One-jet Analysis 87
5.2.2 Two-Jet Analysis 89
5.3 Determination of Selection Efficiencies 90
5.3.1 Electron Identification Efficiency 90
5.3.2 Muon Identification Efficiency 91
5.3.3 Trigger Efficiency 92
5.4 Determination of Background Contributions 94
5.4.1 Fake Induced Backgrounds 95
5.4.2 Drell-Yan Background 98
5.4.3 Top Backgrounds 102
5.4.4 WW Background 106
5.4.5 Remaining Backgrounds 108
5.5 Sources of Uncertainty 110
5.5.1 Experimental Uncertainties 110
5.5.2 Theoretical Uncertainties 113
5.6 Original Contributions 116

Chapter 6 Determination of Exclusion Limits and Discovery Significance . . 119
6.1 Overview 119
6.2 Systematic Uncertainties 121
6.3 Profile Likelihood Ratio 122
6.4 Exclusion Limits 123

6.5 Quantifying Excesses 126

Chapter 7 Results and Conclusions 128
7.1 Expected and Observed Yields 128
7.2 Upper Limits on Higgs Boson Production 131
7.3 Discovery of a Higgs-like Boson 134

Bibliography 138

Appendix A Expected and Observed Yields 146

Appendix B Detailed Limits by Channel 158

Appendix C Fake Rates 166

LIST OF FIGURES

Figure 2.1: The list of fundamental Standard Model particles broken down by particle type 7
Figure 2.2: Depiction of the shape of the self-interacting potential of the Higgs field 10
Figure 2.3: A summary of the allowed interactions between particle types in the Standard Model 11
Figure 2.4: Difference between the test statistic for the precision electroweak fits with respect to the best fit as a function of m_{H} [1]. 13

Figure 3.1: The Large Hadron complex seen underground on the outskirts of Geneva, Switzerland 16
Figure 3.2: Parton distribution functions for protons at $Q^2 = 10$ GeV^2 and $Q^2 =$ 10000 GeV^2 19
Figure 3.3: Depiction of the pseudorapidity and transverse momentum variables used in proton-proton collisions. 20
Figure 3.4: Overview of the Compact Muon Solenoid detector. 20
Figure 3.5: Photograph of the CMS detector underground at Point 5. 23
Figure 3.6: Layout of the tracking system projected into the rz plane 25
Figure 3.7: Radiation length and number of layers crossed in the CMS tracker as a function of pseudorapidity 27
Figure 3.8: Muon transverse impact parameter resolution and transverse momentum resolution as a function of pseudorapidity 27
Figure 3.9: One quarter of the electromagnetic calorimeter system projected into the yz plane. 29
Figure 3.10: Overview of the CMS muon subdetector system 32
Figure 3.11: Muon momentum resolution for two different pseudorapidity regions 35
Figure 3.12: The amount of data delivered by the LHC (red) and the amount of data collected by the CMS detector (blue) as a function of date in the year 2011. 36
Figure 3.13: Pictorial representation of the data acquisition system and the flow of data from the CMS detector through both trigger levels. 38
Figure 3.14: Efficiency and fake rates versus pseudorapidity and transverse momentum for reconstructed tracks in simulated $t\bar{t}$ events 41
Figure 3.15: Depiction of the different portions of the electron reconstruction algorithm 44
Figure 3.16: pf$\not\!\!E_{\mathrm{T}}$ and tk$\not\!\!E_{\mathrm{T}}$ simulated distributions for events containing sources of real and fake missing transverse energy 48
Figure 3.17: Data versus simulation of pf$\not\!\!E_{\mathrm{T}}$ distributions for $W \to \mu\nu$ events . . 49
Figure 3.18: Correlation between tk$\not\!\!E_{\mathrm{T}}$ and pf$\not\!\!E_{\mathrm{T}}$ in signal and background events 50
Figure 3.19: Track counting high efficiency algortihm discriminant for data and simulation 52

Figure 3.20: b-jet efficiency for the track counting high effeciency b-tagging algortithm . . . 53
Figure 3.21: Light flavor mistag rate for the track counting high effeciency b-tagging algortithm . . . 54

Figure 4.1: Standard model processes as a function of center of mass collision energy . . . 57
Figure 4.2: Leading-order Feynman diagrams for the production of the Higgs boson . . . 58
Figure 4.3: Leading-order Feynman diagrams for the associated production of the Higgs boson . . . 58
Figure 4.4: Theoretical cross sections for each Higgs production mechanism as a function of Higgs mass . . . 59
Figure 4.5: Feynman diagram for Higgs decay to a pair of bosons (left) and to a pair of fermions (right). . . . 61
Figure 4.6: Theoretical branching fractions for each Higgs decay product as a function of Higgs mass . . . 62
Figure 4.7: Leading order Feynman diagrams for $W+$jets and Drell-Yan production . . . 63
Figure 4.8: Simulated W event in the presence of a "lepton-like" jet in the CMS detector. . . . 64
Figure 4.9: Invariant mass distribution of dilepton events produced via the Drell-Yan process . . . 66
Figure 4.10: Simulated Drell-Yan event in the CMS detector. . . . 67
Figure 4.11: Leading order Feynman diagrams for $t\bar{t}$ and associated top quark production . . . 68
Figure 4.12: Simulated $t\bar{t}$ event in the CMS detector. . . . 69
Figure 4.13: Leading order Feynman diagrams for production of two W bosons . 70
Figure 4.14: Simulated WW event in the CMS detector. . . . 71
Figure 4.15: Leading order Feynman diagrams for diboson production . . . 72

Figure 5.1: A graphical display in the η-ϕ plane of the Jurassic electron isolation technique in the tracker and the ECAL. . . . 76
Figure 5.2: A graphical display of the detector-based muon isolation technique 78
Figure 5.3: Output descriminant variable from the boosted decision tree electron identification for electrons with pseudorapidity $|\eta| < 1.0$ and transverse momentum $p_{\mathrm{T}} < 20$ (left) and $p_{\mathrm{T}} > 20$ (right). . . . 82
Figure 5.4: Minimum of the angle between the pf$\not{E}_{\mathrm{T}}$ direction and each of the leptons for Z to $\tau\tau$ Higgs events . . . 84
Figure 5.5: Fit for electron efficiency for probes with $|\eta| < 1.48$ and $15 < p_{\mathrm{T}} < 20$ 91
Figure 5.6: Fit for muon efficiency for probes with $|\eta| > 1.48$ and $15 < p_{\mathrm{T}} < 20$ 93
Figure 5.7: Fake rate as a function of the loose lepton p_{T} for muons and electrons 97

Figure 5.8: Dilepton invariant mass distribution in the 0-jet, 1-jet and 2-jet categories after removing the Z veto 100
Figure 5.9: Distribution of $R_{\mathrm{sim}}^{\mathrm{out/in}}$ for $m_{\mathrm{H}} = 120$ in the 0-jet and the 1-jet category 102
Figure 5.10: b-tagging discriminant for various control regions 105
Figure 5.11: Dilepton invariant mass distributions for the WW continuum background and four Higgs boson mass hypotheses 107

Figure 6.1: Example of test stastistics for both the CL_s and CL_{s+b} methods . . 125
Figure 6.2: Calculation of the significance, Z, from a p-value 127

Figure 7.1: Comparison of $\Delta\phi_{\ell\ell}$, $m_{\ell\ell}$ and m_T^H in all three jet categories after data-driven corrections. 129
Figure 7.2: Comparison of $p_{\mathrm{T}}^{\ell,\mathrm{min}}$, $p_{\mathrm{T}}^{\ell,\mathrm{max}}$ and $p_T^{\ell\ell}$ in all three jet categories after data-driven corrections. 130
Figure 7.3: Result of the profile likelihood best fit for $\mu = \sigma/\sigma_{\mathrm{SM}}$ 134
Figure 7.4: Individual 0-jet and 1-jet category best-fit values for $\mu = \sigma/\sigma_{\mathrm{SM}}$ compared to the overall best fit 135
Figure 7.5: Observed and expected upper limits on the signal strength modifier, μ, at a 95% confidence level 136
Figure 7.6: Local p-values as a function of Higgs mass for the combined 2011 and 2012 CMS data 137

Figure B.1: 95% confidence limits in the 0-jet category 159
Figure B.2: 95% confidence limits in the 1-jet category 162
Figure B.3: 95% confidence limits in the 2-jet category 163

LIST OF TABLES

Table 3.1: Default values for the variables required to calculate the designed instantaneous luminosity for the LHC. 18

Table 4.1: Summary of Higgs production cross sections via gluon-gluon fusion and vector-boson production 60
Table 4.2: The event generator software and corresponding production cross sections multiplied by branching ratio for each of the backgrounds studied for this analysis. 72

Table 5.1: Parameters used in the detector-based isolation algorithm for electrons 76
Table 5.2: Parameters used in the particle-based isolation algorithms for electrons. 77
Table 5.3: Parameters used in the particle-based isolation algorithms for electrons and muons. 78
Table 5.4: Particle-based isolation selection values for muons 79
Table 5.5: Pre-selection requirements applied to all electrons to ensure tighter requirements than those applied at the trigger level. 80
Table 5.6: Electron identification BDT output values for the six different training samples. 81
Table 5.7: Mass-dependent selections applied for each Higgs mass hypothesis designed for maximum sensitivity over the non-resonant WW background. The parenthesis in the $p_{\mathrm{T}}^{\ell,\mathrm{min}}$ column represent the higher threshold for the same-flavor channels. 88
Table 5.8: Summary of selection criteria for the 2-jet analysis for each value of m_{H}. 89
Table 5.9: Data to simulation electron identification efficiency scale factors. . . 91
Table 5.10: Data to simulation muon identification efficiency scale factors. . . . 92
Table 5.11: Trigger efficiencies (%) for the selections in various Higgs mass hypotheses. 94
Table 5.12: $W+$jets yield at the Higgs selection level 98
Table 5.13: Estimation of the Drell-Yan background at the Higgs selection level in the 0-jet category 101
Table 5.14: Estimation of the Drell-Yan background at the Higgs selection level in the 1-jet category 101
Table 5.15: Estimation of top backgrounds in the 0-jet and 1-jet categories. . . . 104
Table 5.16: B-tagging efficiency measured in the 2-jet control region in bins of $|\eta|$ for the most central tag jet. 106
Table 5.17: Estimation of the WW background at the mass-independent selection level in the 0-jet and 1-jet categories. 108
Table 5.18: Summary of fake lepton background yields in the same sign sample after the mass independent selection. 110

Table 5.19: Jet category fractions and inclusive cross section uncertainties for various values of m_{H} 115
Table 5.20: Formulas used to compute uncertainties on jet category fractions from uncertainties on inclusive cross sections 115

Table 7.1: Expected yields from data and simulation after data-driven corrections for $4.6\,\mathrm{fb}^{-1}$ at the mass-independent level, for the 0-jet, 1-jet and 2-jet categories. Only the statistical errors are reported. 131
Table 7.2: Background contributions and data yields for $4.6\,\mathrm{fb}^{-1}$ of integrated luminosity after the full cut-based selection in the 0-jet bin for a Higgs boson mass of $m_{\mathrm{H}} = 130$. The data-driven correction are applied and the errors reported reflect all systematic uncertainties. . . 132
Table 7.3: Expected and observed 95 % C.L. upper limits and uncertainty band for events in the combined 0, 1 and 2 jet category. 133

Table A.1: Background contributions and data yields for $4.6\,\mathrm{fb}^{-1}$ of integrated luminosity after the full selection in the 0-jet category for low Higgs masses ($110 \leq m_{\mathrm{H}} \leq 128\,\mathrm{GeV}$). The data-driven correction are applied and the errors reported reflect all systematic uncertanties. . . . 147
Table A.2: Background contributions and data yields for $4.6\,\mathrm{fb}^{-1}$ of integrated luminosity after the full selection in the 0-jet category for intermediate Higgs masses ($130 \leq m_{\mathrm{H}} \leq 160\,\mathrm{GeV}$). The data-driven correction are applied and the errors reported reflect all systematic uncertanties. 148
Table A.3: Background contributions and data yields for $4.6\,\mathrm{fb}^{-1}$ of integrated luminosity after the full selection in the 0-jet category for intermediate Higgs masses ($170 \leq m_{\mathrm{H}} \leq 200\,\mathrm{GeV}$). The data-driven correction are applied and the errors reported reflect all systematic uncertanties. 149
Table A.4: Background contributions and data yields for $4.6\,\mathrm{fb}^{-1}$ of integrated luminosity after the full selection in the 0-jet bin for high Higgs masses ($250 \leq m_{\mathrm{H}} \leq 400\,\mathrm{GeV}$). The data-driven correction are applied and the errors reported reflect all systematic uncertanties. . . . 150
Table A.5: Background contributions and data yields for $4.6\,\mathrm{fb}^{-1}$ of integrated luminosity after the full selection in the 0-jet bin for high Higgs masses ($450 \leq m_{\mathrm{H}} \leq 600\,\mathrm{GeV}$). The data-driven correction are applied and the errors reported reflect all systematic uncertanties. . . . 151
Table A.6: Background contributions and data yields for $4.6\,\mathrm{fb}^{-1}$ of integrated luminosity after the full selection in the 1-jet bin for low Higgs masses ($110 \leq m_{\mathrm{H}} \leq 128\,\mathrm{GeV}$). The data-driven correction are applied and the errors reported reflect all systematic uncertanties. 152
Table A.7: Background contributions and data yields for $4.6\,\mathrm{fb}^{-1}$ of integrated luminosity after the full selection in the 1-jet bin for intermediate Higgs masses ($130 \leq m_{\mathrm{H}} \leq 160\,\mathrm{GeV}$). The data-driven correction are applied and the errors reported reflect all systematic uncertanties. 153

Table A.8: Background contributions and data yields for $4.6\,\text{fb}^{-1}$ of integrated luminosity after the full selection in the 1-jet bin for intermediate Higgs masses ($170 \leq m_{\text{H}} \leq 200\,\text{GeV}$). The data-driven correction are applied and the errors reported reflect all systematic uncertanties. 154
Table A.9: Background contributions and data yields for $4.6\,\text{fb}^{-1}$ of integrated luminosity after the full selection in the 1-jet bin for high Higgs masses ($250 \leq m_{\text{H}} \leq 400\,\text{GeV}$). The data-driven correction are applied and the errors reported reflect all systematic uncertanties. . . . 155
Table A.10: Background contributions and data yields for $4.6\,\text{fb}^{-1}$ of integrated luminosity after the full selection in the 1-jet bin for high Higgs masses ($450 \leq m_{\text{H}} \leq 600\,\text{GeV}$). The data-driven correction are applied and the errors reported reflect all systematic uncertanties. . . . 156
Table A.11: Background contributions and data yields for $4.6\,\text{fb}^{-1}$ of integrated luminosity after the full selection in the 2-jet bin for all Higgs masses ($110 \leq m_{\text{H}} \leq 600\,\text{GeV}$). The data-driven correction are applied and the errors reported reflect all systematic uncertanties. 157

Table B.1: Expected and observed 95% C.L. upper limits and uncertainty band for opposite flavour events in the 0-jet category. 160
Table B.2: Expected and observed 95% C.L. upper limits and uncertainty band for same flavour events in the 0-jet category. 161
Table B.3: Expected and observed 95% C.L. upper limits and uncertainty band for opposite flavour events in the 1-jet category. 163
Table B.4: Expected and observed 95% C.L. upper limits and uncertainty band for same flavour events in the 1-jet category. 164
Table B.5: Expected and observed 95% C.L. upper limits and uncertainty band for events in the 2-jet category. 165

Table C.1: Measured prompt rate for muons in bins of η, p_{T} and number of primary vertices. Errors are statistical only. 166
Table C.2: Measured prompt rate for electrons in bins of η, p_{T} and number of primary vertices. Errors are statistical only. 167
Table C.3: Measured fake rates in bins of η and p_{T}. Errors are statistical only. . 167
Table C.4: W+jets yields in the 0-jet bin. Errors are statistical only. 168
Table C.5: W+jets yields in the 1-jet bin. Errors are statistical only. 168
Table C.6: W+jets yields in the 2-jet bin. Errors are statistical only. 168

ACKNOWLEDGEMENTS

The people who kept me sane:

Mine might be the only name written at the beginning of this thesis, however, as is the norm in high energy particle physics, many many more people deserve credit than just this humble primary author. This work could definitely not have been completed without the direct or indirect support of the following people.

First, I must thank my father and my mother who have given and continue to give tremendous advice for which I am ever grateful. I hope they both realize how much this is their work as much as it was mine.

I have had many great science and math teacher through the years. Most importantly, a big thank you to Mr. Butcher. His energy, enthusiasm and humor were infectious. I walked into his classroom with but a flicker of interest in science and walked out ablaze. I must also thank Mr. May, Ms. Maddox and Mrs. Haynes, three teachers who not only put up with me for many years, but also allowed me to continue to fan the flames.

I would also like to thank the great professors and scientists who have employed, guided and mentored me through this journey. Starting with thanks for Dr. Alexandre Freundlich and his group at SVEC, they gave me my first job and showed me what science is really all about. Also, thanks to Larry Pinsky, along with Bill Mayes and Anton Empl, who led me into the world of particle physics. Special thanks also to the professors in my graduate career whose doors were always open: Avi Yagil, Frank W urthwein and Claudio Campagnari. Finally, thanks to Vivek Sharma, my advisor, who allowed me the privilege of staying in particle physics and eventually allowed me to write this thesis, my special little place in physics history.

In addition, I must acknowledge the hard work of all the people who directly contributed to this analysis. These “Latinos” were not only my collaborators, they were my teammates and my partners in crime. Notably from the Latinos, I must acknowledge Ema and Chiara; their drive was inspiring. My two office mates in Geneva, Adish Vartak and Giovanni Petruciani, I must also thank for putting up with (and sometimes answering!) my endless stream of questions, rants and curses. Finally, extra special thanks goes to Boris Mangano; we fought in the trenches together for many years, not

just as co-workers, but as friends.

I am lucky to have so many friends who have provided me with the distractions away from physics which have allowed me to keep my sanity. They were always there to share a round of golf, a round of beers or a rousing set of Rock Band. For these things, I will forever be grateful. In quasi-chronological order: Walk, Thani, Drew, Ryan and Randy, Jeff, Whit, Golf, Toby, Diego, Jake, Pun, Ben, Maria, Jean Roch and Virginia (and their amazing daughter Elizabeth) and Steven and Didar. Most especially, thanks goes to Alex and Rachel who have been the best of roommates and friends. San Diego would not have been the same with out them–bring on Boston.

Finally, I would like to thank Nora, my fiancée. I was lucky to find her before the writing started for I can not imagine how hard this process would have been without the knowledge that she would be the prize at the end of the last chapter.

VITA

2005	B. S. in Physics *magna cum laude*, University of Houston
2007	M. S. in Physics, University of California, San Diego
2012	Ph. D. in Physics, University of California, San Diego

PUBLICATIONS

Search for the Higgs Boson Decaying to W^+W^- in the Fully Leptonic Final State, *CMS Collaboration*, Expected Phys. Lett. B .

Measurement of W^+W^- Production and Search for the Higgs Boson in pp Collisions at $\sqrt{s} = 7$ TeV, *CMS Collaboration*, Phys. Lett. B **699**, 25 (2011) [arXiv:1102.5429 [hep-ex]]

Measurement of Inclusive W and Z Cross Sections in pp Collisions at $\sqrt{s} = 7$ TeV, *CMS Collaboration*, JHEP **1101**, 080 (2011) [arXiv:1012.2466 [hep-ex]]

ABSTRACT OF THE DISSERTATION

Search for the Standard Model Higgs Boson in the Fully Leptonic WW Decay Channel at CMS

by

Matthew LeBourgeois

Doctor of Philosophy in Physics

University of California, San Diego, 2012

Professor Vivek Sharma, Chair

A search for the Standard Model Higgs boson decaying to W^+W^- is presented. Data is taken from pp collisions with center of mass energy $\sqrt{s} = 7\,\text{TeV}$ at the LHC using the CMS detector over the course of 2011. The sum of the data collected amounts to an integrated luminosity of 4.6 fb^{-1}. Identification of W^+W^- candidates is performed by searching for leptonic decays of both W bosons. The resulting signature is two oppositely charged leptons, electrons or muons, plus significant missing transverse energy in the final state.

The other Standard Model processes which only serve as background to the Higgs boson search are removed via a series of selections aimed to reduce the backgrounds while keeping the highest possible signal-to-background ratio. The Higgs bo-

son signal is identified over the non-resonant W^+W^- production by exploiting the spin correlation of the $H \to W^+W^-$ decays. Details concerning the analysis selection criteria, the data-driven estimates of the major background processes and the systematic uncertainties of the analysis are all presented in detail.

As no significant excess of events are observed above the Standard Model background estimates, upper limits are set on the Higgs boson production with respect to the Standard Model prediction. Exclusion of the Higgs boson is extended with respect to previous measurements to a range of 132-238 GeV with a 95% confidence level.

Chapter 1

Introduction

Phycisists working in the field of particle physics have long sought to understand the most basic laws of physics, the fundamental particles that make up matter and the fundamental forces through which they interact. Ernest Lawrence built the first particle accelerator on our sister campus, the University of California, Berkley, and particle accelerators have continued to increase in size ever since. With each increase has come an increase in particle energy allowing for newer and newer avenues of particle physics research.

These experiments have allowed for the development of the theory of Standard Model of particle physics in the 1960's, and every generation of accelerators since has only confirmed the hypotheses therein[2]. While the success of the Standard Model has been confirmed many times over, one nagging question remains: what is the origin of mass? In the simplest form of the Standard Model, this question is addressed via the spontaneous breaking of the electroweak symmetry from which falls the existance of a yet unobserved scalar particle: the Higgs boson [3, 4, 5, 6, 7, 8].

The latest particle accelerator, the Large Hadron Collider (LHC), continues the tradition of building more energetic particle accelerators, this time with a mind to make a final conclusion on the existance of the Higgs boson. The LHC, built along the Franco-Swiss border, will eventually operate at a design energy seven times larger than the previous generation accelerator and will eventually deliver enough data to reach its goal. Built to observe the high energy proton collisions delivered by the LHC, the Compact Muon Solenoid (CMS) is a multipurpose particle detector serving to quench the cu-

riosity of its collaboration of thousands of scientists. With goals in line with those of the LHC, some of these scientists, including myself, hope to close the chapter on the existance of the Higgs boson.

It is with this goal in mind that I present a thesis on a search for the Higgs boson in the $H \to W^+W^- \to \ell\nu\ell'\overline{\nu}$ channel using $4.6\,\text{fb}^{-1}$ of data taken by CMS over the course of 2011. This analysis is one of many searches for the Higgs boson at CMS, each with its own strength and weaknesses. This analysis is particularly suited for searching for the Higgs boson in a wide mass range between 120 to 200 GeV but is performed over a fuller range of possible Higgs masses: 110 to 600 GeV. The decay of each W boson to a lepton and a neutrino gives a clean signature of two prompt leptons and significant missing transverse energy mostly free of the dominating QCD production at the LHC.

The results presented in this thesis expand on results previously published using 35 pb^{-1} of 2010 CMS data [9] as well as results presented in public conferences during the Summer of 2011 [10, 11]. Many changes were made with resepect to these analysis including changes to deal with the increase in proton-proton collision rates at the LHC and changes to increase the search sensitivity.

The thesis is organized as follows. First, I will present a review of the Standard Model of particle physics in Ch. 2, touching on the parts most important for this search. The LHC apparatus is briefly overviewed followed by a more detailed discussion of the CMS detector making sure to touch on the design considerations particularly important for this analysis. Then, the algorithms used to reconstruct the particles traversing the CMS detector are outlined, namely charged particles including electrons and muons, hadronic jets and through passive means, neutrinos. All of these aspects are covered in Ch. 3.

Other SM processes are produced at a rate much larger than the SM Higgs boson. These processes can be produced either with exactly the same final state, irreducible backgrounds, or with a different set of final state particles, reducible backgrounds, but with a large enough rate such that if a fraction are misreconstructed they can mimick the final state under analysis and hamper the sensitivity of this study. Non-resonant WW production is the only irriducible background as it can decay in the exact same manner as $H \to W^+W^-$. It is therefore the main background to this analysis. The reducible

backgrounds to this search are:

- $W+$**jets production**: The production of a single W boson decaying leptonically results (33% of the time) in only one lepton and missing transverse energy. However, the W can be produced in the presence of one or more jets, only one of which would then need to "fake" the signature of a prompt muon or electron. While this probability is low, single W production has a cross section over four orders of magnitude higher than Higgs production.

- **Drell-Yan production**: Produced at a slightly lower rate than W production, the Drell-Yan process, i.e. Z/γ^* production, can decay to two oppositely charged leptons (10% of the time). Then, the only missing ingredient to reproduce the signal is the presence of missing transverse energy. However, due to detector resolution and exacerbated by multiple interactions present in each proton-proton collision, many $Z/\gamma^* \to \ell\ell$ events do present themselves with large amounts of transverse missing energy.

- $t\bar{t}$ **and** tW **production**: The top quark decays to a W boson and a b-quark 100% of the time. Thus, $t\bar{t}$ production has all the elements of the signal with the addition of two b-jets. The identification of these b-jets will be of upmost importance to remove $t\bar{t}$ background. Single top quark production in association with a W boson has a smaller cross section than $t\bar{t}$, however, only one b-jet is produced in the final state reducing the number of rejection handles by half.

- WZ**,** ZZ **and** $W\gamma$ **production**: Other diboson processes which are backgrounds to this process are produced with more than two leptons in the final state. The main handle to limiting their impact is to require two and only two leptons, however when one lepton is missed during reconstruction, they can still be an issue.

The production of the Higgs boson along with all of these backgrounds is discussed in full in Ch. 4.

This analysis starts by splitting events into different categories based on the composition of final state particles allowing for better sensitivity due to the different backgrounds contributing in each category. First, events are split into "same flavor",

($e^{\pm}e^{\mp}$,$\mu^{\pm}\mu^{\mp}$) and "opposite flavor" ($e^{\pm}\mu^{\mp}$,$\mu^{\pm}e^{\mp}$) categories allowing for the large Drell-Yan background to only contribute to the opposite flavor. Then, the events are further split into three categories based on the number of jets in the event: zero, one or greater than two. WW is the main contribution across the first two jet categories with $t\bar{t}$ becoming more and more dominant with each additional jet.

The analysis then continues by applying selection criteria designed to reduce each of the reducible backgrounds. These "mass-independent" selections are discussed in Sec. 5.1. Then, the search is branched into multiple sets of different selection criteria, one for each Higgs mass hypothesis under study. These selections exploit the spin-0 nature of the Higgs boson and are designed to maximally separate the Higgs production from the non-resonant WW production thereby giving maximum search sensitivity. These "mass-dependent" selections are discussed in Sec. 5.2.

This analysis does not have a characteristic mass peak which would help to identify the presense of the Higgs boson due to the two nutrinos carrying away a significant amount of energy undetected. Therefore, this analysis is essentially a counting experiment, checking the expected number of background events against the number of events seen in data. Precise knowledge of the yields of all of the backgrounds is therefore essential and is discussed in full in Sec. 5.4. A good understanding of the uncertainties present in this analysis are of equal importance and are discussed in Sec. 5.5.

Finally, before presenting the results in Ch. 7, a discussion of the statistical tools needed to make a quantitative statement about the existance of the Higgs boson is presented in Ch. 6.

Chapter 2

The Standard Model of Particle Physics

At the end of the nineteenth century, the field of particle physics was very much in its infancy. Through the course of the twentieth century, the Standard Model (SM) of particle physics was built up piece-wise to what we know today. While the SM does in fact have its limitations, every experimental observation of the twentieth, and now twenty-first, century has confirmed the predictions set forth by the SM. The last pieces were put in place by Weinberg in 1967 to describe, within a common framework, the theory of the electromagnetic and weak interactions [12]. The SM also explains the theory of the strong force, i.e. Quantum Chromodynamics (QCD).

A minimal choice of theoretical predictions is added to account for the particles that permeate our universe and that have been observed experimentally. These are made up of fermions, spin-$1/2$ particles interacting via bosons, spin-1 particles, which propagate the fundamental forces. The SM also contains additional theoretical predictions, notably the scalar Higgs field, which breaks the electroweak symmetry, gives mass to the other particles of the theory and predicts the existance of the only remaining undiscovered particle: the Higgs boson.

As successful as the SM has proven to be over the last century, it still leaves many questions unanswered. For one, the matter predicted by the SM only accounts for 5% of the known universe. A currently unknown form of matter accounts for another 25% of the universe while the remaining 70% of the universe is permeated by an invisible source of energy. Scientists refer to the latter two as dark matter and dark energy, respectively, and the SM currently has no particle candidate that could account for this discrepancy. In

addition, the neutrinos in the SM have no mass, contradictory to the latest experimental results. The SM also fails to place a restriction on the number of fermion families—we only know three exist due to experimental observation. The last, and maybe the largest, shortcoming of the SM is that it fails to incorporate the fourth known force: gravity.

A more detailed discussion of the Standard Model can be found in Ref. [13] and unless otherwise indicated, the following information is summarized from Ref. [13].

2.1 Building the Standard Model

Noether's theorem generically states any physical system invariant under a group of transformations produces at least one conserved quantity [14]. Two simple examples produce two of the universal conservation laws: invariance under a translation in time leads to the conservation of energy and invariance under a spatial translation leads to the conservation of momentum. These are examples of "space-time symmetries."

The theorem can be extended to yield the symmetries seen in, and hence can explain the interactions of, the SM. Departing from classical interactions, one must employ the use of quantum field theory (QFT) to explain the interactions of quantum particles (QFT utilizes both quantum mechanics and special relativity). Using QFT, the "gauge sector" of the SM can be described by the lie group $SU(3) \times SU(2)_L \times U(1)_Y$ [15]. Adopted for QFT from Noether's theorem, the Ward-Takahashi identity [16, 17] states each of these subgroups have an "internal symmetry," analogous to the space-time symmetries in Noether's theorem, which produce a conserved quantity, also referred to as quantum number, of the SM.

These internal symmetries require the existence of spin-1 particles (bosons) which preserve local invariance and mediate the interactions between particles. When mediating an interaction, these "force-carrying" particles preserve their group's corresponding quantum number.

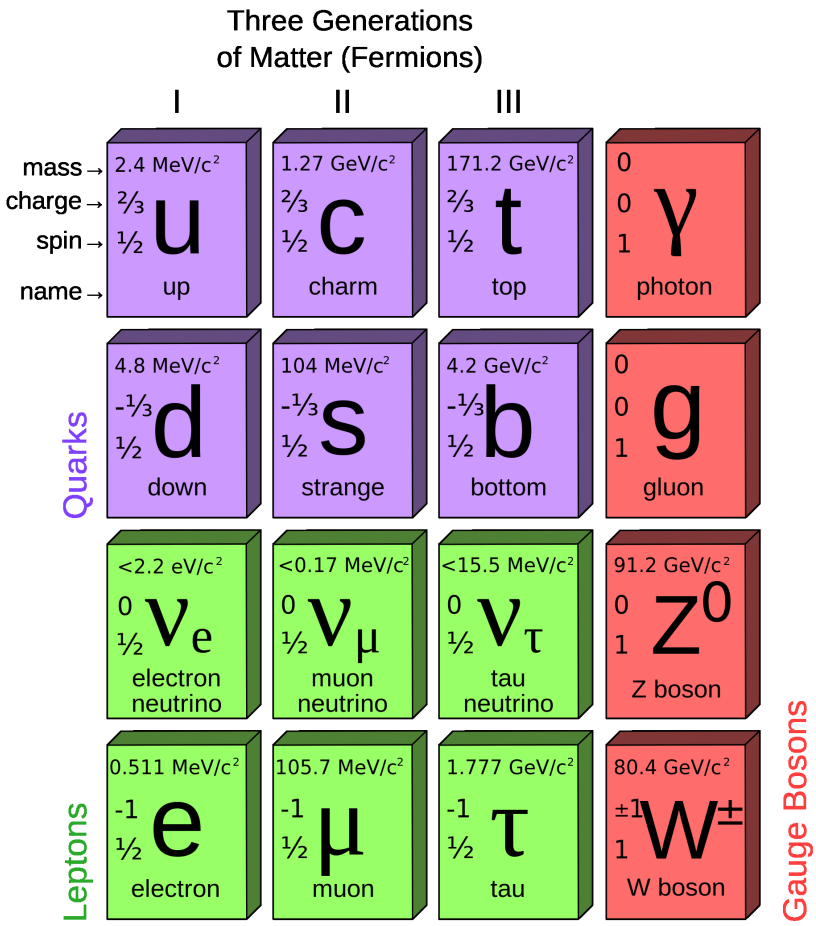

Figure 2.1: The list of fundamental Standard Model particles broken down by particle type: quarks in blue, leptons in green and gauge bosons in red. The anti-quarks and anti-leptons are not shown, nor is the Standard Model Higgs boson[18].

2.2 The Gauge Sector

Quantum Chromodynamics

Quantum chromodynamics describes the interaction of particles via the strong force and can be described by the $SU(3)$ group. The symmetry of the $SU(3)$ group has a conserved quantity called color and is mediated by gluons, eight spin-one bosons corresponding to the eight generators of the $SU(3)$ group. Gluons mediate the interaction between spin-½ particles called quarks, which carry color. Quarks consequently interact via the strong force and are highlighted in purple in Fig. 2.1. There are three families of two quarks plus each quark's anti-particle (cutely labeled: up, down, charm, strange, top and bottom). The "up-type" quarks also carry an electromagnetic charge of $+2/3$ while the "down-type" quarks have an electromagnetic charge of $-1/3$.

At larger distances, the strong force increases proportionally with the distance between two color carrying particles. This is unlike other forces (e.g. gravity) since the further one separates two quarks, the more energy will be required for further separation. As the separation between two color carrying particles increases so does the energy density between the two particles, eventually increasing enough to produce a pair of quarks out of the vacuum. This process continues until there is no longer enough energy left in the system. For this reason, quarks are never found in isolation, but rather are always found in colorless bound states. A quark and anti-quark pair is called a meson (e.g. pions and kaons) while a system of three quarks is called a baryon (e.g. protons and neutrons). A two quark system can by colorless (i.e. white) by combining a colored quark with an oppositely colored anti-quark (i.e. blue plus anti-blue). A three quark system can be colorless by requiring equal amounts of red, green and blue color (very much in analog to the electromagnetic color spectrum, hence the name color).

Electoweak Interaction

The electroweak interaction can be described by the $SU(2)_L \times U(1)_Y$ group. The interaction is mediated by three spin-1 bosons (W^1,W^2,W^3), corresponding to the generators of the $SU(2)_L$ group, which preserve a quantity called weak isospin, and by one spin-1 boson, (B) corresponding to the generator of the $U(1)_Y$ group which conserves a

quantity labelled hypercharge. In addition to the previously discussed quarks, there are three more pairs of fermions (and their anti-particles) which are introduced to the SM and can interact electroweakly: the electron ($e^{\pm}$) and electron-neutrino (ν_e), the muon ($\mu^{\pm}$) and muon-neutrino (ν_μ) and the tau (τ) and tau-neutrino (ν_τ). These particles can be seen in green in the bottom left hand side of Fig. 2.3. All fermions except neutrinos, which do not carry hypercharge, can interact via a B.

In addition to isospin, fermions also preserve another quantity: helicity. Helicity is the projection of a particle's spin along its momentum direction and hence a particle can have its spin either aligned along its momentum (right-handed) or anti-aligned along it's momentum (left-handed). In fact, the matter fields can be represented independently for left-handed fermions and right-handed fermions with each being described by a different representation of the $SU(2)_L$ group. Two consequence of the different representation are that one, fermions cannot be massive, else the gauge invariance of the model breaks down, and two, the three bosons from the $SU(2)_L$ group can only couple to left-handed fermions. The same preservation of gauge invariance also requires that the four electroweak bosons cannot be massive.

2.3 Electroweak Symmetry Breaking

The electroweak gauge symmetry in the previous section required that all four gauge bosons be massless. However, from experimental evidence, we know that some of the bosons due indeed have mass. In order to impart masses on these particles, the electroweak symmetry must be broken. This is done in the simplest form by the Higgs mechanism.

The solution was theorized separately by three groups of theorists in 1964: R. Brout and F. Englert [3], P. Higgs [4, 5, 6], and G. Guralnik, C. R. Hagen, and T. Kibble [7, 8]. They introduced a complex scalar field, the Higgs field, which has a self-interacting potential with a minimum value less than the potential at the origin. The $SU(2)_L \times U(1)_Y$ symmetry of the SM "breaks" when the Higgs field chooses a minimum at the bottom (the vacuum expectation value) of this potential. To get a sense of this mechanism, the shape of the potential in the real and imaginary plane is shown in

Fig. 2.2.

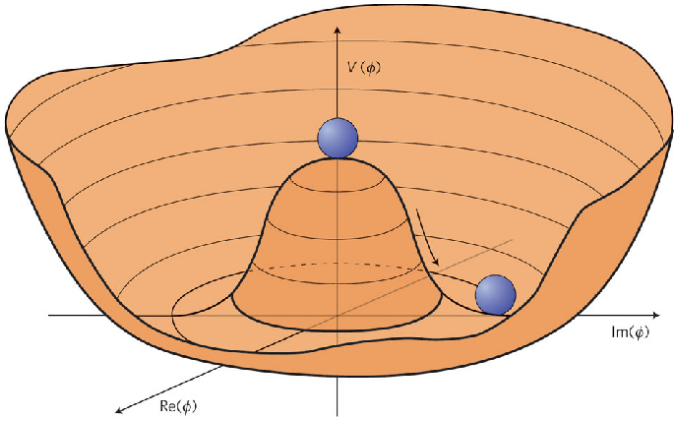

Figure 2.2: Depiction of the shape of the self-interacting potential of the Higgs field. When the Higgs field choses a location at the lowest value of the potential, the vacuum expectation value, the electroweak symmetry is broken and the only remaining symmetry is the electromagnetic charge [19].

The broken symmetry of the $SU(2)_L \times U(1)_Y$ group results in the formation of a smaller group, $U(1)_Q$. Q, the electric charge (the one for which we we are familiar) is the only remaining symmetry and relates to the initial isospin (T_3) and hypercharge (Y) symmetries via the relation $Q = T_3 + Y/2$. Also unfolding from the introduction of the Higgs field are the massive gauge bosons. Re-parameterizing the three bosons, W^1,W^2,W^2, of the $SU(2)_L$ group and the single boson, B, of the $U(1)_Y$ group after symmetry breaking gives the three massive weakly interacting bosons, the positively charged W^+, the negatively charged W^- and the neutral Z^0, as well as the massless photon (γ), which interacts electromagnetically. These bosons can be seen in red on the right side of Fig. 2.1. The $W^\pm$ bosons retain the unique ability to only couple to left-handed fermions.

As the Higgs field is a complex scalar in the doublet representation of the $SU(2)_L$ group, four extra degrees of freedom have been introduced to the theory. Three degrees of freedom are absorbed in giving the $W^\pm$ and Z their mass with the last remaining degree of freedom becoming the Higgs boson. One free paramater in the theory remains: the Higgs mass, m_{H}. The addition of the Higgs field also allows for the addition of

fermion mass couplings which no longer violate gauge invariance. These Yukawa couplings produce interactions between the fermions and the Higgs field and impart mass to all fermions. It should be pointed out, however, that this theory does not predict the coupling strength between the Higgs field and the fermions and hence all particle masses can only be determined experimentally.

2.4 Current Higgs Exclusions Limits

As previously mentioned, every prediction set forth by the SM has been confirmed by experimental data. A summary of interactions found in the SM can be seen in Fig. 2.3. Every particle except the Higgs boson shown in Fig. 2.3 has been measured experimentally leaving only the mass of Higgs to be measured, if it exists.

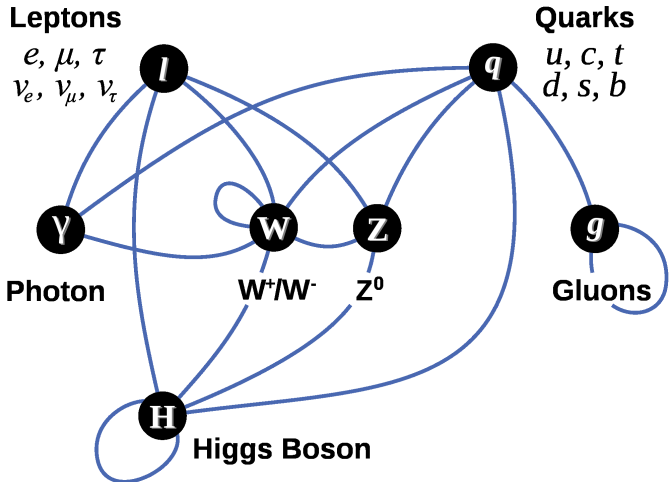

Figure 2.3: A summary of the allowed interactions between particle types in the Standard Model. A line connecting two particles indicates coupling occurs between those particles. A looped line from one particle to itself indicates that particular particle self-couples[20].

Results from previous experiments have contributed to excluding ranges of possible m_{H} values. Experiments situated on the Large Electron Positron (LEP) collider in Geneva, Switzerland (decommissioned in 2000) placed a lower limit at a 95% confidence level of 114.4 GeV on m_{H} [21]. Furthermore, the two experiments located on the

Tevatron accelerator outside of Chicago, the Collider Detector at Fermilab (CDF) and DØ, have excluded the mass ranges $100 - 109$ GeV and $156 - 177$ GeV [22].

Theoretical predictions require m_{H} must be less than approximately 600 GeV to ensure that unitarity is not violated via the scattering of two W bosons. Furthermore, indirect limits on the Higgs boson mass were calculated using a combination of data from experiments at LEP, the Stanford Linear Collider and the Tevatron [1]. These limits use the accurate measurements of SM parameters from these experiments to constrain the Higgs mass based on higher order loop corrections involving the Higgs boson to the production of the W and Z bosons. This analysis prefers a lighter Higgs mass, giving a best fit value of just under 90 GeV and a 95% confidence upper limit of 158 GeV. The difference between the test statistic, χ^2 and the best fit value, χ^2_{min}, is plotted in Fig. 2.4 along side the best direct search constraints available at the time of the publication.

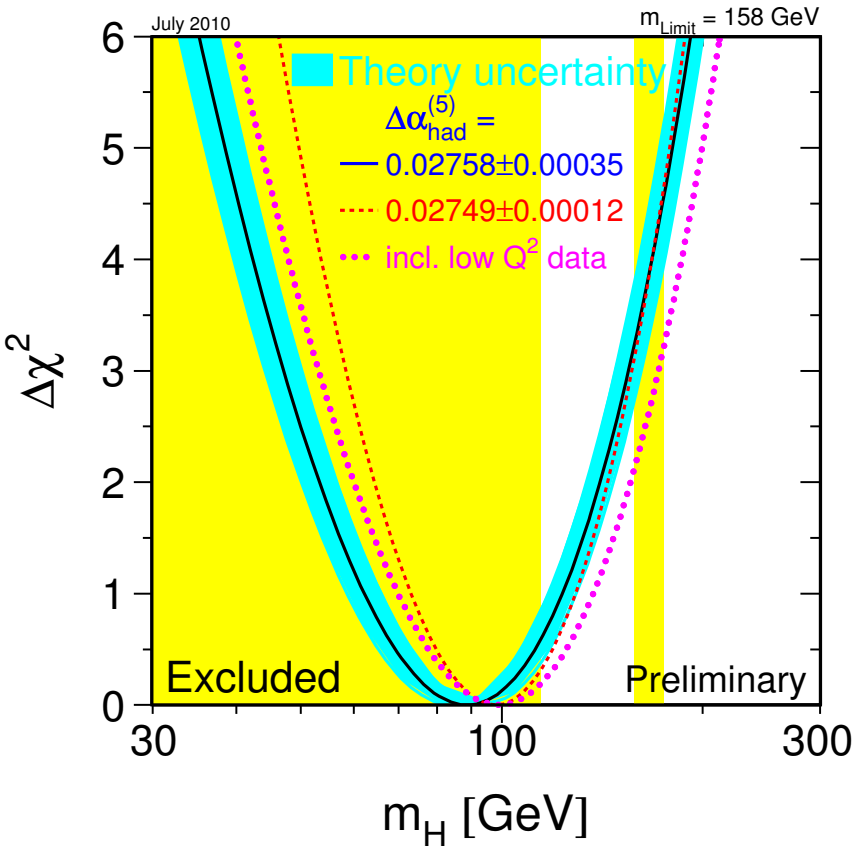

Figure 2.4: Difference between the test statistic for the precision electroweak fits with respect to the best fit as a function of m_{H} [1].

Chapter 3

The LHC Accelerator and CMS Experiment

The Compact Muon Solenoid (CMS) experiment is a collaboration of nearly 3000 scientists working together to discover new phenomenon in the plethora of data made available by the Large Hadron Collider (LHC). This chapter will give an overview of the experimental setup used by these scientists, first by describing the Large Hadron Collider, then by describing the different aspects of the Compact Muon Solenoid itself. It concludes with a description of the algorithms used to measure particles traversing the detector.

3.1 The Large Hadron Collider

The LHC is a particle accelerator and collider located underground along the French-Swiss border near Geneva, Switzerland [23, 24, 25]. Built by the European Organization for Nuclear Research (CERN) with a collaboration of over 10,000 scientists from over 100 countries, it is currently the largest and highest energy collider ever constructed. Completed in 2008, it is approximately 27 kilometers in circumference, sits up to 170 meters underground and was designed to accelerate protons to energies up to 14 Teraelectronvolts (TeV), seven times larger than the previous record set by the Tevatron outside of Chicago, Illinois. An electron volt is the amount of energy required to move an electron through one volt of potential and 14 TeV is approximately equivalent to the

amount of kinetic energy contained in an average sized Harley Davidson [26] traveling at a speed of 850 feet per year. The LHC also collides heavy ions, such as lead, and when doing so has a full physics program in and of itself, the details of which will be left for the inquisitive reader to discover on his or her own.

Many design considerations went into ensuring that the LHC would have a strong physics program over the life of the accelerator—it is currently scheduled to run through 2020. Arguably the most important search expected to have been performed at the LHC was the determination the cause of electroweak symmetry breaking, and specifically, whether or not the Higgs mechanism is this cause. One of the first results which was expected to arrive after the completion of the LHC was a determination on the existence or absence of the Higgs boson. Of course, many other important analyses were planned including searches for supersymmetry, extra dimensions, particles that could explain dark matter and ways to unify the electroweak and strong forces, all of which are beyond the scope of this thesis.

Construction started on the LHC in 1998 following the shut down of the previous collider housed in the same underground tunnel, the Large Electron-Positron Collider (LEP). Specific choices were made to ensure that the LHC would have maximum discovery potential. To allow for significantly higher energies than its predecessor in the tunnel, the LHC is a proton-proton collider instead of an electron-positron collider taking advantage of the significantly heavier mass of the protons and hence significantly reducing the loss of energy due to synchrotron radiation. Proton-proton collisions were chosen instead of proton-anti-proton as anti-protons annihilate in the presesnce of matter and hence have a significantly shorter lifetime.

In order to reach high energy and large interaction rates (luminosity), the LHC has two separate parallel rings which house the protons accelerated in opposite directions. The rings are evacuated to a pressure less than 10^{-10} Torr to minimize unintentional proton interactions and run through thousands of superconducting magnets which accelerate, bend and attenuate the protons. Protons are injected into the LHC in large bunches. The separation time between two successive bunches was designed to be 25ns and consequently the LHC can hold up to 2800 bunches in each beam. At four points along the circumference of the LHC, the beams of protons are bent to collide where a

detector sits ready to record the resulting particles produced by the proton collisions. There are two general purpose detectors, ATLAS and CMS, stationed at the two high luminosity interaction points (IP), Point 1 and Point 5, respectively, as can be seen in Fig. 3.1.

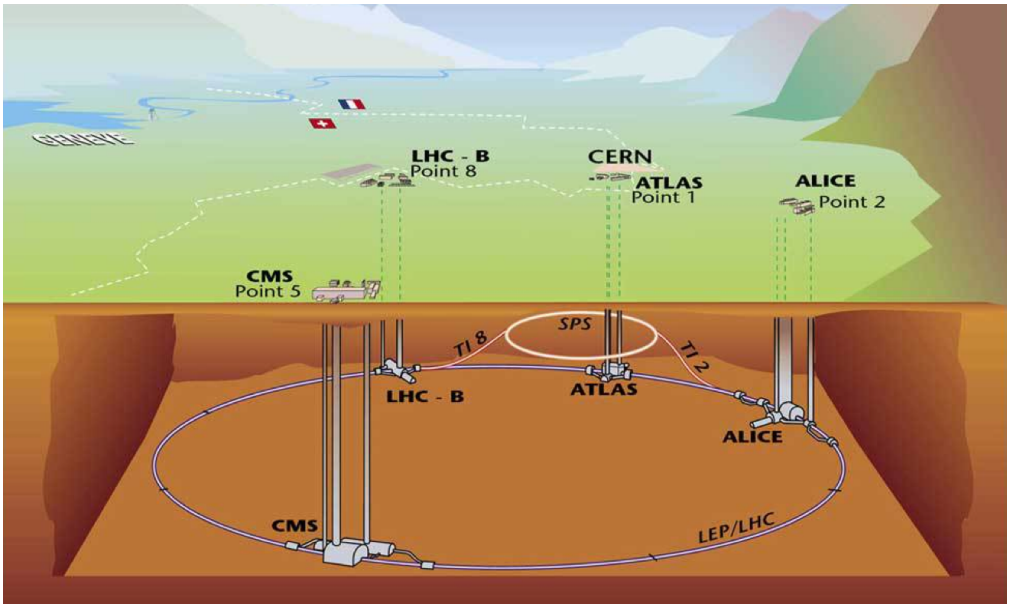

Figure 3.1: The Large Hadron complex seen underground on the outskirts of Geneva, Switzerland. The four detectors are also shown, most notably, CMS at Point 5.

The LHC is still in the process of ramping up to its designed energy and the data used in this analysis, taken over the course of 2011, is from collisions at energies half of the maximum design energy, 7 TeV.

3.1.1 The Physics of Proton Collisions

In order to speak coherently about the kinematics of colliding particles, one must first introduce the idea of a "cross section." The cross section of a particle interaction indicates the "effective area" and gives a quantitative value to the probability for an interaction to occur. Imagine shooting pool, the size of the billiard balls is directly proportional to the "area" of interaction between two billiard balls. The larger the billiard balls, the larger the cross section and the higher the probability of the two billiard balls colliding.

The same is true for particle collisions; the higher an interaction's cross section the more likely that interaction will occur. The total cross section of two protons colliding at the energy of the LHC running in 2011 is 110 millibarns (mb). A barn is a unit of area equivalent to 1×10^{-28} square meters. Many types of particle interactions can occur when two protons collide. 40 mb of the 110 mb cross section comes from elastic scattering of the two protons, that is the protons remain intact and only interact electromagnetically. Approximately 10 mb comes from soft inelastic (single diffractive) collisions which do not contain a strong enough exchange of energy to probe new physics. The remaining 60 mb is the cross section for inelastic proton scattering where the protons actually dissociate due to a hard scattering between two of the partons ("parts" of the proton, i.e. the quarks and gluons). In fact, these are the interactions that will help to discover the Higgs.

Instantaneous luminosity is a measure of the rate of interaction between colliding beams of particles and can therefore be used alongside a cross section to determine the rate of production of a certain process. It is dependent on the number of particles in the beam, the density of the beam and the frequency of revolution, among other things. It is measured in units per area per second and hence, when integrated over time and multiplied by a cross section, gives the total number of expected interactions for a given process. The equation to calculate the instantaneous luminosity for two colliding proton bunches that have an assumed Gaussian distribution (in length) is:

$$L = \frac{N_b^2 n_b f_{\text{rev}} \gamma_r}{4\pi \varepsilon_n \beta^*} F, \tag{3.1}$$

where F is a factor which reduces the overall luminosity based on the angle for which the two bunches cross at the interaction point and is given by:

$$F = \left(1 + \left(\frac{\theta_c \sigma_z}{2\sigma^*}\right)^2\right)^{-\frac{1}{2}}. \tag{3.2}$$

Tab. 3.1 describes each variable defined in the previous two equations and gives each value at the design luminosity of the LHC (approximately $10^{34}\,\text{cm}^{-2}s^{-1}$). The amount of energy stored in all protons circulating the LHC at design luminsity is equivalent to the same Harley Davidson traveling at a speed of over 300 miles per hour. However, the maximum instantaneous luminosity deemed safe for the LHC operation is a bit smaller

with maximum instantaneous luminosity of approximately $5 \times 10^{33}\,\mathrm{cm}^{-2}s^{-1}$ reached in 2011.

Table 3.1: Default values for the variables required to calculate the designed instantaneous luminosity for the LHC.

Parameter	Value	Description
N_b	1.15×10^{11}	number of particles per bunch
n_b	2808	number of bunches per beam
f_{rev}	11245	revolution frequency (Hz)
γ_r	7461	relativistic gamma factor
ε_n	3.75	normalized transverse beam emittance (μrad)
β^*	0.55	beta function at collision point (m)
F	0.836	geometric reduction factor due to beam crossing angle
θ_c	± 285	full crossing angle (μrad)
σ_z	7.55	root mean square of the bunch length (cm)
σ^*	16.7	transverse root mean square beam size (μm)

Parton collisions are further complicated by the fact that protons do not solely contain two up quarks and a down quark bound by gluons. While the sum of the constituents of the proton has to always have a colorless group of two up quarks and a down quark (the valence quarks), the gluons binding the proton together can pair produce quarks and anti-quarks which we call "sea-quarks."

To understand what interactions are actually occurring when two protons collide, one has to understand the fraction of the proton's momentum and energy each of the partons carry. Deep inelastic scattering of electrons off of protons and neutrons help to shed light on this issue. In a series of experiments, high energy electrons are fired at protons such that they scatter inelastically, breaking up the proton in the process. By measuring the resulting momentum and angular distributions of particles resulting from these experiments, one can determine the fraction of energy and momentum carried by the partons which comprise the proton. As an example, Fig. 3.2 shows the fraction of energy carried by gluons, the valence quarks and the sea quarks for two different energy protons. Notice that while the up quark, down quark and gluons are the dominant high momentum carriers, there is still significant contribution from sea quarks.

Now is a good time to introduce two important observable quantities used in

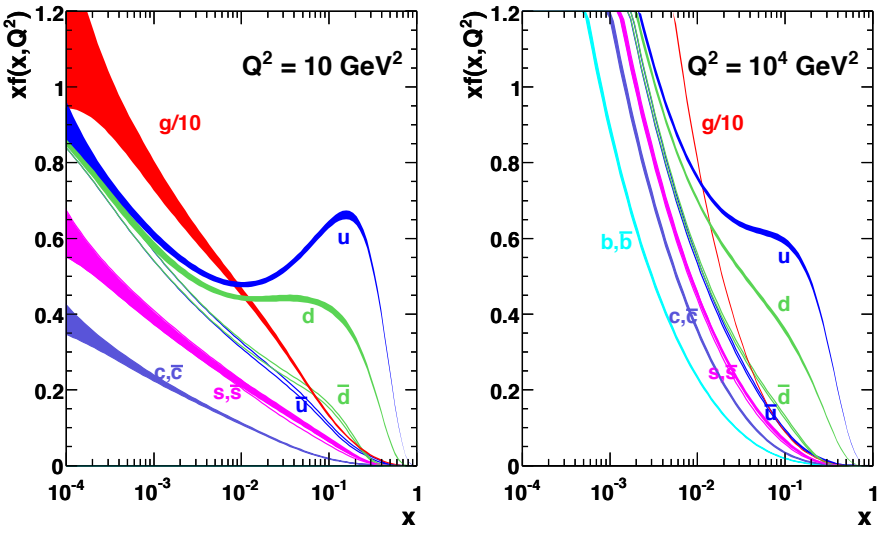

Figure 3.2: The parton distribution functions and their associated error for a proton at a momentum transfer scale of $Q^2 = 10$ GeV^2 (left) and $Q^2 = 10000$ GeV^2 (right) as a function of x, the fraction of the proton's momentum carried by the parton.

particle physics. While we do know the center of momentum frame for two colliding protons, we do not know the center of mass frame of the two colliding partons. For this reason, particle physicists use two quantities which are invariant under changes in parton momentum along the proton momentum direction. The first quantity, transverse momentum (p_T), measures the amount of momentum a particle has transverse (i.e. perpendicular) to the collision direction. The second quantity, pseudorapidity (η) is a transformation from the polar angle (see the coordinate layout description in Sec. 3.2) into a quantity which is invariant to the rest frame of the collision (i.e. if the two partons have the same momentum or if the two partons have vastly different momentum):

$$\eta = -\ln\left[\tan\left(\frac{\theta}{2}\right)\right], \tag{3.3}$$

where θ is the angle between the incoming proton and an outgoing particle. as shown in Fig. 3.3.

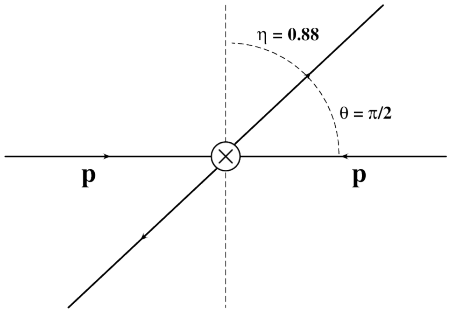

Figure 3.3: Depiction of the pseudorapidity and transverse momentum variables used in proton-proton collisions.

3.2 The CMS Detector

CMS is one of two general purpose detectors situated along the beam line of the LHC. While compact compared to its sister experiment, A Toroidal LHC Apparatus (ATLAS), CMS is by no means small. Weighing in at over 12,000 tons, cylindrical in shape, it is over 21 meters in length with a diameter over 14 meters . It sits 100 meters underground at LHC Point 5 (see Fig. 3.1) near Cessy, France. An overview of the CMS detector can be seen in Fig. 3.4.

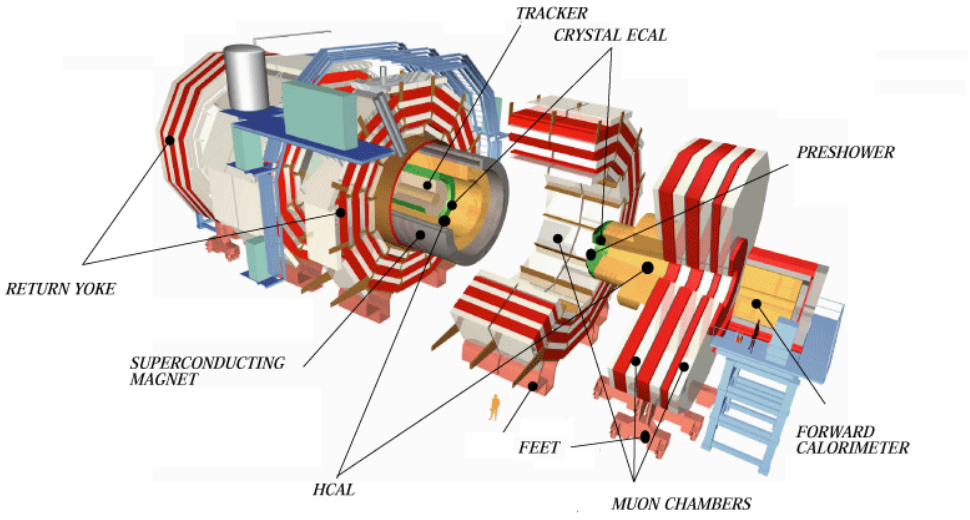

Figure 3.4: Overview of the Compact Muon Solenoid detector.

Compatible with the LHC physics program, it was designed to allow the study of

many different questions plaguing particle physics during its conception. To achieve its diversity, CMS is capable of measuring, with high precision, the location, momentum and energy of many different types of particles. In addition, it is able to handle the challenging conditions presented to it by the high luminosity and high energy conditions of the LHC. To deal with the over one billion expected interactions per section expected from the LHC at design luminosity, CMS is a very high granularity detector, and hence has many many electronic channels each with excellent time resolution and is designed to be radiation hard to deal with the multitude or particles produced during each bunch crossing.

CMS contains a strong magnetic field produced by a superconducting solenoid. An inner field strength of 3.8 Tesla ensures that even the highest momentum particles propagating through the detector bend enough to have a precise momentum measurement. Inside the solenoid sit both the silicon and pixel tracker systems and both the electromagnetic (ECAL) and hadronic calorimeters (HCAL). The large number of channels in the pixel tracker ensures precise measurement on the origin of particles both produced near the beamline and those with longer lifetimes decaying at larger diameters. The silicon strip detector has at least 10 layers along any particles' path allowing precise particle "tracking" and momentum measurement. The ECAL, with over 75,000 lead-tungstate ($PbWO_4$) scintillating crystals, gives excellent energy measurements to particles which interact electromagnetically, namely electrons and photons. The HCAL, a sampling calorimeter made of brass, completes the sub-detectors existing inside of solenoid and gives decent energy resolution for particles which interact hadronically, e.g. pions and kaons.

Outside of the solenoid magnet exists the final sub-detector, the muon detector. Made up of three separate sub-detectors, the muons chambers exist between large iron frames (yokes) which serve two purposes. First, they prevent particles other than muons from reaching the outermost muon chambers and hence allow for excellent muon identification. In addition, the yoke allows for a strong return magnetic field to fill the entirety of the muon detector system which allows for better muon momentum resolution.

The coordinate system of CMS is centered at the nominal interaction point at the center of CMS's cylindrical shape. For simplicity, we define the y-axis to point

vertically upward (towards the heavens), the x-axis then points towards the center of the LHC ring and hence the z-axis points along the beam line, counter-clockwise around the LHC. The azimuthal angle, ϕ, is measured from the zero position of the x-axis in the x-y plane while the polar angle, θ, is measured from the positive z-axis which now gives perspective to Eq. (3.3).

A picture of the CMS detector can be seen in Fig. 3.5. For a complete description of the CMS detector, please have a look at Ref. [27], from which all information, unless explicitly stated otherwise, in this section derives. The following sub-sections give a fuller description of each of the various pieces that make up the CMS detector. This is by no means meant to be a full detector description, however, any details of importance to this specific analysis are explicitly mentioned.

3.2.1 The Superconducting Solenoid

Particles influenced by electromagnetic fields experience the Lorentz force:

$$F = q\left(\mathbf{E} + \mathbf{v} \times \mathbf{B}\right),$$

where q is the charge of the particle, $\mathbf{E}$ is the electric field vector, $\mathbf{v}$ is the velocity vector of the charged particle and $\mathbf{B}$ is the magnetic field vector. Therefore, the curvature (the inverse of the radius of curvature) of a charged particle in a magnetic field is directly proportional to the magnetic field strength and inversely proportional to the particle's momentum. Achieving maximum particle curvature, among other things, allows for the maximum precision measurement of a charged particles momentum. Therefore, in the three meters a particle has to traverse from the interaction point to outside the CMS solenoid, gaining maximum curvature is key. CMS achieves this with its superconducting solenoid.

Made up of Niobium-Titanium (NbTi), the solenoid was designed to operate with a magnetic field strength of 4 Tesla but is being safely operated at a strength of 3.8 Tesla. At maximum strength, the solenoid stores over 2 billion Joules of energy, and with a mass of over 220 tons, far and away exceeds the design of any other particle physics solenoidal magnet.

To allow for stronger magnetic field, and hence better momentum resolution, for

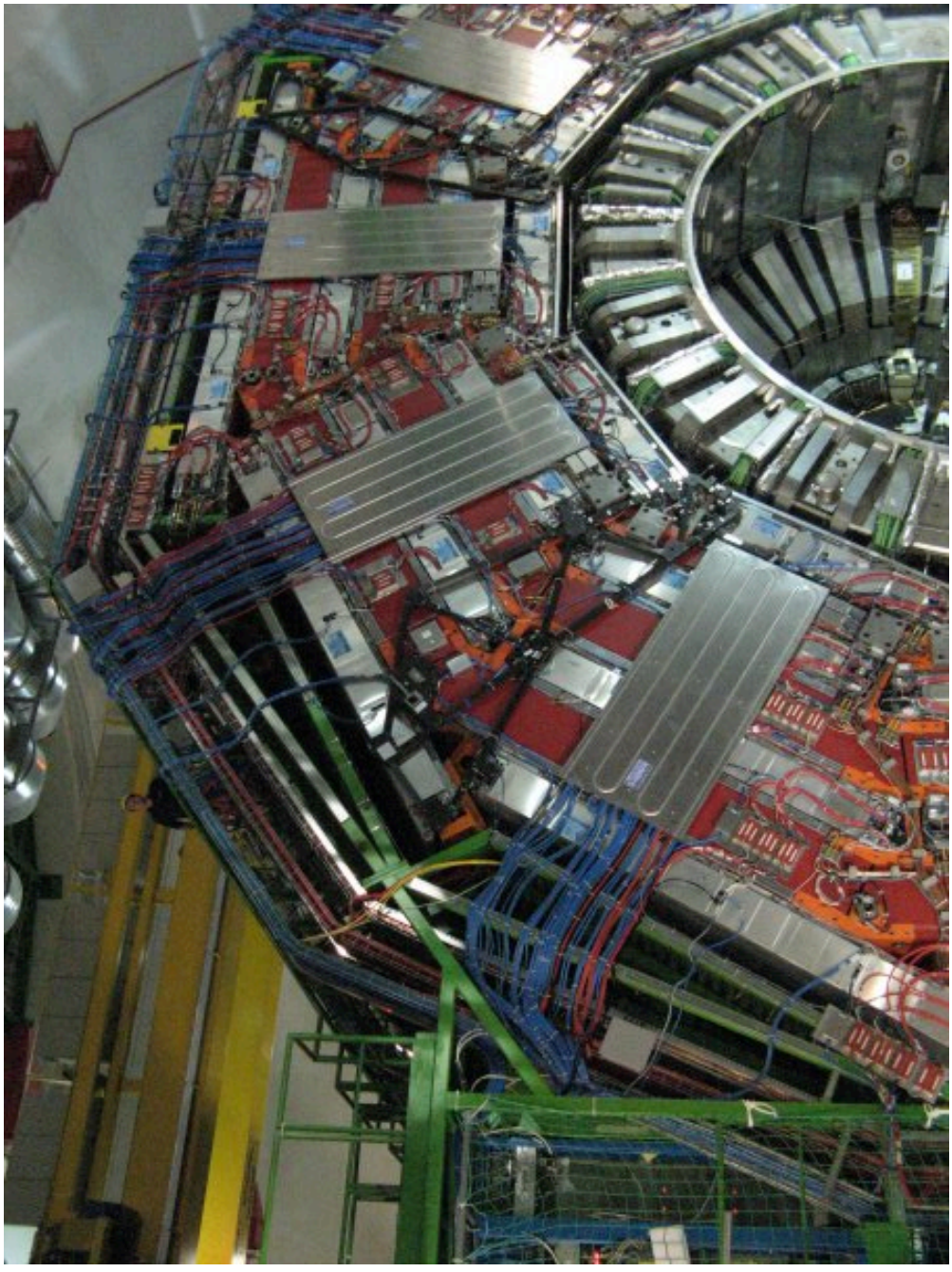

Figure 3.5: Photograph of the CMS detector underground at Point 5.

the muon chambers, the outside of the solenoid has been designed with iron yokes which offer integral support, provide additional stopping power for non-muons and propagate the magnetic field. The yokes can be seen in red in Fig. 3.4 The yokes help to steer the field back around the outside of the solenoid, thus increasing the magnetic field around the muon detectors.

3.2.2 The Silicon Detector

The innermost portion of the CMS detector is comprised of silicon particle detectors. Doped and negatively biased, when charged particles pass through the active region of a silicon detector, electric current is produced and measured such that the location of the particle is recorded. Combining the multiple positional measurements, the tracker also is used to determine the curvature of the particles, and thus, using the magnetic field strength, the particles momenta. The tracker was designed to have high charged particle "reconstruction" efficiency, good momentum resolution and be able to identify secondary vertices from longer lived particles.

To achieve these design considerations in the environment of the LHC all while fitting within the CMS solenoid, many aspects of the tracker had to be specifically tailored. First, in order to deal with the large particle multiplicities, the detector needed to be radiation hard, have a high granularity and a fast response time. The high granularity was achieved by using pixel silicon detectors in the inner most region. Outside of the pixel detector, silicon strips are used as the particle multiplicity density decreases as the square of the radius from the interaction point. This design achieves the desired position, momentum and vertexing resolution while keeping the occupancy down to a manageable 1% throughout. An overview of the silicon detector can be seen in Fig. 3.6 and details about the pixel and strip detector follow in the following two paragraphs.

The Pixel Detector

In order to achieve the 1% occupancy nearest the beam line, pixel silicon detectors must be used within a radius of 10 cm. The CMS pixel detector consists of three concentric cylindrical layers at 4.4, 7.3 and 10.2 cm with two sets of two disks at 34.5 and 45.6 cm on each side along the z-coordinate. Together, the "barrel" and "endcap"

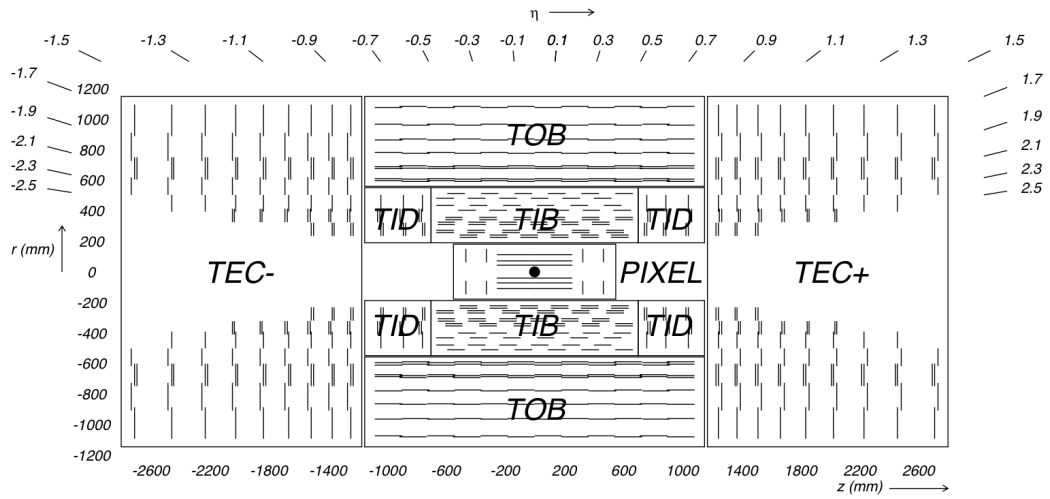

Figure 3.6: Layout of the tracking system projected into the rz plane. Modules are shown as lines and modules with back-to-back labels appear as double parallel lines.

pixel detectors cover a pseudorapidity range up to $|\eta| < 2.5$. The pixels themselves are approximately square with a size of 100 to 150 μm per side and give a spatial resolution of 10 μm in $r-\phi$ and 20 μm in z. Besides allowing for low occupancy, the pixel detectors can also be made radiation hard and are designed to give precise vertex position measurements.

Outside of the pixel detector sits the silicon strip detector. At these distances from the interaction point, a lower density of sensors can be used to still obtain the same occupancy. Strip detectors (long rectangular active regions instead of small pixels) are significantly cheaper to manufacture than pixel detectors while still providing the desired momentum resolution and channel occupancy. The strip detector can be divided into four different regions: the tracker inner barrel (TIB), the tracker inner disks (TID), the tracker outer barrel (TOB) and the tracker endcaps (TEC). Each region can be seen in Fig. 3.6. The TIB consists of four cylindrical layers in the barrel and is surrounded on each side by three disks from the TID. The TIB and TID extend out to a radius of approximately 55 cm and provide a position measurement resolution between 23 and 35 μm. The TOB surrounds the TIB and TID and provides another 6 cylindrical layers and provides slightly less resolution of around 35 to 53 μm. Finally, the TEC extends

out the detector in the z-direction by providing an additional 9 disk layers with resolution between 97 and 184 μm. The silicon strip detector also provides a pseudorapidity coverage inside $|\eta| < 2.5$. Some of the layers in the strip detector, namely the first two layers in each the TIB, TID, TOB and TEC as well as layer five in the TEC, carry an additional silicon strip detector mounted at a slight angle. This allows not just for an additional positional measurement but an additional measurement in the the "non-strip" direction (z in the barrel and r in the endcap).

With over 200 square meters of silicon, the inner silicon detector of CMS, or "tracker", is the largest in the world. Unfortunately, material comes at a performance cost. The silicon must all be powered, and in turn, the powered units must all be cooled (operating temperature is $-10°C$). The amount of material in the CMS tracker is shown in units of radiation length in Fig. 3.7. A radiation length is a characteristic of a material that describes the distance over which electrons and photons lose energy. After one radiation length, an electron, on average, will have lost all but $1/e$ of its energy via bremsstrahlung and $7/9X_0$ is the mean free path for photon pair-production. All of this material inside the CMS detector causes a few problems. First, particle momentum resolution is degraded as each particle has a higher probability for nuclear interaction and multiple scattering as it traverses the detector. Electrons and photons have higher probabilities to bremsstrahlung and pair create, respectively, causing issues measuring their energy in the electromagnetic calorimeter (see next section).

The tracker provides at least ten particle position measurements for any trajectory a particle can take through the detector. Fig. 3.8 shows the number of hits as a function of pseudorapidity. The overall initial transverse position (transverse impact parameter, $d0$) and the momentum resolution is shown in Fig. 3.8. The overall charged particle reconstruction efficiency, calculated using standard tag and probe techniques (see Sec. 5.3), is on average greater than 99% [28].

3.2.3 The Calorimeters

CMS has two calorimetry detectors, both situated inside the solenoid magnet. The first, directly behind the silicon tracker, is the electromagnetic calorimeter (ECAL), designed to measure the energy of particles which interact electromagnetically, i.e. elec-

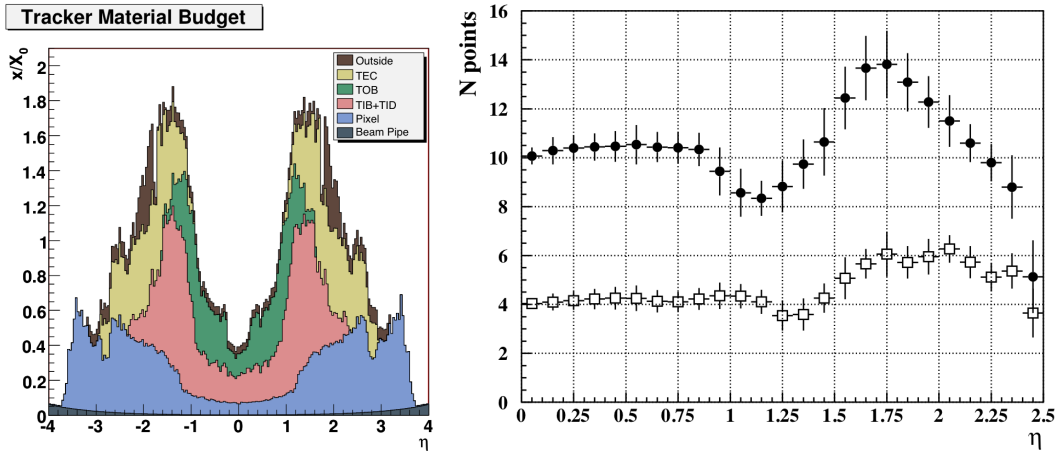

Figure 3.7: Radiation length of the CMS tracker as a function of pseudorapidity (left). Number of layers passed as a function of pseudorapidity (right). Black circles represent total layers while hollow squares represent the number of layers with a stereo measurement.

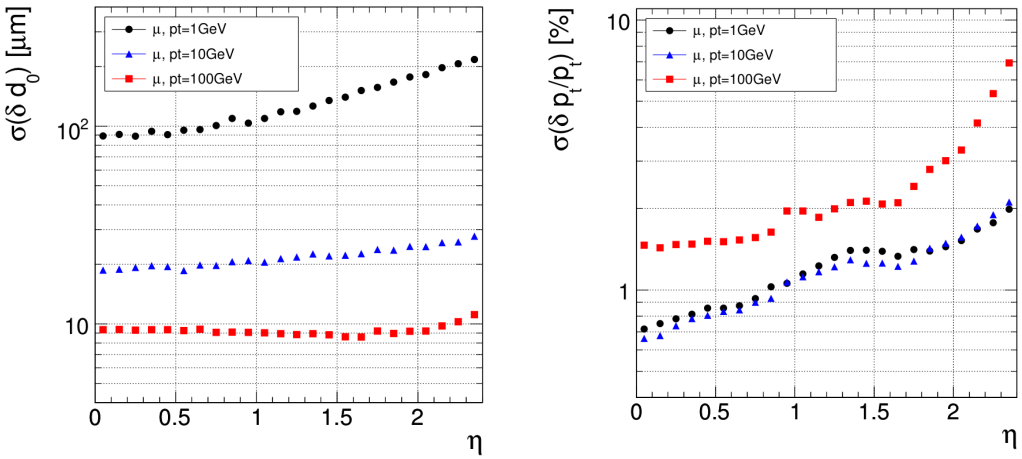

Figure 3.8: Muon transverse impact parameter resolution (left) and transverse momentum resolution as a function of pseudorapidity for various muon momenta: 1 GeV as circles, 10 GeV as triangles and 100 GeV as squares.

trons and photons. The second, directly behind the ECAL, is the hadronic calorimeter (HCAL), designed to measure particles interacting via the strong force. Both subdetectors were designed to be fully hermetic, have good energy resolution over a large area of the detector, and hence be able to accurately reconstruct the total amount of energy released for each bunch crossing. Combined, the calorimeters allow for the detection of neutrinos escaping from the CMS detector by measuring any energy imbalance. In addition, the calorimeters are designed to be thick enough to prevent most particles from piercing through the solenoid and into the muon chambers. To achieve these features in the small space between the tracker and solenoid, both detectors had to be composed of dense and highly segmented material.

Electromagnetic Calorimeter

Lead Tungstate ($PbWO_4$) crystals were chosen to comprise the fully hermetic and homogeneous ECAL. $PbWO_4$ satisfies the needs imposed by the LHC environment: the radiation resistance allows for long lifetime and the high density ($8.28\ g/\mathrm{cm}^3$) conquers the space constraints as well as allows for fine granularity and quick read out times. The homogeneity of the detector also allows for good overall energy resolution. $PbWO_4$ has a radiation length (X_0) of 0.89 cm and a Molière radius of 2.2 cm. The Molière radius gives a measure of the spread of energy from showering electron and photons and is defined as the radius which contains 90% of the shower energy. Having a small Molière radius also allows the use of smaller crystals and hence gives higher segmentation. Finally, $PbWO_4$ has a quick scintillation decay time which allows for read out times fast enough to deal with the designed 25 ns bunch cross spacing of the LHC.

The ECAL barrel (EB) contains 61,200 $PbWO_4$ crystals arranged in a cylindrical formation around the silicon tracker. Each crystal is rectangular in shape, 240 mm long ($25.8\ X_0$), 22×22 mm on the front surface and 26×26 mm on the rear surface. The EB covers a pseudorapidity range $|\eta| < 1.479$ with each crystal having a size in $\eta - \phi$ space of 0.0174×0.0174.

The ECAL endcaps (EE+ and EE-) each contain 7,324 $PbWO_4$ crystals and covers a pseudorapidity range $1.479 < |\eta| < 3.0$. Each EE is split into an upper and lower

disk, Dees, which arrange the crystals in an $x-y$ pattern while maintaining that the crystals point in the direction of the nominal impact position. The crystals are approximately 30×30 mm on their face with a length of 220 mm (24.7 X_0).

In addition to the EB and EE, there is an additional electromagnetic calorimeter stationed on each side directly in front of the EE. Called the preshower (ES), this detector gives additional radiation length and helps differentiate electrons and photons from pions. A full schematic of the ECAL system can be seen in Fig. 3.9.

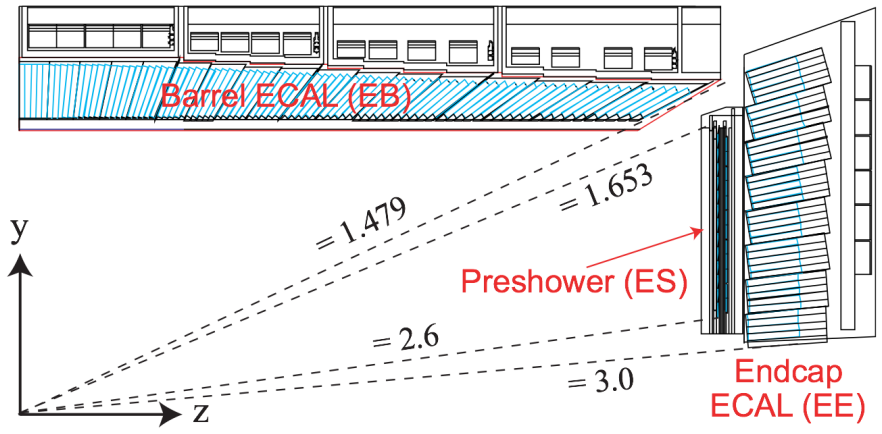

Figure 3.9: One quarter of the electromagnetic calorimeter system projected into the yz plane.

To convert the light created in the crystals to energy, silicon avalanche diodes (APDs) and vacuum phototriodes (VPDs) are used in the barrel and endcap, respectively. Both photodetectors were designed to be fast, have a high radiation tolerance and be able to operate in the presence of the CMS's magnetic field. In addition, the photodetectors have to be able to withstand the bombardment of hadronic particles passing through their active area without and to be able to amplify the, relatively, low light output of the $PbWO_4$ crystals.

Hadronic Calorimeter

The HCAL sits between the ECAL and the solenoid and is important for the identification and reconstruction of hadronic energy [29]. The hermetic and homoge-

neous nature of the HCAL also allows for a full reconstruction of each bunch crossings energy output and thus allows the inference on the direction and energy of any neutrinos that might have escaped the detector (which show up as a large imbalance in the measured energy). The HCAL is comprised of four different sets of detectors, the HCAL barrel (HB), the HCAL endcaps (HE), the outer HCAL (HO), and the forward HCAL (HF).

The HB and HE both use brass (70% Cu, 30% Zn), which has an interaction length, the length for which $1/e$ of hadrons have not interacted hadronically, of 15 cm, to cause as much hadronic showering as possible while still falling within the monetary budget. The HB covers a pseudorapidity gap $|\eta| < 1.3$ and contains 36 wedge shaped blocks of detector (18 around the cylinder on each half of the HB). Each wedge consists of flat brass absorber plates which run parallel to the beam axis with plastic scintillators interspersed throughout which convert the hadronizing energy into light for detection. The scintillators are distributed to give a spacial segmentation of 0.087×0.087 in $\eta - \phi$ space. The total interaction length of the HB varies from 5.92 to 10.6 λ_I depending on pseudorapidity. The HE takes over where the HB leaves off and covers a pseudorapidity range $1.3 < |\eta| < 3.0$. The granularity in this region allows for positional measurements with a size of 0.087×0.087 up to $|\eta| < 1.6$ and 0.17×0.17 beyond $|\eta| > 1.6$. The total depth of the HE is 9 interaction lengths. Both the HB and HE utilize multipixel hybrid photodiodes (HPD), which operate well in strong magnetic fields, to convert the scintillator light to electric signal.

After the HE and between $3.0 < |\eta| < 5.0$ sits the HF which, instead of brass, uses steel to absorb the hadronic particles. Due to the very large particle fluxes in this region, scintillator was scrapped for more radiation hard quartz fibers. These quartz fibers emit Cherenkov light which is then channeled to the readout photomultipliers. The segmentation in the HF gives the approximate size of each readout channel as 0.18×0.35 in $\eta - \phi$.

Finally, to supplement the energy measurement in the barrel, the region with the lowest interaction length, the HO sits outside the solenoid. In fact, it uses the solenoid as extra absorber material, which gives at least another 1.5 interaction lengths, depending on pseudorapidity. The HO utilizes scintillator material directly behind the solenoid

to measure the energy of any particles which hadronize inside the solenoid. With the ECAL giving approximately 1 interaction length of material, the total interaction length of CMS is always greater than 11.8, giving a less than 0.1% chance a hadron can survive through to the muon detectors.

3.2.4 The Muon Detectors

As the name implies, the Compact Muon Solenoid, was designed to efficiently and precisely detect muons. Muons, unlike the much lighter, and hence, radiative electrons, interact very minimally with matter, traversing even the densest parts of CMS (the ECAL and HCAL) with relative ease while at the same time depositing very little energy. Muons are also relatively long lived, and their lifetime easily allows them to escape the CMS detector before decaying. It is these reasons that the muon detectors are situated outside the solenoid, far from the interaction point (in both distance and material).

The muon system employs three different gas-based particle detectors which allow for excellent muon measuring capabilities. In addition to positional measurements, the muon detectors also provide muon identification, momentum and triggering (see Sec. 3.4). The chambers sit inside CMS's iron return yoke which acts as an absorbing material for hadrons and other non-muon particles which try to penetrate throughout the solenoid. In the barrel, the drift tube (DT) sub-detector sits, similarly shaped to other barrel sub-detectors, cylindrically concentric. The endcap houses cathode strip chambers (CSC) which exist in four layers on each side of the barrel. Finally, interspersed throughout the barrel and endcap, sit resistive plate chambers (RPC) used to enhance the timing resolution on the detection of muons. A graphic overview of the CMS muon system can be seen in Fig. 3.10.

Drift Tubes

Drift tubes are long cylindrical tubes filled with gas and threaded with an equally long conductive wire (the anode). The inside of the cylinder is also lined with a conductive material (the cathode). The gas, always a mixture containing a noble gas with a full set of valence electrons, relinquishes electrons as charged particles traverse through. A

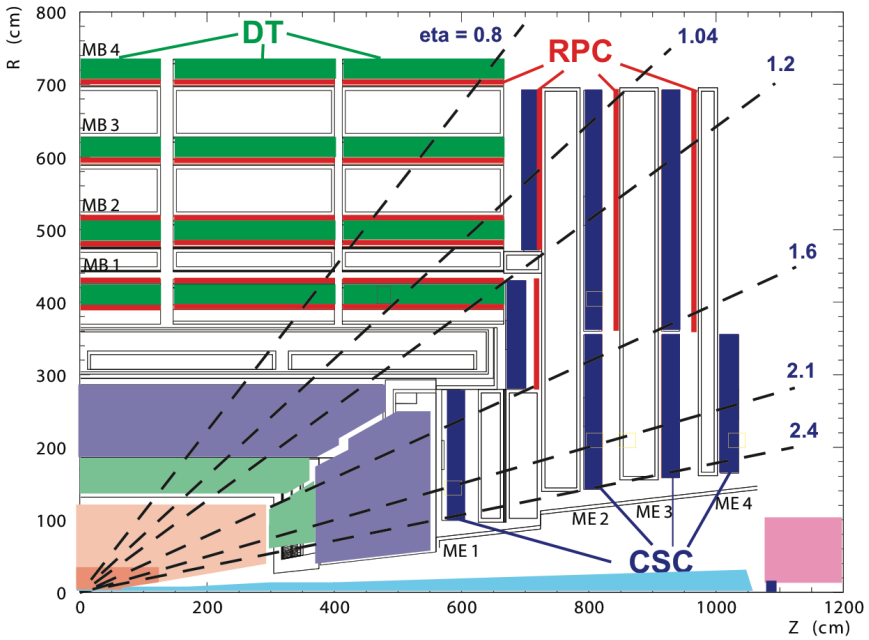

Figure 3.10: Overview of the CMS muon subdetector system. The drift tubes, situated in the barrel region, are shown in green, the cathode strip chambers, situated in the endcap region, are shown in blue and the resistive plate chambers, situated throughout, are shown in red.

bias voltage is applied across the wire and the cylinder causing the electrons to flow one way and the positively charged ions they have vanquished the other. Particle detection is then achieved through measuring the amount of induced current.

The DT system of CMS sits in the barrel region outside the solenoid and covers a pseudorapidity range $|\eta| < 1.2$. Each set of drift tubes are arranged as a rectangular chamber and staggered throughout the return yoke. There are 250 chambers arranged in four concentric cylinders of chambers (stations) divided by the five rings (wheels) of the return yoke. The chambers have a slight overlap to ensure hermeticity in 12 different sectors of each ring and wheel, each covering 30° in azimuthal angle. The four stations and two and a half of the wheels can be seen in green in Fig. 3.10.

Each chamber except the last has three sets (superlayers) of four planes of drift tubes. Two of the superlayers in each chamber run parallel to the beam direction to measure the $r-\phi$ position. The third superlayer in the first three chambers have drift tubes that run perpendicular to the beam line allowing an additional measurement in the z direction.

In all, there are over 172,000 drift tubes in the DT system each with an approximate length of 2.5 m. This length, coupled with the low background and muon rates and the uniform magnetic field in this region of the detector allow for the one-dimensional position measurements of the DT system. The DTs give a time resolution on the order of a few ns, well within the timing constraints of the LHC, and a global resolution in the $r-\phi$ direction of 100 μm.

Cathode Strip Chambers

A cathode strip chambers is similar to a drift tube chamber in that it is a gaseous detector filled with anode wires. Instead of a cathode tube per wire, the anode wires are stretched in parallel and surrounded on either side by a plane of cathode material. One plane of the cathode is segmented into strips which run perpendicular to the anode wires. The induced charge distribution on the wires and strips then gives a fully two-dimensional measurement of a passing particle (in addition to the third dimension known by the position of the detector). In addition to giving three-dimensional positional measurements, the CSCs were also designed with a fast response time, fine segmentation

and to be radiation hard in order to deal with increased background and muon rates and the non-uniform magnetic field in the endcap region (as opposed to the lower rates in the barrel in which positional ambiguity can be tolerated).

The CSCs operate in the pseudorapidity region $0.9 < |\eta| < 2.4$. Like in the barrel, there are four stations in each endcap region, arranged in radial disks perpendicular to the beam line. There are 468 chambers in total, each trapezoidal in shape and arranged side-by-side circularly around the beam line in two concentric circles. The anode wires run along the azimuthal direction and provide the radial measurement while the strips run lengthwise in a radial direction and give a measurement in ϕ. The overall positional resolution of the CSC is between 75 and 150 μm. The CSC system is shown in blue in Fig. 3.10.

Resistive Plate Chambers

The goal of the RPC muon detector system is to compliment the CSCs and DTs by adding faster readout times at the expense of positional resolution. The RPC chambers of CMS consist of two gaseous regions separated by a common strip readout anode plane which gives adequate positional resolution. Operating with a time resolution well below the minimum bunch crossing, the RPCs are ideal detectors to be used to "trigger" the CMS detector (see Sec. 3.4). The RPC system covers a pseudorapidity range $|\eta| < 1.6$, originally designed to cover the full range, it will be completed during the next upgrade. The RPC chambers can been see in in red in Fig. 3.10. Running along the beam direction (and hence measuring the azimuthal angle), six (three) layers of chambers exist in the barrel (endcap) with over 480 chambers in total each approximately 2.5 meters in length.

Summary

Overall, the muon system was designed to have an efficiency of over 95% for detecting muons with a resolution of less than 10% for muons up to 200 GeV in transverse momentum, increasing to a resolution between 15% and 40% for TeV muons (depending on η). Using the tracker as an additional set of measurements, the expected resolution drop to around 1% for lower p_{T} muons and down to approximately 5% for

muons in the TeV range. The expected resolution on the transverse momentum muon measurement can be seen for two different pseudorapidity ranges in Fig. 3.11.

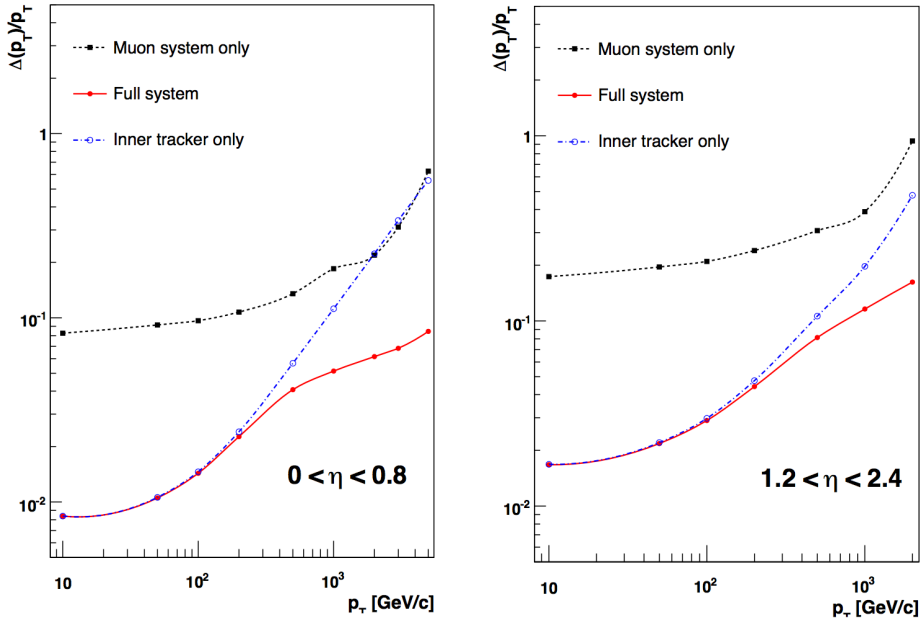

Figure 3.11: Muon momentum resolution for two different pseudorapidity regions, $0 < |\eta| < 0.8$ (left) $1.2 < |\eta| < 2.4$ and (right), as a function of transverse momentum using only the muon system (black), only the inner tracker (blue) and the combined muon and tracker detectors (red).

3.3 Integrated Luminosity Calculation

CMS uses two different techniques to measure the instantaneous luminosity, and subsequently the total integrated luminosity [30, 31]. Both methods employ the use of Van der Meer scans [32], modulation of the two beam positions until maximum overlap is achieved to determine the maximum instantaneous luminosity.

The first method uses the HF calorimeters which are very far forward at $|\eta| > 3.0$ and measures the average fraction of empty calorimeter readouts when triggering on zero-bias events defined by random triggers which are completely agnostic of activities

in the detector. This fraction can then be converted into a cross sectional measurement which in turn can be used to measure the instantaneous luminosity using Eq. (3.1).

Problems with non-linear HF response as a function of instantaneous luminosity, among other problems, led to the creation and use of the second method. This method relies on the fine granularity of the pixel detector. With a very small fraction ($\sim 0.1\%$) of particles leaving deposits in the same pixel, the number of pixel clusters found during a bunch crossing can be directly related to the proton-proton cross section, again deriving the luminosity through (3.1).

The data used in this analysis was taken over the course of 2011 during which time the LHC delivered approximately 5.7 fb^{-1}. Between March and October of that year, CMS was able to record 5.2 fb^{-1} of this data of which 4.6 fb^{-1} was certified by the CMS collaboration as usable for this analysis. The uncertainty from this luminosity measurement used for all analyses using 2011 data in CMS is 4.5%. This error must be taken into account for any process which is estimated from simulation. Fig. 3.12 shows the amount of data delivered by the LHC and recorded by the CMS detector as a function of time in the year 2011.

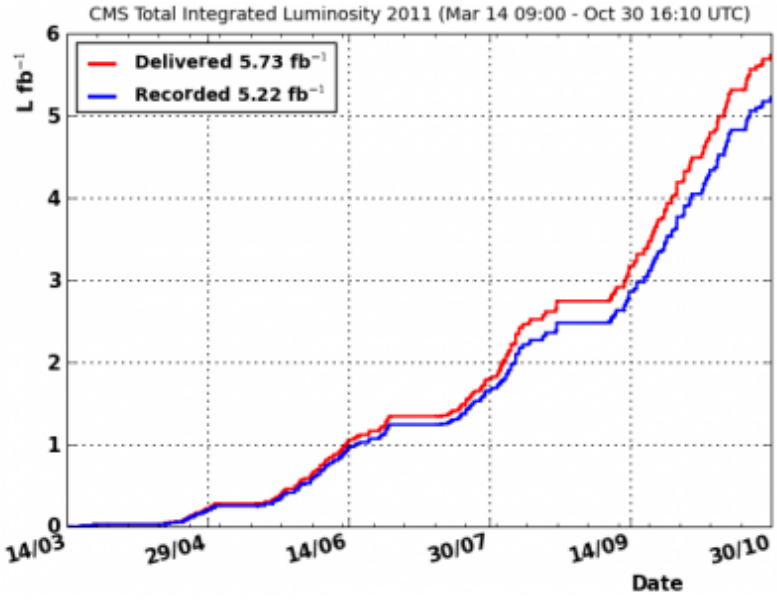

Figure 3.12: The amount of data delivered by the LHC (red) and the amount of data collected by the CMS detector (blue) as a function of date in the year 2011.

3.4 Data Acquisition and Triggering

With nearly 80 million channels, and a bunch crossing every 25 ns having up to 20 proton-proton interactions per crossing, an inordinate amount of data is produced by the CMS detector when the LHC is running at design luminosity. At approximately 100 kilobytes of data per interaction, computing design constraints limit the number of interactions that can be written to disk to the order of a few hundred per second. The 25 nanoseconds between bunches gives an interaction rate of 40 MHz resulting in a data reduction need on the order of 10^5. To accomplish this feat, CMS has designed a data acquisition (DAQ) and triggering system which utilizes massive computing infrastructure and custom hardware designs. It is designed to keep the most interesting interactions across a broad range of physics goals. If an interaction (from here on, I'll refer to an interaction by the high-energy community's nomenclature: an event) doesn't pass the trigger system, it is lost forever.

Triggering occurs in two steps, the first of which, predictably referred to as Level 1 (L1), has the task of reducing the load from 40 MHz down to 100 kHz[33]. To do so, it employs a farm of custom hardware processors using only coarse and lower resolution data to make decisions while storing the rest of the event data in pipelines awaiting instruction. Here, only calorimetric and muon chamber information is available to make decisions based on the energy and quantity of depositions in the detector. The data from the events passing the L1 trigger are processed, compressed and zero-suppressed and sent for handling by the DAQ. The DAQ then stores and processes the information and sends it along to the second trigger step. The high level trigger (HLT), again aptly named, is a farm of standard CPUs running in parallel that can run a fuller event reconstruction on the event to make more informed decisions about which events to keep. In fact, each computer is running the same software suite and executes code very similar to algorithms described in the next section. A pictorial representation of the trigger and DAQ chain can bee seen in Fig. 3.13.

As the LHC ramped up its instantaneous luminosity over the course of 2011, and hence the rate of interactions, the triggering requirements had to become more and more stringent to keep the recorded event rate around 300 Hz. Triggers appropriate for this search were designed to search for pairs of high p_{T} leptons, either muons or electrons.

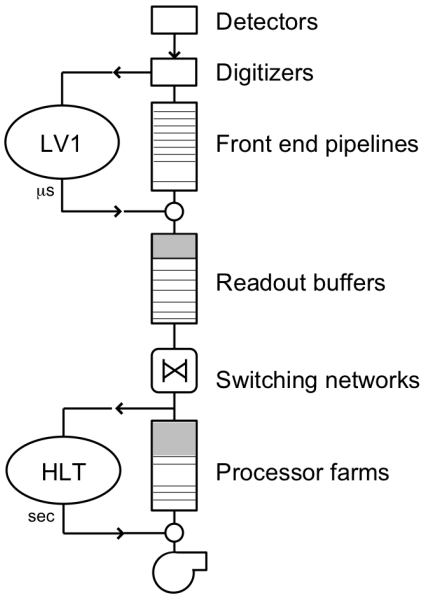

Figure 3.13: Pictorial representation of the data acquisition system and the flow of data from the CMS detector through both trigger levels.

The implications of the increasing luminosity were such that the p_{T} thresholds at the HLT trigger level had to continue to increase throughout the year. Unfortunately, this results in lower acceptance rates of the interesting events.

3.5 Particle Reconstruction and Identification

The digitization of the events selected by the trigger needs to be "reconstructed" into a fuller, higher-level, description of the particles present as a result of the proton-proton interaction. Many algorithms have been developed by the CMS collaboration to reconstruct particles, but only the ones used in this analysis will be described here.

Charged particles, electrons, muons and jets are all important pieces of this analysis and must be identified precisely. All of these algorithms are described in the following sections.

3.5.1 Charged Particle Reconstruction

Charged particles traversing the CMS detector first deposit energy in the CMS tracker, leaving thousands of positional measurements to interpret per bunch crossing. Determining the trajectory of these charged particles amongst this mess is then an exercise in pattern recognition. Each charged particle can be described using five parameters which model its trajectory through a magnetic field. "Tracking" is the process of finding "tracks," paths of charged particles, through the CMS tracking system [34, 35, 28].

Individual silicon strip and pixel channels with a threshold above an acceptable signal-to-noise ratio are clustered together based on proximity producing a collection positional measurements (along with the error). The "hits" in the inner portion of the detector are then used to seed multiple tracking steps, each designed to find tracks from charged particles with different properties. Each step takes an initial trajectory measurement from a seed and propagates the trajectory from the inside to the outside of the tracker using a combinatorial Kalman filter (CKF) [36]. After propagation ends, the tracks are measured for quality and any hits on good quality tracks are removed from consideration before creating the seeds for the next tracking step. The tracks produced with each step are then merged into a single collection, throwing out any duplicate tracks by comparing shared hits and keeping the track of higher quality.

The seeding step proceeds by searching for combinations of two or three hits near the beam line compatible with a particle trajectory with high enough energy coming from the interaction point. The initial particle trajectory is estimated using either a seed triplet or a seed pair and the beam spot. In all there are seven tracking iterations. The first two steps are seeded using only triplets from the pixel detector, the second step dropping the p_{T} threshold after the higher p_{T}, and hence lower background, first step. The third step uses pairs of pixel hits to gain additional efficiency. The fourth step again uses pixel triplets, but with a looser requirement on the compatibility with the interaction point to search for displaced tracks from particles with longer lifetimes. The fifth step again uses triplets, but allows for combinations of hits in both the pixel and the strip detectors, allowing for the seeding of particles which have slightly longer decay lengths or might have missed a pixel hit (due to detector inefficiency). The final two steps uses pairs and triplets of hits at further radii in the strip detector to search for particles which

have a large displacement.

In each step, after the seeds have been created, the initial trajectory estimate is propagated inside-out layer by layer through the detector using the CKM algorithm. The algorithm accounts for losses of energy as the particle traverses the material in the detector as well as the possibility of multiple scattering. At each layer, the position of the trajectory is estimated and any hits compatible with the position are added to the trajectory. If more than one compatible hit is found, multiple trajectories are kept and further propagated. In addition, for each layer, a new trajectory is created with no hit to allow for detector inefficiency. The process continues until either too many layers have been crossed without a hit or the trajectory reaches the last layer of the tracker.

After all trajectories have been propagated, a final trajectory fit to the collected hits is performed. Any outlying hits that fall too far away from the overall fit are removed. This gives a final, accurate measurement of the track's parameters. Vertex compatibility, numbers of hits in the track and the χ^2 of the fit are used as quality control selections. Hits from tracks passing tight quality selections are removed from consideration in subsequent tracking steps.

After all seven steps have been performed, the resulting tracks from each step are merged into a single collection. To ensure that no charged particles have been reconstructed twice, any tracks which share a large fraction of hits are compared and only the best quality track is kept.

3.5.2 Vertex Reconstruction

In the high multiplicity environment of the LHC, it is essential to measure the number of proton-proton interactions for each bunch crossing. Typically, only one of these interactions is responsible for the high p_{T} process which triggered the event, and measuring lepton impact parameters with respect to the correct vertex is essential for the rejection of muons from semileptonic heavy flavor decays and electrons from photon conversion. Thus, a high vertex reconstruction efficiency, a low fake vertex rate and the ability to differentiate nearby interactions are all properties needed for vertex reconstruction at CMS.

Vertex reconstruction is performed in two steps. First, tracks are clustered to-

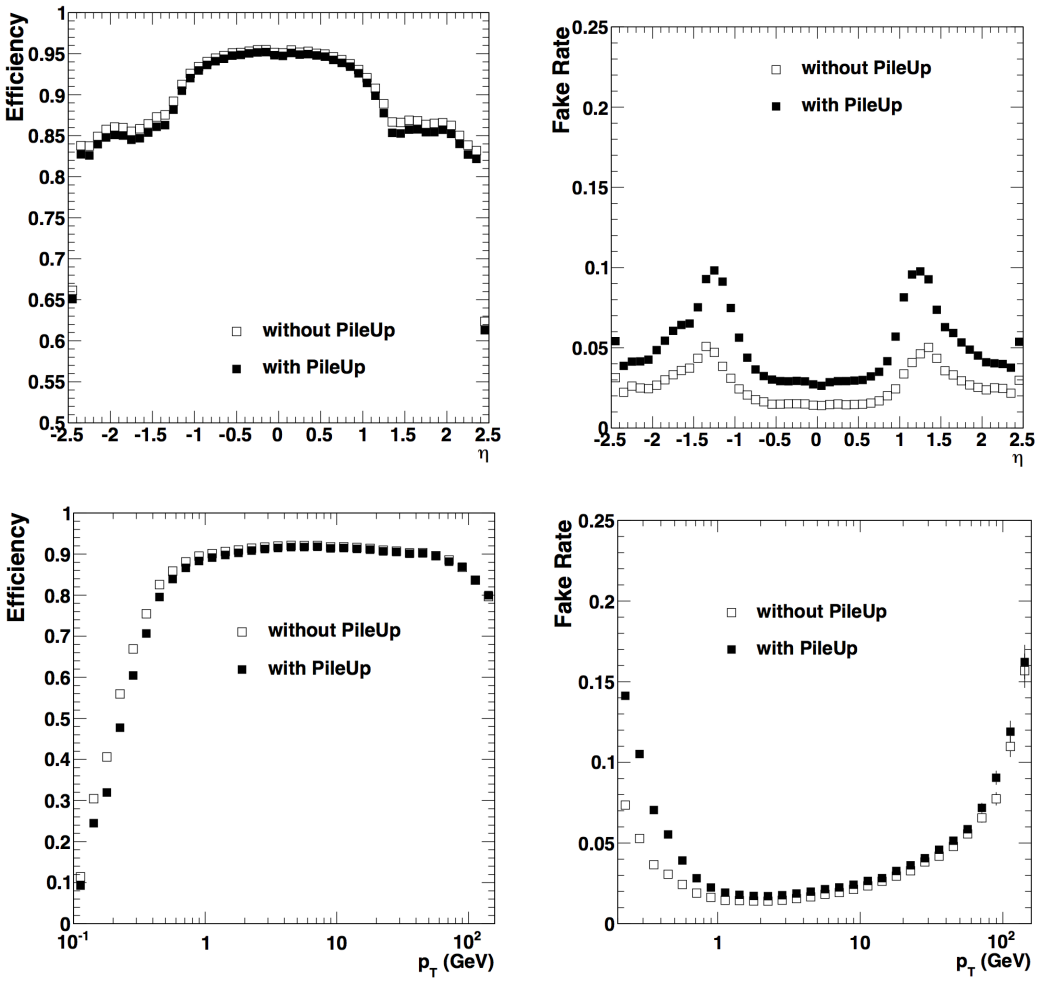

Figure 3.14: Efficiency (left) and fake rates (right) versus pseudorapidity (top) and transverse momentum (bottom) for reconstructed tracks in simulated $t\bar{t}$ events. Efficiency is defined as the fraction of simulated charged particles reconstructed as tracks while the fake rate is defined as the fraction of reconstructed particles not matched to a simulated particle. The open squares are for events with no pile-up (one interaction per crossing) while the filled squares are with high pile-up (eight interactions per crossing).

gether using the deterministic annealing algorithm [37, 38]. This algorithm iteratively clusters tracks with nearby impact parameters first with large windows and allowing a single track to be clustered multiple times. Each interaction tightens the clustering window until a stopping condition is met. Tracks are not allowed to cluster to vertices if their transverse impact parameter is larger than 3 cm or the longitudinal impact parameter is larger than 4 cm. The deterministic annealing algorithm was specifically chose due to its high clustering efficiency even in the face of the noisy LHC environment. Studies on the vertexing efficiency in fact show that the vertex reconstruction response as a function of the number of interactions is linear.

The second step takes each cluster of tracks and fits the vertex position using the adaptive vertex fitting algorithm [39, 40]. This algorithm weights tracks in the cluster based on compatibility with the vertex position (and de-weights the tracks that are more incompatible) giving a good vertex resolution of less than 50 μm depending on the number of tracks present in the cluster. More vertex reconstruction performance results can be found in Ref. [41].

3.5.3 Electron Reconstruction and Identification

Electrons are one of the two detectable final state particles used to identify W decays in this analysis, therefore, it is important to reconstruct and identify electrons efficiently and to know their energy to a high precision. Electrons interact primarily via the electromagnetic force and hence deposit a majority of their energy in the ECAL. However, due to the large amount of material the electron must traverse in the silicon tracker, the electron radiates a significant amount of energy via bremsstrahlung and hence the "footprint" of the electron is very complex. In addition, other particles also leave a significant amount of energy in the ECAL, namely hadrons and the π^0, which decays predominantly to two photons and 100% of the time electromagnetically. Therefore, strong fake electron rejection is needed in the form of electron identification. The identification of electrons and rejection of fake electrons are left to be presented in the context of this analysis in Sec. 5.1.1 while the reconstruction alorithm is summarized in the next paragraphs. More information about electron reconstruction can be found in Ref. [42, 43].

The first step of electron reconstruction is to identify clusters of energy in the ECAL, i.e. areas where many crystals in close proximity have large energy deposits. As the electron travels through the silicon tracker, bremsstrahlung (brem) causes losses of energy to photons which then also deposit energy in the ECAL. The strong magnetic field bends the electron further and further in the azimuthal direction the more energy it has lost. Therefore the footprint of the electron is such that it is long in ϕ and narrow in η and multiple clusters of energy need to be clustered together to form a "Super Cluster (SC)" containing the full amount of energy originally possessed by the electron.

After all SCs have been clustered, electron reconstruction continues by searching for the footprint of the electron in the tracker. Hits in the pixel detector compatible with pointing to the energy-weighted center of the SC are identified allowing for both positive and negative charge hypothesis. If two or three compatible pixel hits are discovered, they are used to seed a track building algorithm similar to that described in Sec. 3.5.1. The sole difference in the case of electrons is that track fitting is done with a Gaussian sum filter (GSF) [44] algorithm which can handle the large changes in electron energy due to bremsstrahlung.

In addition to this approach seeded by SCs, a separate algorithm is run in parallel. This is a "particle-flow" based approach which will be described in full in Sec. 3.5.5. Instead of first building a SC, the algorithm searches for pixels seeds for all clustered energy. For each found seed, the algorithm completes the trajectory building and then searches for clusters to add to the electron. At each layer in the tracker along the electron track, the position in the ECAL pointed to by the electron's current momentum is used to search for addition compatible clusters which could have come from a bremmed photon. After both algorithms are complete, the two collections of electrons are merged. The SC seeded algorithm dominates at higher energies ($> 20\,\text{GeV}$) while the track-seeded algorithm adds significant efficiency at lower energies as well as in crowded environments such as in the midst of a jet. A graphic showing the different pieces of the two algorithms can be seen in Fig. 3.15.

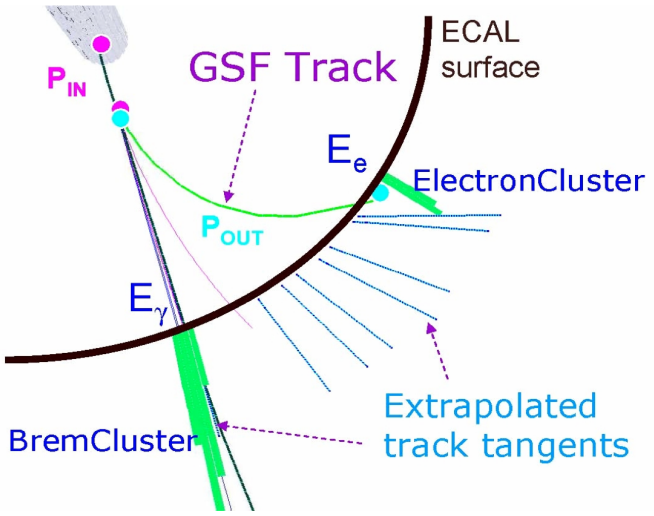

Figure 3.15: Depiction of the different portions of the electron reconstruction algorithm. Here the electron bremmed a photon with a significant amount of energy early in its traversal of the tracker and therefore there are two large clusters (depicted in green) of energy present in the ECAL (depicted in black)

3.5.4 Muon Reconstruction and Identification

Muons are the other final state lepton populating the final states of this analysis. Muons, in contrast to electrons, penetrate through to the outer regions of the CMS detector and hence have a smaller background contamination. Fake muons in this analysis come mostly from high energy hadrons which "punch-through" the dense calorimeters and leave deposits in the muon detector. Another source of background muons come from semi-leptonic decays of pions and kaons to real muons. Reconstruction efficiency for muons is quite high and we can therefore apply tight identification requirements to reduce these backgrounds for this analysis. This is discussed in Sec. 5.1.1. The muon reconstruction algorithm is described in the following paragraphs, with more detailed information available in Refs. [45, 46].

Muon reconstruction starts by first building segments in the muon subdetector. Positions of hits in the DT and CSCs are matched together to form small segments compatible with a single particle passing through each chamber. Using these segments (as well as hits in the RPCs) as positional measurements, another round of tracking is

performed starting from the inside of the muon chamber and working out to the edge of the detector. Here, the KF is used to propagate and fit the muon tracks making sure to account for losses of energy and multiple scattering as the muon passes through the iron yoke. These tracks built in the muon system are called "Stand-Alone" muons (SAM).

To use the information in the CMS tracker, where the muons also leave information, the SAMs are used to look for tracks built in the silicon tracker matching the expected location and energy. Matched tracks are combined with the muon-only tracks and a global refit is performed (again with the KF algorithm). The resulting muons are called "global muons."

In addition, another muon reconstruction algorithm is run to build muons with information from the both the tracker and the muon system. "Tracker" muons are seeded from the tracks built in the silicon tracker. Each track is extrapolated through both the ECAL and HCAL taking into account the expected trajectory and errors based on the magnetic field and the amount of material it crosses. The energy deposited in the ECAL and HCAL at the expected position of the muon's trajectory is checked to ensure compatibility with the expectation from the minimum ionizing particle. The expected muon trajectory is then extended into the muon system checking for matching segments. This algorithm gives higher efficiency for lower p_{T} muons at the expense of a larger background, however muon identification selections can be applied for further suppression.

3.5.5 Particle Flow Reconstruction

The algorithms described thus far fall under a category of "detector-based" algorithms. That is, reconstruction in each of the local subdetectors drives the higher level reconstruction of the particles that leave their signature in the respective subdetectors. The "particle-flow" (PF) algorithm is a paradigm shift from this type of algorithm in that it uses the very fine segmentation of the CMS detector to search for an individual particles across all the subdetectors. For example, a charged hadron will leave a track in the silicon tracker, a bit of energy in the ECAL and be stopped in the HCAL, depositing all of this energy. PF specializes in finding particles in this manner. When complete, the algorithm aims to have produced a list of all particles produced during the collision.

One large disadvantage of detector-based methods is the fact that energy could

be double counted, while with the PF algorithm, a global reconstruction of the event is done on a particle by particle basis ensuring that no energy is double counted. The resulting list of particles produced by this algorithm is used extensively throughout analyses at CMS. The calculation of missing energy ($\not\!\!E_{\mathrm{T}}$), jet clustering, τ reconstruction and identification are among the most important. The following briefly describes the particle flow algorithm, however, a complete description can be found in Refs. [47, 48].

Before the PF reconstruction commences, local reconstruction in each of the subdetectors is completed and provides tracks from the silicon detector (Sec. 3.5.1), clustered energy in both the ECAL and HCAL (similar to those discussed in Sec. 3.5.3) and the local reconstruction product in the muon system (Sec. 3.5.4). The general strategy is then to "link" these different inputs together to form the complete picture of particles traversing through the detector. Pieces from each of the subdetectors sufficiency near geometrically are first grouped together in blocks. Each block usually contains a few different inputs from each of the detectors, i.e. a track pointing to an ECAL cluster, or an ECAL and HCAL energy cluster on top of each other. The PF algorithm then proceeds as follows.

Any blocks linked to signatures from isolated muons or electrons are removed, as these have a very clean signature with very little background. The blocks belonging to these particles (including the clusters from brem products as discussed in Sec. 3.5.3) are then removed from the list of unidentified blocks. Next, the momentum of any track pointing to calorimetric clusters is compared to the energy contained in the ECAL or HCAL clusters. If the energy and momentum of the two are compatible, the object is labeled as a charged hadron, its energy is estimated as a weighted sum from both objects, and its constituents are removed from the list. If there is significantly more energy in the track than deposited in the calorimeter, a secondary muon identification is performed searching for non-isolated lower p_{T} muons. If identified, again, these constituents are removed. If no muon is found, tighter track requirements are applied to reject misreconstructed tracks. If there is significantly more energy in the calorimeters, neutral hadrons and photons are created comprising the energy unaccounted for by the track. At this point, only unlinked clusters remain and all ECAL clusters are hypothesized to be photons with all HCAL clusters hypothesized to be neutral hadrons.

3.5.6 Calculation of Missing Transverse Energy

Until now, particle detection algorithm that have been defined were all active, that is, they searched for traces of energy left by particles in the various subdetectors. However, neutrinos and other non-interacting particles from more outlandish non-SM theories not described here, leave no traces as they traverse the detector. Yet, we can infer their existence, direction and energy by looking at the sum of all of the energy in the event. As the two protons collide, all of their momentum is in the z-direction (and negative-z), with no momentum transverse to the beam line. Momentum conservation then requires that the transverse vectorial sum of all energy in the event should sum to zero. If this calculation is performed and an imbalance (missing transverse energy, $\not\!\!E_{\mathrm{T}}$) is detected, a non-interacting particle is hypothesized to have escaped from the detector. In the case of SM searches such as this one, the assumption is that this particle is a neutrino. Two $\not\!\!E_{\mathrm{T}}$ algorithms are used in this analysis, both of which are described in the following two sections.

Particle Flow $\not\!\!E_{\mathrm{T}}$

The first $\not\!\!E_{\mathrm{T}}$ algorithm takes as input the full collection of particle flow candidates and produces the negative vectorial sum. Particle flow $\not\!\!E_{\mathrm{T}}$ (pf$\not\!\!E_{\mathrm{T}}$) is defined as

$$\mathrm{pf}\not\!\!E_{\mathrm{T}} = -\sum_i p_{\mathrm{T}}^i,$$

where the summation runs over all particles reconstructed with the particle flow algorithm described in the previous section. For reference, the pf$\not\!\!E_{\mathrm{T}}$ distributions for $H \to W^+W^-$ events, WW continuum background, both of which have a source of real $\not\!\!E_{\mathrm{T}}$, and for Drell-Yan events, which do not have a source of real $\not\!\!E_{\mathrm{T}}$, see Sec. 4.4, are shown on the left of Fig. 3.16. Of importance, notice the large tails in the distribution for Drell-Yan. These come from two sources, instrumental and reconstruction problems affecting the PF algorithm, and hence giving a fake $\not\!\!E_{\mathrm{T}}$ signal as well as from decreased $\not\!\!E_{\mathrm{T}}$ resolution from the high pile-up environment during the 2011 run. Further information about pf$\not\!\!E_{\mathrm{T}}$ may be found in Ref. [49].

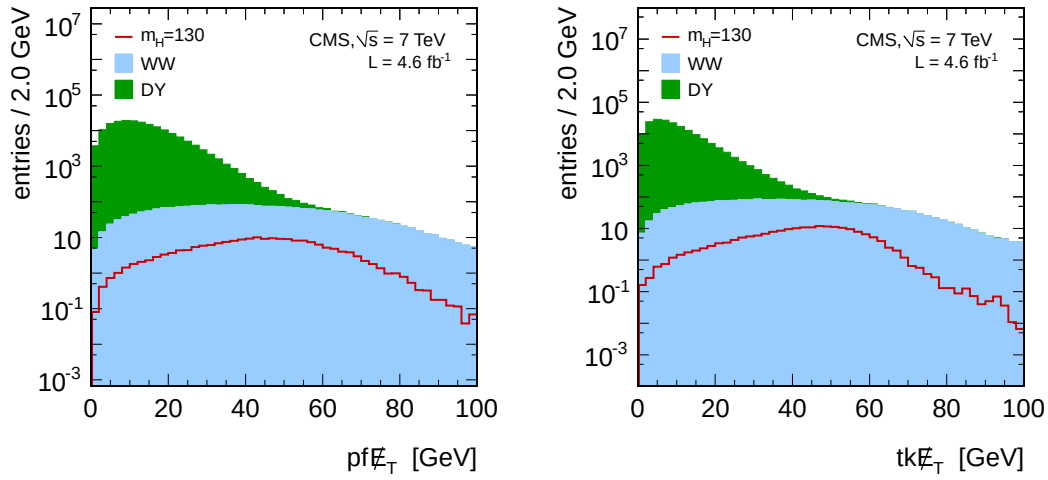

Figure 3.16: pf$\not\!\!E_{\mathrm{T}}$ (left) and tk$\not\!\!E_{\mathrm{T}}$ (right) simulated distributions for events containing sources of $\not\!\!E_{\mathrm{T}}$, signal ($H \to W^+W^-$, red) and WW continuum (blue), as well as for Drell-Yan background (green) which has no source of $\not\!\!E_{\mathrm{T}}$. The large tails of the Drell-Yan distributions cause significant background contamination and must be controlled carefully.

Charged $\not\!\!E_T$

In general, good agreement in $\not\!\!E_T$ distributions are seen between simulation and data in the presence of no pile-up. The agreement can be seen on the left in Fig. 3.17 which shows the pf$\not\!\!E_T$ distribution for data and simulation with a dedicated selection of prompt W production events with only one interaction vertex. However, with increasing pile-up, the situation worsens, as can be seen in the right plot of Fig. 3.17 where the pf$\not\!\!E_T$ distribution is significantly shifted towards higher values.

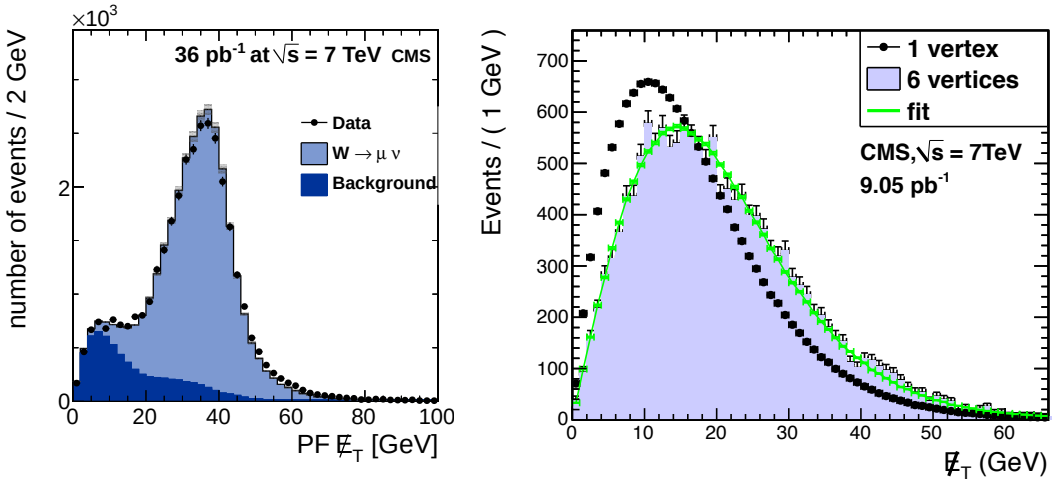

Figure 3.17: Data versus simulation of pf$\not\!\!E_T$ distributions for $W \to \mu\nu$ events which have real missing energy and shows good agreement (left). Comparison of the pf$\not\!\!E_T$ distribution for events with only one reconstructed vertex (black points) and for events with six vertices (histogram) along with a fit to the latter (right).

To combat this, a separate $\not\!\!E_T$ algorithm, tk$\not\!\!E_T$, is run which only uses charged PF candidates associated to the primary interaction vertex. In exchange for losing the information contained in the neutral particles in the event, tk$\not\!\!E_T$ has the advantage of only calculating the $\not\!\!E_T$ for particles known to be produced in the hard collision which triggered the event. tk$\not\!\!E_T$ is calculated as:

$$\text{tk}\not\!\!E_T = -\overrightarrow{p_T}(\ell_1) - \overrightarrow{p_T}(\ell_2) - \sum_i \overrightarrow{p_T}(i), \tag{3.4}$$

where $\overrightarrow{p_T}(\ell_1)$ and $\overrightarrow{p_T}(\ell_2)$ are the transverse momentum vectors of the identified leptons

in the event. $\overrightarrow{p_{\mathrm{T}}}(i)$ represent the transverse momentum vectors of charged PF particles which satisfy the following:

- the particle's track has $d_z < 0.1\,\mathrm{cm}$ with respect to the first primary vertex
- the track has $\Delta R > 0.1$ with respect to both leptons to avoid double-counting

Simulated tk$\not\!\!E_{\mathrm{T}}$ distributions can be seen in the right plot of Fig. 3.16. For events with real $\not\!\!E_{\mathrm{T}}$, the tk$\not\!\!E_{\mathrm{T}}$ still gives a reasonable measure of the $\not\!\!E_{\mathrm{T}}$. However, the real advantage comes when comparing tk$\not\!\!E_{\mathrm{T}}$ and pf$\not\!\!E_{\mathrm{T}}$ in events with no sources of $\not\!\!E_{\mathrm{T}}$. Very little correlation is seen between the two implementations hinting that instrumental sources of fake $\not\!\!E_{\mathrm{T}}$ affect the two distributions differently. In fact, the main cause of large pf$\not\!\!E_{\mathrm{T}}$ comes from detector resolution effects due to pile-up, while the main cause of misreconstructed tk$\not\!\!E_{\mathrm{T}}$ stems from the misreconstruction of leptons. Fig. 3.18 shows the tk$\not\!\!E_{\mathrm{T}}$ versus pf$\not\!\!E_{\mathrm{T}}$ distributions in Drell-Yan events on the left and signal events on the right. Exploiting this lack of correlation in background events, and strong correlation in signal events, we will use the minimum of both algorithms.

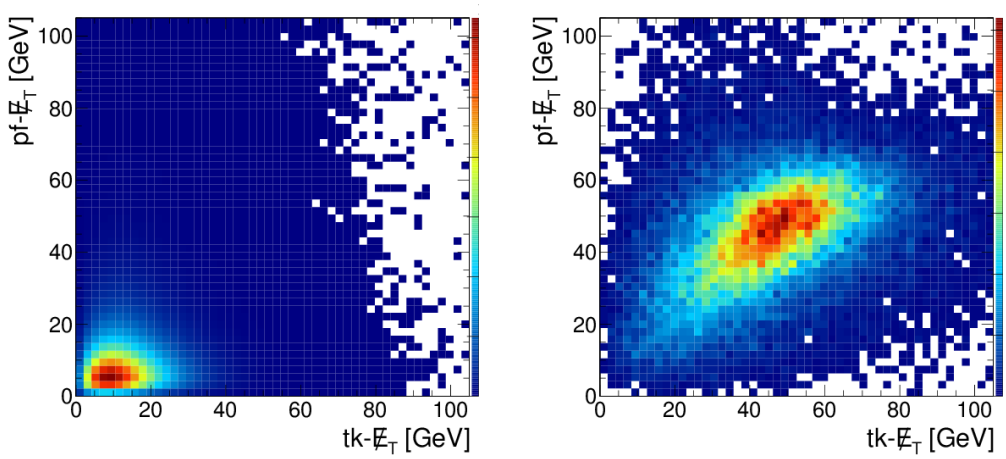

Figure 3.18: Correlation between the tk$\not\!\!E_{\mathrm{T}}$ and the pf$\not\!\!E_{\mathrm{T}}$ in events with no source of missing energy (left) and for signal (right). The correlation, and non-correlation of the signal and Drell-Yan events, respectively, is exploited to give better background rejection.

3.5.7 Jet Reconstruction

The reconstruction of momentum and direction of quarks and gluons ejected from the proton-proton collision, which then hadronize into a multitude of lower momentum particles (a jet), is done by clustering nearby reconstructed PF candidates. Starting with the highest p_{T} candidates as seeds, clustering is done using the anti-k_T algorithm [50] with a distance parameter of ΔR, defined in the $\eta - \phi$ plane, equal to 0.5. This clustering algorithm uses a distance measurement inversely proportional to the square of each particle's transverse momentum and thus gives stability in the cases of infrared or collinear radiation.

The use of PF inputs gives good jet energy response due to the high reconstruction efficiencies of charged hadrons and photons which make up on average 90% of a jet's energy. However, some corrections still need to be made to the jet energy and these energy scale corrections are factorized into three steps. First, an offset correction is applied to reduce the energy of the jet based on the amount of pile-up in the event. A pile-up density is calculated using the FastJet method[51] to compute mean energy of jets in the event and the ghost particle method for calculating jet areas[52].

Next, corrections for the detector response are made as a function of jet p_{T} and η. The first portion of this correction is applied based on measurements of simulated jet energies. The last correction is made to account for the differences in the true CMS response between the physical and the simulated detector. The differences are measured by looking at jet energies in di-jet, γ+jet and Z+jet events where the object recoiling against the jet can be used to measure the true jet energy. The uncertainty on this method is less than 5%, smaller than the overall jet energy resolution which ranges between 8% and 15% depending on the jet p_{T} and η. A full picture of jet reconstruction and energy corrections can be read in Ref. [53].

3.5.8 b-Jet Identification

The identification of b-jets will be a major handle to reducing $t\bar{t}$ and tW events contaminating the signal region. The tracker was in part designed to find the displaced vertices of the long lived hadrons produced in the hadronization of b-jets. Many algo-

rithms were designed to identify displaced vertices present in b-jets, but only the one used in this analysis will be discussed here, the track counting high efficiency algorithm (TCHE) [54].

The THCE algorithm considers the signed three dimensional impact parameter significance of every reconstructed track associated to a jet. The direction is computed using the nearest reconstructed vertex and the centroid of the jet as computed from the energy deposits in the calorimeters. The discriminating variable for this particular algorithm uses the second largest impact parameter significance of all tracks in the jet. The significance is calculated as the distance of the signed impact parameter divided by the estimated error on the measurement due to the large range of possible errors dependent on the p_{T} and η of the tracks in the jet. This allows good discrimination even for low transverse momentum jets. The TCHE discriminating variable is plotted for simulated b-jets and lighter flavor jets and compared with data in Fig. 3.19.

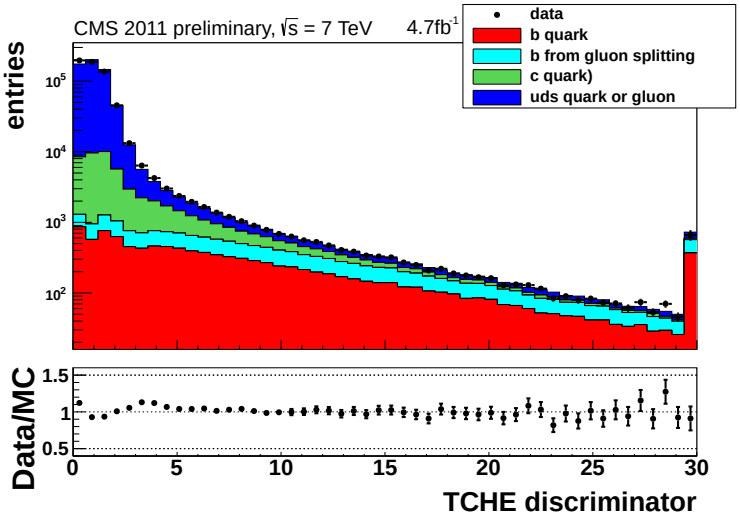

Figure 3.19: Track counting high efficiency algortihm discriminant for data (black points) and compared to simulation of lighter flavor jets (green and blue) as well as b-jets (cyan and red). Larger values of the discriminant are more indicative of heavy flavor jets. The ratio between data simulation is shown at bottom [54].

Tagging efficiency's and mistag rates have been studied extensively [55] using exclusive samples of $t\bar{t}$ events with two b-jets for signal efficiency measurments and

exclusive QCD samples for background measurements. Good agreement is seen in both the efficiency for tagging b-jets as well as the mistag rate for light flavor quarks, with the mistag rates being only approximately 10% higher than that of estimations from simulation.

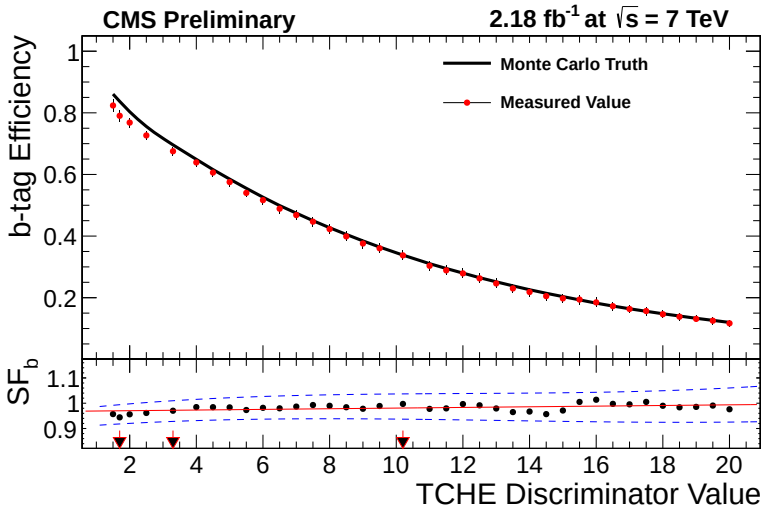

Figure 3.20: b-jet efficiency for the track counting high effeciency b-tagging algortithm in data (red points) and simulation (black line) as a function of the track counting high efficiency algortihm output disciriminant. The ratio of data to simulation is plotted below with the blue band indicating the uncertainty on the measurement [55].

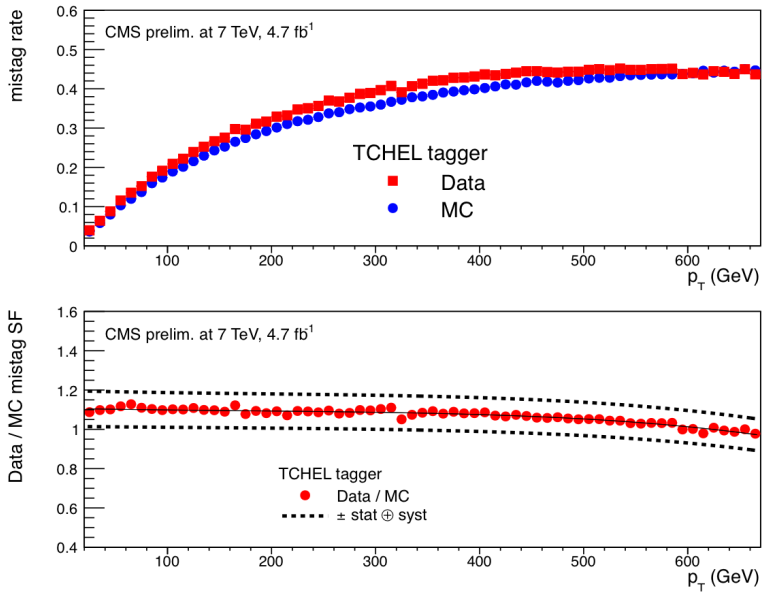

Figure 3.21: Light flavor mistag rate for the track counting high effeciency b-tagging algortithm in data (red squares) and simulation (blue circles) as a function of the jet p_{T} (top). The ratio of data to simulation is plotted below (red circles) with the dashed black line indicating the total uncertainty on the measurement [55].

Chapter 4

Production of the Higgs Boson and Other Standard Model Processes

The integrated luminosity of the LHC over the course of data taking used for this analysis was over 5.0 fb^{-1}. In all, over 5×10^{14} proton-proton interactions were produced while only of a few thousand were ultimately used to search for the Higgs boson in this analysis. In order to determine the event selection and to facilitate the understanding of the background processes, the entire chain of proton-proton collisions inside the CMS detector is simulated using Monte-Carlo (MC) techniques [56]. Generally good agreement is seen between simulation and data collected with the physical detector.

The process starts by taking the PDF distributions from CTEQ6L [57] for leading order (LO) and CT10 [58] for next-to-leading order (NLO) processes. The cross sections and simulation of the background processes use various MC packages, each of which is explicitly stated in the following sections. Regardless of the MC package, all particles are passed to PYTHIA 6 [59] for the simulation of hadronization. The final step is done using a full simulation of the CMS detector, including all active channels, with the GEANT4 package [60] which propagates the long lived particles through the detector taking into account proper decay times and accurate matter interactions. Due to the changing luminosity regime throughout the year, pile-up interactions could not be added in advance which mimicked the number of interactions delivered by the LHC. All MC samples were generated with a "flat" PU distribution and later re-weighted to match that

delivered by the LHC. Systematic uncertainty from this process is calculated by scaling the number of PU interactions up and down and re-calculating the final event yields. The effect is on the order of 1-2%.

The following sections describe the production of the Higgs boson as well as the background SM interactions hiding it. Fig. 4.1 shows the production rate for a few Higgs masses as well as the substantially higher rate of other SM processes as a function of center-of-mass collision energy. The background samples are broken into two major categories. The first, irreducible backgrounds, are processes which are produced with the same final state of this search, i.e. two prompt isolated leptons with significant missing energy. WW continuum production is the only irreducible background for this analysis (Sec. 4.6). Reducible backgrounds consist of production mechanisms with dissimilar final states which "fake" the final states due to instrumental noise, particle mis-reconstruction and other sources described therein (Secs. 4.3, 4.4, 4.5, 4.7).

4.1 Higgs Boson Production

Richard Feynman introduced a paradigm for drawing these processes as diagrams to facilitate simple calculation of the amplitude of these processes. Diagrams in this thesis increase in time from left to right with initial state particles represented as incoming lines from the left and any final state particles as lines exiting on the right. Initial and final state particle are "detectable" in the lab and carry momentum, energy and spin. Each vertex of the diagram represents an interaction of one of the fundamental forces while each internal line (non-initial or non-final) represents the propagation of said force. In addition to amplitude calculation, these diagrams are useful in visualizing particle interactions at a basic level.

The Higgs boson is produced predominantly at the LHC via gluon fusion through a quark loop [62]. The leading-order Feynman diagram representing this process is shown on the left in Fig. 4.2. As the Higgs boson coupling strength to fermions is proportional to fermion mass, the gluon fusion process is almost completely dominated by a top quark loop. Next-to-leading order (NLO), next-to-next-to-leading order (NNLO) and next-to-next-to-leading-logarithmic (NNLL) corrections increase the leading-order

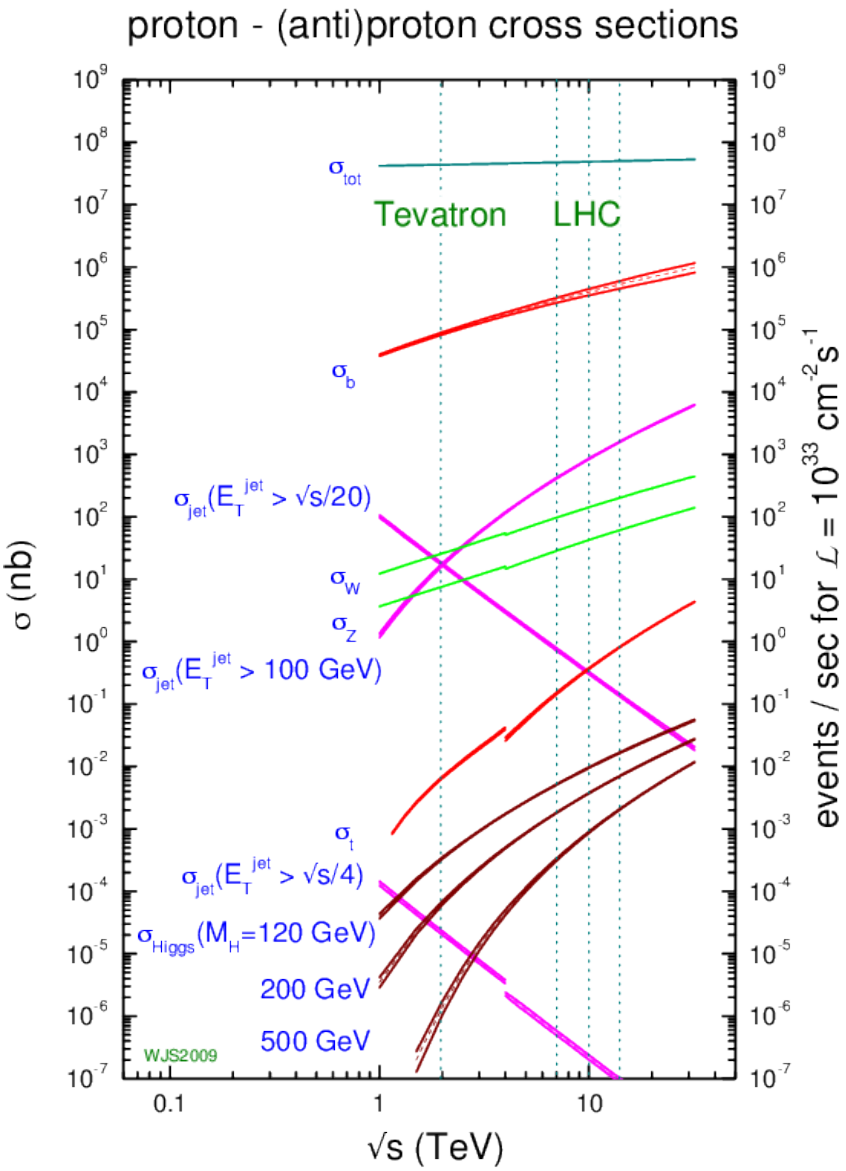

Figure 4.1: Standard model processes as a function of center of mass collision energy. 7 TeV is marked as a vertical dotted line [61].

cross section by over 100% to values between 0.2 and 20 picobarns (pb) depending on m_{H}.

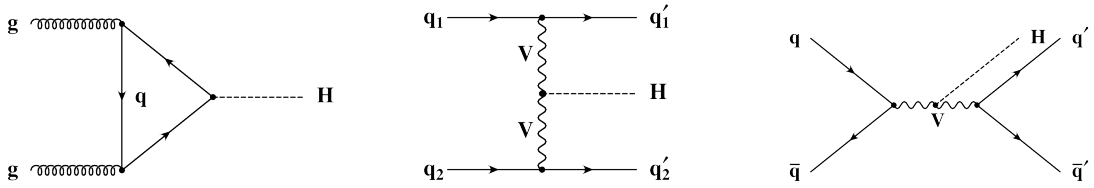

Figure 4.2: Leading-order Feynman diagrams for the production of the Higgs boson via gluon fusion (left), t-channel vector boson fusion (center) and s-channel vector boson fusion (right) at the LHC.

Vector boson fusion (VBF) is the next largest production mechanism for the Higgs boson with a cross section approximately 10% that of gluon fusion. The two leading-order diagrams for this mechanism are shown in the center and the right of Fig. 4.2. The central diagram is particularly suited for searches in the 2-jet category, and this analysis is tailored to do so, as two forward jets are present in the event. A major handle for this search utilizes the fact that the hadronic activity tends to be absent between the two forward jets (in η) as no QCD interaction occurs between them.

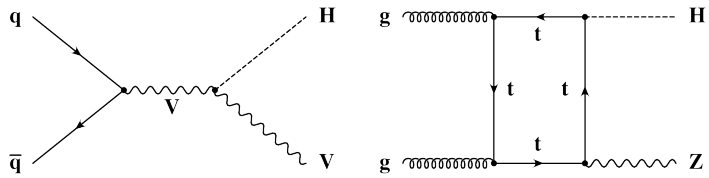

Figure 4.3: Leading-order Feynman diagrams for the associated production of the Higgs boson via s-channel vector "Higgstralung" (left) and a top quark loop (right) at the LHC.

Finally, three other mechanisms exist which also produce the Higgs at an appreciable level, and while this search includes them in the final event yields, this analysis makes no special consideration for their presence as their final state includes additional particles. For these three processes, the Higgs is produced in association with either a W

or Z boson or in the presence of a top/anti-top quark pair. The leading order Feynman diagrams can be seen in Fig. 4.3 and their overall cross section all fall below the VBF process at the 10% level.

Fig. 4.4 shows the production cross section and their theoretical errors as a function of Higgs mass over a range of m_{H} from $m_{\mathrm{H}} = 90$ all the way up to $m_{\mathrm{H}} = 1000$ GeV. All production cross sections are taken from Ref. [62] and the values used for this analysis are shown in Tab. 4.1.

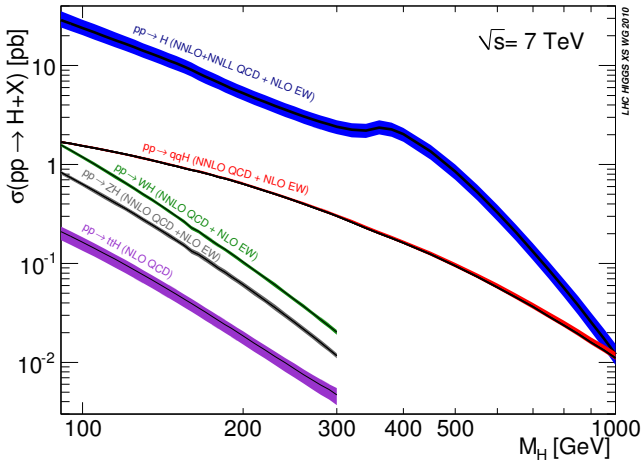

Figure 4.4: Theoretical cross sections for each Higgs production mechanism as a function of Higgs mass for proton-proton collisions at $\sqrt{s} = 7\,\mathrm{TeV}$ [62].

The POWHEG Monte Carlo program is used to simulate the production of the Higgs boson in each of the production mechanisms. For the $gg \to H$ production mode however, higher order corrections result in a stiffer cross section distribution as a function of Higgs transverse momentum. The latest theoretical predictions are made with HQT [63, 64, 65] and the resulting differential cross section is used as a template to re-weight the POWHEG distribution to match. The weights are applied to the simulated events ensuring the inclusive cross section remains the same.

Table 4.1: Summary of Higgs production cross sections via gluon-gluon fusion and vector-boson production for various possible values of m_{H}. The branching ratio (BR) for $H \to W^+W^-$ is shown in the rightmost column.

m_{H} [GeV]	$gg \to H$ [pb]	VBF [pb]	BR($H \to WW$)
110	$19.84^{+4.05}_{-3.04}$	$1.40^{+0.039}_{-0.032}$	$0.048^{+0.003}_{-0.003}$
115	$18.13^{+3.63}_{-2.77}$	$1.33^{+0.033}_{-0.031}$	$0.086^{+0.004}_{-0.004}$
118	$17.21^{+3.41}_{-2.60}$	$1.29^{+0.035}_{-0.031}$	$0.117^{+0.006}_{-0.006}$
120	$16.63^{+3.28}_{-2.51}$	$1.27^{+0.036}_{-0.032}$	$0.141^{+0.007}_{-0.007}$
122	$16.08^{+3.17}_{-2.43}$	$1.25^{+0.034}_{-0.030}$	$0.169^{+0.008}_{-0.008}$
124	$15.56^{+3.03}_{-2.35}$	$1.22^{+0.033}_{-0.029}$	$0.198^{+0.009}_{-0.009}$
126	$15.06^{+2.92}_{-2.27}$	$1.20^{+0.034}_{-0.029}$	$0.231^{+0.009}_{-0.009}$
128	$14.58^{+2.81}_{-2.20}$	$1.18^{+0.033}_{-0.027}$	$0.266^{+0.010}_{-0.010}$
130	$14.12^{+2.71}_{-2.13}$	$1.15^{+0.032}_{-0.027}$	$0.303^{+0.011}_{-0.011}$
135	$13.08^{+2.47}_{-1.96}$	$1.10^{+0.033}_{-0.024}$	$0.400^{+0.012}_{-0.012}$
140	$12.13^{+2.28}_{-1.81}$	$1.05^{+0.029}_{-0.023}$	$0.501^{+0.009}_{-0.009}$
150	$10.50^{+1.96}_{-1.56}$	$0.962^{+0.028}_{-0.021}$	$0.696^{+0.006}_{-0.006}$
160	$9.08^{+1.69}_{-1.36}$	$0.879^{+0.025}_{-0.020}$	$0.908^{+0.002}_{-0.002}$
170	$7.73^{+1.38}_{-1.15}$	$0.817^{+0.025}_{-0.018}$	$0.964^{+0.001}_{-0.001}$
180	$6.74^{+1.22}_{-0.99}$	$0.748^{+0.023}_{-0.018}$	$0.932^{+0.000}_{-0.000}$
190	$5.90^{+1.02}_{-0.88}$	$0.693^{+0.023}_{-0.015}$	$0.786^{+0.000}_{-0.000}$
200	$5.25^{+0.90}_{-0.80}$	$0.637^{+0.022}_{-0.015}$	$0.741^{+0.000}_{-0.000}$
250	$3.31^{+0.55}_{-0.52}$	$0.430^{+0.017}_{-0.011}$	$0.701^{+0.000}_{-0.000}$
300	$2.42^{+0.41}_{-0.38}$	$0.301^{+0.014}_{-0.008}$	$0.692^{+0.000}_{-0.000}$
350	$2.31^{+0.45}_{-0.34}$	$0.213^{+0.011}_{-0.006}$	$0.676^{+0.009}_{-0.014}$
400	$2.03^{+0.32}_{-0.33}$	$0.162^{+0.010}_{-0.005}$	$0.582^{+0.018}_{-0.012}$
450	$1.36^{+0.22}_{-0.24}$	$0.124^{+0.008}_{-0.004}$	$0.551^{+0.016}_{-0.009}$
500	$0.849^{+0.150}_{-0.149}$	$0.095^{+0.007}_{-0.003}$	$0.546^{+0.013}_{-0.006}$
550	$0.526^{+0.097}_{-0.093}$	$0.074^{+0.006}_{-0.003}$	$0.550^{+0.013}_{-0.007}$
600	$0.327^{+0.063}_{-0.058}$	$0.058^{+0.005}_{-0.002}$	$0.558^{+0.014}_{-0.007}$

4.2 Higgs Boson Decays into two W Bosons

The Higgs boson is short lived and immediately decays to one of many possible decay products. Two different couplings dictate the decay of the Higgs boson, the Yukawa coupling to a pair of fermions and the weak decay coupling to a pair of vector bosons (either W's or Z's). Diagrams for both interactions are shown in Fig. 4.5.

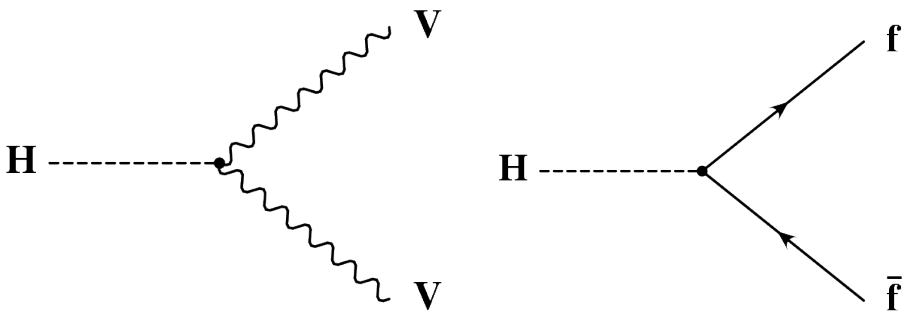

Figure 4.5: Feynman diagram for Higgs decay to a pair of bosons (left) and to a pair of fermions (right).

The Yukawa coupling strength is proportional to the square of the fermion mass and so is dominated by decay into a pair b-quarks in the mass region below that of which a pair of top quarks are kinematically allowed ($\sim 2m_t$). The coupling to a pair of dibosons is proportional to the cube of the Higgs boson mass with the more kinematically favored WW decay dominating over a wide range in the high Higgs mass region starting approximately at 140 GeV. Fig. 4.6 shows all possible decay mechanisms including to a pair of gluons and photons via a quark loop. The large branching fraction of $H \rightarrow W^+W^-$ over a wide range allows for a very sensitive analysis over a wide range of Higgs boson masses. The branching fractions are also taken from the extensive work done by the Higgs Cross Section Working Group [62]. The theoretical branching fractions used in this analysis can be seen in the last column of Tab. 4.2.

W Boson Decays

A W boson will decay to a lepton/neutrino pair 33% of the time. The τ has a mean lifetime of 291 femtoseconds causing it to decay before exiting the CMS detector.

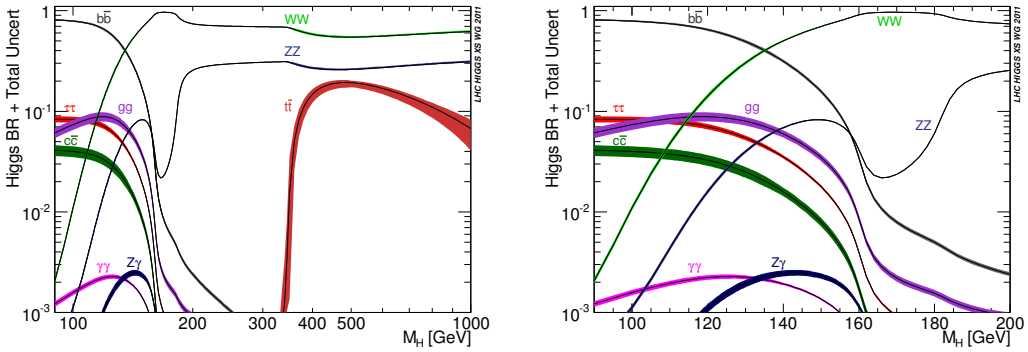

Figure 4.6: Theoretical branching fractions for each Higgs decay product as a function of Higgs mass for masses up to 1000 GeV (left) and zoomed between 90 and 200 GeV (right) [62].

A τ with 20 GeV of energy will on average decay at a distance of 800 μm from its point of production. This is in contrast to the electron which is stable and the muon which has a significantly longer lifetime, 2.2 μs and easily has a long enough lifetime to escape the CMS detector before decaying. Only a fraction of the time does the τ then decay leptonically into either an electron or muon, along with other particles, all of which share the momentum and energy of the originally produced τ. Considering this, along with the fact that a majority of the time the τ decays hadronically, makes τ reconstruction significantly more difficult. For these reasons, this analysis only searches for electrons and muons in the final state. Taking into account the leptonic decay of the τ along with the prompt W decay to either a muon or an electron, only 7% of the time will both W's decay leptonically and produce two electrons or muons and at least two neutrinos in the final state.

Spin Dynamics of $H \to W^+W^-$ decays

In the WW decay channel, spin correlations between the Higgs and decay products help to distinguish Higgs interactions from the WW continuum background discussed in Sec. 4.6. To conserve spin, the spin-0 Higgs decaying to two spin-1 W boson forces the spin of each boson to be anti-aligned with respect to the other. At a mass of $2m_W$, the Higgs boson will decay to the two W bosons such that the bosons are at

rest. To continue to conserve spin, and remembering that the W bosons only couple to left-handed fermions (and right-handed anti-fermions), the two leptons will be produced collinearly to conserve spin and helicity. Helicity is only fully conserved in the massless fermion case and thus the effect is partly diluted. Further, for increasing values of the Higgs boson mass, the two W bosons will be produced with higher and higher transverse momentum. This boost in momentum completely cancel out the helicity conservation at very high Higgs boson mass ($\gtrsim 225\,\text{GeV}$). Both effects will be utilized to help extract Higgs signal over the WW continuum background.

4.3 W Boson Production

Single W boson production has the largest cross section of all of the reducible backgrounds to this analysis. However, as only one W is produced in the final state, there exists the requisite missing energy but only one prompt lepton when the W decays leptonically. The W must be produced in the presence of one or multiple jets, one of which then fakes a prompt isolated lepton. While the probability of a jet to fake a lepton, the fake rate, is small, the large cross section still gives non-negligible contribution in the 0-jet category, and to a lesser extent the 1-jet category. A few example Feynman diagrams of W bosons produced in the presence of a single jet can be seen in the left and center of Fig. 4.7 while Fig. 4.8 shows a simulated W event with a single "lepton-like" jet in the CMS detector. The $W+$jets processes are simulated using MADGRAPH [66] while the NNLO cross section is predicted using FEWZ [67].

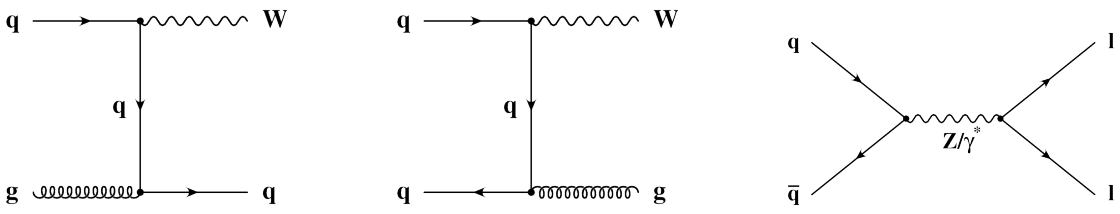

Figure 4.7: Two examples of leading order Feynman diagrams for W production in the presence of a jet (left, center) and Drell-Yan production (right).

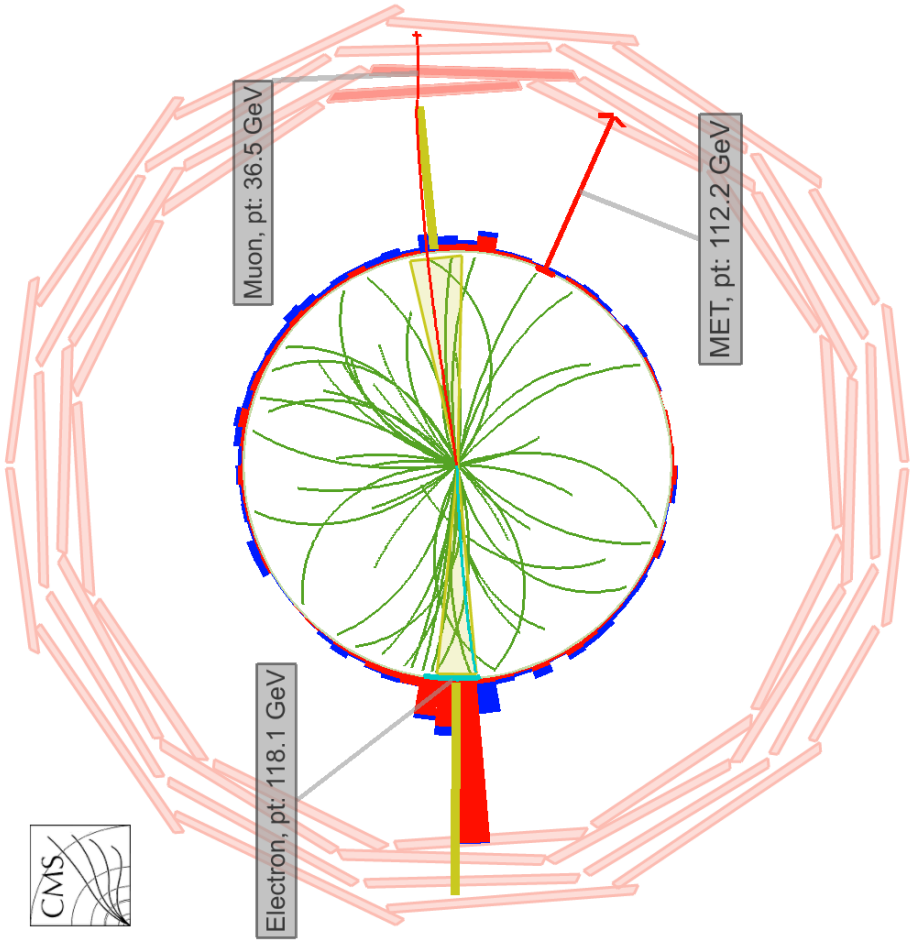

Figure 4.8: Simulated W event in the presence of a "lepton-like" jet in the CMS detector.

4.4 Drell-Yan Production

The Drell-Yan process, shown in Fig. 4.7, is the annihilation of two quarks into a photon or Z boson, and for this analysis, would contaminate the signal region by then decaying to two leptons. This process, in contradiction to W boson production, then is reducible as there is no neutrinos in the final state, and hence no source of missing energy. However, like W production, the cross section is significantly large that detector effects impart enough Drell-Yan events with fake missing energy that this process becomes an appreciable background.

The main handle for this background comes from the capability to measure the mass of the Z/γ^* producing the dileptons, and removing any events compatible with the mass of the Z ($\sim 91\,\text{GeV}$), however mis-reconstructed leptons can cause events to fall out of this mass region while creating inducing fake $\not\!\!E_{\text{T}}$ at the same time.

One final wrinkle from the Drell-Yan process comes from the decay into two τ leptons. When each τ decays leptonically, two leptons (albeit not as prompt) are produced alongside multiple neutrinos, resulting in missing energy. This mimics our signal, but additional handles exist do deal with this background as discussed in Sec. 5.1.2.

POWHEG [68] is used to simulate Drell-Yan events with invariant mass above 20 GeV while PYTHIA [59] is used to simulate Drell-Yan events with invariant mass between 10 and 20 GeV. The cross sections for Drell-Yan production is calculated at NNLO using FEWZ [67]. An example of a simulated Drell-Yan event produced at the Z boson mass resonance can be seen in Fig. 4.10.

4.5 Top-Quark Production

Top quarks decay immediately and 100% of the time to a W boson and a b-quark. Therefore, a major background with similar final state particles is the production of a top/anti-top quark pair ($t\bar{t}$). The $t\bar{t}$ pair will decay 100% of the time to two b-quarks (which will hadronize into jets) and two oppositely charged W bosons which can decay leptonically producing the requisite two prompt leptons and missing energy. This background is reducible however as b-hadrons produced from the hadronization of the

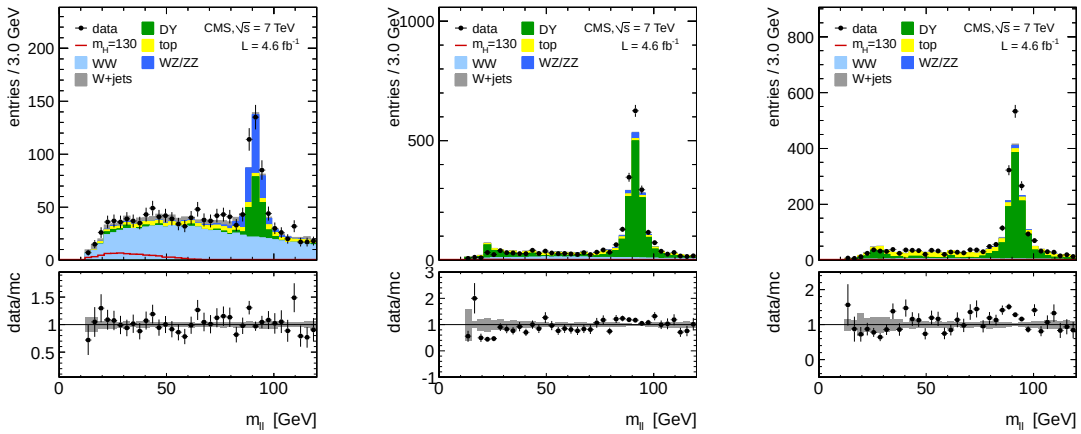

Figure 4.9: Invariant mass distribution of dilepton events produced via the Drell-Yan process in the 0-jet (left), 1-jet (center) and 2-jet (right) categories. The peak at 91 GeV comes from the Z mass resonance.

b-quark have lifetimes long enough, greater than a picosecond, such that they decay a measurable distance, > 500 μm, from the interaction vertex. The pixel detector was designed with this purpose in mind, allowing for the measurement of displaced vertices, and hence, the ability to "tag" b-jets as explained in Sec. 5.1.3. The leading order Feynman diagrams for $t\bar{t}$ production are shown in Fig. 4.11.

Single top quark production is also a measurable background, especially in the associated W boson production channel, shown in the bottom right of Fig. 4.11. While the cross section of this is lower than that of $t\bar{t}$ production, only one b-jet is produced, thus removing one of the handles used to reduce this background. The other single top quark production mechanisms (s-channel and t-channel production) only contain one W boson, hence one prompt lepton and contribute only slightly when the b-jet decays leptonically and does not get tagged by one of the tagging algorithms.

POWHEG [68] is used to simulate both single top quark and tW production while MADGRAPH [66] is used to simulate $t\bar{t}$ production. The cross sections for all top quark production mechanisms are calculated at NLO using MCFM [69]. A simulated $t\bar{t}$ event in the CMS detector is shown in Fig. 4.12 where the distinguishing dilepton signature is seen alongside the additional two jets produced from the two $t \to Wb$ decays.

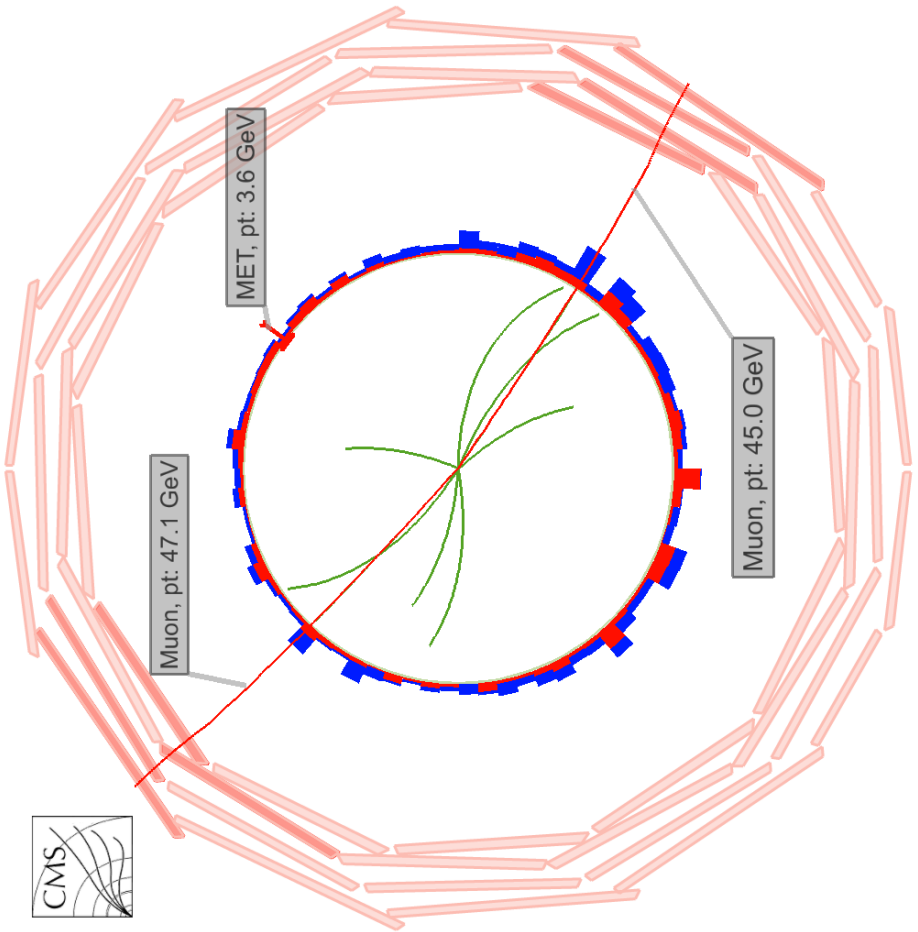

Figure 4.10: Simulated Drell-Yan event in the CMS detector.

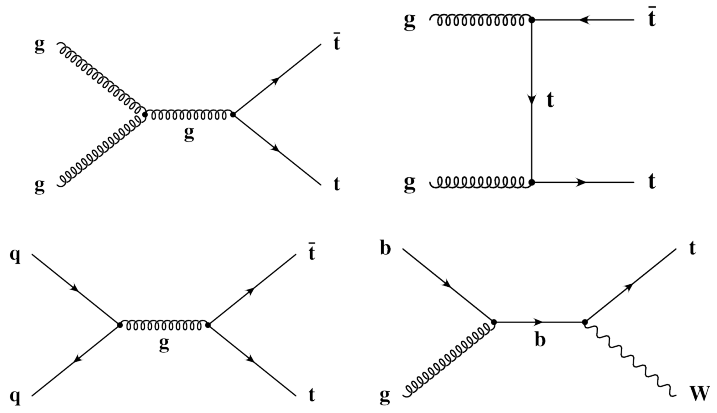

Figure 4.11: Leading order Feynman diagrams for $t\bar{t}$ production (top left, top right, bottom left) and associated top quark production with a W boson (bottom right) at the LHC.

4.6 WW Production

WW production at the LHC is dominated by the s-channel and t-channel quark/anti-quark scattering as shown on the left and in the center of Fig. 4.13. Further production is via a quark loop in the gluon fusion process as shown rightmost in the same figure. The fully leptonic final states of this process are indistinguishable from the Higgs signal and can only be reduced using kinematical considerations based on spin conservation as discussed in Sec. 4.2. An example of a simulated WW event in the CMS detector decaying to $e^{-}\overline{\nu}_{e}\mu^{+}\nu_{\mu}$ can be seen in Fig. 4.14. This is indicative of a typical WW event with significant missing energy, very little hadronic activity and two prompt, isolated leptons which show no directional correlation. $qq \rightarrow WW$ production is simulated using MADGRAPH while the production cross section of 47.04 pb is calculated at NLO using the latest MCFM calculations [70]. The $gg \rightarrow WW$ production is simulated, and the cross section is predicted, using the GG2WW analysis package [71].

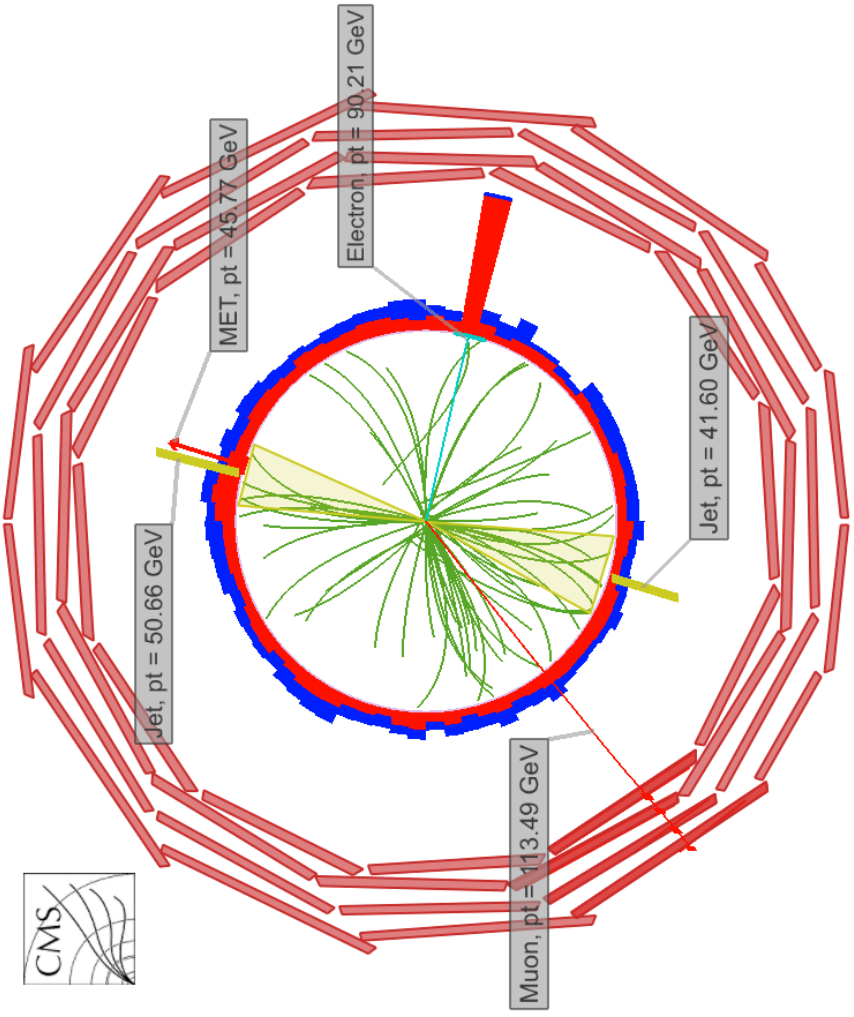

Figure 4.12: Simulated $t\bar{t}$ event in the CMS detector.

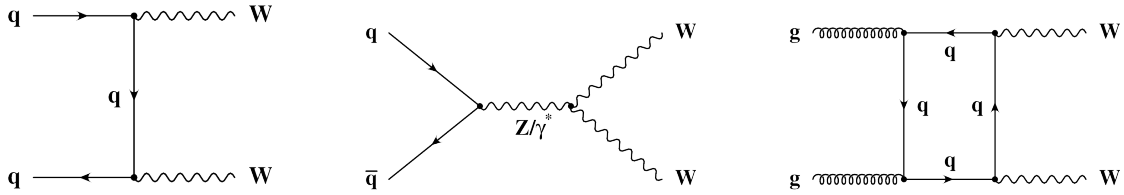

Figure 4.13: Leading order Feynman diagrams for production of two W bosons in the t-channel (left), s-channel (center) and via gluons (right) at the LHC.

4.7 Other Di-boson Processes

The final source of reducible backgrounds come from diboson production, i.e. WZ, ZZ and $W\gamma$. Feynman diagrams for these processes can be seen in Fig. 4.15. Each of these processes produces three or more leptons in the final states, occasionally alongside neutrinos. In the case of WZ background, if one lepton is not reconstructed, this background can appear in the signal region. In the case the lepton from the W is lost, the other two leptons from the Z are identifiable and can be removed. The same can be said for ZZ production where one Z decays to two neutrinos and the other decays to muons or electrons. However, no additional handles are available if the two remaining leptons come from separate boson decays. Luckily, this rate is small.

For $W\gamma$ production, the photon can decay to two electrons and contaminate the signal region if one of the two electrons is not reconstructed. A dedicated study to measure the contribution from this process is performed in Sec. 5.4.5. The simulation of WZ and $W\gamma$ is done using MADGRAPH [66] while PYTHIA [59] is used for ZZ. All cross Sec. predictions are perfomred with MCFM [69].

4.8 Summary

A summary of the background processes contributing to the final yields, along with the sinmulation software and cross section, is shown in Tab. 4.2.

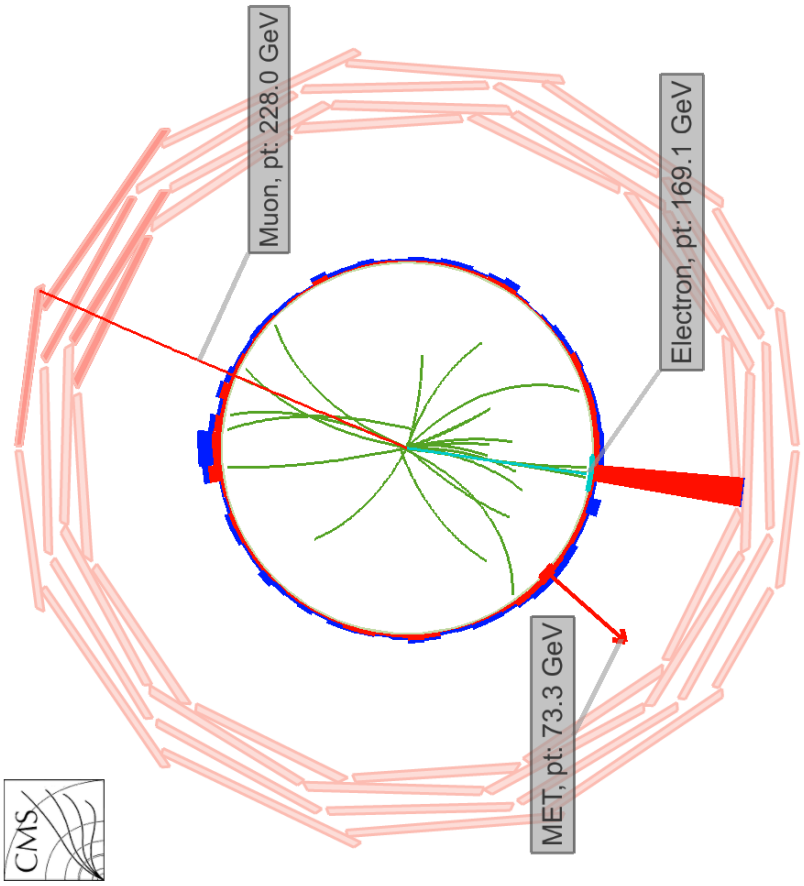

Figure 4.14: Simulated WW event in the CMS detector.

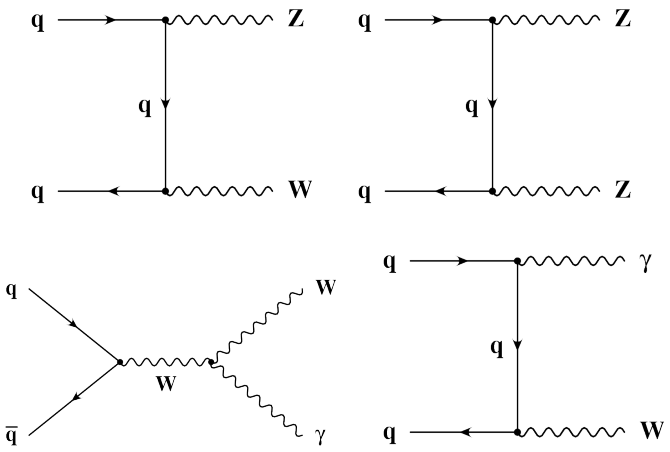

Figure 4.15: Leading order Feynman diagrams for diboson production of WW, WZ or $W\gamma$ at the LHC.

Table 4.2: The event generator software and corresponding production cross sections multiplied by branching ratio for each of the backgrounds studied for this analysis.

background samples	generator	$\sigma[\text{pb}] \cdot \text{BR}$
$qq \to WW$	MADGRAPH	4.79
$gg \to WW$	GG2WW	0.153
$t\bar{t}$	MADGRAPH	17.1
tW	POWHEG	7.87
Single top, t-channel	POWHEG	41.92
Single anti-top, t-channel	POWHEG	22.65
Single top, s-channel	POWHEG	3.19
Single anti-top, s-channel	POWHEG	1.44
$Z/\gamma^* \to \ell\ell$ ($m_{\ell\ell} > 20\,\text{GeV}$)	POWHEG	1666
$Z/\gamma^* \to \ell\ell$ ($10 < m_{\ell\ell} < 20\,\text{GeV}$)	POWHEG	3319
WZ	PYTHIA	18.2
ZZ	MADGRAPH	7.67
$W+\text{jets}$	MADGRAPH	31314
$W\gamma$	MADGRAPH	14.85
$W\gamma$	MADGRAPH	14.85
$W\gamma$	MADGRAPH	14.85
$W\gamma^*$ ($\ell\nu 2\mu$)	MADGRAPH	1.60
$W\gamma^*$ ($\ell\nu 2\text{e}$)	MADGRAPH	5.55

Chapter 5

Search for the Higgs Boson in the WW Decay Channel

The general strategy for finding Higgs boson signal among the large SM backgrounds will be to employ a series of selections which reduce these backgrounds while simultaneously allowing any possibly produced Higgs boson events to remain (as described by the Monte Carlo simulations defined in Sec. 4). Once the backgrounds are at a manageable level, statistical analysis of the remaining events will determine the significance on the presence or absence of the Higgs boson—this statistical discussion is left to Ch. 6.

This analysis searches for the Higgs boson decaying to two W bosons with each W boson decaying leptonically, $H \to W^+W^- \to \ell\nu\ell'\overline{\nu}$. Therefore, the starting point is to search for two isolated, large transverse momentum leptons coming from the leptonic weak decay of the two W bosons, and, as the Higgs boson is a neutral boson and the neutrinos carry no charge, these leptons must be oppositely charged. We will also require the selected events to have a large amount of missing transverse energy ($\not\!\!E_{\mathrm{T}}$) due to the undetected neutrinos. The analysis is also split into different jet bins as the main Higgs boson production mechanism, gluon fusion, can easily contain one or more jets and the background composition is significantly different depending on how many jets are present. The first selections remove the SM backgrounds agnostically of Higgs boson mass—this is called the "mass-independent" selection. The strategy then continues by applying a "mass-dependent" set of selections on a few discriminating variables which,

depending on the mass hypothesis under study, exploit the scalar properties of the Higgs boson and are chose to maximize sensitivity over the non-resonant WW production.

Also discussed in the final sections of this chapter are the corrections applied to the simulation for the signal selection efficiencies measured in data as well as the "data-driven" estimates of the remaining background contributions. Finally, a summary of all sources of uncertainty are summarized.

5.1 Mass-Independent Selection

After requiring two oppositely charged muons or electrons, more selections are required to reduce the other major SM backgrounds. The following describes the selections used to reduce each type of background.

5.1.1 Suppression of Backgrounds with Fake Leptons

$W+$jets prodcution, and to a lesser extent QCD production, can fake the signal signature when one (or two) of the jets fake the appearance of a prompt lepton as from electroweak decays. To combat this, tight identification selections are applied to both electrons and muons. The identification algorithms come in three flavors. First, a determination is made on how "isolated" a lepton appears by measure the amount of nearby energy in the event. Fake leptons from jets will appear alongside other particles while those from electroweak decays are produced singularly in association with no other particles. Leptons from electroweak decays are also prompt, i.e. they are produced at the interaction point as opposed to leptons produced from semileptonic b-decays or photon conversion, so a selection on the proximity to the primary vertex, inmpact parameter, will be used. Finally, selections are made on the individual traits of the leptons themselves. All of these handles are described in the following few sections.

Isolation Overview

As leptons from electroweak decays are produced unaccompanied by other particles, they appear isolated in the detector, whereas jets that are misreconstructed as

leptons tend to have many other particles nearby. To measure isolation, we sum the energy produced by other particles in a cone around the lepton in η-ϕ space. Both neutral and charged particles must be accounted for in order to fully understand the measure of a lepton's isolation. To help with this exercise, we define ΔR as the distance in η-ϕ space between two objects: $\Delta R = \sqrt{\Delta\eta^2 + \Delta\phi^2}$.

Two types of isolation measurements are used in this analysis. The first, "detector-based" isolation, uses reconstructed tracks to measure charged particle activity and ECAL and HCAL energy depositions to measure electromagnetic and hadronic energy near the lepton. With this method, care must be taken to properly "veto" all energy that corresponds to the lepton itself, its "footprint," otherwise the isolation sum will be artificially inflated and the lepton will appear non-isolated. Detector-based isolation is algorithmically simple and is therefore used for lepton identification in the trigger system.

Electron Isolation

The electron footprint contains the electron, any bremsstrahlung photons, and any photons that then pair create and on down the cycle. In order to capture this footprint, we not only use a veto cone around the electron, but we also use a strip that extends in the ϕ direction and has a constant width in η. The isolation method consisting of the strip and the cone will be referred to as the "Jurassic Method" and a cartoon of this method is shown in Fig. 5.1. Additionaly, charged particles are ensured to come from the primary vertex before summation, ensuring the isolation sum is not artificially inflated by charged particles from pile-up interactions. The full set of isolation parameters for electrons is listed in Tab. 5.1.

The second type of isolation method used in this analysis, "particle-based," involves summing the p_{T} of particles reconstructed using the PF method defined in Sec. 3.5.5. This method is conceptually simpler once the PF particles have been reconstructed. The PF particles which fall within the ΔR cone around the electron are summed. As each electron is reconstructed in the PF algorithm, we can mostly remove their footprint by removing the corresponding PF electron from the isolation sum. Some additional parameters corresponding to a Jurrasic veto region are then used to fully re-

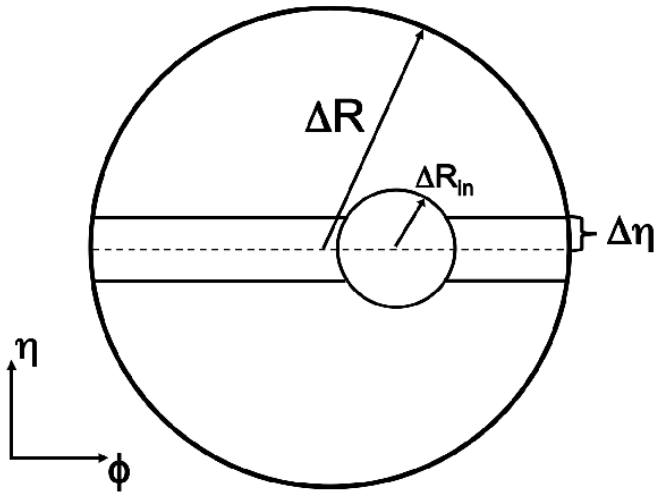

Figure 5.1: A graphical display in the η-ϕ plane of the Jurassic electron isolation technique in the tracker and the ECAL.

Table 5.1: Parameters used in the detector-based isolation algorithm for electrons. While signal electrons tend to deposit all of their energy in the ECAL, the reconstruction of electrons uses the inner 0.15 in ΔR of the HCAL as a selection criteria, and hence is removed from the isolation sum to prevent double counting. In addition, energy thresholds are applied to ensure that the inputs all have values greater than the measured noise of the detector.

Parameter	Tracks	ECAL	HCAL
d_z [cm]	0.2	–	–
ΔR_{out}	0.3	0.4	0.4
ΔR_{in}	0.015	3 crystals	0.15
$\Delta\eta_{\text{in}}$	0.015	1.5 crystals	–

move the electrons footprint. These parameters depend on the type of particle and the full set of particle-based definitions are listed in Tab. 5.2.

Table 5.2: Parameters used in the particle-based isolation algorithms for electrons.

Parameter	Charged	Neutral Hadronic	Photons and Electrons
p_{T} [GeV] >	–	1.0	1.0
d_z [cm] <	0.1	–	–
ΔR_{out} <	0.4	0.4	0.4
ΔR_{in} >	0.015	0.07	–
$\Delta\eta_{\mathrm{in}}$ >	0.015	0.025	0.025

Electrons which pass the final selection for this analysis must have a relative PF-based isolation ($\Sigma p_{\mathrm{T}}/p_{\mathrm{T}}^{\mathrm{e}}$) less than 0.13 if in the barrel region or less than 0.09 if in the endcap region.

Muon Isolation

Muon isolation calculations are significantly simpler than for electrons. As a muon passes through the detector, it produces a single, easily reconstructable track in the silicon detector, and, as the muon is minimum ionizing, only leaves a small energy deposit in the ECAL and HCAL. A veto cone is then created around the muon in each of the subdetectors and any energy found in this veto cone is assumed to come from the muon, ignored, and the rest of the energy in a larger ΔR cone around the muon is summed. A cartoon of this method is shown in Fig. 5.2.

PF based muon isolation proceeds in a similar fashion, albeit again simpler than for electrons. The muon itself can be removed from the PF collection before summation of nearby particles. The full set of parameters used for PF based muon isolation is shown in Tab. 5.3 and muons which are used in this analysis must pass the relative isolation requirements, $\Sigma p_{\mathrm{T}}/p_{\mathrm{T}}^{\mu}$, shown in Tab. 5.4.

Impact Parameter Selection

To help reject fakes from photon conversion, electrons are required to have a transverse impact parameter less than 0.02 cm and longitudinal impact parameter less

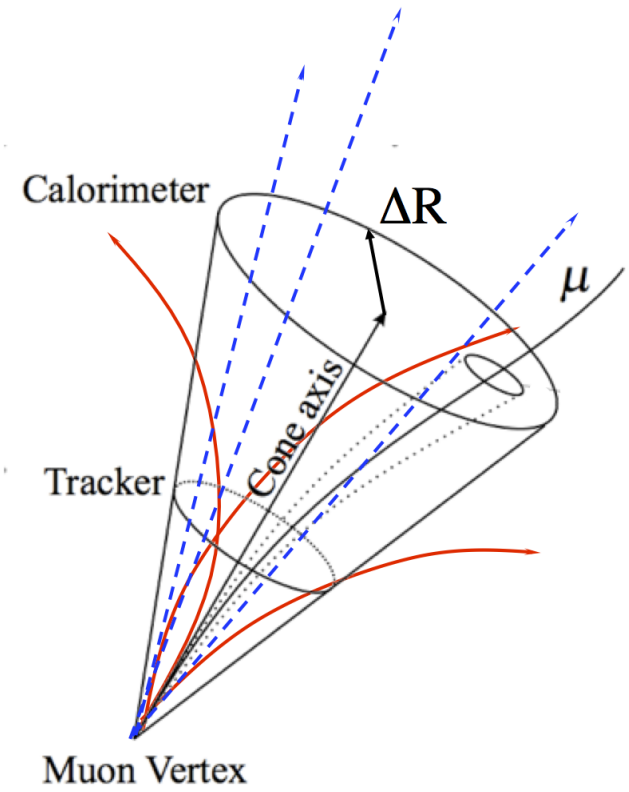

Figure 5.2: A graphical display of the detector-based muon isolation technique. As the muon passes through the different portions of the CMS detector, veto cones are drawn around the muon to veto any energy that comes from the muon itself. Neutral particles are depicted in blue and charged particles are depicted in red.

Table 5.3: Parameters used in the particle-based isolation algorithms for electrons and muons.

Parameter	Charged	Neutral Hadronic	Photons and Electrons
p_{T} [GeV] >	–	1.0	1.0
d_z [cm] <	0.1	–	–
ΔR_{out} <	0.3	0.3	0.3

Table 5.4: Particle-based isolation selection values for muons. The leptons must have relative isolation values ($\Sigma p_{\mathrm{T}}/p_{\mathrm{T}}^{\mu}$) less than those listed.

	Muons ($<20\,\mathrm{GeV}$)	Muons ($>=20\,\mathrm{GeV}$)
Barrel	<0.06	<0.13
Endcap	<0.05	<0.09

than 0.1 cm with respect to the first primary vertex in the event (as sorted by the square of the sum of the p_{T} of the tracks associated to each vertex). With respect again to the first vertex, muons with p_{T} less than 20 GeV are required to have a transverse impact parameter less than 0.01 cm while muons with p_{T} greater than 20 GeV are required to have a transverse impact parameter less than 0.02 cm. All muons must have a longitudinal impact parameter less than 0.1 cm to the first vertex.

Electron Identification

A pre-selection is applied to the electrons to ensure all requirements are tighter than those found in the trigger selection. In addition to using standard detector based isolation values, the following discriminating variables are used:

- $\sigma_{\mathrm{i}\eta\mathrm{i}\eta}$ - measure of the spread in η of the electron's energy deposit in the ECAL.
- $\Delta\eta_{\mathrm{in}}$ - difference in η between the inner most state of the electron track and the electron super cluster.
- $\Delta\phi_{\mathrm{in}}$ - difference in ϕ between the inner most state of the electron track and the electron super cluster.
- H/E - the ratio of the hadronic calorimeter energy deposited behind the electron super cluster and the energy of the electron super cluster.
- N_{miss} - number of hits in the inner most layers of the silicon pixel detector that does not contain a hit associated to the electron when the hit is expected, within reconstruction error, to be attached to electron.
- Conversion Vertex Matching - an additional vertex reconstruction algorithm is run on the tracks in the event looking for possible vertices away the beam line. If

the electron and another track appear to be collinear and coming from the same secondary vertex, we assume that we have found a conversion partner for the electron from a photon and the electron is vetoed.

The full set of pre-selections are defined in Tab. 5.5. Further electron identification is then done using a multivariate analysis (MVA). The MVA is trained using the TMVA[72] analysis framework selecting a decision tree[73] as the classifier and further boosting the classifier with the AdaBoost[74] algorithm. After applying pre-selections, electrons from Z decays and electrons found in QCD-like events are binned in η and p_{T} and passed to TMVA for training as signal-like and background-like electrons, respectively, by the boosted decision tree (BDT). A BDT is more robust than other MVA techniques in that it converges to achieve maximum significance with less training and is not biased by input variables that do not discriminate well between the signal and the background.

Table 5.5: Pre-selection requirements applied to all electrons to ensure tighter requirements than those applied at the trigger level.

Variable	Barrel Selection ($\lvert\eta\rvert < 1.479$)	Endcap Selection ($\lvert\eta\rvert > 1.479$)
$\sigma_{i\eta i\eta}$	< 0.01	< 0.03
$\lvert\Delta\eta\rvert$	< 0.007	< 0.009
$\lvert\Delta\phi\rvert$	< 0.15	< 0.20
H/E	< 0.12	< 0.10
track isolation $\sum p_{\mathrm{T}}/p_{\mathrm{T}}^{\ell}$	< 0.2	
ECAL isolation $\sum p_{\mathrm{T}}/p_{\mathrm{T}}^{\ell}$	< 0.2	
HCAL isolation $\sum p_{\mathrm{T}}/p_{\mathrm{T}}^{\ell}$	< 0.2	
d_0 [cm]	< 0.02	
N_{miss}	$= 0$	

In addition to the variables listed above, the MVA uses the following additional discriminating variables:

- $\sigma_{\mathrm{i}\phi\mathrm{i}\phi}$ - a measure of the spread in ϕ of the electron's energy deposit in the ECAL.
- f_{brem} - the fraction of momentum carried away by bremsstrahlung while the electron courses through the tracker.

- N_{clust} - the number of individual clusters comprising the full electron super cluster. An electron which has more than one cluster tends to have a large early bremsstrahlung.

- $1/E_{\text{SC}} - 1/p_{\text{track}}$ - the difference in the electron track momentum and the electron super cluster energy.

- $E_{\text{SC}}/p_{\text{track}}$ - simply another measure of the electrons difference in track momentum and ECAL energy

- $E_{\text{seed}}/p_{\text{out}}$ - the ratio of the electron super cluster seed energy to the momentum of the electron track in the final state

- $E_{\text{seed}}/p_{\text{out}}$ - the ratio of the electron super cluster seed energy to the momentum of the electron track in the initial state

- d_0 - transverse impact parameter

- $d_{3\text{D}}$ - three-dimensional impact parameter

- $d_{3\text{D}}/\delta\left(d_{3\text{D}}\right)$ - three-dimensional impact parameter significance

The output of the training in the lowest p_{T} bins are shown in Fig. 5.3. The larger the value of the output discriminant, the more likely an electron is to be signal-like. To select electrons for this analysis, we use the selections defined in Tab. 5.6, which select real signal electrons with an efficiency of approximately 80% and keep the fake electrons at a manageable level.

Table 5.6: Electron identification BDT output values for the six different training samples.

	$p_{\text{T}} < 20\,\text{GeV}$	$p_{\text{T}} >= 20\,\text{GeV}$
$0.0 <= \lvert\eta\rvert <= 1.0$	> 0.139	> 0.947
$1.0 < \lvert\eta\rvert < 1.479$	> 0.525	> 0.950
$1.479 < \lvert\eta\rvert < 2.5$	> 0.543	> 0.884

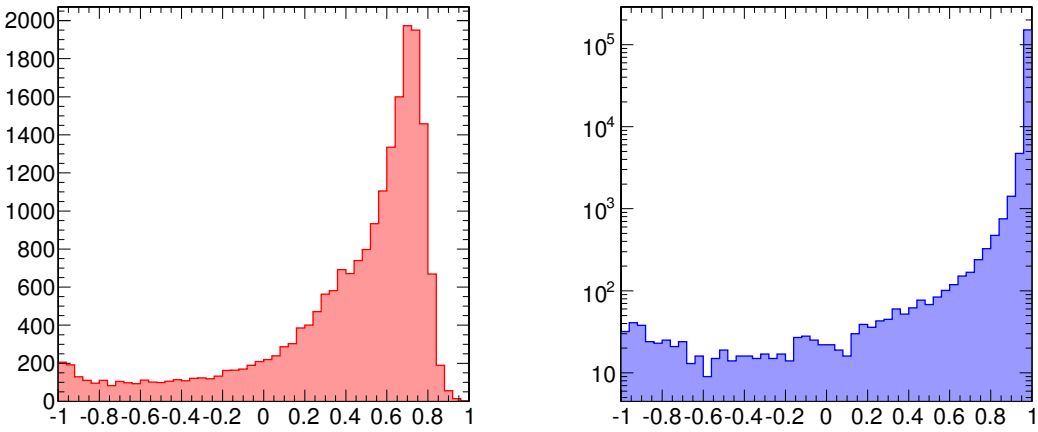

Figure 5.3: Output descriminant variable from the boosted decision tree electron identification for electrons with pseudorapidity $|\eta| < 1.0$ and transverse momentum $p_{\mathrm{T}} < 20$ (left) and $p_{\mathrm{T}} > 20$ (right).

Muon Identification

Both global and tracker muons are accepted in this analysis having a p_{T} greater than 10 GeV. Requirements on the inner track of the muon are made to reduce the combinatorial background coming from fake tracks matched to stray tracks in the muon chamber. Greater than 10 hits are required to be attached to the inner track as well as at least one pixel hit, the latter also reducing the background contribution from semi-lepton heavy flavor decays. In addition, the relative error on the inner track p_{T} must be less than 10%. For muons with p_{T} less than 200 GeV, the inner track dominates the momentum resolution measurement and any significant misreconstruction can lead to increases in fake $\not\!\!E_{\mathrm{T}}$ (see Sec. 3.5.6).

Additional selections are also applied depending on whether the muon was reconstructed as a global muon or a tracker muon. Global muons must have a normalized χ^2, with respect to the number of degrees of freedom, less than 10 to ensure a good global fit. One hit from the muon system must be present in the global muon fit and two different stations must record a hit. Tracker muons must pass additional requirements on the positions of the hits in the last chamber the muon is expected to cross. If no hit exists

in this chamber, or the hit is significantly displaced from expectation, the tracker muon fails the selection. These selections help to reduce backgrounds from punch-through, hadronic jets which have enough energy to pass through both calorimeters and scatter particles through the muon detector.

To help further reject pions and kaons which decay in flight through the inner portion of the CMS detector, a "kink-finding" algorithm was developed. When the pion or kaon direction is significantly different than the outgoing muon direction, the tracking algorithm will no longer be able to collect hits along the track and reconstruction will cease. However, if the incoming and outgoing decay products are collinear, the tracking will continue and attach the muon hits to the hits created by the pion or kaon. To combat this, the hits in each silicon layer are removed from the inner track, the track is refit and the χ^2 of the original and the new fit are compared. If the new fit is significantly worse, we assume the portion before the layer belongs to the hadron, the outer to the muon and reject the event.

5.1.2 Drell-Yan Background Suppression

Events with two electrons or two muons whose invariant mass falls within 15 GeV of the Z-mass (91.2 GeV) are removed killing a majority of the Drell-Yan background. Then, all events are required to have pf$\not\!\!E_{\mathrm{T}}$ greater than 20 GeV as Drell-Yan events do not have real $\not\!\!E_{\mathrm{T}}$. However, the cross section for Drell-Yan is quite large compared to the Higgs signal, so event mis-reconstruction caused by mis-measurement of one of the two lepton's transverse momentum can lead to Drell-Yan events passing the $\not\!\!E_{\mathrm{T}}$ selection. Most lepton mis-reconstructions will underestimate the true momentum of the lepton, and therefore, the $\not\!\!E_{\mathrm{T}}$ will point in the direction of the mis-reconstructed lepton. In addition, Z events which decay into two τ leptons, with each τ decaying leptonically, do have neutrinos in the final state. In these events, the $\not\!\!E_{\mathrm{T}}$ is also aligned along the direction of one of the lepton as the leptons and neutrinos are both boosted in the original direction of the τ.

To combat both types of backgrounds, we define proj–$\not\!\!E_{\mathrm{T}}$ as the projected $\not\!\!E_{\mathrm{T}}$

perpendicular to the direction of a lepton if the lepton falls within 90° of the $\not\!\!E_{\mathrm{T}}$ direction:

$$\text{proj–}\not\!\!E_{\mathrm{T}} = \begin{cases} \not\!\!E_{\mathrm{T}} & \text{if } \Delta\phi_{\mathrm{min}} > \frac{\pi}{2}, \\ \not\!\!E_{\mathrm{T}} \cdot \sin(\Delta\phi_{\mathrm{min}}) & \text{if } \Delta\phi_{\mathrm{min}} < \frac{\pi}{2} \end{cases}$$

$$\text{with } \Delta\phi_{\mathrm{min}} = \min(\Delta\phi(\ell_1, \not\!\!E_{\mathrm{T}}), \Delta\phi(\ell_2, \not\!\!E_{\mathrm{T}}))$$

where $\Delta\phi(\ell_i, \not\!\!E_{\mathrm{T}})$ is the angle between $\not\!\!E_{\mathrm{T}}$ and the ith lepton in the transverse plane. For illustrative purposes, the angle between the pf$\not\!\!E_{\mathrm{T}}$ and the nearest event is shown for Z to $\tau\tau$ events in Fig. 5.4 where one can see how the $\not\!\!E_{\mathrm{T}}$ and the nearest lepton are very near to each other while the opposite is the case for the signal events.

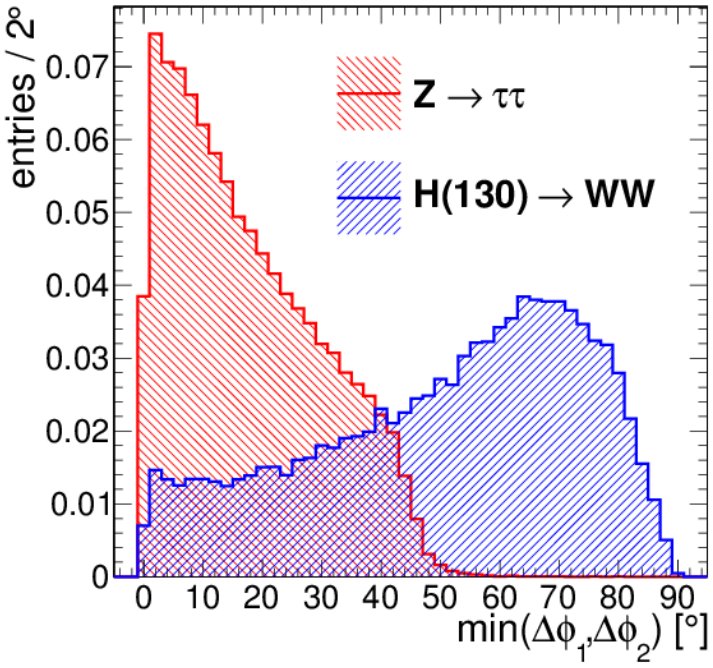

Figure 5.4: Minimum of the angle between the pf$\not\!\!E_{\mathrm{T}}$ direction and each of the leptons for Z to $\tau\tau$ events (red) and signal Higgs events (blue). The $\not\!\!E_{\mathrm{T}}$ and the leptons tend to be aligned for the former, allowing for better rejection with the projected $\not\!\!E_{\mathrm{T}}$ algorithm.

The final discriminating variable is formed as the minimum of the projection of each of the two $\not\!\!E_{\mathrm{T}}$ algorithms, min–$\not\!\!E_{\mathrm{T}}$:

$$\text{min–}\not\!\!E_{\mathrm{T}} = \min\left(\text{proj–pf}\not\!\!E_{\mathrm{T}}, \text{proj–tk}\not\!\!E_{\mathrm{T}}\right).$$

A decrease in the $\not\!\!E_{\rm T}$ resolution also has the effect of reducing the value of the real $\not\!\!E_{\rm T}$ measured in events with real $\not\!\!E_{\rm T}$. In order not to lose too much signal, we introduce a sliding $\not\!\!E_{\rm T}$ selection based on the number of pile-up interactions in the event. The final $\not\!\!E_{\rm T}$ selection requirements are:

- min–$\not\!\!E_{\rm T} > 20$ GeV for eμ final states, and
- min–$\not\!\!E_{\rm T} > (37 + N_{\rm vtx}/2)$ GeV for ee and $\mu\mu$ final states.

Finally, two other selections are applied to help dampen the contribution from Drell-Yan events. First, to remove Drell-Yan events recoiling against a jet, which contribute significantly to the mis-measured Drell-Yan background, we look for events where the two leptons are recoiling against a jet. By comparing the $\Delta\phi$ between the dilepton system and the most energetic jet in the event (if the most energetic jet is above 15 GeV), we remove events if the separation is great than 165°. Second, we reduce the available phase space for same flavor final states by requiring the minimum lepton $p_{\rm T}$, $p_{\rm T}^{\ell,\rm min}$, to be greater than 15 GeV.

5.1.3 Top Background Suppression

Jets are reconstructed as defined in Sec. 3.5.7 and all jets are required to fall within a fiducial of $|\eta| < 5.0$ and fall further than $\Delta R > 0.3$ from the two identified leptons. We define a "countable jet" as a jet which has a $p_{\rm T}$ larger than 30 GeV. Events are categorized into different categories based on the number of countable jets in the event, 0-jet, 1-jet or 2-jets. This allows for better background estimation as the background composition, especially the top background, in each of these categories is significantly different.

Top quarks immediately decay 100% of the time to a W boson and b-quark. In order to reduce the top background contribution, two different methods are used to identify and remove events with b-quarks. The first method identifies extra muons which might have originated from decays of hadrons containing a b-quark. We call these "soft-muons" as they tend to be produced in three body semileptonic b-decays and thus have lower transverse momentum. Any event containing a soft-muon meeting the following requirements is removed:

- $p_{\mathrm{T}} > 3$ GeV;
- reconstructed as a tracker muon
- passes stricter identifcation
- have greater than 10 hits associated with its inner track
- the longitudinal and transverse impact parameter must be less than 0.2 cm w.r.t. the first primary vertex
- if the p_{T} is greater than 20 GeV, the muon must be non-isolated

The second method uses the TCHE algorithm defined in Sec. 3.5.8 to identify events with b-quarks by searching for displaced vertices. The working point chosen for this analysis, a significance of 2.1, allows for strong top rejection while keeping the signal efficiency due to mis-identification at a high level. $t\bar{t}$ events in the 0-jet category can be rejected at a rate of 50% while keeping the rejection of the signal respectively low: 2%.

To combat against jets originating from secondary pile-up vertices being mis-tagged as a b-jet, the following "jet longitudinal impact parameter" is defined:

$$d_z^{\mathrm{jet}} = \frac{\left|\sum^i d_z^i \cdot (p_{\mathrm{T}}^i)^2\right|}{\sum^i (p_{\mathrm{T}}^i)^2}, \tag{5.1}$$

where the sums run over all tracks associated to the jet and d_z^i is the longitudinal impact parameter of the ith track. We remove events which have a jet with p_{T} greater than 10 GeV, d_z^{jet} less than 2 cm and identified by the TCHE method as a b-jet.

5.1.4 Other Background Suppression Selections

The minimum invariant mass for the dilepton system must be greater than 20 GeV for same flavor events. This removes the contribution from low-mass resonances like the Υ and J/ψ. It is also employed to reduce systematic uncertainty coming from poor Monte-Carlo simulation of the low-mass Drell-Yan region. We also use a 12 GeV selection on the $e\mu$ final states to reduce the uncertainty on the poorly modelled event generators in the low $m_{\ell\ell}$ region.

We further require the transverse momentum of the dilepton system to be greater than 45 GeV. This reduces the contribution from W+jet events which tend to have lower values of $p_T^{\ell\ell}$ while the signal fills the region above 45 GeV. This also helps to reduce the Drell-Yan background as the Z-boson from which the two leptons decay is, to first order, produced at rest.

Finally, events which have a third lepton with p_{T} greater than 10 GeV are removed to help eliminate contributions from WZ and ZZ production.

5.2 Mass-Dependent Selection

The following sections describe the mass-dependent selections designed to separate the $H \to W^+W^-$ events from non-resonant WW production. Two sets of selections are applied, one in the 0-jet and 1-jet category and the second for the 2-jet category designed to select Higgs boson events produced via the VBF process.

5.2.1 Zero-jet and One-jet Analysis

For each m_{H} hypothesis further selections are applied which maximize the expected sensitivity for the signal over the background (each mass-hypothesis considered in this analysis can been seen e.g. in Tab. 5.7). Five additional variables are used which help to discriminate the Higgs from the continuum WW background in the 0-jet category and from WW and $t\bar{t}$ in the 1-jet category: the transverse momentum of the leading and trailing lepton, $p_{\mathrm{T}}^{\ell,\mathrm{max}}$ and $p_{\mathrm{T}}^{\ell,\mathrm{min}}$; the invariant dilepton mass, $m_{\ell\ell}$; the opening angle in the azimuthal direction between the two leptons, $\Delta\phi_{\ell\ell}$; and finally, a "mass-like" variable called transverse mass between the dilepton system and the $\not{E}_{\mathrm{T}}$ defined as:

$$m_T^H = \sqrt{2p_{\mathrm{T}}^{\ell\ell}\,|\not{E}_{\mathrm{T}}|\,(1-\cos\Delta\phi\,(\ell\ell,\not{E}_{\mathrm{T}}))}.$$

The simulated distribution of these variables for signal and background can be seen later in Figs. 7.1 and 7.1. The exact selection criteria are shown in Tab. 5.7.

Table 5.7: Mass-dependent selections applied for each Higgs mass hypothesis designed for maximum sensitivity over the non-resonant WW background. The parenthesis in the $p_{\mathrm{T}}^{\ell,\mathrm{min}}$ column represent the higher threshold for the same-flavor channels.

m_{H} [GeV]	$p_{\mathrm{T}}^{\ell,\mathrm{max}}$ [GeV] $>$	$p_{\mathrm{T}}^{\ell,\mathrm{min}}$ [GeV] $>$	$m_{\ell\ell}$ [GeV] $<$	$\Delta\phi_{\ell\ell}$ [$\circ$] $<$	$m_T^{\ell\ell}$ [GeV] [,]
110	20	10(15)	40	115	[80,110]
115	20	10(15)	40	115	[80,110]
118	20	10(15)	40	115	[80,115]
120	20	10(15)	40	115	[80,120]
122	21	10(15)	41	110	[80,121]
124	22	10(15)	42	105	[80,122]
126	23	10(15)	43	100	[80,123]
128	24	10(15)	44	95	[80,124]
130	25	10(15)	45	90	[80,125]
135	25	12(15)	45	90	[80,128]
140	25	15	45	90	[80,130]
150	27	25	50	90	[80,150]
160	30	25	50	60	[90,160]
170	34	25	50	60	[110,170]
180	36	25	60	70	[120,180]
190	38	25	80	90	[120,190]
200	40	25	90	100	[120,200]
250	55	25	150	140	[120,250]
300	70	25	200	175	[120,300]
350	80	25	250	175	[120,350]
400	90	25	300	175	[120,400]
450	110	25	350	175	[120,450]
500	120	25	400	175	[120,500]
550	130	25	450	175	[120,550]
600	140	25	500	175	[120,600]

5.2.2 Two-Jet Analysis

For the 2-jet category, in addition to looking for the two leptons and missing transverse energy, we also look for two forward jets to explicitly target Higgs produced via the VBF production mode. No other jets with p_{T} greater than 30 GeV should be present between (in η) the two counted jets. The two counted jets in the event are then required to have an η separation, $\Delta\eta_{jj}$, greater than 3.5 and an invariant mass, m_{jj}, greater than 450 GeV. The two leptons in the event are also required to be between the two jets in η.

To further increase the signal to background ratio, we require a mass-dependent dilepton invariant mass selection. Tab. 5.8 shows the $m_{\ell\ell}$ selections for each Higgs mass hypothesis.

Table 5.8: Summary of selection criteria for the 2-jet analysis for each value of m_{H}.

m_{H} [GeV]	$m_{\ell\ell}$ [GeV] $<$	m_{H} [GeV]	$m_{\ell\ell}$ [GeV] $<$	m_{H} [GeV]	$m_{\ell\ell}$ [GeV] $<$	m_{H} [GeV]	$m_{\ell\ell}$ [GeV] $<$	m_{H} [GeV]	$m_{\ell\ell}$ [GeV] $<$
110	70	124	70	140	90	190	120	400	400
115	70	126	80	150	100	200	130	450	450
118	70	128	80	160	100	250	250	500	500
120	70	130	80	170	100	300	300	550	550
122	70	135	90	180	110	350	350	600	600

5.3 Determination of Selection Efficiencies

Final yield predictions from simulation need to be corrected for reconstruction and identification differences between simulation and data. To measure lepton trigger and identification efficiencies, a "tag-and-probe" technique is used. This method relies on the high purity control sample of dileptons near the Z boson mass resonance. "Tag" leptons are first selected using the full lepton identification defined in Sec. 5.1.1. Matching "probe" leptons are then identified with a loose identification which, along with the tag lepton, fall within an invariant mass window of $|m_{\ell\ell} - m_Z| < 15\,\text{GeV}$. Probe leptons are then probed to determine the efficiency for which they pass the criterion under study.

While the control sample is very pure, some background contribution is present. A simultanous fit of the $m_{\ell\ell}$ line shape is performed using different shape distribution hypotheses for the prompt dileptons from the Z decays and the other processes also present. The fit is performed for the "pass-pass" sample, where both leptons pass the criterion under staudy, and the "pass-fail" sample, where the probe lepton fails the criterion. The efficiency for the probe to pass the criterion is also used in the simultaneous fit.

5.3.1 Electron Identification Efficiency

Electron identification efficiencies are measured using an assymeteric Gaussian distribution to allow for acurate discription of the tails due to electron resolution for the Z line shape. Tag electrons are required to pass the full electron identification as well as a single electron trigger. The denominator probe electron definition is any reconstructed electron while the numerator condition is to require the full electron identification. The fit is done in separate bins based on the probe's p_{T} and η as well as for two different running periods where the pile-up distributions were significantly different, labelled 2011A and 2011B.

The process is repeated in data and in simulation using a normalized mix of appropriate background samples. The ratio of the efficiencies in each bin is taken as a correction factor for simulated events, re-weighting on an event by event basis. The weights for electrons in each bin is shown in Tab. 5.9. An example fit for barrel electrons

with p_T between 15 and 20 GeV is shown in Fig. 5.5.

Table 5.9: Data to simulation electron identification efficiency scale factors.

	p_T range [GeV]	$\|\eta\| < 1.4442$	$1.4442 < \|\eta\| < 1.556$	$\|\eta\| > 1.556$
2011A	$p_T < 15$	1.009 ± 0.030	0.792 ± 0.120	1.179 ± 0.064
	$15 < p_T < 20$	0.987 ± 0.015	0.859 ± 0.186	1.038 ± 0.029
	$20 < p_T < 25$	0.959 ± 0.007	1.041 ± 0.051	1.015 ± 0.014
	$25 < p_T < 50$	0.990 ± 0.000	1.014 ± 0.008	1.006 ± 0.002
	$50 < p_T$	0.986 ± 0.002	1.012 ± 0.020	1.014 ± 0.030
2011B	$p_T < 15$	0.916 ± 0.036	1.024 ± 0.198	0.898 ± 0.080
	$15 < p_T < 20$	0.933 ± 0.017	1.130 ± 0.150	1.026 ± 0.042
	$20 < p_T < 25$	0.947 ± 0.008	0.950 ± 0.053	1.006 ± 0.019
	$25 < p_T < 50$	0.988 ± 0.006	1.007 ± 0.007	1.010 ± 0.003
	$50 < p_T$	0.982 ± 0.002	0.992 ± 0.011	0.999 ± 0.006

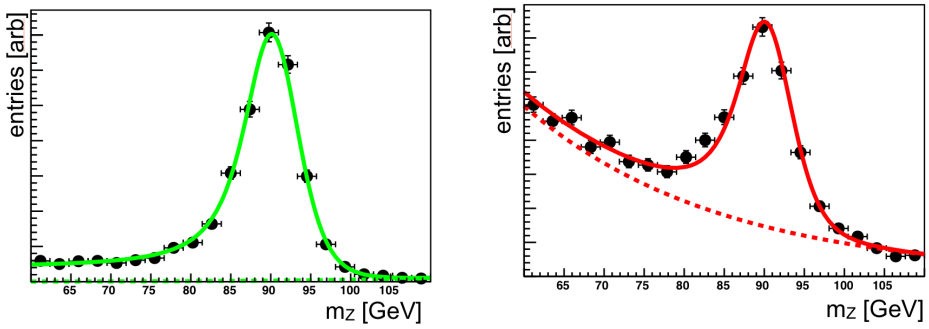

Figure 5.5: Fit for electron efficiency for probes with $|\eta| < 1.48$ and $15 < p_T < 20$. The distribution on the left is for events where the probe also passes the full electron identificaction while the figure on the right shows the fit for probes failing the electron selection.

5.3.2 Muon Identification Efficiency

Muon identification efficiencies are measured using two Voigtian distributions (a mix of normal and Breit-Wigner distributions) for the Z line shape, one for the Z resonance itself, and one to account for the resolution of the CMS detector. Tag muons are required to pass the full muon identification as well as a single muon trigger. The

denominator probe muon definition is all reconstructed muons while the numerator condition is to require the full muon identification. As for electrons, the fit is done in separate bins based on the probe's p_{T} and η as well as for two different running periods where the pile-up distributions were significantly different, labelled 2011A and 2011B.

The same procedure is applied to properly re-weight simulated events. Good agreement is found for muons in the barrel, while some deterctor inneficiency is seen for muons in the forward region due to temporarily missing channels which were never simulated as well as for a CSC readout issue affecting the higher luminosity runs. The full set of scale factors can be seen in Tab. 5.10 while an example of the simultaneous signal and background fits is shown for muons between 15 and 20 GeV in p_{T} in the endcap region.

Table 5.10: Data to simulation muon identification efficiency scale factors.

	p_{T} range [GeV]	$\lvert\eta\rvert < 1.48$	$\lvert\eta\rvert > 1.48$
2011A	$p_{\mathrm{T}} < 15$	0.973 ± 0.015	0.989 ± 0.013
	$15 < p_{\mathrm{T}} < 20$	0.991 ± 0.008	0.985 ± 0.008
	$20 < p_{\mathrm{T}} < 50$	0.994 ± 0.000	0.995 ± 0.001
	$50 < p_{\mathrm{T}}$	0.993 ± 0.001	0.991 ± 0.002
2011B	$p_{\mathrm{T}} < 15$	0.961 ± 0.017	0.964 ± 0.016
	$15 < p_{\mathrm{T}} < 20$	0.959 ± 0.009	0.972 ± 0.010
	$20 < p_{\mathrm{T}} < 50$	0.985 ± 0.000	0.963 ± 0.001
	$50 < p_{\mathrm{T}}$	0.984 ± 0.001	0.965 ± 0.003

5.3.3 Trigger Efficiency

To determine the trigger efficiency in data, both tag and probe leptons must first pass the full lepton identification requirements. Further, the tag lepton must pass a trigger requirement from one of the single lepton triggers in order not to bias the measurement on the probe lepton. Each single lepton trigger efficiency is then determined by checking whether the probe leptons fire the appropriate trigger path. Dilepton trigger efficiencies can be calculated using the efficiencies of each leg of the trigger individually with the same technique. As the single lepton trigger requirements are always more stringent that the dilepton trigger requirements, and the requirements of the higher p_{T}

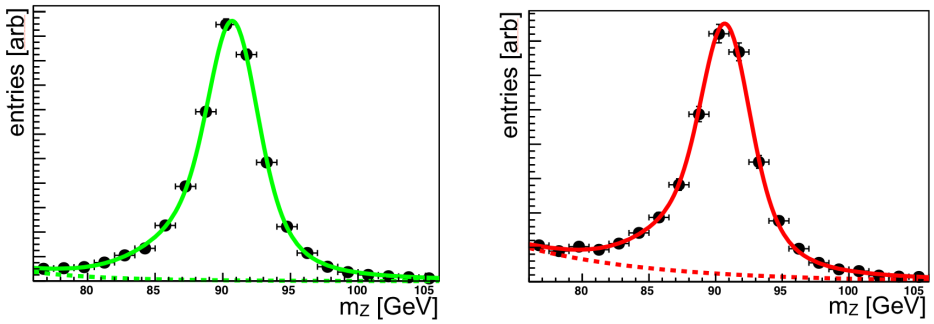

Figure 5.6: Fit for muon efficiency for probes with $|\eta| > 1.48$ and $15 < p_{\mathrm{T}} < 20$. The distribution on the left are for events where the probe also passes the full muon identificaction while the figure on the right shows the fit for probes failing the muon selection.

leg of the dilepton trigger is always more stringent than the lower p_{T} leg, the full event efficiency, $\varepsilon^{\mathrm{tot}}_{\mathrm{trig}}$, can be computed using the following formula:

$$\begin{aligned}
\varepsilon^{\mathrm{tot}}_{\mathrm{trig}} = & \quad \varepsilon_{\mathrm{s}}(\eta_1, p_{\mathrm{T1}}) & \times & \quad 1 & \textit{(single lepton 1)} \\
+ & \quad [\varepsilon_{\mathrm{t}}(\eta_1, p_{\mathrm{T1}}) - \varepsilon_{\mathrm{s}}(\eta_1, p_{\mathrm{T1}})] & \times & \quad \varepsilon_{\mathrm{l}}(\eta_2, p_{\mathrm{T2}}) & \textit{(double lepton 1+2)} \\
+ & \quad [\varepsilon_{\mathrm{l}}(\eta_1, p_{\mathrm{T1}}) - \varepsilon_{\mathrm{t}}(\eta_1, p_{\mathrm{T1}})] & \times & \quad \varepsilon_{\mathrm{t}}(\eta_2, p_{\mathrm{T2}}) & \textit{(double lepton 2+1)} \\
+ & \quad [1 - \varepsilon_{\mathrm{l}}(\eta_1, p_{\mathrm{T1}})] & \times & \quad \varepsilon_{\mathrm{s}}(\eta_2, p_{\mathrm{T2}}) & \textit{(single lepton 2)}
\end{aligned}$$

This formula holds for any luminosity period where the trigger conditions were held consant. Any changes in trigger conditions require a new set of trigger efficiency computations. The average trigger efficiency over the entire 2011 run is then averaged, weighting each period by its integrated luminosity. The superscripts in the formular refer to the higher (1) or lower (2) p_{T} lepton while the subscripts refer to the efficiencies for the single triggers (s), the tighter leg of the dilepton trigger (t) and the looser leg of the dilepton triggers (l). Also, the dependence on p_{T} and η indicate the trigger efficiencies are calculated in separate p_{T} and η bins.

Finally, the trigger is not simulated, so each simulated event is assigned a probability to pass any of the trigger requirements by using the efficiencies from data, binned in the p_{T} and η of the two leptons. This probability is then used to de-weight the final simulated yield on an event by event basis to accurately reflect the loss of events due to

the trigger. The overall trigger efficiencies are generally above 95% and are listed for a few Higgs mass hypothesis selection in Tab. 5.11.

Table 5.11: Trigger efficiencies (%) for the selections in various Higgs mass hypotheses.

	m_{H} [GeV]	120	140	160	200	400
$\mu\mu$	($p_{\mathrm{T}} > 20/15$ GeV)	96.958	97.625	98.363	98.763	99.626
ee	($p_{\mathrm{T}} > 20/15$ GeV)	97.280	97.775	98.122	98.390	99.340
eμ and μe	($p_{\mathrm{T}} > 20/10$ GeV)	94.665	95.043	95.386	95.957	98.119

5.4 Determination of Background Contributions

As this analysis is a counting experiment where the discovery or exclusion sensitivity is largely based on knowing as precisely as possible the number of extra events over the expectation, measuring the background contribution to the signal region as precisely as possible is paramount. Background estimates for non-resonant WW, $Z/\gamma^* \to \ell\ell$, WW, $t\bar{t}$ and tW processes are all measured using a "data-driven" technique. That is, instead of relying on simulation, control regions in data are defined such that the background under measurement is enriched with respect to other backgrounds and such that the expected signal contribution would be negligible. The measurement in the control region is then extrapolated back into the signal region. For each background measurement, any differences due to jet category, lepton flavor or m_{H} hypothesis are taken into account by performing separate measurements in each channel. Further, the measurements are done as close as possible to the signal region to limit the uncertainty on the extrapolation, however, if a background contribution is too small (statistically limited) in the signal region, the measurement is done at the mass-independent level and propagated to the final signal region using the ratio measured in simulation.

$W\gamma^*$ and $Z/\gamma^* \to \tau\tau$ backgrounds are taken from simulation, however cross checks are performed in data to ensure their viability. Finally, as their contributions are well understood and no available control regions can be defined to measure their contribution, the WZ and ZZ backgrounds, as well as the non-resonant WW in the large Higgs mass hypothesis ($m_{\mathrm{H}} > 200\,\mathrm{GeV}$), are taken directly from simulation.

5.4.1 Fake Induced Backgrounds

Measurement of the final contribution of $W+$jets and QCD events is done in two steps. First, the probability for jet mis-identification, referred to as the "fake rate," ε_{F}, is measured in a sample enriched in hadronic activity, namely QCD events. Then, the fake rate is applied to a control region defined in data by inverting the full electron and muon identification criteria.

Fake Rate Measurement

The fake rate is the measure of the probability for a fake lepton to be fully identified as a prompt isolated lepton. For this analysis, the fake rate will be defined loosening a few of the full lepton identification requirements. A full reduction of identification requirements would create problems by increasing the systematical uncertainty in the propagation from control region to signal region due to the difference in the hadronic make up in these regions. A looser lepton selection thus "normalizes" the two regions. For electrons, the MVA and isolation selections are reduced and the following criteria are applied (multiple definitions indicate separate selections for the barrel and endcap, respectively):

- $\sigma_{i\eta i\eta} < 0.01/0.03$
- $|\Delta\phi_{in}| < 0.15/0.10$
- $|\Delta\eta_{in}| < 0.007/0.009$
- $H/E < 0.12/0.10$
- full conversion rejection
- $|d_0| < 0.02$ cm
- $|d_{\mathrm{z}}| < 0.1$ cm
- $\frac{\Sigma_{\mathrm{trk}} E_{\mathrm{T}}}{p_{\mathrm{T}}^{\mathrm{ele}}} < 0.2$
- $\frac{\Sigma_{\mathrm{ECAL}} E_{\mathrm{T}}}{p_{\mathrm{T}}^{\mathrm{ele}}} < 0.2$
- $\frac{\Sigma_{\mathrm{HCAL}} E_{\mathrm{T}}}{p_{\mathrm{T}}^{\mathrm{ele}}} < 0.2$

While for the loose muon definition, the impact parameter and isolation selections are relaxed thusly:

- $|d_0| < 0.2$ cm
- $\frac{\mathrm{Iso}_{\mathrm{Total}}}{p_{\mathrm{T}}} < 0.4$

To measure the fake rate, a region rich in jets is defined by searching for QCD di-jet events. Events are chosen with two high p_{T} jets in which the leading jet is above threshold (35 GeV for the electron measurement and 15 GeV for the muon measurement) and the trailing jet passes the loose lepton criteria. The leading jet threshold is used to ensure a proper momentum range for the loose leptons which will ultimately appear in the signal region. An additional requirement on the separation of the two jets ($\Delta\phi\,(\ell\ell, j) > 1$) is used to ensure QCD like events. Contamination from $W+$jets and $Z+$jets events are minimized by requiring the following criteria for the muon fake rate measurement (left) and the electron fake rate measurement (right):

- pf$\not{E}_{\mathrm{T}} < 20\,\mathrm{GeV}$ and $m_T < 20\,\mathrm{GeV}$
- $m_{\ell\ell} > 20\,\mathrm{GeV}$
- $m_{\ell\ell} > |m_Z - 15|$

- pf$\not{E}_{\mathrm{T}} < 20\,\mathrm{GeV}$
- $m_{\ell\ell} > 20\,\mathrm{GeV}$
- $m_{\ell\ell} > |m_Z - 30|$

The missing energy selections help to remove the $W+$jets events, while the invariant mass selections remove $Z+$jets events. Contribution from electroweak processes is still visible for the jets on the higher end of the p_{T} spectrum. To not bias the fake rate measurement, the remaining electroweak contribution is removed statistically based on measurements in simulation. The fake rate is then the number of loose leptons (trailing jets) which pass the full identification. The fake rate is separated in various p_{T} and η bins as well as for low and high pile-up regions. The fake rate as a function of pseudorapidity can be seen in Fig. 5.7 both before and after the simulated electroweak correction. The fake rates for each bin can be found in Appx. C.

Propagation to Signal Region

Once the fake rate has been calculated, it is then possible to calculate the contribution from $W+$jets and QCD events in the signal region. The following formula shows the contribution from real dilepton events, $N\ell\ell$, $W+$jets events, $N_{\mathrm{W+jets}}$ and

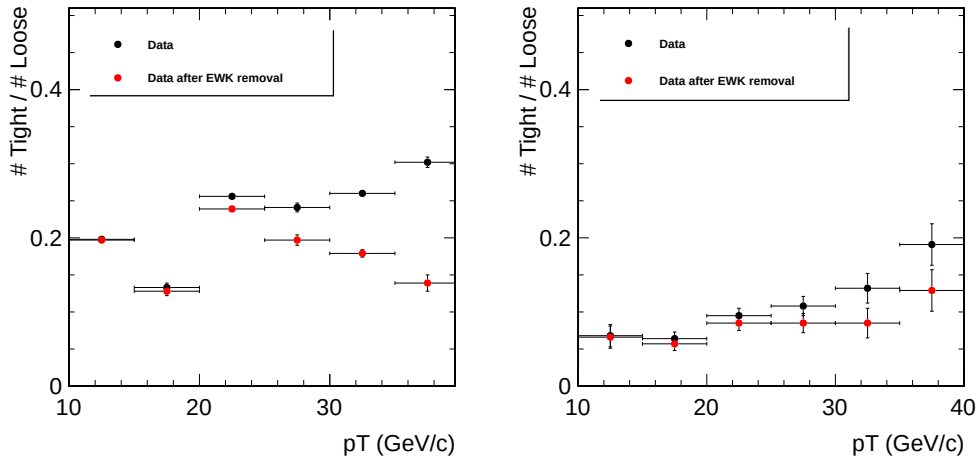

Figure 5.7: Fake rate as a function of the loose lepton p_{T} for muons (left) and electrons (right) in the pseudorapidity region $|\eta| < 1$, before (black) and after (red) EWK statistical subtraction. The plots correspond to the $\eta < 1$ region.

QCD events, N_{QCD}, in three dilepton categorizations: N_{PP}, N_{PF} and N_{FF}:

$$\begin{aligned} N_{\mathrm{FF}} = \quad & (1-\varepsilon_{\mathrm{P}})^2 N_{\ell\ell} + \quad (1-\varepsilon_{\mathrm{P}})(1-\varepsilon_{\mathrm{F}}) N_{\mathrm{W+jets}} + \quad (1-\varepsilon_{\mathrm{F}})^2 N_{\mathrm{QCD}} \\ N_{\mathrm{PF}} = \quad & 2\varepsilon_{\mathrm{P}}(1-\varepsilon_{\mathrm{P}}) N_{\ell\ell} + \quad (\varepsilon_{\mathrm{P}}+\varepsilon_{\mathrm{F}}-2\varepsilon_{\mathrm{P}}\varepsilon_{\mathrm{F}}) N_{\mathrm{W+jets}} + \quad 2\varepsilon_{\mathrm{F}}(1-\varepsilon_{\mathrm{F}}) N_{\mathrm{QCD}} \\ N_{\mathrm{PP}} = \quad & \varepsilon_{\mathrm{P}}^2 N_{\ell\ell} + \quad \varepsilon_{\mathrm{P}}\varepsilon_{\mathrm{F}} N_{\mathrm{W+jets}} + \quad \varepsilon_{\mathrm{F}}^2 N_{\mathrm{QCD}} \end{aligned} \tag{5.2}$$

N_{PP} is the number of events where two leptons pass the tight lepton selection, N_{PF} is the number of events where one lepton passes the full selection with the other lepton only passing the loose identification, and N_{FF} is the number of events where both leptons only pass the loose definition. The only piece of the puzzle left undiscussed is ε_{P}, the "prompt rate," defined similarly as the fake rate, but using prompt leptons taken from a sample of $Z/\gamma^* \to \ell\ell$ events and measured using the standard tag-and-probe technique.

The three formulas can be thought of as a simplification to the problem at hand in which there is only one value of the fake rate and the prompt rate (instead of multiple bins in p_{T}, η and N_{vtx}, as well as two different types of leptons). In actuality, there is a separate set of equations for each measured fake rate bin. These three formulas are a system of equations and can be inverted to solve for $N_{\mathrm{W+jets}}$ and N_{QCD} as only a function

of N_{FF}, N_{PF}, N_{PP}, ε_{P} and ε_{F}, the latter two already calculated with the former three are easily countable in data. Effectively, this procedure is done in every region one needs to estimate the fake contribution, including at the full selection level for each Higgs mass hypothesis. In actuality, the situation is simpler. Each event can be assigned a weight based on its fake rate bin and dilepton final state. These weights are carried around and summed for each event passing the desired selection. The agreement between data and simulation for this procedure is quite good and can be seen looking at the trailing lepton p_{T} distribution which is dominated by fakes on the low end, top left of Fig. 7.2. The full estimate of the $W+$jets contribution (QCD is negligible) can be seen in Tab. 5.12.

Table 5.12: $W+$jets yield at the Higgs selection level. Errors are statistical only.

m_{H} [GeV]	0-jet bin	1-jet bin	2-jet bin
120	15 ± 2.1	5.4 ± 1.4	0.85 ± 0.60
130	18 ± 2.4	6.5 ± 1.6	0.85 ± 0.60
140	15 ± 2.0	5.8 ± 1.4	0.85 ± 0.60
150	6.4 ± 1.4	4.4 ± 1.1	0.85 ± 0.60
160	3.0 ± 1.1	3.1 ± 1.0	0.85 ± 0.60
180	1.5 ± 0.9	3.4 ± 1.1	0.85 ± 0.60
200	3.3 ± 1.1	5.3 ± 1.3	0.85 ± 0.60
300	6.5 ± 1.1	6.2 ± 1.2	0.73 ± 0.61

The systematic uncertainty in this procedure comes from two sources. The first is statistical in nature and comes from the number of events used to determine the fake rate in each bin. Then, the difference in jet composition between the sample used to measure the fake rate, and the control sample used to calculate the final yields is measured by performing a closure test on simulation, comparing the expected yield from simulation to the measured yield from the fake rate procedure. The closure is on the order of 30% depending on m_{H} hypothesis. Finally, the difference in the jet kinematical distribution is covered by varying the nominal leading jet p_{T} requirement which also gives a 30% uncertainty.

5.4.2 Drell-Yan Background

The Drell-Yan process contributes to the same flavor final states when instrumental noise or reconstruction errors cause fake missing energy. The instrumental noise

is exasperated by increases in the luminosity due to the large number of pile-up particles flooding the detector. Events near the Z resonance, which are removed in this analysis, create a natural control region. The Drell-Yan yield after full selection but with the Z veto inverted, is estimated, stripped of contamination from non Drell-Yan processes and then propagated to the signal region using the ratio from simulation. This ratio is cross-checked in data, found to perform similarly and forgotten in favor of the higher statistics found from simulation. This procedure is performed for each m_{H} hypothesis in each jet category at a selection very close to the final selection. Only the m_T^H requirements are relaxed and the rest of the propagation is performed from the simulated ratio. The Drell-Yan contribution in opposite flavor final states is minute due to the low probability for a muon to fake an electron, or vice versa. The opposite flavor contribution is measured from simulation.

To get as pure of a sample of Drell-Yan events as possible, a tight window around the resonance of $\pm 7.5\,\mathrm{GeV}$ is used. Remaining background can then be categorized as either diboson backgrounds where both leptons originate from a Z boson or from other non-resonant dilepton events (e.g. $t\bar{t}$ or WW). Both are removed from the in-peak yield using estimates from simulation. The diboson events which pass the full selection have a real source of $\not\!\!E_{\mathrm{T}}$ (either a single neutrino from the W in the WZ production, or two neutrinos from the other Z in ZZ production) which is well-modeled by simulation and therefore their contribution can be accurately removed with the simulated estimate. A 10% error is assigned to this subtraction. For the non-resonant contribution in the Z peak, the same flavor contribution can be estimated from the opposite flavor contribution, making sure to account for the differences in the lepton selection efficiency. A factor, $k_{\ell\ell}$, is introduced which properly takes this into account:

$$k_{\ell\ell} = \frac{1}{2} \cdot \left(\sqrt{\frac{N_{\mathrm{ee}}^{\mathrm{peak}}}{N_{\mu\mu}^{\mathrm{peak}}}} + \sqrt{\frac{N_{\mu\mu}^{\mathrm{peak}}}{N_{\mathrm{ee}}^{\mathrm{peak}}}} \right) \tag{5.3}$$

where $N_{\ell\ell}^{\mathrm{peak}}$ are the yields for the same flavor events in the Z-peak. The final estimate of the Drell-Yan events in the control region is then:

$$N_{\mathrm{DY}}^{\mathrm{peak}} = N_{\ell\ell}^{\mathrm{peak,data}} - \frac{k_{\ell\ell}}{2} \cdot N_{\mathrm{e}\mu}^{\mathrm{peak,data}} - N_{\mathrm{ZV}}^{\mathrm{peak,sim}} \tag{5.4}$$

and the propagation back to the signal region is done using the ratio, $R_{\text{sim}}^{\text{out/in}}$, taken from simulation:

$$N_{\text{DY}}^{\text{signal}} = N_{\text{DY}}^{\text{peak}} \cdot R_{\text{sim}}^{\text{out/in}} \quad \text{with} \quad R_{\text{sim}}^{\text{out/in}} = \frac{N_{\text{DY}}^{\text{peak,sim}}}{N_{\text{DY}}^{\text{yield,sim}}} \tag{5.5}$$

Fig. 5.8 shows the distribution of events inside the control region for each of the three jet categories. In general, three times as many Drell-Yan events are present than expected, indicated a gross misunderstanding of the $\not\!\!E_{\text{T}}$ resolution and the contribution from pile-up. In fact, moving to events with lower pile-up up, or applying a $\not\!\!E_{\text{T}}$ selection not so far into the tail of the Drell-Yan $\not\!\!E_{\text{T}}$ distribution gives significantly closer ratios of data to expectation from simulation. The calculation of $R_{\text{sim}}^{\text{out/in}}$ is done in simulation

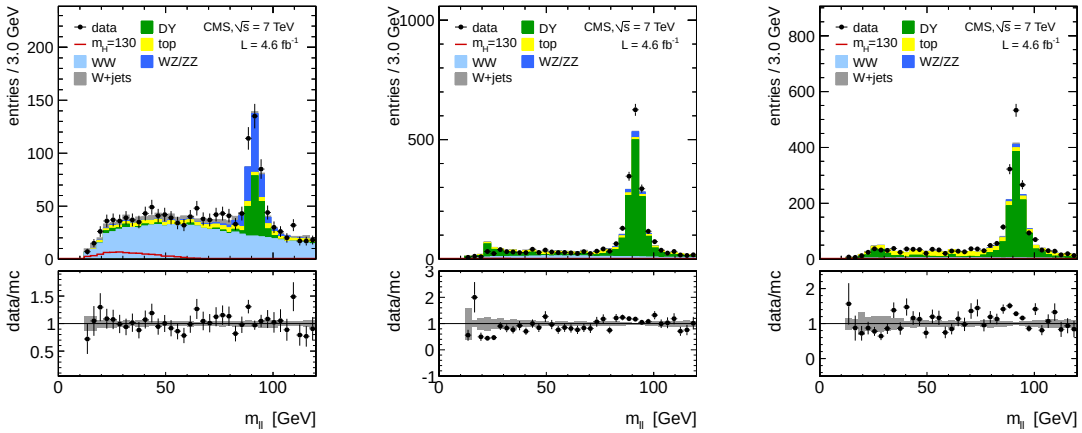

Figure 5.8: Dilepton invariant mass distribution in the 0-jet, 1-jet and 2-jet categories after removing the Z veto and after applying the mass-independent selection. A similar distribution with more stringent selections is used for each Higgs mass hypothesis to calculate the in-peak yield for propagation back to the signal region.

after the full using the full missing energy selection of min–$\not\!\!E_{\text{T}} > (37 + N_{\text{vtx}}/2)\,\text{GeV}$ except in cases where too few events in the control region cause an unreasonably large statistical error, greater than 15%. In this case, $R_{\text{sim}}^{\text{out/in}}$ is estimated in the min–$\not\!\!E_{\text{T}}$ region $30 < \text{min–}\not\!\!E_{\text{T}} < (37 + N_{\text{vtx}}/2)\,\text{GeV}$. The Drell-Yan estimate to the same flavor states is shown for various Higgs masses in Tab. 5.13 for the 0-jet category and Tab. 5.14 for the 1-jet category.

Table 5.13: Estimation of the Drell-Yan background at the Higgs selection level in the 0-jet category for various Higgs masses. The first uncertainty on $R_{\text{sim}}^{\text{out/in}}$ represents the statistical uncertainty in the simulation. The second value is the systematic uncertainty due to the $\not{E}_{\text{T}}$ dependency.

m_{H} [GeV]	$N_{\ell\ell}^{\text{peak,data}}$	$R_{\text{sim}}^{\text{out/in}}$	$N_{\text{DY}}^{\text{signal}}$	$N_{\text{DY}}^{\text{signal,MC}}$
120	64	$0.17 \pm 0.05 \pm 0.08$	7.5 ± 9	1.3 ± 0.74
140	29	$0.34 \pm 0.17 \pm 0.17$	15 ± 9.9	1.9 ± 0.86
160	10	$0.91 \pm 0.27 \pm 0.10$	3.4 ± 6.5	0.75 ± 0.54
180	13	$0.63 \pm 0.22 \pm 0.20$	2.3 ± 2.7	0.44 ± 0.43
200	45	$0.25 \pm 0.19 \pm 0.27$	2.7 ± 4	0.44 ± 0.43

Table 5.14: Estimation of the Drell-Yan background at the Higgs selection level in the 1-jet category for various Higgs masses. The first uncertainty on $R_{\text{sim}}^{\text{out/in}}$ represents the statistical uncertainty in the simulation. The second value is the systematic uncertainty due to the $\not{E}_{\text{T}}$ dependency.

m_{H} [GeV]	$N_{\ell\ell}^{\text{peak,data}}$	$R_{\text{sim}}^{\text{out/in}}$	$N_{\text{DY}}^{\text{signal}}$	$N_{\text{DY}}^{\text{signal,MC}}$
120	84	$0.08 \pm 0.02 \pm 0.01$	5.4 ± 1.5	2.5 ± 0.84
140	47	$0.13 \pm 0.05 \pm 0.04$	5.5 ± 2.5	3.6 ± 0.97
160	27	$0.19 \pm 0.08 \pm 0.04$	4.2 ± 2.4	1.8 ± 0.7
180	38	$0.23 \pm 0.10 \pm 0.03$	7.2 ± 2.7	0.9 ± 0.43
200	112	$0.16 \pm 0.10 \pm 0.05$	15 ± 5.6	1.7 ± 0.60

Systematic errors for this procedure come from the small number of Drell-Yan events in the control region as well as the systematic error on $R_{\mathrm{sim}}^{\mathrm{out/in}}$. To calculate the latter, $R_{\mathrm{sim}}^{\mathrm{out/in}}$ is plotted as a function of min–$\not\!\!E_{\mathrm{T}}$ and the largest deviation from the nominal bin is taken as the systematic error. Examples of the $R_{\mathrm{sim}}^{\mathrm{out/in}}$ value plotted against min–$\not\!\!E_{\mathrm{T}}$ is shown in Fig. 5.9 for the 0-jet and 1-jet categories using the selection criteria from the $m_{\mathrm{H}} = 120$ hypothesis. Overall, the systematic uncertainty on this measurement is quite large, exceeding 50% for most hypotheses.

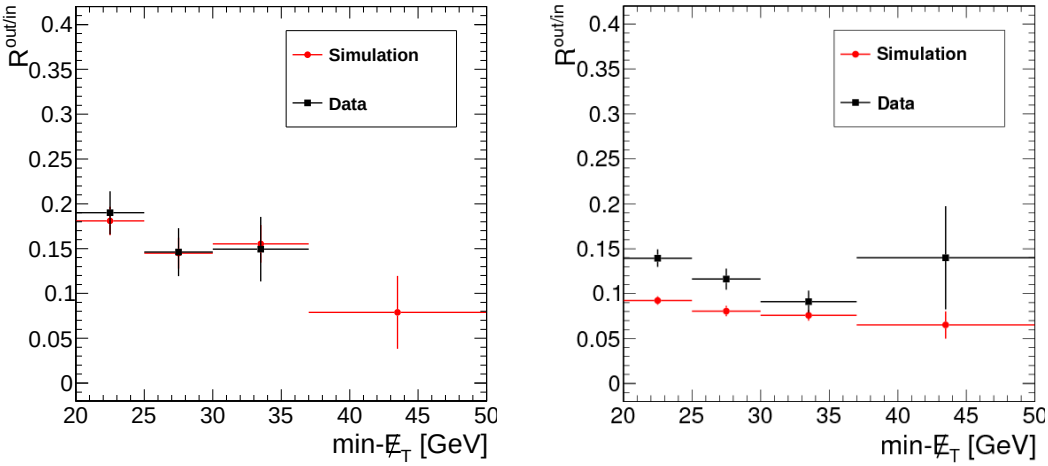

Figure 5.9: Distribution of $R_{\mathrm{sim}}^{\mathrm{out/in}}$ for $m_{\mathrm{H}} = 120$ in the 0-jet category (left) and the 1-jet category (right) as a function of min–$\not\!\!E_{\mathrm{T}}$. The deviation in $R_{\mathrm{sim}}^{\mathrm{out/in}}$ as a function of min–$\not\!\!E_{\mathrm{T}}$ is taken as a systematic for the Drell-Yan background estimate.

5.4.3 Top Backgrounds

This analysis is separated into jet categories in part due to the significantly different composition of the backgrounds containing top quarks in each category. Necessarily, the control regions to estimate the $t\bar{t}$ and tW backgrounds in each jet category are also significantly different. The backgrounds are measured in control regions defined by inverting one or both of the b-tagging vetoes and then using the b-tagging efficiencies to extrapolate back to the signal region. Separate control regions are also defined to measure the b-tagging efficiencies directly from data. Each measurement is first performed

at the mass-independent level and then extrapolated to each mass-dependent signal region using the expected ratio from simulation.

Zero-jet Bin

For a $t\bar{t}$ event to fall into the 0-jet category, both b-jets must have a transverse energy less than 30 GeV and both b-jets must fail the b-tagging algorithms defined in Sec. 5.1.3. To measure the b-tagging efficiency for "soft" jets, events with one and only one high p_{T} b-tagged jet are identified. The majority of these events come from $t\bar{t}$ production, with a fraction from tW production and finally an even smaller contribution from other non-top quark processes. For $t\bar{t}$ events, one soft b-jet remains which will be used to determining the b-tagging efficiency. The denominator for the efficiency calculation are all events in the control region subtracting out the expected contribution from tW and from other backgrounds. The expected contributions from $W+$jets and $Z+$jets events are rescaled based on the previous data-driven estimates. The expected contribution from non-resonant WW production is scaled up by 10% due to the measured simulated to data b-tagging fake rate discrepancy. The numerator is then the fraction of events passing the b-tagging requirements (both soft muon and TCHE methods) again correcting for tW and other backgrounds. Formulaically, the efficiency to tag a soft jet as a b-jet, $\varepsilon_{1\mathrm{b}}$, is defined as:

$$\varepsilon_{1\mathrm{b}} = \frac{N_{\mathrm{data}}(\mathrm{tag}) - N_{\mathrm{sim}}^{\mathrm{tW}}(\mathrm{tag}) - N_{\mathrm{sim}}^{\mathrm{other}}(\mathrm{tag})}{N_{\mathrm{data}}(\mathrm{all}) - N_{\mathrm{sim}}^{\mathrm{tW}}(\mathrm{all}) - N_{\mathrm{sim}}^{\mathrm{other}}(\mathrm{all})}, \tag{5.6}$$

The overall top-tagging efficiency in the 0-jet category can then be calculated as:

$$\varepsilon_{\mathrm{top}} = f_{t\bar{t}} \cdot \left[1 - (1 - \varepsilon_{1\mathrm{b}})^2\right] + (1 - f_{t\bar{t}}) \cdot \varepsilon_{1\mathrm{b}}, \tag{5.7}$$

where $f_{t\bar{t}}$ is the expected fraction of $t\bar{t}$ events (having two soft b-jets) and $1 - f_{t\bar{t}}$ is the remaining fraction comprised of tW production (having only one soft b-jet). The $1 - \left(1 - \varepsilon_{1\mathrm{b}}\right)^2$ term represents the probability for tagging neither soft b-jet in the $t\bar{t}$ process. This efficiency can then be used to determine the amount of top contribution in the signal region by counting events in the control region defined by the inversion of the top tagging veto and extrapolating back to the signal region:

$$N_{\mathrm{signal}}^{\mathrm{top}} = \left(N_{\mathrm{tag}}^{\mathrm{data}} - N_{\mathrm{tag}}^{\mathrm{other}}\right) \cdot \left[\frac{1 - \varepsilon_{\mathrm{top}}}{\varepsilon_{\mathrm{top}}}\right] \tag{5.8}$$

Again, here the expected non-top backgrounds are subtracted out using the expected contribution from simulation. The top two plots in Fig. 5.10 compare data and simulation of the TCHE discriminating variable in the two control regions. The left half of Tab. 5.15 shows the measured values used in the calculation of the top yield in the 0-jet category.

Table 5.15: Estimation of top backgrounds in the 0-jet and 1-jet categories.

0-jet category				1-jet category			
N_{data}(all)	1276			N_{data}(all)	2149		
$N_{\text{sim}}^{\text{tW}}$(all)	255.3	$\pm$	6.8				
$N_{\text{sim}}^{\text{other}}$(all)	74.9	$\pm$	15.3	$N_{\text{sim}}^{\text{other}}$(all)	10.6	$\pm$	0.5
N_{data}(tag)	363			N_{data}(tag)	1413		
$N_{\text{sim}}^{\text{tW}}$(tag)	36.1	$\pm$	2.5				
$N_{\text{sim}}^{\text{other}}$(tag)	5.9	$\pm$	3.8	$N_{\text{sim}}^{\text{other}}$(tag)	1.8	$\pm$	0.2
ε_{1b}	0.34	$\pm$	0.02				
$f_{t\bar{t}}$	0.66	$\pm$	0.11				
ε_{top}	0.49	$\pm$	0.07	ε_{b}	0.66	$\pm$	0.01
$N_{\text{tag}}^{\text{data}}$	193			$N_{\text{tag}}^{\text{data}}$	794		
$N_{\text{tag}}^{\text{other}}$	32.0	$\pm$	3.5	$N_{\text{tag}}^{\text{other}}$	83	$\pm$	23
$N_{\text{signal}}^{\text{top}}$	171	$\pm$	27	$N_{\text{signal}}^{\text{top}}$	370	$\pm$	17

One-jet Bin

In the 1-jet category, the $t\bar{t}$ and tW processes contribute when a high p_{T} b-jet does not get identified by the b-tagging algorithms. The high p_{T} b-tagging efficiency, ε_{b}, is measured in a control region selecting two jets where the subleading jet, in p_{T}, is tagged as a b-jet. This sample is completely dominating by $t\bar{t}$ events, however the efficiency measurement is corrected by the expected number of non-top quark events as estimated by simulation, similar to the 0-jet case:

$$\varepsilon_{\text{b}} = \frac{N_{\text{data}}\,(\text{tag}) - N_{\text{sim}}^{\text{other}}\,(\text{tag})}{N_{\text{data}}\,(\text{all}) - N_{\text{sim}}^{\text{other}}\,(\text{all})}, \tag{5.9}$$

The denominator is the number of background corrected top events in the efficiency control region, and the numerator is the subset of those events in which the leading jet is also tagged as a b-jet. Inverting the counted jet b-veto in the 1-jet category and utilizing

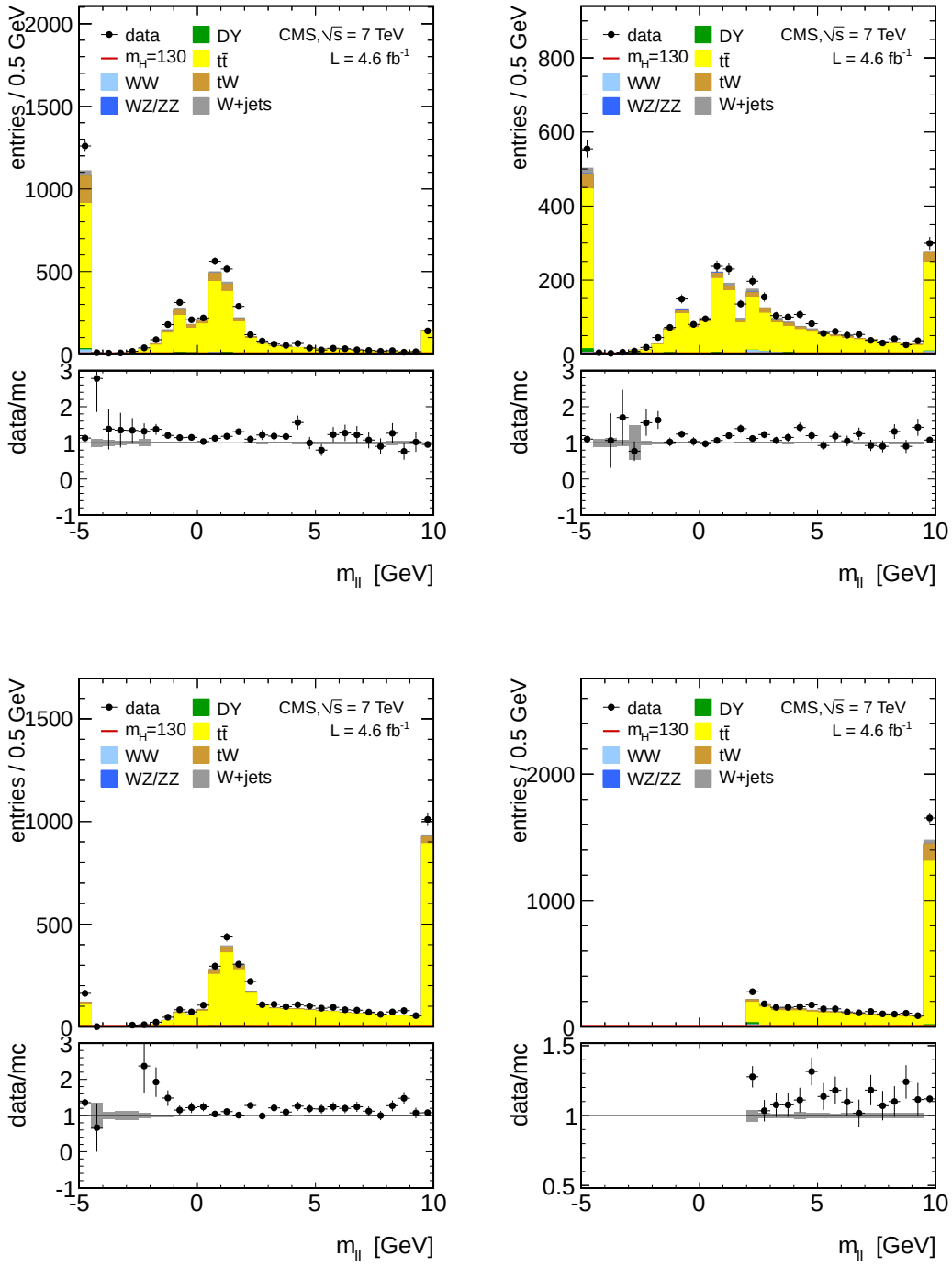

Figure 5.10: b-tagging discriminant for various control regions in the 0-jet (top) and 1-jet (bottom) categories. The b-tagging discriminant with the denominator selection is shown on the left while the b-tagging discriminant in the control region is shown on the right.

the measured value of ε_b to extrapolate yields the final top contribution in the signal region (again once backgrounds are subtracted):

$$N_{\text{signal}}^{\text{top}} = \left(N_{\text{tag}} - N_{\text{tag}}^{\text{other}}\right) \cdot \left[\frac{1-\varepsilon_b}{\varepsilon_b}\right] \tag{5.10}$$

The bottom two plots in Fig. 5.10 compare data and simulation of the TCHE discriminating variable in the two control regions for the 1-jet category. The right half of Tab. 5.15 shows the measured values used in the calculation of the top yield in the 1-jet category.

Two-jet Bin

To measure the b-tagging efficiency for the 2-jet category, an inclusive two jet sample is used and the procedure from the previous section is used. However, due to the significantly different jet spectrum in the VBF selection, the b-tagging efficiency is measured as a function of η. The control region for extrapolation back to the signal region is defined as the full VBF selection inverting the most central jet's b-veto. Eq. (5.10) is then used selecting ε_b from the proper η bin. The final yield is inflated by approximately 10% based on studies done on simulation due to $t\bar{t}$ events in which the most central jet falls outside of the tracking region ($|\eta| > 2.5$) and for which this method has no way to measure. The b-tagging efficiencies for each pseudorapidity bin are shown in Tab. 5.16.

Table 5.16: B-tagging efficiency measured in the 2-jet control region in bins of $|\eta|$ for the most central tag jet.

$\|\eta^{cj}\|$ bin	$0 < \|\eta\| < 0.5$	$0.5 < \|\eta\| < 1$	$1 < \|\eta\| < 1.5$	$1.5 < \|\eta\| < 2.5$
$\varepsilon(\|\eta^{cj}\|)$	0.68 ± 0.02	0.63 ± 0.03	0.57 ± 0.05	0.53 ± 0.10

5.4.4 WW Background

Fig. 5.11 shows the simulated dilepton invariant mass distributions for various Higgs boson masses as well as the non-resonant WW production. While the WW production populates the full width of the histogram, Higgs boson with a mass less than

around 200 GeV only populate the region with $m_{\ell\ell} < 100\,\text{GeV}$. This observation gives a very nice control region for measuring the WW continuum background from data. For Higgs boson production with a mass greater than 200 GeV, the WW estimate will have to be take from simulation because no suitable control region can be found.

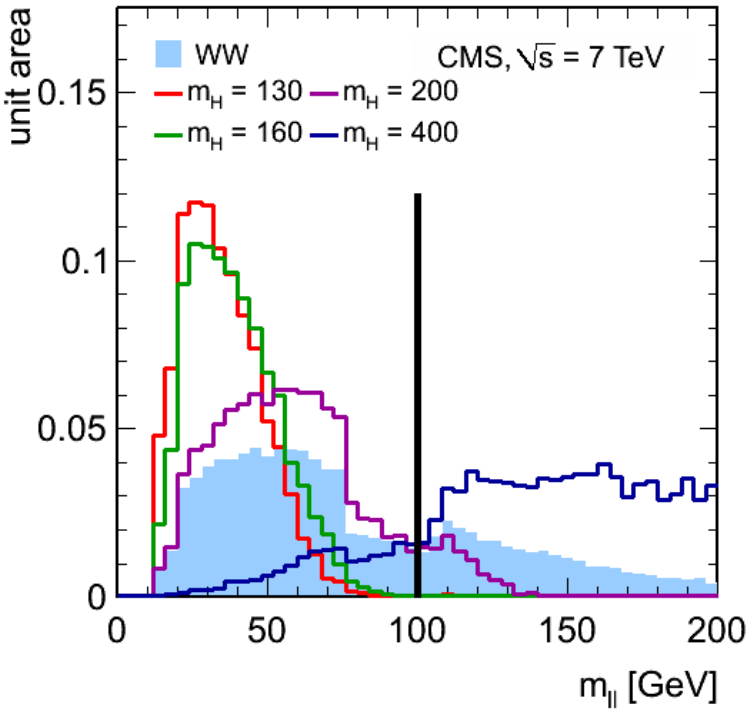

Figure 5.11: Dilepton invariant mass distributions for the WW continuum background and four Higgs boson mass hypotheses ($m_{\text{H}} = 120$, $m_{\text{H}} = 160$, $m_{\text{H}} = 200$, $m_{\text{H}} = 400$). The lower mass Higgs boson hypotheses all fill the area outside the control region at $m_{\ell\ell} < 100\,\text{GeV}$, while masses starting around 200 GeV start to leak into the control region.

The number of events in data with $m_{\ell\ell}$ greater than 100 GeV is first counted. Using the previously discussed data driven methods when possible, the other background contributions in the control region are measured, subtracted out, and the remaining yield is assumed to come from WW production. Simulation is then used to estimate the WW

contribution in each signal region. Mathematically, the formula can be expressed as:

$$N_{\mathrm{WW}}^{\mathrm{signal}} = \left(N_{\mathrm{control}} - N_{\mathrm{control}}^{\mathrm{other}}\right) \cdot \left[\frac{N_{\mathrm{signal}}^{\mathrm{WW}}}{N_{\mathrm{control}}^{\mathrm{WW}}}\right]_{\mathrm{sim}} \tag{5.11}$$

This procedure is repeated in each jet bin and for each m_{H} hypothesis. An error is applied to the ratio measured from simulation which covers the uncertainty on the knowledge of the shape of the $m_{\ell\ell}$ distribution. This value is taken as 6% via the difference between the prediction at leading order from MADGRAPH and next-to-leading order from MC@NLO. The final estimate of the WW background at the mass-independent selection level for the 0-jet and 1-jet bins is shown in Tab. 5.17.

Table 5.17: Estimation of the WW background at the mass-independent selection level in the 0-jet and 1-jet categories.

0-jet bin					
$m_{\ell\ell}$ region	data	all bkg	$N_{\mathrm{WW}}^{\mathrm{data}}$	$N_{\mathrm{WW}}^{\mathrm{sim}}$	data/sim
control	484	124 ± 11	360 ± 24	317 ± 2.3	1.14 ± 0.08
all	1386	-	1031 ± 94	908 ± 4.0	-
1-jet bin					
$m_{\ell\ell}$ region	data	all bkg	$N_{\mathrm{WW}}^{\mathrm{data}}$	$N_{\mathrm{WW}}^{\mathrm{sim}}$	data/sim
control	360	196 ± 10	164 ± 21	142.3 ± 1.6	1.15 ± 0.16
all	947	-	420 ± 100	364.0 ± 2.5	-

5.4.5 Remaining Backgrounds

The remaining backgrounds are taken from simulation: WZ, ZZ, $W\gamma$, $W\gamma^*$, and $Z/\gamma^* \to \tau\tau$, and in a few cases, extra cross checks are done for peace of mind. The contribution from WZ and ZZ in which one the two remaining leptons originate from the same Z boson can be estimated using the same procedure as $Z/\gamma^* \to \ell\ell$, however, they have true missing energy in the final state (either one neutrino from the W or two from the other Z). These events are well modeled, their contribution to the final yield is small and hence their expected contribution is taken from simulation.

Tau leptons can decay to a muon or electron and two neutrinos. In the cases where both tau leptons in $Z/\gamma^* \to \tau\tau$ events decay leptonically, the final state particles

are exactly the same as in this search. However, kinematically, there is significant difference between the signal and $Z/\gamma^* \to \tau\tau$ events such that the final contribution is quite small. These events have softer lepton p_{T} spectrum, displaced τ vertices rejected by impact parameter requirements, but most importantly are significantly reduced by the project missing energy requirement as the neutrinos are aligned along the lepton direction. However, to ensure the contribution is as negligible as simulation predicts, one cross check is performed. Drell-Yan to $\mu\mu$ events are taken from data and the kinematics of each muon is replaced with that of a simulated τ. This procedure allows the instrumental noise to be taken from the actual detector response with the only simulated response coming from the τ products. This procedure gives a result in good agreement with the fully simulated prediction, and the expected signal contribution from simulation is used.

$W\gamma$ events in which the photon decays to two electrons can appear to be signal-like if one of the electrons is not reconstructed and the other fails to be identified by the conversion rejection selections. This process could be measured using the methods described in Sec. 5.4.1, however the measurement of the fake rate in the QCD-rich sample fails to account for this type of fake rate due to the very small fraction of QCD events containing high energy photons. Instead, this process is taken from simulation applying a conservative systematic uncertainty. This can also happen in $W\gamma^*$ production [75], however a cross check of the production cross section is done on a sample of trilepton events. These events are selected with either a high energy electron or muon (hypothesized to come from the W) as well as two oppositely charged muons with invariant mass less than 12 GeV. The cross section is compared to the simulated prediction in MADGRAPH and used to scale the $W\gamma^*$ contribution in the signal region. A scale factor of 1.5 is found.

As a final cross check for $W\gamma$ and $W\gamma^*$ production (and for $W+$jets), events in which the final state leptons instead have the same charge are measured in data. The majority of these events are comprised of $W+$jets, $W\gamma$ and $W\gamma^*$, with a small contribution from WZ and ZZ. The fake rate method can be used to estimate the $W+$jets contribution to this region. Then the expected same-sign contribution from the other diboson processes are taken from simulation. The observed and expected values are then

compared, giving a 20% difference, far smaller than the error in the $W+$jets fake rate method. This closure test gives nice assurance that the $W+$jets, $W\gamma$ and $W\gamma^*$ estimates are within reason. Tab. 5.18 summarizes these findings.

Table 5.18: Summary of fake lepton background yields in the same sign sample after the mass independent selection.

Sample	Yield
$W+$jets fake rate estimation	$46.08 \pm 3.00 \pm 16.59$
Simulated WZ expectation	14.16 ± 1.94
Simulated ZZ expectation	0.72 ± 0.92
Simulated $W\gamma$ expectation	8.67 ± 1.72
Simulated $W\gamma^*$ expectation	12.74 ± 1.69
Sum of estimated same-sign events	82.38 ± 17.16
Observed same-sign events	65

5.5 Sources of Uncertainty

The following summarized the experimental and describes the theoretical sources of uncertainty.

5.5.1 Experimental Uncertainties

The experimental systematic uncertainties were discussed previously during the discussion of each method used in this analysis, however, a complete concise summary is provided here. In addition to those mentioned below, all statistical errors are also taken into account.

Luminosity

The luminosity measurement performed at CMS in 2011 has a relative error of 4.5%. Any final yield estimated from simulation is subject to this uncertainty, including the signal yields, and this uncertainty is correlated throughout all channels.

Lepton Identification and Trigger

The lepton and trigger efficiencies are measured in data using the tag-and-probe technique described in detail in Sec. 5.3. The statistical error from the number of events in the Z peak is rather small, but a small systematic from the fit of the line shapes, estimated using multiple shape possibilities, gives a 2% error for each lepton.

Momentum Scale

The p_{T} resoultion for muon and electron reconstruction is in general very good. However, due to a lack of ECAL calibration at the time of this anlaysis, this uncertainty can propagate to an uncertainty on the final yields calculated via simulation. To evaluate this uncertainty, the changes in the final signal yields are evaluated by varying the electron and muon energies in a range compatible with the uncertainty on the momentum resolution. Electrons in the barrel, electrons in the endcap and muons are varied by 2%, 5% and 1%, respectively. Very little change is seen when varying the muon momentum, therefore, a 0.5% uncertainty is taken per muon leg. Electrons on the otherhand exhibit a slightly higher variation resulting in a 2% uncertainty per electron leg.

The same evaluation is done for the jet energy uncertainty. Prescriptions from the CMS jet working group give an overall uncertainty of 2%.

$\not\!\!E_{\mathrm{T}}$ Modeling

Similar to the uncertainty on lepton momentum, processes where expected yields are taken from simulation, notably the signal, must be tested for systematical uncertainty to the modeling of the $\not\!\!E_{\mathrm{T}}$. The resolution for events with real $\not\!\!E_{\mathrm{T}}$ is less than 1%, however, studying W events, an approximate 1% shift in the average $\not\!\!E_{\mathrm{T}}$ is seen between data and simulation. To study this effect, the $\not\!\!E_{\mathrm{T}}$ distribution in signal higgs events is shifted up and down by 10% leading to a systematic uncertainty on the signal acceptance of 2%.

Background Estimation

- **WW background.** For math hypotheses less than 200 GeV, the WW background is estimated from data. A 6% error on the shape of the simulated $m_{\ell\ell}$ variable used for extrapolation back to the signal region is added in quadrature to the statistical uncertainty from the proceduce. Additional uncertainty comes from the removal of background processes in the control region. In all, the error for the WW estimate is approximately 10%. For math hypotheses above 200 GeV and above, the WW yield is taken from simulation. For $qq \to WW$, the proper inclusive jet cross section uncertainties, similarly calculated as for the Higgs production in Sec. 4.1, are applied: 3.4%, 15% and 42% for $\sigma_{\geq 0}$, $\sigma_{\geq 1}$ and $\sigma_{\geq 2}$, respectively. For the smaller $gg \to WW$ contribution, the uncertainty on the cross section from GG2WW of 30% is used.

- **Top backgrounds.** Estimated in data by inverting the b-vetos, the uncertainty on the top background is dominated by statistical error in the control regions. For the 0-jet, 1-jet and 2-jet categories, the uncertainty reaches as high as 20%, 10% and 50%, respectively, depending on Higgs mass hypothesis.

- **Drell-Yan background.** The total uncertainty on the Drell-Yan estimate comes from both the statistical uncertainty due to the small yield in the control region as well as the systematic uncertainty associated with the extrapolation using $R_{\text{sim}}^{\text{out/in}}$. Depending on Higgs the acceptance of a given mass hypothesis, this uncertainty can be as low as 30% or as high as 100%.

- $W+$**jets background.** The $W+$jets uncertainty comes strictly from the systematical uncertainty associated with the closure test done in simulation and results in an average of around 40%.

- **WZ, ZZ and** $W\gamma$ **backgrounds.** Cross section uncertainties on these processes are computed using MCFM giving 3% for WZ and ZZ and 30% for $W\gamma$. In addition, due to the low acceptance, statistical uncertanties for these events can be as high as 10%.

Pileup

As only a tiny fraction of the pp collisions produce high p_{T} objects on which CMS triggers, a very large majority of the other interactions occuring when two proton bunches collide are glancing blows. Of these "minimum bias" interactions, only 63% produce enough charged particles to allow for vertex reconstruction. As the simulation pileup distribution is reweighed by the number of reconstructed vertices, any mismodelling of the pileup or difference in vertex reconstruction can lead to changes in the final yields. The simulation pileup distribution is reweighted from the nominal expectation by increasing or decreasing the mean number of interactions by one. The result on the final yields is small and 0.5% is taken as the systematic uncertainty.

5.5.2 Theoretical Uncertainties

Uncertainties on Higgs Jet Categorization Fractions

While the theoretical total inclusive cross section, $\sigma_{\geq 0}$, for Higgs production are taken directly from the LHC Higgs cross section working group [62], this analysis is split into 0-jet, 1-jet and 2-jet categories, requiring additional work to properly treat the systematical uncertainty in each category. The procedure is further motivated by the high probability of the $gg \to H$ process to radiate additional gluons: nearly 40% of events have one or more jets in the final state. The procedure to treat the uncertainties on the $gg \to H$ production are completely outlined in Ref. [76, 77], however, a brief overview follows.

The signal yield in each jet category, $N_{0\mathrm{j}}$, $N_{1\mathrm{j}}$ and $N_{2\mathrm{j}}$, can be summarized mathematically as:

$$N_{0\mathrm{j}} = \sigma_{\geq 0} f_0 A_0, \qquad N_{1\mathrm{j}} = \sigma_{\geq 0} f_1 A_1, \qquad N_{2\mathrm{j}} = \sigma_{\geq 0} f_2 A_2, \tag{5.12}$$

where $\sigma_{\geq 0}$ is defined as the inclusive $gg \to H$ cross section, A_0, A_1 and A_2 are the acceptances in each of the jet categories of this analysis, and f_0, f_1, f_2, is the fraction of the total cross section containing 0, 1 or greater than two jets:

$$f_0 = \frac{\sigma_{\geq 0} - \sigma_{\geq 1}}{\sigma_{\geq 0}}, \qquad f_2 = \frac{\sigma_{\geq 1} - \sigma_{\geq 2}}{\sigma_{\geq 0}}, \qquad f_2 = \frac{\sigma_{\geq 2}}{\sigma_{\geq 0}}, \tag{5.13}$$

where $\sigma_{\geq 1}$ and $\sigma_{\geq 2}$ are the inclusive cross sections for Higgs production with one or more and two or more jets in the final state, respectively. The total uncertainty in each jet category will then have contributions from the uncertainties on the inclusive cross sections, $\sigma_{\geq 0}$, $\sigma_{\geq 1}$ and $\sigma_{\geq 2}$, as well as any uncertainties from the acceptances, A_0, A_1 and A_2.

The uncertainties on the inclusive cross sections due to higher order QCD correction, $\kappa_{\geq 0}$, $\kappa_{\geq 1}$ and $\kappa_{\geq 2}$, are computed using MCFM [78] by varying the renormalization scale, μ_r, and factorization scale, μ_f up and down by multiplicative factors of two with respect to the nominal scale, m_{H}, in four scenarios:

$$\begin{aligned} \mu_f &= m_{\mathrm{H}} & \mu_r &= m_{\mathrm{H}} \\ \mu_f &= m_{\mathrm{H}}/4 & \mu_r &= m_{\mathrm{H}}/4 \\ \mu_f &= m_{\mathrm{H}} & \mu_r &= m_{\mathrm{H}}/2 \\ \mu_f &= m_{\mathrm{H}}/2 & \mu_r &= m_{\mathrm{H}} \end{aligned}$$

The envelope of the deviations with respect to the nominal value are taken as the systematical error on the inclusive cross sections. This procedure is repeated for each Higgs mass hypothesis and the results, along with the category fractions, are shown in Tab. 5.19.

The uncertainties on the inclusive cross sections are then used to calculate the uncertainty on each jet category fraction. The uncertainty on each fraction is correlated with the uncertainty on the respective inclusive cross section and anti-correlated with the uncertainty on the next jet category. The uncertainties are thus given in Tab. 5.20 with the correlations across jet categories preserved appropriately.

In addition to the ignorance of higher order terms which affect the cross section uncertainty, the underlying event uncertainty, effects of soft QCD radiation, i.e. the parton showering, and hadronization modelling all contribute to the cross section uncertainty as well. To evaluate these contributions, a similar algorithm was performed as above, only this time using alternate Monte-Carlo approaches. The default Higgs simulated events are generated with POWHEG [68] and passed to PYTHIA [59] for hadronization and for the modelling of the underlying event. These results are then compared to the exact same process but using MC@NLO [79] as the generator, interfaced to HERWIG

Table 5.19: Jet category fractions and inclusive cross section uncertainties for various values of m_{H} due to higher order corrections computed by varying the renormalization and factorization scales in MCFM, reported in log-normal format, for representative mass hypothesis considered in this analysis.

m_{H}	f_0	f_1	f_1	$\kappa_{\geq 0}$	$\kappa_{\geq 0}$	$\kappa_{\geq 0}$
110	0.64	0.26	0.10	1.11	1.38	1.10
120	0.64	0.25	0.11	1.10	1.24	1.09
130	0.62	0.26	0.12	1.10	1.22	1.10
140	0.61	0.26	0.12	1.09	1.32	1.11
160	0.58	0.29	0.14	1.09	1.25	1.12
180	0.53	0.31	0.16	1.09	1.24	1.15
200	0.49	0.34	0.18	1.09	1.24	1.15
300	0.44	0.33	0.23	1.08	1.22	1.18
400	0.44	0.31	0.25	1.08	1.21	1.19
500	0.61	0.21	0.18	1.09	1.20	1.20
600	0.75	0.14	0.11	1.09	1.18	1.20

Table 5.20: Formulas used to compute uncertainties on jet category fractions from uncertainties on inclusive cross sections. Anti-correlation of the uncertainties between jet categories can be seen and is due to the uncertainty of a jet fluctuation from one category to another.

	uncertainties on f_0	uncertainties on f_1	uncertainties on f_2
correlations with $\kappa_{\geq 0}$	$\left(\kappa_{\geq 0}\right)^{\frac{1}{f_0}}$	—	—
correlations with $\kappa_{\geq 1}$	$\left(\kappa_{\geq 1}\right)^{-\frac{f_1+f_2}{f_0}}$	$\left(\kappa_{\geq 1}\right)^{\frac{f_1+f_2}{f_0}}$	—
correlations with $\kappa_{\geq 2}$	—	$\left(\kappa_{\geq 2}\right)^{-\frac{f_2}{f_1}}$	$\kappa_{\geq 2}$

[80, 81] for the hadronization modelling with the use of JIMMY [82] as the model for the underlying event. The same categorization of the uncertainty in jet categories is done using the difference in cross section computed with these two procedures as the uncertainty. The results give a 5.7% uncertainty in the 0-jet category anti-correlated with an 8.4% and 13.8% uncertainty in 1-jet and 2-jet categories.

The cross sections computed here are all computed under and assumption of a zero-width Higgs. However, at large mass hypothesis, this approximation becomes troublesome as interference terms from other SM processes can change the lineshape of the Higgs width [83]. A parameterization of this uncertainty has been developed by the LHC Higgs Cross Section working group [84]:

$$\frac{\Delta\sigma}{\sigma} = 150\% \cdot \left(\frac{m_{\mathrm{H}}}{1\,\mathrm{TeV}}\right)^3$$

Finally, the uncertainties on the acceptances, A_0, A_1 and A_2, due to the knowledge (or lack there of) of the parton density functions as well as the strong coupling constants are calculated according to the prescription set forth by the PDF4LHC working group [85]. Three PDF sets are used and each have their own prescription for determining their uncertainty for both the PDF and the strong coupling: MSTW2008 [86], CTEQ10 [87] and NNPDF [88]. The envelope for the change in the lepton and missing energy acceptances in each of the jet categories calculated for each of the three prescriptions is taken as the systematic uncertainty. For the $gg \to H$ process, the errors range from 8% at low Higgs masses to as high as 14% at $m_{\mathrm{H}} = 600$.

5.6 Original Contributions

In all, forty-three people were in some way involved to produce the results of this analysis by either direct contribution, providing valuable commentary or insight or even the occasional documentation edit. I like to think I fell into the first category, providing a significant contribution knowing that the result and quality of this analysis would directly affect my future livelihood. While I will not claim to have been the original contributor to every aspect of this analysis, my fingerprints can be seen on many key ingredients. These fingerprints, as well as this thesis, could only have been

possible due to the time and effort I spent understanding all intricacies of this analysis. So, if the reader will allow one section of vanity, the following paragraphs document the direct contributions I have made to this complex analysis.

I started on the CMS experiment in the Spring of 2007, taking on my first task of trying to improve CMS's ability to isolate leptons from electroweak interactions against the large QCD background. After a brief look at muon isolation, I moved onto the more difficult task of isolating electrons. Electrons, as was mentioned in Sec. 3.5.3, bremsstrahlung a significant fraction of their energy. The work culminated with an optimal Jurassic method giving significantly better performance (10% more signal efficiency or 50% more background rejection) which was implemented and still remains within the CMS software framework to this day. These isolation methods were only supplanted by algorithms using PF products within the last year when the PF algorithm became robust enough to finally compete (though the Jurassic geometry still remains).

My work in isolation continued with early electroweak analyses (W and Z production) as well as commissioning exercises on the first sips of data recorded by the CMS detector (2.9 pb^{-1}) [89]. All of these experiences led to my first work on the $H \to W^+W^- \to \ell\nu\ell'\overline{\nu}$ analysis. The decision to move to a PF based isolation algorithm was only done after extensive studies showing the added benefits of the PF isolation inputs. Still, the use of the Jurassic area for electrons had to be maintained as the PF algorithm is still not capable of collecting all bremsstrahlung energy.

Isolation studies are easily the largest contribution I have made to CMS on the whole and the $H \to W^+W^- \to \ell\nu\ell'\overline{\nu}$ analysis generally. However, my time was devoted particularly to a few aspects of this analysis. In chronological order, the most important contributions follow.

First, in order for this analysis to be competitive on the timescale of data taking at the LHC, a complex, well-oiled, computing machinery had to be put in place on top of the extensive work already done by the CMS computing group. This framework, designed by myself and two others, allowed for quick turnaround from data streaming off the detector to final analysis results.

Then, a major innovation in vertexing was taking place during the infancy of this analysis. The deterministic annealing algorithm had just been introduced into the CMS

computing framework. In order to take advantage of this new algorithm, I studied its performance, tuning parameters to give the best possible vertex reconstruction efficiency maintaining as small of a fake vertex rate as possible.

Additionally, I contributed much work to both the top quark background and Drell-Yan background data-driven estimates. While the "essence" of these algorithms had been in place long before I arrived on the scene, much of my time was devoted to providing more robust estimates. On the top quark estimate, I helped to optimize the analysis by further accounting for the mixing between the single top and $t\bar{t}$ contributions. On the Drell-Yan side, much time was spent stabilizing the uncertainty due to the lack of statistics in the control region.

Finally, every single final yield appearing in this document was calculated, cross-checked or verified independently by myself.

Chapter 6

Determination of Exclusion Limits and Discovery Significance

Given the outcome of the analysis laid out previously, the ultimate goal is to determine quantitatively the existence (or non-existence) of the SM Higgs boson. To do so, statistical analysis incorporating the result of the analysis, the expected SM Higgs yields, the measured background yields, and the systematic uncertainties will be used to place confidence limits on the cross section for Higgs production or to place a significance on an any excess of events.

The statistical procedure to be used in Higgs searches by both CMS and ATLAS is summarized in a document provided by the LHC Higgs Combination Group [77]. The rest of this chapter will give an overview of the statistical methods needed to perform the procedure as well as a summary of the procedure itself. A more rigorous treatment of the statistical tools used in the field of particle physics can be found in Ref. [90] while further insight can be taken from the lectures found in Ref. [91].

6.1 Overview

Statistical inference deals in understanding the properties of data subjected to random variation. Concretely, estimating variables which describe the data is performed by building estimators, the best of which should be consistent, i.e. converge on the correct value given infinite data, and unbiased. For this statistical analysis, the parameter of

interest is the cross section of the Higgs boson. However, as the mass is unknown, this parameter will need to be estimated independently for each mass hypothesis. Specifically, the ratio of the cross section of a SM-like Higgs, having all the same kinematical and decay properties, with respect to the theoretical SM prediction, $\mu = \sigma/\sigma_{\mathrm{SM}}$, will be estimated. This "signal strength modifier" is used to allow combination between this analysis and all other Higgs analyses performed at the LHC via a common estimator.

For a given probability density function (p.d.f.), $f(\boldsymbol{x};\boldsymbol{\theta})$, defined as a function of a given set of data, $\boldsymbol{x} = (x_1, \cdots, x_N)$, and unknown parameters, $\boldsymbol{\theta}$, the likelihood function, LH, is defined only as a function of $\boldsymbol{\theta}$, $L(\boldsymbol{\theta}) = f(\boldsymbol{x};\boldsymbol{\theta})$. The LH function gives an estimate of the likelihood for a given set of $\boldsymbol{\theta}$ based on the available data. If the p.d.f. can be decomposed into a p.d.f. for each individual measurement, x_i, the LH function may be written as a product of each p.d.f.:

$$L(\boldsymbol{\theta}) = \prod_{i=1}^{N} f(x_i;\boldsymbol{\theta}).$$

The method of maximum likelihood gives an estimate, $\hat{\boldsymbol{\theta}}$, of the unknown parameters by maximizing the LH with respect to each parameter θ_i:

$$\frac{\partial \ln L}{\partial \theta_i} = 0, \qquad i = 1, \cdots, n.$$

Notice that here the natural logarithm of the LH function is being maximized which gives equivalent values of $\hat{\boldsymbol{\theta}}$ to the maximization of the LH itself due to the monotonic nature of the logarithmic function. The method of maximum likelihood gives an unbiased and efficient estimate of the parameters for a wide variety of statistical problems [92].

To exclude the existence of the SM Higgs, a comparison in the hypothesis of a background-only model ($\mu = 0$) and in the hypothesis of a signal+background model ($\mu = \mu'$) will be made, excluding the SM Higgs boson with a confidence level (CL) of $1 - \alpha$ when the experimental outcome has a probability of occurrence less than α were the signal to exist. In the case with zero unknown parameters, the Neyman-Pearson lemma [93] states that the most powerful test statistic comparing two outcomes is the ratio of the LH of the two hypotheses:

$$q = -2 \ln \frac{L(\mu s + b)}{L(b)} \tag{6.1}$$

Here, s denotes for the expected signal yield which is scaled by the signal strength modifier while b denotes the expected yield for the background. Consequently, Eq. (6.1) would give an optimal test statistic for the comparison of the signal+background hypothesis to the background-only hypothesis. Unfortunately, this LH ratio test statistic is only optimal in cases where all parameters, save the statistic being tested, are known. Given this analysis has multiple source of systematic error, modifications to this test statistic for this search must be pursued. These will be described in the next section.

In addition, a search for an upper limit on the Higgs cross section requires a comparison between the background-only hypothesis and a hypothesis with signal strength $\mu > 0$. The Neyman-Pearson lemma is only valid for comparison of two "point" hypotheses and thus even further modification will have to be made to accommodate comparison between the background-only model and an unknown value of μ greater than zero. This modification will be discussed in the section describing the procedure for setting upper limits, Sec. 6.4.

6.2 Systematic Uncertainties

The signal and background yields are both functions of the true, unknown, values of the parameters modelled by the systematic uncertainties which quantify the limited accuracy with which the parameters are known. While these uncertainties need to be taken into account in the final statistical analysis, the outcome of their estimate are not required to make a quantitative statement on the value of the signal strength modifier and are therefore introduced as nuisance parameters.

Each nuisance parameter, θ_i, is modeled via a p.d.f., $f_i\left(\tilde{\theta}_i;\theta_i\right)$, chosen to best represent the parameter. The true value of the nuisance parameter, θ_i, is unknown while the best estimate (if available) is defined as $\tilde{\theta}$. For statistical uncertainties on the yields of each process the Poisson distribution propery parameterizes the p.d.f. of the uncertainty:

$$\text{Pois}\,(n;b) = \frac{e^{-b}\cdot b^n}{n!},$$

where n represents the observed yield and b the expected yield.

For the remainder of the uncertainties, the p.d.f.s are represented as a log-normal

distribution:

$$f_i\left(\tilde{\theta}_i;\theta_i\right) = \frac{1}{\sqrt{2\pi}\ln\left(\kappa\right)}\exp\left(-\frac{\left(\ln\left(\theta_i/\tilde{\theta}_i\right)\right)^2}{2\left(\ln\left(\kappa\right)\right)^2}\right)\frac{1}{\theta_i},$$

where $\tilde{\theta}_i$ represents the expected central value and κ is a measure of the width (or size) of the uncertainty. Log-normal distributions are built from a normal (Gaussian) distribution via a change in variable from θ to $\ln\theta$ and well-represent the uncertainty on positively defined values as the p.d.f. falls to zero as θ approaches zero. A given unknown value, A, with log-normal uncertainty κ can be simulated via a reparameterization back to the normal distribution with a mean of zero and width of one as:

$$A = \tilde{A}\cdot\kappa^{\theta} = \tilde{A}\cdot\left(1+\frac{\Delta A}{\tilde{A}}\right)^{\theta},$$

where $\Delta A/\tilde{A}$ is the relative size of the measured uncertainty. As an example, a 10% uncertainty ($\kappa = 1.10$), gives a 32% (1σ) probability for A to fall in the range $\tilde{A}/1.10 < A < \tilde{A}\cdot 1.10$.

6.3 Profile Likelihood Ratio

The LH for this analysis can now be constructed as the product of the LHs for each channel multiplied by the p.d.f.s for each nuisance parameter:

$$L\left(\mu,\boldsymbol{\theta}\right) = \prod_{k=1}^{N_C} L_k\left(\mu,\boldsymbol{\theta}\right)\times\prod_{i=1}^{N_\theta} f_i\left(\tilde{\theta}_i;\theta_i\right),$$

where $L_k\left(\mu,\boldsymbol{\theta}\right)$ is the likelihood for a given channel as a function of the measured data and k runs over each channel. Notice the LH is a function of the parameter of interest, μ, as well as the nuisance parameters. The LH for each individual channel can be represented as a Poisson distribution with an observed number of events n_k and the expected number of events:

$$L_k\left(\mu,\boldsymbol{\theta}\right) = \mathrm{Pois}\left(\ n_k\ ;\ \mu\cdot s_k\left(\boldsymbol{\theta}\right)+b_k\left(\boldsymbol{\theta}\right)\ \right).$$

The signal strength modifier enters directly as a product with the expected signal rate, s_k, added to the expected number of background events, b_k, for that specific channel. Both

the signal and background yields are written as functions of the nuisance parameters due to their dependence on their true value of each nuisance parameter.

As mentioned previously, the best test statistic for a given parameter is the likelihood ratio. In order to compare two values of μ, namely the background-only hypothesis ($\mu = 0$) and the signal+background hypothesis ($\mu > 0$), the nuisance parameters are profiled and a profile likelihood ratio is constructed:

$$\lambda(\mu) = \frac{L\left(\mu, \hat{\hat{\boldsymbol{\theta}}}\right)}{L\left(\hat{\mu}, \hat{\boldsymbol{\theta}}\right)}, \tag{6.2}$$

where $\lambda(\mu)$ is only a function of the parameter of interest, μ. The values of the nuisance parameters and the signal strength modifier in the denominator are chosen to maximize the LH and are denoted by $\hat{\mu}$ and $\hat{\boldsymbol{\theta}}$, respectively. The LH in the numerator remains a function of the signal strength modifier being tested and the "double hat" notation on the nuisance parameters, $\hat{\hat{\boldsymbol{\theta}}}$, denotes that the nuisance parameters are chosen which maximize the LH for the value of μ under test. This test statistic, for purposes of this analysis, gives as powerful a statistical test in the presence of nuisance parameters as the standard likelihood ratio [92].

6.4 Exclusion Limits

A common test in the search for a yet-undiscovered process is to determine the maximum cross section for the process compatible with the given data. In this search, in the parameterization with the signal strength modifier μ, the SM Higgs boson would be excluded for a given mass hypothesis in the event a value of $\mu = 1$ is excluded at a defined statistical strength. A statistical test at 95% CL would imply the observed data for a given hypotheses μ would only occur 5% of the time or less.

The test statistic used to set upper limits is defined as:

$$q_\mu = -2\ln\lambda(\mu) \quad \text{if } 0 \leq \hat{\mu} \leq \mu, \tag{6.3}$$

where $\lambda(\mu)$ is defined in Eq. (6.2). The value $\hat{\mu}$ is constrained to be less than the value of μ under test so as not to penalize the test statistic in the event of an over fluctuation

of the background. That is, a large over fluctuation of the background, even if the fluctuation is larger than the expected signal+background yields, gives a value of the test statistic compatible with signal strength μ. The lower bound on $\hat{\mu}$ is motivated by physical reasons: the signal rate has to at least be positive.

Small values of q_μ represent compatibility between the parameter under test μ and the best fit value, $\hat{\mu}$. The numerator and denominator of Eq. (6.2) would be near unity and hence the natural log near zero. This test statistic is one-sided, as the LH ratio can only ever be smaller than one due to the upper restriction on the value of $\hat{\mu}$. Increasingly large values of q_μ would then represent incompatibility with the value of μ under test. The probability to obtain an observed value of q_μ, q_μ^{obs}, at least as incompatible with the signal+background hypothesis is then:

$$\text{CL}_{s+b} = p_{s+b} = \int_{q_\mu^{\text{obs}}}^{\infty} f\left(q_\mu\right)\ \mathrm{d}q_\mu,$$

where $f\left(q_\mu\right)$ is the p.d.f. for the test statistic q_μ. The 95% CL would then be defined as $\text{CL}_{s+b} \leq 5\%$.

The p.d.f. for q_μ cannot be formulated analytically and therefore must be constructed using Monte-Carlo methods. Pseudo-data is generated using the p.d.f.s for the signal and background yields as well as the nuisance parameters fixing the values of the nuisance parameters to $\hat{\hat{\boldsymbol{\theta}}}$. For each pseudo-dataset, q_μ is recalculated again allowing $\hat{\hat{\boldsymbol{\theta}}}$ to float. The amount of pseudo-data generated is large enough such that a complete parameterization of the p.d.f. is achieved.

A problem exists with this test statistic. Imagine calculating CL_{s+b} in the background-only hypothesis, $\mu = 0$. By construction, the test statistic will give a 95% CL in 5% of the cases, thus excluding a signal strength of zero simply via an under fluctuation of the background regardless of the sensitivity of the analysis. To combat this pratfall, the so-called CL_s method is introduced [94, 95, 96]. The entire procedure described above is run again in the background-only hypothesis:

$$q'_\mu = -2\ln\lambda\left(0\right) \quad \text{for } 0 \leq \hat{\mu} \leq \mu, \tag{6.4}$$

and the probability to obtain a value of q_μ at least as incompatible as the observed q_μ^{obs}

in background-only hypothesis is obtained:

$$\mathrm{CL}_b = 1 - p_b = \int_{q_\mu^{\mathrm{obs}}}^{\infty} f\left(q'_\mu\right)\, \mathrm{d}q_\mu .$$

Then, an exclusion at 95% CL is obtained when $\mathrm{CL}_{s+b}/\mathrm{CL}_b \leq 0.05$. This method is in general more conservative, but protects against spurious exclusion when the p.d.f.s for the background-only hypothesis and the signal+background hypothesis are very similar, i.e. the analysis has a low sensitivity. This becomes relevant in the $H \to W^+W^- \to \ell\nu\ell'\overline{\nu}$ analysis at very low mass hypotheses ($m_{\mathrm{H}} < 130\,\mathrm{GeV}$) where the expected signal yield is small compared to the background yields. A cartoon representing the CL_s and CL_{s+b} test statistics for a low and high significance analysis is shown in Fig. 6.1.

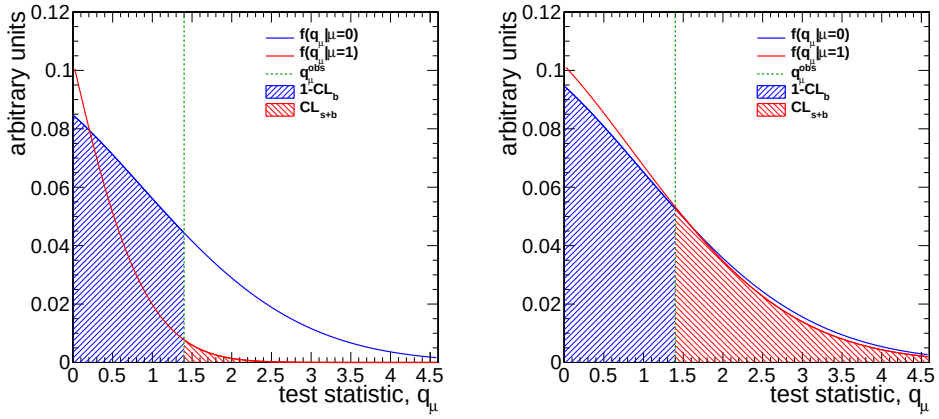

Figure 6.1: Example of test stastistics for both the CL_s and CL_{s+b} methods for a high (left) and low (right) sensitivity analysis. For the high sensitivity depiction, the sensitivity is high enough such that significant separation between the two methods can be seen. On the other hand, on the right, where the sensitivity is significantly lower, the overlap between the two methods is apparent.

This procedure is run for a range of possible signal strength modifiers, with the upper limit being set at the largest value of μ for which a 95% limit is obtained using the CL_s method.

6.5 Quantifying Excesses

In the event of an excess of events over the background-only hypothesis, a similar statistical analysis is run to determine the significance of the excess. The statistic in this case is defined as:

$$q_0 = -2\ln\lambda\,(0) \quad \text{for } \hat{\mu} \geq 0$$

where this time the only limit on $\hat{\mu}$ is the lower physical constraint. In this case, larger and larger values of q_0 are interpreted as higher and higher probabilities of incompatibility with the background-only hypothesis.

The p.d.f. of the test statistic, $f\left(q_0|0,\hat{\theta}_0^{\text{obs}}\right)$, is again formulated by simulating pseudo-data experiments allowing the yields to fluctuate under the background-only Poisson distribution while fixing the nuisance parameters to those evaluated as the best fit under the background-only hypothesis.

The probability for an observed test statistic to be at least as incompatible with the background-only hypothesis, the p-value, is defined from the p.d.f. as:

$$p_0 = \int_{q_0^{\text{obs}}}^{\infty} f\,(q_0)\ \mathrm{d}q_0.$$

This is converted into a significance, Z, using the one-sided normal distribution with mean zero and width one:

$$p_0 = \int_Z^{\infty} \frac{1}{\sqrt{2\pi}} \exp\left(-x^2/2\right)\ \mathrm{d}x = 1 - \Phi\,(Z)$$

such that $Z = \Phi^{-1}\,(1-p_0)$ as can be seen in Fig. 6.2. General consensus in the field of particle physics requires a significance of $Z = 5$ ($p_0 = 2.8 \times 10^{-7}$) to claim a discovery of a new process over the SM background.

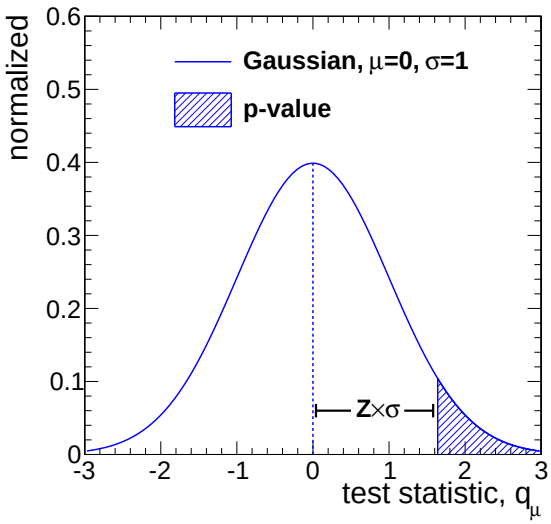

Figure 6.2: Calculation of the significance, Z, from a p-value. The normal distribution with mean zero and width one is shown as a solid blue line while the p-value is represented by the filled blue area. The significance is calculated as the number of "width's" away from zero.

Chapter 7

Results and Conclusions

The results of the analysis are presented in the following sections. First, the signal and background expected yields are compared to the observation from data. The statistical treatment from the previous chapter is then applied to set exclusion limits on the presence of a Standard Model Higgs boson.

7.1 Expected and Observed Yields

The observed event counts and data-driven expectation on the background processes for each jet category after the mass-independent selection is shown in Tab. 7.1. Good agreement is seen between expectation and observation. Figs. 7.1 and 7.2 show various kinematic distributions at the mass-independent selection for all three jet categories after scaling the simulation by the data-driven background estimates. Again, excellent agreement is seen. A full set of yields for each mass hypothesis in each category is reported in Appx. A. One example, $m_{\mathrm{H}} = 130$, is shown in Tab. 7.2. No significant excesses are seen for any Higgs boson mass hypothesis so we proceed by using the statistical tools presented in the previous chapter to set upper limits on the Higgs production cross section.

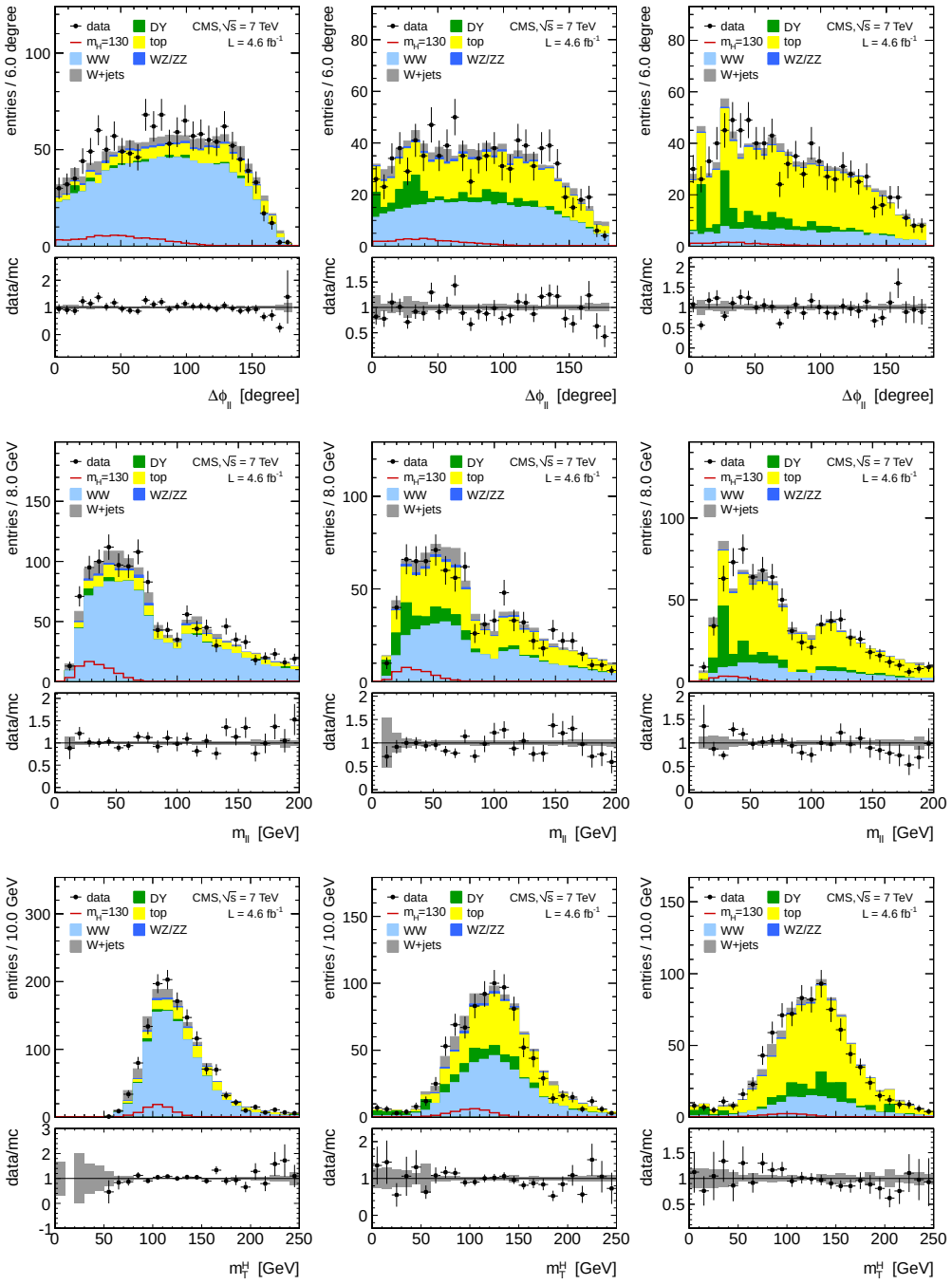

Figure 7.1: Comparison of data to simulation after scaling simulation by the data-driven estimates in the 0-jet (left), 1-jet (center) and 2-jet (right) categories. $\Delta\phi_{\ell\ell}$, $m_{\ell\ell}$ and m_T^H are shown on the first, second and third row, respectively. A Higgs boson mass hypothesis of $m_{\mathrm{H}} = 130$ is shown in red.

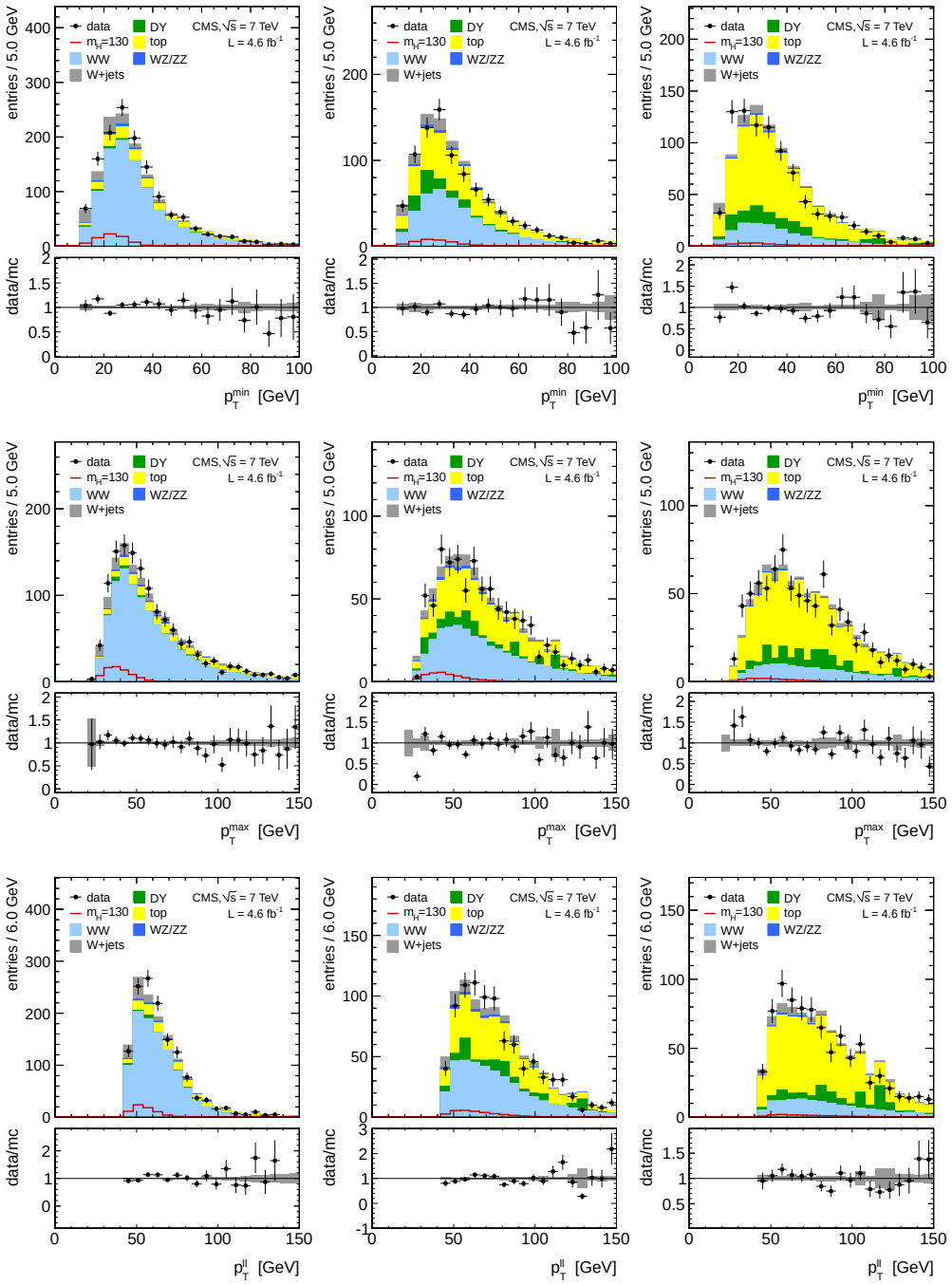

Figure 7.2: Comparison of data to simulation after scaling simulation by the data-driven estimates in the 0-jet (left), 1-jet (center) and 2-jet (right) categories. $p_{\mathrm{T}}^{\ell,\mathrm{min}}$, $p_{\mathrm{T}}^{\ell,\mathrm{max}}$ and $p_T^{\ell\ell}$ are shown on the first, second and third row, respectively. A Higgs boson mass hypothesis of $m_{\mathrm{H}} = 130$ is shown in red.

Table 7.1: Expected yields from data and simulation after data-driven corrections for $4.6\,\text{fb}^{-1}$ at the mass-independent level, for the 0-jet, 1-jet and 2-jet categories. Only the statistical errors are reported.

	data	tot bkg.	WW	$gg \to WW$	$t\bar{t}$ and tW
0-jets	1363	1339 ± 10	959.1 ± 4.9	58.86 ± 0.71	159.3 ± 3.2
1-jet	926	965.1 ± 16.5	388.1 ± 3.1	23.99 ± 0.46	366.4 ± 3.8
2-jets	892	914.9 ± 16.1	149.9 ± 1.8	4.90 ± 0.19	591.3 ± 3.7
	$W+$jets	WZ and ZZ	Z/γ^*	$W\gamma$	$Z/\gamma^* \to \tau\tau$
0-jets	94.47 ± 5.57	26.19 ± 0.39	16.45 ± 4.61	24.53 ± 3.16	0.19 ± 0.19
1-jet	67.28 ± 4.83	20.37 ± 0.29	67.20 ± 12.73	8.69 ± 1.81	23.00 ± 7.78
2-jets	42.42 ± 4.26	12.16 ± 0.21	93.31 ± 14.41	7.51 ± 3.06	13.33 ± 2.44

7.2 Upper Limits on Higgs Boson Production

With no excess of events, upper limits on the signal strength modifier are calculated for each Higgs boson mass hypothesis using the CL_s procedure described in Sec. 6.4. All yields are those explicitly found in Appx. A. The systematic uncertainties are taken from Sec. 5.5. The profile likelihood best fit values of $\hat{\mu} = \sigma/\sigma_{\text{SM}}$, which is calculated for the denominator of Eq. (6.2), for each Higgs boson mass hypothesis is shown in Fig. 7.3. Comparison between the overall best fit value and the best fit value of $\hat{\mu}$ for the 0-jet and 1-jet categories is shown in Fig. 7.4 for Higgs boson mass hypothesis of $m_{\text{H}} = 120$, $m_{\text{H}} = 130$, $m_{\text{H}} = 140$ and $m_{\text{H}} = 160$. A slight fluctuation above expectation can be seen in the same flavor 1-jet category and is present across a wide range of masses due to the correlation between hypothesis selections.

Continuing with the CL_s procedure, the 95% CL observed median upper limits are calculated for each Higgs mass hypothesis. A comparison is made between the observed limit and the expectatted limit in the background-only hypothesis. In addition, the one and two standard deviation probability intervals around the expected limit are also calculated. The full set of expected and observed upper limits are reported in Tab. 7.3. The same information is expressed graphically in Fig. 7.5 where the expected median upper limit is represented by a dotted line, the observed upper limit by a solid line and the 1σ and 2σ bands are represented by the green and yellow fill areas, respectively.

While no significant excesses are seen, this analysis extends the current best

Table 7.2: Background contributions and data yields for $4.6\,\mathrm{fb}^{-1}$ of integrated luminosity after the full cut-based selection in the 0-jet bin for a Higgs boson mass of $m_{\mathrm{H}} = 130$. The data-driven correction are applied and the errors reported reflect all systematic uncertainties.

	$\mathrm{Z}\gamma^*$	$t\bar{t}$ +tW	$W+$jets	WZ +ZZ	$gg \to WW$	$qq \to WW$	all bkg.	$m_{\mathrm{H}} = 130$	data
0-jet, $ee/\mu\mu$	12.3 ± 7.6	3.1 ± 0.6	4.6 ± 2.0	2.3 ± 0.4	2.4 ± 0.2	52.8 ± 5.4	77.5 ± 9.5	15.6 ± 3.6	80
0-jet, $e\mu/\mu e$	1.4 ± 2.0	7.5 ± 1.4	13.0 ± 5.1	5.1 ± 1.9	4.1 ± 0.4	83.0 ± 8.4	114.0 ± 10.4	29.6 ± 6.7	113
0-jet, total	13.7 ± 7.8	10.6 ± 1.6	17.6 ± 5.5	7.4 ± 2.0	6.5 ± 0.5	135.7 ± 10.0	191.5 ± 14.1	45.2 ± 7.6	193
1-jet, $ee/\mu\mu$	4.1 ± 1.9	7.9 ± 0.6	1.1 ± 0.8	1.4 ± 0.3	0.8 ± 0.2	12.1 ± 3.0	27.4 ± 3.7	5.6 ± 1.8	40
1-jet, $e\mu/\mu e$	1.2 ± 1.7	17.7 ± 1.2	5.4 ± 2.4	2.7 ± 0.6	1.4 ± 0.3	24.1 ± 5.9	52.5 ± 6.7	12.1 ± 3.8	65
1-jet, total	5.3 ± 2.5	25.6 ± 1.4	6.5 ± 2.5	4.0 ± 0.7	2.2 ± 0.4	36.3 ± 6.6	79.9 ± 7.7	17.6 ± 4.2	105
2-jet, total	2.7 ± 1.9	6.5 ± 3.2	0.7 ± 0.6	1.8 ± 1.6	0.3 ± 0.0	1.4 ± 0.2	13.3 ± 4.1	2.7 ± 0.2	10

Table 7.3: Expected and observed 95 % C.L. upper limits and uncertainty band for events in the combined 0, 1 and 2 jet category.

m_{H} [GeV]	observed	median expected	expected 68% range	expected 95% range
110	8.6	6.7	[5.1 , 9.4]	[3.5 , 12.9]
115	4.0	3.2	[2.4 , 4.6]	[1.9 , 6.3]
120	2.4	1.9	[1.4 , 2.7]	[1.0 , 3.7]
130	1.2	0.9	[0.6 , 1.2]	[0.5 , 1.7]
140	0.6	0.5	[0.4 , 0.8]	[0.3 , 1.0]
150	0.5	0.4	[0.3 , 0.5]	[0.2 , 0.8]
160	0.3	0.2	[0.2 , 0.3]	[0.1 , 0.4]
170	0.2	0.2	[0.2 , 0.3]	[0.1 , 0.4]
180	0.2	0.3	[0.2 , 0.4]	[0.2 , 0.6]
190	0.3	0.4	[0.3 , 0.6]	[0.2 , 0.8]
200	0.6	0.6	[0.5 , 0.9]	[0.4 , 1.2]
250	1.2	1.3	[0.9 , 1.8]	[0.7 , 2.5]
300	1.7	1.5	[1.1 , 2.2]	[0.9 , 2.9]
350	1.5	1.4	[1.0 , 2.0]	[0.8 , 2.9]
400	1.6	1.5	[1.1 , 2.2]	[0.9 , 3.2]
450	1.9	1.9	[1.4 , 2.8]	[1.0 , 4.1]
500	2.3	2.6	[1.8 , 3.8]	[1.5 , 6.0]
550	3.9	3.5	[2.3 , 5.5]	[1.9 , 8.5]
600	5.9	4.6	[3.6 , 7.8]	[2.4 , 12.7]

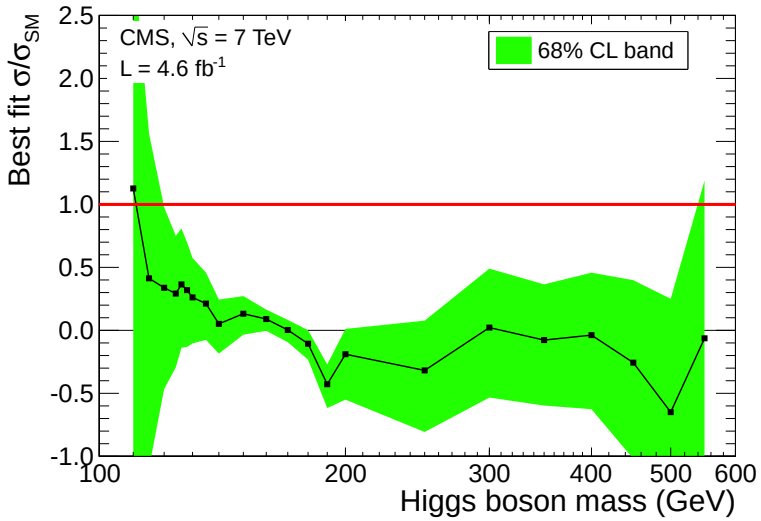

Figure 7.3: Result of the profile likelihood best fit for $\mu = \sigma/\sigma_{\mathrm{SM}}$ as a function of the Higgs boson mass. The fit is performed with a combination of all channels.

exclusion on the presence of a Standard Model Higgs boson to include the range 132-238 GeV at 95% CL. The expected exclusion in the background-only hypothesis is 129-236 GeV.

7.3 Discovery of a Higgs-like Boson

As previously mentioned, the data for this thesis was taken over the course of 2011. However, while writing this dissertation during the first half of 2012, CMS and ATLAS were continuing to take data at the higher center of mass energy of $\sqrt{s} = 8\,\mathrm{TeV}$. Obtaining slightly more data (up to 5.9 fb^{-1}) and combining the results with those from 2011 (including this analysis), on July 4th, 2012, the CMS and ATLAS collaborations jointly announced independent discoveries of a Higgs-like boson with a mass near 125 GeV [97, 98]. The local p-value from CMS for the two modes with best mass resolution ($H \to \gamma\gamma$ and $H \to ZZ$) plus the full $H \to W^+W^-$ analysis as a function of Higgs mass can be seen in Fig. 7.6. Five standard deviations can be seen around $m_{\mathrm{H}} = 125$ GeV with the best-fit mass from the $H \to \gamma\gamma$ and $H \to ZZ$ analyses giving 125.3 ± 0.4 (stat) $\pm$ 0.5 (syst) GeV.

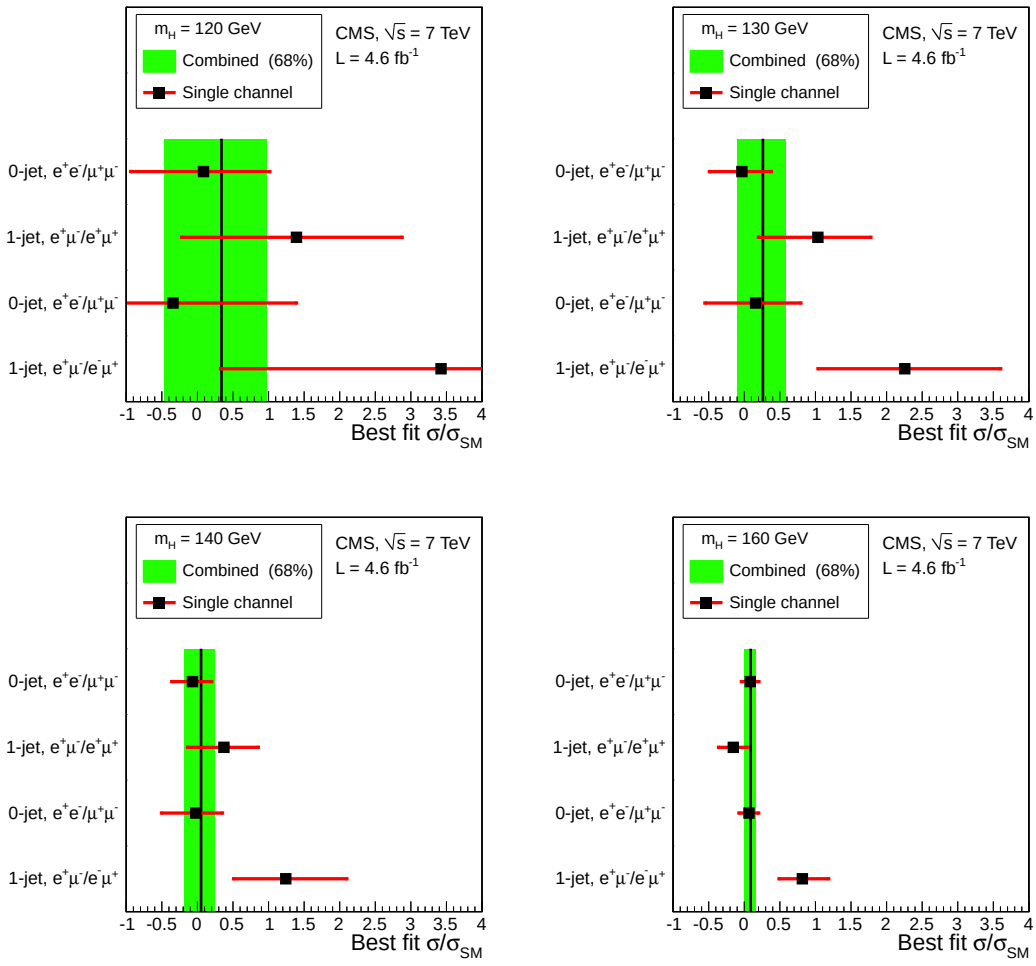

Figure 7.4: Individual 0-jet and 1-jet category best-fit values (black points) for $\mu = \sigma/\sigma_{\mathrm{SM}}$ compared to the overall best fit (solid black line) for four Higgs boson mass hypotheses: $m_{\mathrm{H}} = 120$ (top left), $m_{\mathrm{H}} = 130$ (top right), $m_{\mathrm{H}} = 140$ (bottom left) and $m_{\mathrm{H}} = 160$ (bottom right). The one standard deviation bands for each individual channel are shown in red and for the combined case in green.

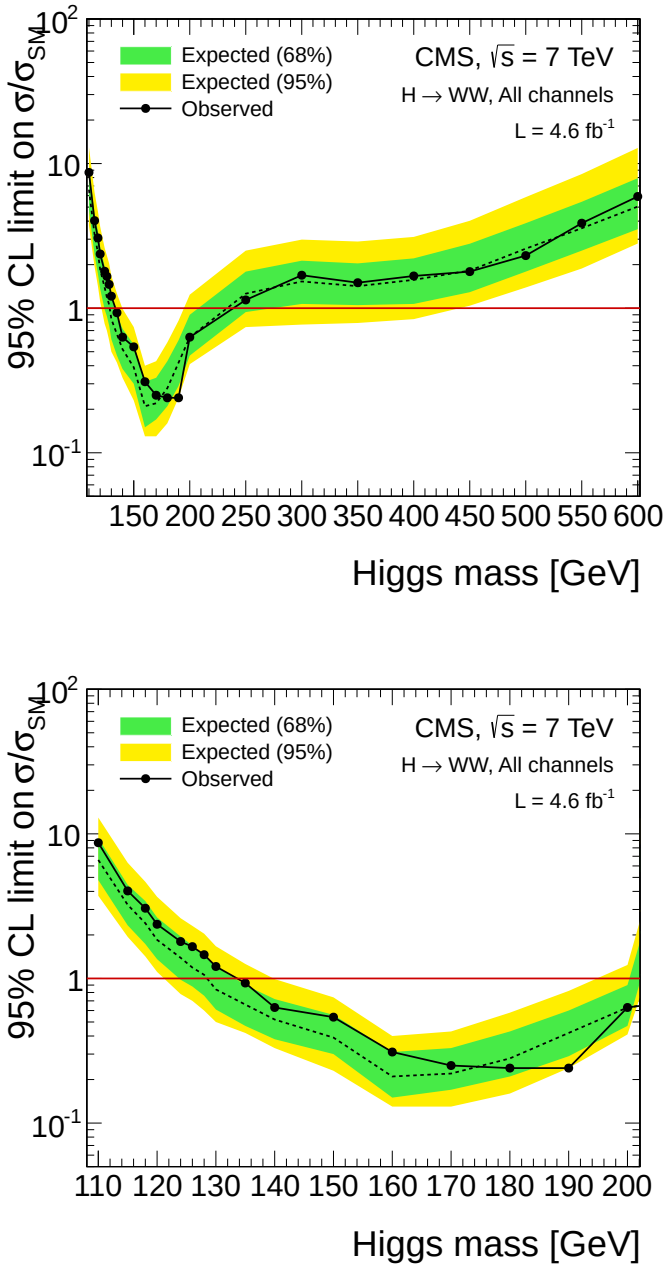

Figure 7.5: Observed (solid) and expected (dashed) upper limits on the signal strength modifier, $\mu = \sigma/\sigma_{\mathrm{SM}}$, at a 95% confidence level. The green and yellow bands represent one and two standard deviation ranges away from the expected value. The top plot shows the limits in the full Higgs boson mass range while the lower plot is zoomed around lower masses for better detail.

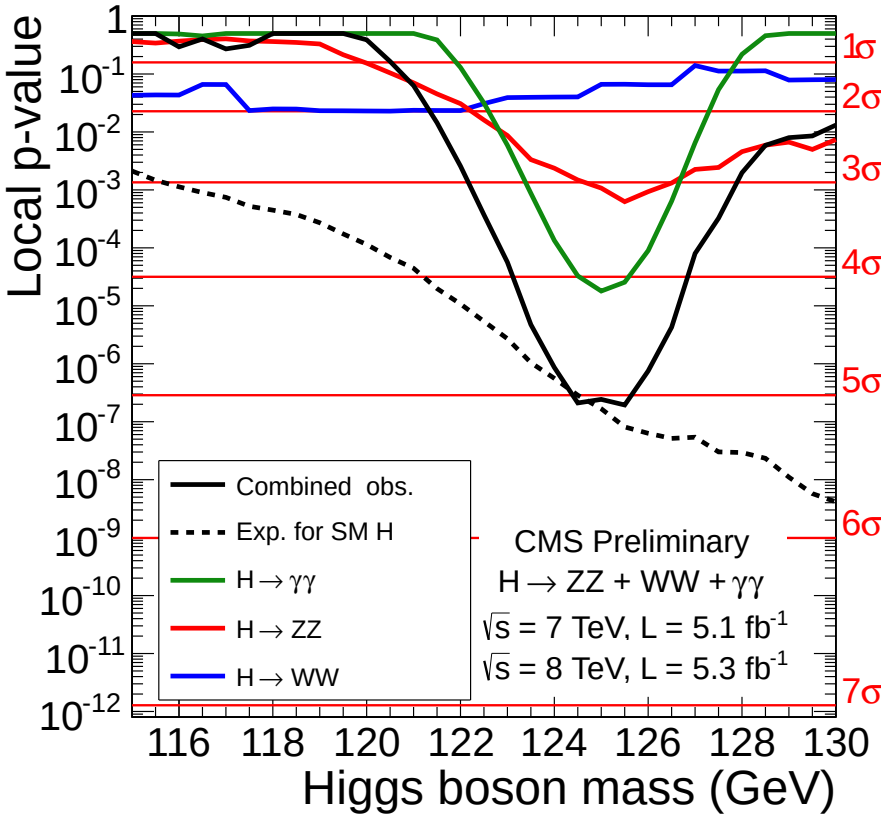

Figure 7.6: Local p-values as a function of Higgs mass for the combined 2011 and 2012 CMS $H \to \gamma\gamma$ analysis (green), $H \to ZZ$ analysis (red), $H \to W^+W^-$ analysis (blue) and combined (solid black) compared to the expected p-value in the hypothesis of a SM Higgs boson (dashed) [97].

Bibliography

[1] ALEPH and CDF and D0 and DELPHI and L3 and OPAL and SLD Collaboration Collaboration, "Precision Electroweak Measurements and Constraints on the Standard Model", arXiv:0911.2604.

[2] W.-M. Yao, C. Amsler, D. Asner et al., "Review of Particle Physics", *Journal of Physics G* **33** (2006) 1+.

[3] F. Englert and R. Brout, "Broken Symmetry and the Mass of Gauge Vector Mesons", *Phys. Rev. Lett.* **13** (Aug, 1964) 321–323. doi:10.1103/PhysRevLett.13.321.

[4] P. Higgs, "Broken symmetries, massless particles and gauge fields", *Physics Letters* **12** (1964), no. 2, 132 – 133. doi:10.1016/0031-9163(64)91136-9.

[5] P. W. Higgs, "Broken Symmetries and the Masses of Gauge Bosons", *Phys. Rev. Lett.* **13** (Oct, 1964) 508–509. doi:10.1103/PhysRevLett.13.508.

[6] P. W. Higgs, "Spontaneous Symmetry Breakdown without Massless Bosons", *Phys. Rev.* **145** (May, 1966) 1156–1163. doi:10.1103/PhysRev.145.1156.

[7] G. S. Guralnik, C. R. Hagen, and T. W. B. Kibble, "Global Conservation Laws and Massless Particles", *Phys. Rev. Lett.* **13** (Nov, 1964) 585–587. doi:10.1103/PhysRevLett.13.585.

[8] T. W. B. Kibble, "Symmetry Breaking in Non-Abelian Gauge Theories", *Phys. Rev.* **155** (Mar, 1967) 1554–1561. doi:10.1103/PhysRev.155.1554.

[9] CMS Collaboration, "Measurement of W^+W^- Production and Search for the Higgs Boson in pp Collisions at $\sqrt{s} = 7$ TeV", *Phys.Lett.* **B699** (2011) 25–47, arXiv:1102.5429. doi:10.1016/j.physletb.2011.03.056.

[10] CMS Collaboration, "Search for the Higgs Boson in the Fully Leptonic W^+W^- Final State", *CMS Physics Analysis Summary* **CMS-PAS-HIG-11-003** (2011).

[11] CMS Collaboration, "Search for the Higgs Boson in the Fully Leptonic W^+W^- Final State", *CMS Physics Analysis Summary* **CMS-PAS-HIG-11-014** (2011).

[12] S. Weinberg, "A Model of Leptons", *Phys. Rev. Lett.* **19** (Nov, 1967) 1264–1266. doi:10.1103/PhysRevLett.19.1264.

[13] F. Halzen and A. D. Martin, "Quarks & Leptons: An Introductory Course in Modern Particle Physics". John Wiley & Sons, Inc., 1984.

[14] E. Noether, "Invariante Variationsprobleme", *Nachr. d. König. Gesellsch. d. Wiss. zu Göttingen, Math-phys. Klasse, Seite 235-157* (1918) arXiv:www.physics.ucla.edu/~cwp/articles/noether.trans/german/emmy235.html.

[15] C. Quigg, "Gauge Theories of the Strong, Weak, and Electromagnetic Interactions". Frontiers in physics. Addison-Wesley, 1997.

[16] J. C. Ward, "An Identity in Quantum Electrodynamics", *Phys. Rev.* **78** (Apr, 1950) 182–182. doi:10.1103/PhysRev.78.182.

[17] Y. Takahashi, "On the generalized Ward identity", *Nuovo Cimento* **Ser 10** (1957).

[18] http://upload.wikimedia.org/wikipedia/commons/thumb/0/00/Standard_Model_of_Elementary_Particles.svg/2000px-Standard_Model_of_Elementary_Particles.svg.png.

[19] http://www.nature.com/nphys/journal/v7/n1/images/nphys1874-f1.jpg.

[20] http://upload.wikimedia.org/wikipedia/commons/thumb/4/4c/Elementary_particle_interactions.svg/2000px-Elementary_particle_interactions.svg.png.

[21] ALEPH, DELPHI, L3, OPAL Collaborations, and the LEP Working Group for Higgs Boson Searches, "Search for the Standard Model Higgs boson at LEP", *Phys. Lett. B* **565** (2003) 61. doi:10.1016/S0370-2693(03)00614-2.

[22] CDF and D0 Collaboration, "Combined CDF and D0 Upper Limits on Standard Model Higgs Boson Production with up to 8.2 fb^{-1} of Data", arXiv:1103.3233.

[23] L. Evans and P. Bryant, "LHC Machine", *Journal of Instrumentation* **3** (2008), no. 08, S08001.

[24] O. S. Brüning, P. Collier, P. Lebrun et al., "LHC Design Report". CERN, Geneva, 2004.

[25] J.-L. Caron, "The LHC injection complex. L'ensemble d'injection du LHC.", (May, 1993). AC Collection. Legacy of AC. Pictures from 1992 to 2002.

[26] http://www.harley-davidson.com/.

[27] CMS Collaboration, "The CMS experiment at the CERN LHC", *JINST* **3** **S08004** (2008) 361. doi:10.1088/1748-0221/3/08/S08004.

[28] CMS Collaboration, "CMS tracking performance results from early LHC operation", *The European Physical Journal C - Particles and Fields* **70** (2010) 1165–1192. 10.1140/epjc/s10052-010-1491-3.

[29] CMS HCAL Collaboration, "Design, performance, and calibration of CMS hadron-barrel calorimeter wedges", *Eur. Phys. J.* **C55** (2008) 159–171. doi:10.1140/epjc/s10052-008-0573-y.

[30] CMS Collaboration, "Absolute Calibration of Luminosity Measurement at CMS: Summer 2011 Update", *CMS Physics Analysis Summary* **CMS-PAS-EWK-11-001** (2011).

[31] CMS Collaboration, "Absolute Calibration of the Luminosity Measurement at CMS: Winter 2012 Update", *CMS Physics Analysis Summary* **CMS-PAS-SMP-12-008** (2012).

[32] S. van der Meer, "Calibration of the effective beam height in the ISR. oai:cds.cern.ch:296752", Technical Report CERN-ISR-PO-68-31. ISR-PO-68-31, CERN, Geneva, (1968).

[33] CMS Collaboration, "CMS TriDAS project: Technical Design Report; 1, the trigger systems",.

[34] S. Cucciarelli, M. Konecki, D. Kotlinski et al., "Track reconstruction, primary vertex finding and seed generation with the Pixel Detector", Technical Report CMS-NOTE-2006-026. CERN-CMS-NOTE-2006-026, CERN, Geneva, (Jan, 2006).

[35] W. Adam, B. Mangano, T. Speer et al., "Track Reconstruction in the CMS tracker", Technical Report CMS-NOTE-2006-041. CERN-CMS-NOTE-2006-041, CERN, Geneva, (Dec, 2006).

[36] R. Frühwirth, "Application of Kalman filtering to track and vertex fitting", *Nuclear Instruments and Methods in Physics Research Section A: Accelerators, Spectrometers, Detectors and Associated Equipment* **262** (1987), no. 2–3, 444 – 450. doi:10.1016/0168-9002(87)90887-4.

[37] K. Rose, "Deterministic annealing for clustering, compression, classification, regression, and related optimization problems", *Proceedings of the IEEE* **86** (nov, 1998) 2210 –2239. doi:10.1109/5.726788.

[38] CMS Collaboration, A. Aimar, J. Harvey, and N. Knoors, "Deterministic annealing for vertex finding at CMS", in *Computing in High Energy Physics and Nuclear Physics 2004*, CERN. CERN, Geneva, 2005.

[39] T. Speer, K. Prokofiev, R. Frühwirth et al., "Vertex Fitting in the CMS Tracker", Technical Report CMS-NOTE-2006-032. CERN-CMS-NOTE-2006-032, CERN, Geneva, (Feb, 2006).

[40] R. Fruhwirth, W. Waltenberger, and P. Vanlaer, "Adaptive Vertex Fitting", Technical Report CMS-NOTE-2007-008. CERN-CMS-NOTE-2007-008, CERN, Geneva, (Mar, 2007).

[41] CMS Collaboration, "Tracking and Primary Vertex Results in First 7 TeV Collisions", *CMS Physics Analysis Summary* **CMS-PAS-TRK-10-005** (2010).

[42] S. Baffioni, C. Charlot, F. Ferri et al., "Electron reconstruction in CMS", *The European Physical Journal C - Particles and Fields* **49** (2007) 1099–1116. 10.1140/epjc/s10052-006-0175-5.

[43] CMS Collaboration, "Electron reconstruction and identification at $\sqrt{s}$ = 7 TeV", *CMS Physics Analysis Summary* **CMS-PAS-EGM-10-001** (2010).

[44] W. Adam, R. Frühwirth, A. Strandlie et al., "RESEARCH NOTE FROM COLLABORATION: Reconstruction of electrons with the Gaussian-sum filter in the CMS tracker at the LHC", *Journal of Physics G Nuclear Physics* **31** (September, 2005) 9, arXiv:arXiv:physics/0306087. doi:10.1088/0954-3899/31/9/N01.

[45] CMS Collaboration, "The CMS muon project: Technical Design Report",.

[46] CMS Collaboration, "Performance of CMS muon reconstruction in cosmic-ray events", *Journal of Instrumentation* **5** (March, 2010) 3022–+, arXiv:0911.4994. doi:10.1088/1748-0221/5/03/T03022.

[47] CMS Collaboration, "Particle-Flow Event Reconstruction in CMS and Performance for Jets, Taus, and MET", *CMS Physics Analysis Summary* **CMS-PAS-PFT-09-001** (2009).

[48] CMS Collaboration, "Commissioning of the Particle-Flow reconstruction in Minimum-Bias and Jet Events from pp Collisions at 7 TeV", *CMS Physics Analysis Summary* **CMS-PAS-PFT-10-002** (2010).

[49] CMS Collaboration, "Missing transverse energy performance of the CMS detector", *Journal of Instrumentation* **6** (2011), no. 09, P09001.

[50] M. Cacciari, G. P. Salam, and G. Soyez, "The anti-k_t jet clustering algorithm", *Journal of High Energy Physics* **4** (April, 2008) 63–+, arXiv:0802.1189. doi:10.1088/1126-6708/2008/04/063.

[51] M. Cacciari and G. P. Salam, "Pileup subtraction using jet areas", *Physics Letters B* **659** (2008), no. 1–2, 119 – 126. doi:10.1016/j.physletb.2007.09.077.

[52] M. Cacciari, G. P. Salam, and G. Soyez, "The catchment area of jets", *Journal of High Energy Physics* **2008** (2008), no. 04, 005.

[53] CMS Collaboration, "Determination of jet energy calibration and transverse momentum resolution in CMS", *Journal of Instrumentation* **6** (2011), no. 11, P11002.

[54] CMS Collaboration, "b-Jet Identification in the CMS Experiment", *CMS Physics Analysis Summary* **CMS-PAS-BTV-11-004** (2012).

[55] CMS Collaboration, "Measurement of btagging efficiency using ttbar events", *CMS Physics Analysis Summary* **CMS-PAS-BTV-11-003** (2012).

[56] S. Weinzierl, "Introduction to Monte Carlo methods", arXiv:hep-ph/0006269. Topical lectures given at the Research School Subatomic physics, Amsterdam, the Netherlands, June 2000.

[57] H.-L. Lai, J. Huston, Z. Li et al., "Uncertainty induced by QCD coupling in the CTEQ global analysis of parton distributions", *Phys.Rev.* **D82** (2010) 054021, arXiv:1004.4624. doi:10.1103/PhysRevD.82.054021.

[58] H.-L. Lai, M. Guzzi, J. Huston et al., "New parton distributions for collider physics", *Phys.Rev.* **D82** (2010) 074024, arXiv:1007.2241. doi:10.1103/PhysRevD.82.074024.

[59] T. Sjöstrand, S. Mrenna, and P. Skands, "PYTHIA 6.4 physics and manual", *JHEP* **05** (2006) 026. doi:10.1088/1126-6708/2006/05/026.

[60] GEANT4 Collaboration, "GEANT4: A Simulation toolkit", *Nucl. Instrum. Meth.* **A506** (2003) 250. doi:10.1016/S0168-9002(03)01368-8.

[61] W. Stirling, "Standard Model cross sections as a function of collider energy", (2009). private communication.

[62] LHC Higgs Cross Section Working Group, S. Dittmaier, C. Mariotti, G. Passarino, R. Tanaka (Eds.), "Handbook of LHC Higgs Cross Sections: Inclusive Observables", CERN Report CERN-2011-002, CERN, (2011).

[63] G. Bozzi, S. Catani, D. de Florian et al., "The q(T) spectrum of the Higgs boson at the LHC in QCD perturbation theory", *Phys. Lett.* **B564** (2003) 65–72, arXiv:hep-ph/0302104. doi:10.1016/S0370-2693(03)00656-7.

[64] G. Bozzi, S. Catani, D. de Florian et al., "Transverse-momentum resummation and the spectrum of the Higgs boson at the LHC", *Nucl. Phys.* **B737** (2006) 73–120, arXiv:hep-ph/0508068. doi:10.1016/j.nuclphysb.2005.12.022.

[65] D. de Florian, G. Ferrera, M. Grazzini et al., "Transverse-momentum resummation: Higgs boson production at the Tevatron and the LHC", *JHEP* **1111** (2011) 064, arXiv:1109.2109.

[66] J. Alwall, P. Demin, S. de Visscher et al., "MadGraph/MadEvent v4: the new web generation", *Journal of High Energy Physics* **2007** (2007), no. 09, 028.

[67] R. Gavin, Y. Li, F. Petriello and S. Quackenbush, "FEWZ 2.0: A code for hadronic Z production at the next-to-next-to-leading order", *arXiv:1011.3540v1* (2010).

[68] S. Frixione, P. Nason, and C. Oleari, "Matching NLO QCD computations with parton shower simulations: the POWHEG method", *JHEP* **11** (2007) 070. doi:10.1088/1126-6708/2007/11/070.

[69] John M. Campbell, R. K. Ellis, "MCFM for the Tevatron and the LHC", *arXiv:1007.3492* (2010).

[70] J. M. Campbell, R. K. Ellis, and C. Williams, "Vector boson pair production at the LHC", *JHEP* **1107** (2011) 018, arXiv:1105.0020.

[71] T. Binoth, M. Ciccolini, N. Kauer et al., "Gluon-induced W-boson pair production at the LHC", *JHEP* **12** (2006) 046. doi:10.1088/1126-6708/2006/12/046.

[72] A. Hoecker, P. Speckmayer, J. Stelzer et al., "TMVA: Toolkit for Multivariate Data Analysis", *PoS* **ACAT** (2007) 040, arXiv:physics/0703039.

[73] L. Breiman, J. Friedman, R. Olshen et al., "Classification and Regression Trees". Wadsworth and Brooks, Monterey, CA, 1984.

[74] Y. Freund and R. E. Schapire, "A decision-theoretic generalization of on-line learning and an application to boosting", in *Proceedings of the Second European Conference on Computational Learning Theory*, pp. 23–37. Springer-Verlag, London, UK, 1995.

[75] R. C. Gray, C. Kilic, M. Park et al., "Backgrounds To Higgs Boson Searches from $W\gamma^* \to l\nu l(l)$ Asymmetric Internal Conversion", arXiv:1110.1368.

[76] S. Dittmaier, C. Mariotti, G. Passarino et al., "Handbook of LHC Higgs Cross Sections: 2. Differential Distributions", technical report, CERN, (2012).

[77] ATLAS Collaboration, "Procedure for the LHC Higgs boson search combination in Summer 2011", Technical Report CMS-NOTE-2011-005, CERN, Geneva, (Aug, 2011).

[78] J. M. Campbell, R. K. Ellis, and C. Williams, "Hadronic production of a Higgs boson and two jets at next-to-leading order", *Phys. Rev. D* **81** (Apr, 2010) 074023. doi:10.1103/PhysRevD.81.074023.

[79] S. Frixione and B. R. Webber, "Matching NLO QCD computations and parton shower simulations", *JHEP* **0206** (2002) 029, arXiv:hep-ph/0204244.

[80] G. Corcella, I. Knowles, G. Marchesini et al., "HERWIG 6: An Event generator for hadron emission reactions with interfering gluons (including supersymmetric processes)", *JHEP* **0101** (2001) 010, arXiv:hep-ph/0011363.

[81] S. Frixione, F. Stoeckli, P. Torrielli et al., "NLO QCD corrections in Herwig++ with MC@NLO", *JHEP* **1101** (2011) 053, arXiv:1010.0568. doi:10.1007/JHEP01(2011)053.

[82] J. Butterworth, J. R. Forshaw, and M. Seymour, "Multiparton interactions in photoproduction at HERA", *Z.Phys.* **C72** (1996) 637–646, arXiv:hep-ph/9601371. doi:10.1007/s002880050286.

[83] C. Anastasiou, S. Buehler, F. Herzog et al., "Total cross-section for Higgs boson hadroproduction with anomalous Standard Model interactions", *JHEP* **1112** (2011) 058, arXiv:1107.0683. doi:10.1007/JHEP12(2011)058.

[84] http://twiki.cern.ch/twiki/bin/view/LHCPhysics/HeavyHiggs.

[85] PDF4LHC Working Group, http://www.hep.ucl.ac.uk/pdf4lhc/PDF4LHCrecom.pdf.

[86] A. D. Martin, W. J. Stirling, R. S. Thorne et al., "Parton distributions for the LHC", *Eur. Phys. J.* **C63** (2009) 189–285, arXiv:0901.0002. doi:10.1140/epjc/s10052-009-1072-5.

[87] H.-L. Lai, M. Guzzi, J. Huston et al., "New parton distributions for collider physics", *Phys. Rev. D* **82** (Oct, 2010) 074024. doi:10.1103/PhysRevD.82.074024.

[88] R. D. Ball, V. Bertone, F. Cerutti et al., "Impact of Heavy Quark Masses on Parton Distributions and LHC Phenomenology", *Nucl.Phys.* **B849** (2011) 296–363, arXiv:1101.1300. doi:10.1016/j.nuclphysb.2011.03.021.

[89] CMS Collaboration, "Measurements of Inclusive W and Z Cross Sections in pp Collisions at sqrt(s)=7 TeV", *JHEP* **1101** (2011) 080, arXiv:1012.2466. doi:10.1007/JHEP01(2011)080.

[90] L. Lyons, "Statistics for Nuclear and Particle Physicists". Cambridge University Press, 1989.

[91] G. Cowan, "Statistical Methods for Particle Physics". http://indico.cern.ch/conferenceDisplay.py?confId=173726, Apr, 2012.

[92] G. Cowan, K. Cranmer, E. Gross et al., "Asymptotic formulae for likelihood-based tests of new physics", *The European Physical Journal C - Particles and Fields* **71** (2011) 1–19. 10.1140/epjc/s10052-011-1554-0.

[93] J. Neyman, "Outline of a Theory of Statistical Estimation Based on the Classical Theory of Probability", *Philosophical Transactions of the Royal Society of London. Series A, Mathematical and Physical Sciences* **236** (1937), no. 767, pp. 333–380.

[94] A. L. Read, "Modified frequentist analysis of search results (the CL_s method). oai:cds.cern.ch:451614",.

[95] T. Junk, "Confidence level computation for combining searches with small statistics", *Nuclear Instruments and Methods in Physics Research Section A: Accelerators, Spectrometers, Detectors and Associated Equipment* **434** (1999), no. 2âĂŞ3, 435 – 443. doi:10.1016/S0168-9002(99)00498-2.

[96] A. L. Read, "Presentation of search results: the CL s technique", *Journal of Physics G: Nuclear and Particle Physics* **28** (2002), no. 10, 2693.

[97] CMS Collaboration, "Observation of a new boson with a mass near 125 GeV", *CMS Physics Analysis Summary* **CMS-PAS-HIG-12-020** (2012).

[98] "Observation of an Excess of Events in the Search for the Standard Model Higgs boson with the ATLAS detector at the LHC", Technical Report ATLAS-CONF-2012-093, CERN, Geneva, (Jul, 2012).

Appendix A

Expected and Observed Yields

The following pages contain the expected signal and background yields for each channel and for each Higgs mass hypothesis. Tabs. A.1 through A.5 contain the yields for the 0-jet category. Then, Tabs. A.6 through A.10 containt the yields for the 1-jet category. Finally, Tab. A.11 contains the yields in the 2-jet category.

Table A.1: Background contributions and data yields for $4.6\,\mathrm{fb}^{-1}$ of integrated luminosity after the full selection in the 0-jet category for low Higgs masses ($110 \leq m_{\mathrm{H}} \leq 128\,\mathrm{GeV}$). The data-driven correction are applied and the errors reported reflect all systematic uncertanties.

	$Z\gamma^*$	$t\bar{t}$ +tW	W+jets	WZ+ZZ	ggWW	WW	all bkg.	$m_{\mathrm{H}} = 110$ GeV	data
sf	5.7 ± 6.9	1.0 ± 0.3	2.3 ± 1.1	0.9 ± 0.2	0.7 ± 0.1	21.8 ± 2.2	32.4 ± 7.4	0.7 ± 0.2	29
of	1.4 ± 2.0	3.4 ± 0.7	8.7 ± 3.6	4.2 ± 1.8	1.7 ± 0.2	41.3 ± 4.2	60.8 ± 6.2	2.6 ± 0.7	61
total	7.1 ± 7.2	4.4 ± 0.7	11.0 ± 3.7	5.1 ± 1.8	2.4 ± 0.2	63.2 ± 4.8	93.2 ± 9.6	3.4 ± 0.7	90
	$Z\gamma^*$	$t\bar{t}$ +tW	W+jets	WZ+ZZ	ggWW	WW	all bkg.	$m_{\mathrm{H}} = 115$ GeV	data
sf	5.7 ± 6.9	1.0 ± 0.3	2.3 ± 1.1	0.9 ± 0.2	0.7 ± 0.1	21.8 ± 2.2	32.4 ± 7.4	1.9 ± 0.5	29
of	1.4 ± 2.0	3.4 ± 0.7	8.7 ± 3.6	4.2 ± 1.8	1.7 ± 0.2	41.3 ± 4.2	60.8 ± 6.2	5.4 ± 1.4	61
total	7.1 ± 7.2	4.4 ± 0.7	11.0 ± 3.7	5.1 ± 1.8	2.4 ± 0.2	63.2 ± 4.8	93.2 ± 9.6	7.3 ± 1.5	90
	$Z\gamma^*$	$t\bar{t}$ +tW	W+jets	WZ+ZZ	ggWW	WW	all bkg.	$m_{\mathrm{H}} = 120$ GeV	data
sf	7.5 ± 8.9	1.8 ± 0.4	3.7 ± 1.7	1.6 ± 0.3	1.4 ± 0.1	34.7 ± 3.5	50.6 ± 9.8	4.6 ± 1.1	49
of	1.4 ± 2.0	4.9 ± 1.0	11.0 ± 4.4	4.5 ± 1.8	2.8 ± 0.3	61.6 ± 6.3	86.1 ± 8.2	11.0 ± 2.5	87
total	8.8 ± 9.2	6.7 ± 1.0	14.7 ± 4.7	6.1 ± 1.9	4.1 ± 0.3	96.2 ± 7.2	136.7 ± 12.7	15.7 ± 2.7	136
	$Z\gamma^*$	$t\bar{t}$ +tW	W+jets	WZ+ZZ	ggWW	WW	all bkg.	$m_{\mathrm{H}} = 124$ GeV	data
sf	10.7 ± 9.5	2.3 ± 0.5	3.7 ± 1.7	2.0 ± 0.4	1.6 ± 0.2	41.7 ± 4.3	62.1 ± 10.6	7.6 ± 1.7	60
of	1.4 ± 2.0	5.7 ± 1.1	12.0 ± 4.8	4.8 ± 1.9	3.3 ± 0.3	70.5 ± 7.2	97.7 ± 9.1	16.4 ± 3.7	100
total	12.1 ± 9.7	8.0 ± 1.2	15.7 ± 5.0	6.8 ± 1.9	5.0 ± 0.4	112.2 ± 8.4	159.8 ± 13.9	24.0 ± 4.1	160
	$Z\gamma^*$	$t\bar{t}$ +tW	W+jets	WZ+ZZ	ggWW	WW	all bkg.	$m_{\mathrm{H}} = 128$ GeV	data
sf	7.8 ± 6.5	2.8 ± 0.6	4.4 ± 1.9	2.2 ± 0.4	2.2 ± 0.2	49.2 ± 5.0	68.6 ± 8.5	12.8 ± 2.9	71
of	1.4 ± 2.0	6.8 ± 1.3	13.0 ± 5.1	5.1 ± 1.9	3.8 ± 0.4	79.2 ± 8.1	109.2 ± 10.0	23.0 ± 5.3	110
total	9.2 ± 6.8	9.6 ± 1.4	17.4 ± 5.5	7.2 ± 2.0	6.0 ± 0.4	128.4 ± 9.5	177.8 ± 13.1	35.8 ± 6.0	181

Table A.2: Background contributions and data yields for $4.6\,\mathrm{fb}^{-1}$ of integrated luminosity after the full selection in the 0-jet category for intermediate Higgs masses ($130 \leq m_{\mathrm{H}} \leq 160\,\mathrm{GeV}$). The data-driven correction are applied and the errors reported reflect all systematic uncertanties.

	$Z\gamma^*$	$t\bar{t}$ +tW	W+jets	WZ+ZZ	ggWW	WW	all bkg.	$m_{\mathrm{H}} = 130$ GeV	data
sf	12.3 ± 7.6	3.1 ± 0.6	4.6 ± 2.0	2.3 ± 0.4	2.4 ± 0.2	52.8 ± 5.4	77.5 ± 9.5	15.6 ± 3.6	80
of	1.4 ± 2.0	7.5 ± 1.4	13.0 ± 5.1	5.1 ± 1.9	4.1 ± 0.4	83.0 ± 8.4	114.0 ± 10.4	29.6 ± 6.7	113
total	13.7 ± 7.8	10.6 ± 1.6	17.6 ± 5.5	7.4 ± 2.0	6.5 ± 0.5	135.7 ± 10.0	191.5 ± 14.1	45.2 ± 7.6	193
	$Z\gamma^*$	$t\bar{t}$ +tW	W+jets	WZ+ZZ	ggWW	WW	all bkg.	$m_{\mathrm{H}} = 135$ GeV	data
sf	14.6 ± 8.9	3.7 ± 0.7	5.0 ± 2.2	2.4 ± 0.4	2.7 ± 0.3	57.2 ± 5.8	85.5 ± 10.8	22.2 ± 5.3	87
of	0.0 ± 0.0	7.8 ± 1.5	12.0 ± 4.7	3.8 ± 1.4	4.4 ± 0.4	85.3 ± 8.7	113.3 ± 10.1	38.0 ± 9.1	113
total	14.6 ± 8.9	11.4 ± 1.6	17.0 ± 5.2	6.2 ± 1.4	7.1 ± 0.5	142.5 ± 10.4	198.8 ± 14.8	60.1 ± 10.5	200
	$Z\gamma^*$	$t\bar{t}$ +tW	W+jets	WZ+ZZ	ggWW	WW	all bkg.	$m_{\mathrm{H}} = 140$ GeV	data
sf	15.0 ± 8.9	3.8 ± 0.8	5.2 ± 2.2	2.5 ± 0.4	2.9 ± 0.3	60.3 ± 6.2	89.7 ± 11.1	28.6 ± 7.3	89
of	0.0 ± 0.0	7.6 ± 1.4	10.0 ± 3.9	3.8 ± 1.4	4.4 ± 0.4	82.4 ± 8.4	108.1 ± 9.5	44.8 ± 11.4	105
total	15.0 ± 8.9	11.4 ± 1.6	15.2 ± 4.5	6.3 ± 1.4	7.2 ± 0.5	142.7 ± 10.4	197.8 ± 14.6	73.4 ± 13.5	194
	$Z\gamma^*$	$t\bar{t}$ +tW	W+jets	WZ+ZZ	ggWW	WW	all bkg.	$m_{\mathrm{H}} = 150$ GeV	data
sf	13.2 ± 13.5	6.3 ± 1.2	1.5 ± 0.9	1.9 ± 0.4	3.4 ± 0.3	49.0 ± 5.0	75.3 ± 14.5	37.6 ± 9.3	83
of	0.0 ± 0.0	6.2 ± 1.2	5.0 ± 2.2	1.2 ± 0.4	4.7 ± 0.5	61.5 ± 6.3	78.6 ± 6.7	47.4 ± 11.7	84
total	13.2 ± 13.5	12.5 ± 1.7	6.5 ± 2.3	3.1 ± 0.5	8.1 ± 0.6	110.5 ± 8.0	153.9 ± 16.0	84.9 ± 14.9	167
	$Z\gamma^*$	$t\bar{t}$ +tW	W+jets	WZ+ZZ	ggWW	WW	all bkg.	$m_{\mathrm{H}} = 160$ GeV	data
sf	3.4 ± 3.4	5.2 ± 1.0	0.3 ± 0.5	1.4 ± 0.3	3.1 ± 0.3	33.9 ± 3.5	47.4 ± 5.0	54.7 ± 13.6	51
of	0.0 ± 0.0	5.3 ± 1.0	2.7 ± 1.4	0.7 ± 0.3	4.5 ± 0.5	41.0 ± 4.2	54.3 ± 4.6	68.2 ± 17.0	60
total	3.4 ± 3.4	10.5 ± 1.4	3.0 ± 1.5	2.2 ± 0.4	7.6 ± 0.6	75.0 ± 5.4	101.7 ± 6.8	122.9 ± 21.8	111

Table A.3: Background contributions and data yields for $4.6\,\mathrm{fb}^{-1}$ of integrated luminosity after the full selection in the 0-jet category for intermediate Higgs masses ($170 \leq m_{\mathrm{H}} \leq 200\,\mathrm{GeV}$). The data-driven correction are applied and the errors reported reflect all systematic uncertanties.

	$Z\gamma^*$	$t\bar{t}$ +tW	W+jets	WZ+ZZ	ggWW	WW	all bkg.	$m_{\mathrm{H}} = 170$ GeV	data
sf	3.9 ± 3.5	5.2 ± 1.0	0.5 ± 0.5	1.1 ± 0.2	3.1 ± 0.3	28.0 ± 2.9	41.8 ± 4.7	46.9 ± 12.9	42
of	0.0 ± 0.0	5.2 ± 1.0	2.6 ± 1.4	0.5 ± 0.2	4.2 ± 0.4	31.2 ± 3.2	43.7 ± 3.6	54.5 ± 15.1	46
total	3.9 ± 3.5	10.4 ± 1.4	3.1 ± 1.4	1.6 ± 0.3	7.3 ± 0.5	59.1 ± 4.3	85.5 ± 6.0	101.4 ± 19.9	88
	$Z\gamma^*$	$t\bar{t}$ +tW	W+jets	WZ+ZZ	ggWW	WW	all bkg.	$m_{\mathrm{H}} = 180$ GeV	data
sf	2.3 ± 2.7	6.2 ± 1.2	0.5 ± 0.5	1.2 ± 0.1	4.1 ± 0.4	33.5 ± 3.4	47.7 ± 4.5	37.0 ± 9.9	44
of	0.0 ± 0.0	6.9 ± 1.3	1.5 ± 1.0	0.5 ± 0.2	5.2 ± 0.5	36.0 ± 3.7	50.1 ± 4.1	38.6 ± 10.3	53
total	2.3 ± 2.7	13.1 ± 1.8	2.0 ± 1.1	1.7 ± 0.2	9.2 ± 0.7	69.6 ± 5.0	97.9 ± 6.1	75.6 ± 14.3	97
	$Z\gamma^*$	$t\bar{t}$ +tW	W+jets	WZ+ZZ	ggWW	WW	all bkg.	$m_{\mathrm{H}} = 190$ GeV	data
sf	5.6 ± 3.0	8.9 ± 1.6	0.2 ± 0.6	2.0 ± 0.2	5.7 ± 0.6	51.1 ± 5.2	73.5 ± 6.3	31.7 ± 8.7	73
of	0.0 ± 0.0	11.8 ± 2.2	2.3 ± 1.2	1.0 ± 0.3	6.9 ± 0.7	59.2 ± 6.0	81.1 ± 6.5	34.5 ± 9.5	73
total	5.6 ± 3.0	20.6 ± 2.7	2.5 ± 1.3	2.9 ± 0.3	12.6 ± 0.9	110.3 ± 8.0	154.6 ± 9.1	66.2 ± 12.9	146
	$Z\gamma^*$	$t\bar{t}$ +tW	W+jets	WZ+ZZ	ggWW	WW	all bkg.	$m_{\mathrm{H}} = 200$ GeV	data
sf	2.7 ± 3.7	9.7 ± 1.8	1.0 ± 0.8	2.3 ± 0.2	5.1 ± 1.6	42.7 ± 4.8	63.4 ± 6.6	22.5 ± 6.6	71
of	0.0 ± 0.0	13.7 ± 2.5	2.4 ± 1.2	0.9 ± 0.2	6.3 ± 2.0	54.1 ± 6.1	77.4 ± 7.0	26.3 ± 7.6	88
total	2.7 ± 3.7	23.3 ± 3.1	3.4 ± 1.5	3.2 ± 0.3	11.5 ± 2.5	96.7 ± 7.7	140.8 ± 9.6	48.8 ± 10.1	159

Table A.4: Background contributions and data yields for $4.6\,\mathrm{fb}^{-1}$ of integrated luminosity after the full selection in the 0-jet bin for high Higgs masses ($250 \leq m_{\mathrm{H}} \leq 400\,\mathrm{GeV}$). The data-driven correction are applied and the errors reported reflect all systematic uncertanties.

	$Z\gamma^*$	$t\bar{t}$ +tW	W+jets	WZ+ZZ	ggWW	WW	all bkg.	$m_{\mathrm{H}} = 250$ GeV	data
sf	0.3 ± 0.6	12.8 ± 2.3	2.5 ± 1.2	3.7 ± 0.3	3.3 ± 1.0	36.2 ± 4.1	58.8 ± 5.0	8.5 ± 2.7	60
of	0.0 ± 0.0	23.4 ± 4.2	4.2 ± 1.8	2.0 ± 0.7	5.0 ± 1.6	57.4 ± 6.4	92.0 ± 8.1	15.0 ± 4.8	92
total	0.3 ± 0.6	36.2 ± 4.8	6.7 ± 2.1	5.7 ± 0.8	8.3 ± 1.9	93.5 ± 7.6	150.8 ± 9.5	23.5 ± 5.5	152
	$Z\gamma^*$	$t\bar{t}$ +tW	W+jets	WZ+ZZ	ggWW	WW	all bkg.	$m_{\mathrm{H}} = 300$ GeV	data
sf	0.7 ± 1.9	16.4 ± 3.0	2.0 ± 0.9	4.9 ± 0.6	2.4 ± 0.8	33.7 ± 3.8	60.1 ± 5.4	8.8 ± 2.8	70
of	0.0 ± 0.0	25.2 ± 4.5	4.5 ± 1.9	2.1 ± 0.6	3.8 ± 1.2	47.5 ± 5.3	83.2 ± 7.4	11.4 ± 3.6	77
total	0.7 ± 1.9	41.6 ± 5.4	6.5 ± 2.1	7.0 ± 0.9	6.2 ± 1.4	81.2 ± 6.6	143.3 ± 9.1	20.2 ± 4.6	147
	$Z\gamma^*$	$t\bar{t}$ +tW	W+jets	WZ+ZZ	ggWW	WW	all bkg.	$m_{\mathrm{H}} = 350$ GeV	data
sf	6.0 ± 3.6	16.4 ± 3.0	2.4 ± 1.1	8.3 ± 1.8	2.2 ± 0.7	30.3 ± 3.4	65.6 ± 6.2	9.2 ± 3.1	62
of	0.0 ± 0.0	24.5 ± 4.4	4.1 ± 1.7	1.8 ± 0.5	3.1 ± 1.0	39.3 ± 4.4	72.8 ± 6.6	12.2 ± 4.1	72
total	6.0 ± 3.6	40.9 ± 5.3	6.5 ± 2.1	10.2 ± 1.8	5.2 ± 1.2	69.6 ± 5.6	138.4 ± 9.0	21.3 ± 5.2	134
	$Z\gamma^*$	$t\bar{t}$ +tW	W+jets	WZ+ZZ	ggWW	WW	all bkg.	$m_{\mathrm{H}} = 400$ GeV	data
sf	0.2 ± 0.2	14.1 ± 2.6	2.3 ± 1.0	7.6 ± 1.7	1.9 ± 0.6	24.1 ± 2.8	50.2 ± 4.3	7.8 ± 2.5	48
of	0.0 ± 0.0	21.8 ± 3.9	3.2 ± 1.4	1.7 ± 0.5	2.5 ± 0.8	31.4 ± 3.6	60.5 ± 5.5	9.7 ± 3.1	61
total	0.2 ± 0.2	35.9 ± 4.7	5.5 ± 1.8	9.3 ± 1.8	4.4 ± 1.0	55.5 ± 4.5	110.8 ± 7.0	17.5 ± 4.0	109

Table A.5: Background contributions and data yields for $4.6\,\mathrm{fb}^{-1}$ of integrated luminosity after the full selection in the 0-jet bin for high Higgs masses ($450 \leq m_{\mathrm{H}} \leq 600\,\mathrm{GeV}$). The data-driven correction are applied and the errors reported reflect all systematic uncertanties.

	$Z\gamma^*$	$t\bar{t}$ +tW	W+jets	WZ+ZZ	ggWW	WW	all bkg.	$m_{\mathrm{H}} = 450$ GeV	data
sf	0.1 ± 0.1	8.9 ± 1.6	1.8 ± 0.9	3.2 ± 0.7	1.3 ± 0.4	13.2 ± 1.6	28.4 ± 2.5	4.3 ± 1.2	28
of	0.0 ± 0.0	14.5 ± 2.6	1.6 ± 0.7	1.0 ± 0.4	1.6 ± 0.5	18.6 ± 2.1	37.3 ± 3.5	5.6 ± 1.6	37
total	0.1 ± 0.1	23.4 ± 3.1	3.4 ± 1.1	4.2 ± 0.8	2.8 ± 0.6	31.8 ± 2.7	65.7 ± 4.4	9.9 ± 2.0	65
	$Z\gamma^*$	$t\bar{t}$ +tW	W+jets	WZ+ZZ	ggWW	WW	all bkg.	$m_{\mathrm{H}} = 500$ GeV	data
sf	0.1 ± 0.1	7.1 ± 1.3	1.5 ± 0.8	2.4 ± 0.5	1.0 ± 0.3	9.4 ± 1.1	21.6 ± 2.0	2.7 ± 0.8	23
of	0.0 ± 0.0	11.2 ± 2.1	1.6 ± 0.7	0.9 ± 0.3	1.2 ± 0.4	14.3 ± 1.7	29.2 ± 2.8	3.5 ± 1.0	24
total	0.1 ± 0.1	18.4 ± 2.5	3.1 ± 1.0	3.3 ± 0.6	2.3 ± 0.5	23.7 ± 2.0	50.8 ± 3.4	6.2 ± 1.3	47
	$Z\gamma^*$	$t\bar{t}$ +tW	W+jets	WZ+ZZ	ggWW	WW	all bkg.	$m_{\mathrm{H}} = 550$ GeV	data
sf	0.1 ± 0.1	4.9 ± 1.0	1.3 ± 0.7	1.6 ± 0.3	0.7 ± 0.2	6.9 ± 0.9	15.5 ± 1.5	1.6 ± 0.5	21
of	0.0 ± 0.0	9.1 ± 1.7	1.4 ± 0.6	0.8 ± 0.4	1.1 ± 0.4	11.1 ± 1.3	23.5 ± 2.3	2.3 ± 0.7	20
total	0.1 ± 0.1	14.0 ± 1.9	2.7 ± 0.9	2.4 ± 0.5	1.9 ± 0.4	18.1 ± 1.6	39.0 ± 2.8	3.8 ± 0.9	41
	$Z\gamma^*$	$t\bar{t}$ +tW	W+jets	WZ+ZZ	ggWW	WW	all bkg.	$m_{\mathrm{H}} = 600$ GeV	data
sf	0.1 ± 0.1	3.7 ± 0.8	1.1 ± 0.6	1.0 ± 0.1	0.6 ± 0.2	5.2 ± 0.7	11.7 ± 1.2	1.0 ± 0.4	15
of	0.0 ± 0.0	7.4 ± 1.4	0.9 ± 0.5	0.7 ± 0.4	0.8 ± 0.3	9.2 ± 1.1	19.0 ± 1.9	1.4 ± 0.5	18
total	0.1 ± 0.1	11.2 ± 1.6	2.0 ± 0.8	1.7 ± 0.4	1.4 ± 0.3	14.4 ± 1.3	30.7 ± 2.3	2.4 ± 0.6	33

Table A.6: Background contributions and data yields for $4.6\,\mathrm{fb}^{-1}$ of integrated luminosity after the full selection in the 1-jet bin for low Higgs masses ($110 \leq m_{\mathrm{H}} \leq 128\,\mathrm{GeV}$). The data-driven correction are applied and the errors reported reflect all systematic uncertanties.

	$Z\gamma^*$	$t\bar{t}$ +tW	W+jets	WZ+ZZ	ggWW	WW	all bkg.	$m_{\mathrm{H}} = 110$ GeV	data
sf	2.9 ± 0.9	2.9 ± 0.3	0.3 ± 0.3	0.7 ± 0.3	0.2 ± 0.1	5.1 ± 1.2	12.1 ± 1.6	0.3 ± 0.1	14
of	1.2 ± 1.7	8.3 ± 0.7	4.1 ± 2.0	1.7 ± 0.5	0.7 ± 0.2	12.3 ± 3.0	28.4 ± 4.1	1.2 ± 0.6	36
total	4.1 ± 1.9	11.2 ± 0.7	4.4 ± 2.0	2.4 ± 0.5	0.9 ± 0.2	17.4 ± 3.3	40.5 ± 4.4	1.4 ± 0.6	50
	$Z\gamma^*$	$t\bar{t}$ +tW	W+jets	WZ+ZZ	ggWW	WW	all bkg.	$m_{\mathrm{H}} = 115$ GeV	data
sf	2.9 ± 0.9	2.9 ± 0.3	0.3 ± 0.3	0.7 ± 0.3	0.2 ± 0.1	5.1 ± 1.2	12.1 ± 1.6	0.7 ± 0.3	14
of	1.2 ± 1.7	8.3 ± 0.7	4.1 ± 2.0	1.7 ± 0.5	0.7 ± 0.2	12.3 ± 3.0	28.4 ± 4.1	2.2 ± 1.0	36
total	4.1 ± 1.9	11.2 ± 0.7	4.4 ± 2.0	2.4 ± 0.5	0.9 ± 0.2	17.4 ± 3.3	40.5 ± 4.4	2.8 ± 1.1	50
	$Z\gamma^*$	$t\bar{t}$ +tW	W+jets	WZ+ZZ	ggWW	WW	all bkg.	$m_{\mathrm{H}} = 120$ GeV	data
sf	5.4 ± 1.6	5.2 ± 0.5	0.2 ± 0.5	1.1 ± 0.3	0.5 ± 0.1	7.9 ± 1.9	20.4 ± 2.6	1.7 ± 0.5	26
of	1.2 ± 1.7	12.0 ± 0.9	5.2 ± 2.3	2.1 ± 0.6	1.0 ± 0.3	17.6 ± 4.3	39.1 ± 5.3	4.9 ± 1.7	46
total	6.6 ± 2.3	17.2 ± 1.0	5.4 ± 2.4	3.2 ± 0.6	1.5 ± 0.3	25.5 ± 4.7	59.5 ± 5.9	6.5 ± 1.7	72
	$Z\gamma^*$	$t\bar{t}$ +tW	W+jets	WZ+ZZ	ggWW	WW	all bkg.	$m_{\mathrm{H}} = 124$ GeV	data
sf	4.8 ± 1.9	6.0 ± 0.5	0.2 ± 0.5	1.2 ± 0.3	0.6 ± 0.2	9.4 ± 2.3	22.3 ± 3.1	2.6 ± 0.9	33
of	1.2 ± 1.7	14.3 ± 1.0	5.3 ± 2.4	2.3 ± 0.6	1.1 ± 0.3	20.2 ± 4.9	44.4 ± 5.9	6.8 ± 2.3	50
total	6.0 ± 2.5	20.3 ± 1.2	5.5 ± 2.4	3.5 ± 0.7	1.8 ± 0.3	29.6 ± 5.4	66.7 ± 6.6	9.4 ± 2.4	83
	$Z\gamma^*$	$t\bar{t}$ +tW	W+jets	WZ+ZZ	ggWW	WW	all bkg.	$m_{\mathrm{H}} = 128$ GeV	data
sf	4.1 ± 2.2	7.3 ± 0.6	0.8 ± 0.7	1.3 ± 0.3	0.8 ± 0.2	11.3 ± 2.8	25.5 ± 3.7	4.3 ± 1.4	38
of	1.2 ± 1.7	17.0 ± 1.2	5.3 ± 2.4	2.6 ± 0.6	1.3 ± 0.3	22.8 ± 5.6	50.2 ± 6.4	9.4 ± 3.1	59
total	5.3 ± 2.8	24.3 ± 1.3	6.0 ± 2.5	3.9 ± 0.7	2.1 ± 0.4	34.1 ± 6.2	75.7 ± 7.4	13.7 ± 3.4	97

Table A.7: Background contributions and data yields for $4.6\,\text{fb}^{-1}$ of integrated luminosity after the full selection in the 1-jet bin for intermediate Higgs masses ($130 \leq m_{\text{H}} \leq 160\,\text{GeV}$). The data-driven correction are applied and the errors reported reflect all systematic uncertanties.

	$Z\gamma^*$	$t\bar{t}$ +tW	W+jets	WZ+ZZ	ggWW	WW	all bkg.	$m_{\text{H}} = 130$ GeV	data
sf	4.1 ± 1.9	7.9 ± 0.6	1.1 ± 0.8	1.4 ± 0.3	0.8 ± 0.2	12.1 ± 3.0	27.4 ± 3.7	5.6 ± 1.8	40
of	1.2 ± 1.7	17.7 ± 1.2	5.4 ± 2.4	2.7 ± 0.6	1.4 ± 0.3	24.1 ± 5.9	52.5 ± 6.7	12.1 ± 3.8	65
total	5.3 ± 2.5	25.6 ± 1.4	6.5 ± 2.5	4.0 ± 0.7	2.2 ± 0.4	36.3 ± 6.6	79.9 ± 7.7	17.6 ± 4.2	105
	$Z\gamma^*$	$t\bar{t}$ +tW	W+jets	WZ+ZZ	ggWW	WW	all bkg.	$m_{\text{H}} = 135$ GeV	data
sf	5.0 ± 2.4	8.7 ± 0.7	1.0 ± 0.8	1.4 ± 0.4	1.0 ± 0.2	13.7 ± 3.3	30.8 ± 4.3	7.9 ± 2.9	46
of	1.2 ± 1.7	18.5 ± 1.3	4.1 ± 2.0	2.7 ± 0.6	1.5 ± 0.4	24.8 ± 6.1	52.7 ± 6.8	15.5 ± 5.7	66
total	6.2 ± 2.9	27.2 ± 1.4	5.1 ± 2.1	4.1 ± 0.7	2.5 ± 0.4	38.5 ± 6.9	83.5 ± 8.0	23.5 ± 6.4	112
	$Z\gamma^*$	$t\bar{t}$ +tW	W+jets	WZ+ZZ	ggWW	WW	all bkg.	$m_{\text{H}} = 140$ GeV	data
sf	5.5 ± 2.5	9.6 ± 0.7	1.5 ± 1.0	1.6 ± 0.4	1.0 ± 0.3	14.6 ± 3.6	33.9 ± 4.6	10.5 ± 4.7	47
of	1.2 ± 1.7	18.3 ± 1.3	4.2 ± 1.9	2.6 ± 0.6	1.4 ± 0.3	24.4 ± 6.0	52.0 ± 6.6	18.8 ± 8.4	59
total	6.7 ± 3.0	27.8 ± 1.5	5.7 ± 2.1	4.2 ± 0.7	2.4 ± 0.4	39.0 ± 7.0	85.9 ± 8.1	29.3 ± 9.7	106
	$Z\gamma^*$	$t\bar{t}$ +tW	W+jets	WZ+ZZ	ggWW	WW	all bkg.	$m_{\text{H}} = 150$ GeV	data
sf	4.7 ± 1.6	11.9 ± 0.9	2.0 ± 1.2	1.3 ± 0.3	1.2 ± 0.3	14.7 ± 3.6	35.8 ± 4.2	15.4 ± 5.8	51
of	0.0 ± 0.0	18.6 ± 1.3	2.4 ± 1.1	1.8 ± 0.5	1.7 ± 0.4	22.7 ± 5.6	47.2 ± 5.8	22.9 ± 8.5	46
total	4.7 ± 1.6	30.5 ± 1.5	4.4 ± 1.6	3.1 ± 0.6	2.9 ± 0.5	37.4 ± 6.6	83.0 ± 7.2	38.3 ± 10.3	97
	$Z\gamma^*$	$t\bar{t}$ +tW	W+jets	WZ+ZZ	ggWW	WW	all bkg.	$m_{\text{H}} = 160$ GeV	data
sf	4.2 ± 1.4	11.6 ± 0.8	1.0 ± 0.9	0.9 ± 0.2	1.2 ± 0.3	12.5 ± 3.1	31.3 ± 3.6	25.3 ± 9.3	52
of	0.0 ± 0.0	16.3 ± 1.1	2.2 ± 1.0	0.9 ± 0.2	1.6 ± 0.4	18.5 ± 4.5	39.5 ± 4.8	34.9 ± 12.8	34
total	4.2 ± 1.4	27.9 ± 1.4	3.2 ± 1.4	1.9 ± 0.3	2.7 ± 0.5	31.0 ± 5.5	70.8 ± 6.0	60.2 ± 15.8	86

Table A.8: Background contributions and data yields for $4.6\,\mathrm{fb}^{-1}$ of integrated luminosity after the full selection in the 1-jet bin for intermediate Higgs masses ($170 \leq m_{\mathrm{H}} \leq 200\,\mathrm{GeV}$). The data-driven correction are applied and the errors reported reflect all systematic uncertanties.

	$Z\gamma^*$	$t\bar{t}$ +tW	W+jets	WZ+ZZ	ggWW	WW	all bkg.	$m_{\mathrm{H}} = 170$ GeV	data
sf	5.1 ± 1.9	11.1 ± 0.8	1.3 ± 1.0	0.7 ± 0.2	1.1 ± 0.3	10.9 ± 2.7	30.2 ± 3.5	20.4 ± 7.7	44
of	0.0 ± 0.0	14.0 ± 1.0	1.3 ± 0.7	0.6 ± 0.2	1.4 ± 0.3	14.0 ± 3.4	31.3 ± 3.7	26.2 ± 9.7	23
total	5.1 ± 1.9	25.1 ± 1.3	2.6 ± 1.2	1.3 ± 0.3	2.5 ± 0.4	24.9 ± 4.4	61.5 ± 5.1	46.6 ± 12.4	67
	$Z\gamma^*$	$t\bar{t}$ +tW	W+jets	WZ+ZZ	ggWW	WW	all bkg.	$m_{\mathrm{H}} = 180$ GeV	data
sf	7.2 ± 2.6	14.3 ± 1.0	2.1 ± 1.3	0.6 ± 0.1	1.4 ± 0.3	13.6 ± 3.3	39.3 ± 4.6	17.4 ± 6.3	40
of	0.0 ± 0.0	17.2 ± 1.2	1.3 ± 0.7	0.4 ± 0.0	1.7 ± 0.4	16.0 ± 3.9	36.6 ± 4.2	20.6 ± 7.4	27
total	7.2 ± 2.6	31.5 ± 1.6	3.4 ± 1.4	1.0 ± 0.1	3.1 ± 0.5	29.6 ± 5.1	75.9 ± 6.2	38.0 ± 9.7	67
	$Z\gamma^*$	$t\bar{t}$ +tW	W+jets	WZ+ZZ	ggWW	WW	all bkg.	$m_{\mathrm{H}} = 190$ GeV	data
sf	12.5 ± 3.6	23.1 ± 1.5	2.3 ± 1.3	1.1 ± 0.1	2.1 ± 0.5	21.3 ± 5.2	62.3 ± 6.7	15.0 ± 5.7	54
of	0.0 ± 0.0	29.7 ± 1.9	2.2 ± 1.1	0.7 ± 0.1	2.6 ± 0.6	27.6 ± 6.7	62.7 ± 7.1	19.8 ± 7.5	40
total	12.5 ± 3.6	52.7 ± 2.5	4.5 ± 1.7	1.8 ± 0.1	4.6 ± 0.8	48.9 ± 8.5	125.0 ± 9.8	34.8 ± 9.4	94
	$Z\gamma^*$	$t\bar{t}$ +tW	W+jets	WZ+ZZ	ggWW	WW	all bkg.	$m_{\mathrm{H}} = 200$ GeV	data
sf	14.6 ± 5.3	23.8 ± 1.6	2.3 ± 1.3	1.3 ± 0.1	1.8 ± 0.6	18.5 ± 2.9	62.4 ± 6.4	10.7 ± 3.8	61
of	0.0 ± 0.0	35.6 ± 2.3	2.9 ± 1.3	0.8 ± 0.1	2.4 ± 0.7	26.6 ± 4.1	68.4 ± 4.9	15.1 ± 5.3	50
total	14.6 ± 5.3	59.4 ± 2.8	5.2 ± 1.8	2.2 ± 0.2	4.2 ± 0.9	45.1 ± 5.0	130.8 ± 8.1	25.8 ± 6.5	111

Table A.9: Background contributions and data yields for $4.6\,\text{fb}^{-1}$ of integrated luminosity after the full selection in the 1-jet bin for high Higgs masses ($250 \leq m_{\text{H}} \leq 400\,\text{GeV}$). The data-driven correction are applied and the errors reported reflect all systematic uncertanties.

	$Z\gamma^*$	$t\bar{t}$ +tW	W+jets	WZ+ZZ	ggWW	WW	all bkg.	$m_{\text{H}} = 250$ GeV	data
sf	12.9 ± 6.8	28.7 ± 1.9	1.6 ± 1.1	2.1 ± 0.2	1.4 ± 0.4	20.9 ± 3.2	67.6 ± 7.8	5.0 ± 1.7	72
of	0.0 ± 0.0	55.1 ± 3.4	4.3 ± 1.8	1.2 ± 0.1	2.6 ± 0.8	35.5 ± 5.5	98.6 ± 6.7	9.8 ± 3.3	86
total	12.9 ± 6.8	83.8 ± 3.9	5.9 ± 2.1	3.3 ± 0.2	3.9 ± 0.9	56.4 ± 6.4	166.2 ± 10.3	14.8 ± 3.8	158
	$Z\gamma^*$	$t\bar{t}$ +tW	W+jets	WZ+ZZ	ggWW	WW	all bkg.	$m_{\text{H}} = 300$ GeV	data
sf	11.0 ± 4.4	29.5 ± 1.9	1.4 ± 0.9	2.5 ± 0.3	1.2 ± 0.4	19.7 ± 3.1	65.4 ± 5.8	5.3 ± 2.1	79
of	1.8 ± 1.9	54.1 ± 3.4	4.8 ± 2.0	1.3 ± 0.2	2.1 ± 0.7	34.5 ± 5.3	98.5 ± 6.9	8.3 ± 3.2	89
total	12.8 ± 4.8	83.6 ± 3.9	6.2 ± 2.2	3.8 ± 0.4	3.3 ± 0.8	54.2 ± 6.1	163.9 ± 9.0	13.7 ± 3.8	168
	$Z\gamma^*$	$t\bar{t}$ +tW	W+jets	WZ+ZZ	ggWW	WW	all bkg.	$m_{\text{H}} = 350$ GeV	data
sf	6.1 ± 1.9	26.8 ± 1.8	1.3 ± 0.7	3.0 ± 0.6	1.0 ± 0.3	18.3 ± 2.8	56.4 ± 4.0	5.7 ± 2.2	74
of	1.8 ± 1.9	46.9 ± 3.0	4.6 ± 1.9	1.4 ± 0.4	1.7 ± 0.5	31.5 ± 4.9	87.8 ± 6.3	8.6 ± 3.3	76
total	7.8 ± 2.7	73.6 ± 3.4	5.9 ± 2.0	4.3 ± 0.7	2.7 ± 0.6	49.8 ± 5.6	144.2 ± 7.5	14.3 ± 4.0	150
	$Z\gamma^*$	$t\bar{t}$ +tW	W+jets	WZ+ZZ	ggWW	WW	all bkg.	$m_{\text{H}} = 400$ GeV	data
sf	6.5 ± 2.6	22.6 ± 1.5	1.4 ± 0.7	2.7 ± 0.5	0.9 ± 0.3	15.3 ± 2.4	49.4 ± 3.9	5.0 ± 2.2	66
of	1.8 ± 1.9	38.0 ± 2.4	4.8 ± 2.0	1.2 ± 0.3	1.5 ± 0.5	26.9 ± 4.2	74.2 ± 5.6	7.1 ± 3.1	62
total	8.3 ± 3.2	60.6 ± 2.9	6.2 ± 2.1	3.9 ± 0.6	2.4 ± 0.6	42.2 ± 4.8	123.6 ± 6.8	12.2 ± 3.7	128

Table A.10: Background contributions and data yields for $4.6\,\mathrm{fb}^{-1}$ of integrated luminosity after the full selection in the 1-jet bin for high Higgs masses ($450 \leq m_{\mathrm{H}} \leq 600\,\mathrm{GeV}$). The data-driven correction are applied and the errors reported reflect all systematic uncertanties.

	$Z\gamma^*$	$t\bar{t}$ +tW	W+jets	WZ+ZZ	ggWW	WW	all bkg.	$m_{\mathrm{H}} = 450$ GeV	data
sf	4.2 ± 2.0	13.1 ± 0.9	1.6 ± 0.8	1.6 ± 0.4	0.6 ± 0.2	10.0 ± 1.6	31.0 ± 2.8	3.1 ± 1.3	40
of	1.8 ± 1.9	23.2 ± 1.6	3.4 ± 1.5	0.9 ± 0.3	1.0 ± 0.3	17.5 ± 2.7	47.7 ± 4.0	4.5 ± 1.8	36
total	5.9 ± 2.7	36.3 ± 1.8	5.0 ± 1.6	2.5 ± 0.5	1.6 ± 0.4	27.5 ± 3.2	78.7 ± 4.9	7.6 ± 2.2	76
	$Z\gamma^*$	$t\bar{t}$ +tW	W+jets	WZ+ZZ	ggWW	WW	all bkg.	$m_{\mathrm{H}} = 500$ GeV	data
sf	3.9 ± 2.7	10.2 ± 0.8	1.4 ± 0.7	1.1 ± 0.3	0.5 ± 0.2	8.1 ± 1.3	25.2 ± 3.2	2.0 ± 0.9	32
of	1.8 ± 1.9	17.7 ± 1.2	2.8 ± 1.3	0.8 ± 0.3	0.7 ± 0.2	14.1 ± 2.2	37.9 ± 3.4	3.0 ± 1.3	31
total	5.7 ± 3.3	27.9 ± 1.4	4.2 ± 1.4	1.9 ± 0.4	1.2 ± 0.3	22.2 ± 2.6	63.1 ± 4.7	5.0 ± 1.6	63
	$Z\gamma^*$	$t\bar{t}$ +tW	W+jets	WZ+ZZ	ggWW	WW	all bkg.	$m_{\mathrm{H}} = 550$ GeV	data
sf	1.7 ± 1.5	7.6 ± 0.6	1.5 ± 0.7	0.9 ± 0.3	0.4 ± 0.1	6.5 ± 1.1	18.6 ± 2.1	1.4 ± 0.6	22
of	1.8 ± 1.9	13.3 ± 1.0	2.7 ± 1.2	0.8 ± 0.3	0.6 ± 0.2	11.5 ± 1.8	30.6 ± 3.1	2.1 ± 0.9	25
total	3.4 ± 2.4	20.9 ± 1.1	4.2 ± 1.4	1.7 ± 0.4	1.0 ± 0.2	18.0 ± 2.1	49.3 ± 3.7	3.4 ± 1.1	47
	$Z\gamma^*$	$t\bar{t}$ +tW	W+jets	WZ+ZZ	ggWW	WW	all bkg.	$m_{\mathrm{H}} = 600$ GeV	data
sf	0.7 ± 0.9	5.2 ± 0.5	1.1 ± 0.6	0.9 ± 0.3	0.4 ± 0.1	5.0 ± 0.8	13.3 ± 1.4	0.9 ± 0.4	16
of	1.8 ± 1.9	10.2 ± 0.8	2.4 ± 1.1	0.5 ± 0.2	0.5 ± 0.2	9.4 ± 1.5	24.8 ± 2.8	1.4 ± 0.6	21
total	2.5 ± 2.0	15.4 ± 0.9	3.5 ± 1.2	1.4 ± 0.4	0.8 ± 0.2	14.4 ± 1.7	38.1 ± 3.1	2.3 ± 0.7	37

Table A.11: Background contributions and data yields for $4.6\,\mathrm{fb}^{-1}$ of integrated luminosity after the full selection in the 2-jet bin for all Higgs masses ($110 \leq m_{\mathrm{H}} \leq 600\,\mathrm{GeV}$). The data-driven correction are applied and the errors reported reflect all systematic uncertanties.

m_{H} [GeV]	$Z\gamma^*$	$t\bar{t}$ +tW	W+jets	WZ+ZZ	ggWW	WW	all bkg.	signal	data
110	1.9 ± 1.4	5.5 ± 2.8	0.7 ± 0.6	1.8 ± 1.6	0.2 ± 0.0	1.1 ± 0.2	11.3 ± 3.6	0.3 ± 0.0	8
115	1.9 ± 1.4	5.5 ± 2.8	0.7 ± 0.6	1.8 ± 1.6	0.2 ± 0.0	1.1 ± 0.2	11.3 ± 3.6	0.6 ± 0.0	8
120	1.9 ± 1.4	5.5 ± 2.8	0.7 ± 0.6	1.8 ± 1.6	0.2 ± 0.0	1.1 ± 0.2	11.3 ± 3.6	1.1 ± 0.1	8
124	1.9 ± 1.4	5.5 ± 2.8	0.7 ± 0.6	1.8 ± 1.6	0.2 ± 0.0	1.1 ± 0.2	11.3 ± 3.6	1.6 ± 0.1	8
128	2.7 ± 1.9	6.5 ± 3.2	0.7 ± 0.6	1.8 ± 1.6	0.3 ± 0.0	1.4 ± 0.2	13.3 ± 4.1	2.3 ± 0.2	10
130	2.7 ± 1.9	6.5 ± 3.2	0.7 ± 0.6	1.8 ± 1.6	0.3 ± 0.0	1.4 ± 0.2	13.3 ± 4.1	2.7 ± 0.2	10
135	2.7 ± 1.9	7.5 ± 3.5	1.3 ± 0.8	1.8 ± 1.6	0.3 ± 0.0	1.5 ± 0.2	15.0 ± 4.4	4.0 ± 0.3	11
140	2.7 ± 1.9	7.5 ± 3.5	1.3 ± 0.8	1.8 ± 1.6	0.3 ± 0.0	1.5 ± 0.2	15.0 ± 4.4	5.2 ± 0.4	11
150	2.7 ± 1.9	8.4 ± 3.9	1.2 ± 0.8	1.8 ± 1.6	0.3 ± 0.0	1.6 ± 0.2	15.9 ± 4.7	8.1 ± 0.6	12
160	2.7 ± 1.9	8.4 ± 3.9	1.2 ± 0.8	1.8 ± 1.6	0.3 ± 0.0	1.6 ± 0.2	15.9 ± 4.7	12.2 ± 0.9	12
170	2.7 ± 1.9	8.4 ± 3.9	1.2 ± 0.8	1.8 ± 1.6	0.3 ± 0.0	1.6 ± 0.2	15.9 ± 4.7	14.0 ± 1.0	12
180	2.7 ± 1.9	8.5 ± 3.9	1.2 ± 0.8	1.8 ± 1.6	0.3 ± 0.0	1.7 ± 0.2	16.1 ± 4.7	12.6 ± 0.9	13
190	3.2 ± 2.1	8.5 ± 3.9	1.2 ± 0.8	1.8 ± 1.6	0.3 ± 0.0	1.8 ± 0.2	16.8 ± 4.8	10.0 ± 0.7	13
200	3.2 ± 2.1	9.4 ± 4.2	1.2 ± 0.8	1.8 ± 1.6	0.3 ± 0.1	1.9 ± 0.8	17.8 ± 5.1	8.4 ± 0.6	13
250	3.3 ± 2.1	12.2 ± 5.2	1.2 ± 0.8	1.9 ± 1.6	0.4 ± 0.1	2.9 ± 1.3	21.8 ± 6.0	5.6 ± 0.4	19
300	3.3 ± 2.1	14.1 ± 5.8	1.1 ± 0.8	1.9 ± 1.6	0.4 ± 0.1	3.0 ± 1.3	23.7 ± 6.6	4.2 ± 0.4	20
350	3.3 ± 2.1	14.1 ± 5.8	1.1 ± 0.8	1.9 ± 1.6	0.4 ± 0.1	3.0 ± 1.3	23.8 ± 6.6	3.4 ± 0.3	20
400	3.3 ± 2.1	14.1 ± 5.8	1.1 ± 0.8	1.9 ± 1.6	0.4 ± 0.1	3.0 ± 1.3	23.8 ± 6.6	2.5 ± 0.3	20
450	3.3 ± 2.1	14.0 ± 5.8	1.1 ± 0.8	1.9 ± 1.6	0.4 ± 0.1	3.0 ± 1.3	23.8 ± 6.6	1.9 ± 0.3	20
500	3.3 ± 2.1	14.0 ± 5.8	1.1 ± 0.8	1.9 ± 1.6	0.4 ± 0.1	3.0 ± 1.3	23.8 ± 6.6	1.4 ± 0.2	20
550	3.3 ± 2.1	14.0 ± 5.8	1.1 ± 0.8	1.9 ± 1.6	0.4 ± 0.1	3.1 ± 1.3	23.8 ± 6.6	1.1 ± 0.2	20
600	3.3 ± 2.1	14.0 ± 5.8	1.1 ± 0.8	1.9 ± 1.6	0.4 ± 0.1	3.1 ± 1.4	23.8 ± 6.6	0.8 ± 0.2	20

Appendix B

Detailed Limits by Channel

The following pages of this appendix give the individual 95% CL upper limits broken down by channel both graphically and in table form. Fig. B.1, Tab. B.1 and Tab. B.2 give the results for the 0-jet category. Fig. B.2, Tab. B.3 and Tab. B.4 give the results for the 1-jet category. Finally, Fig. B.3 and Tab. B.5 give the results for the 2-jet category.

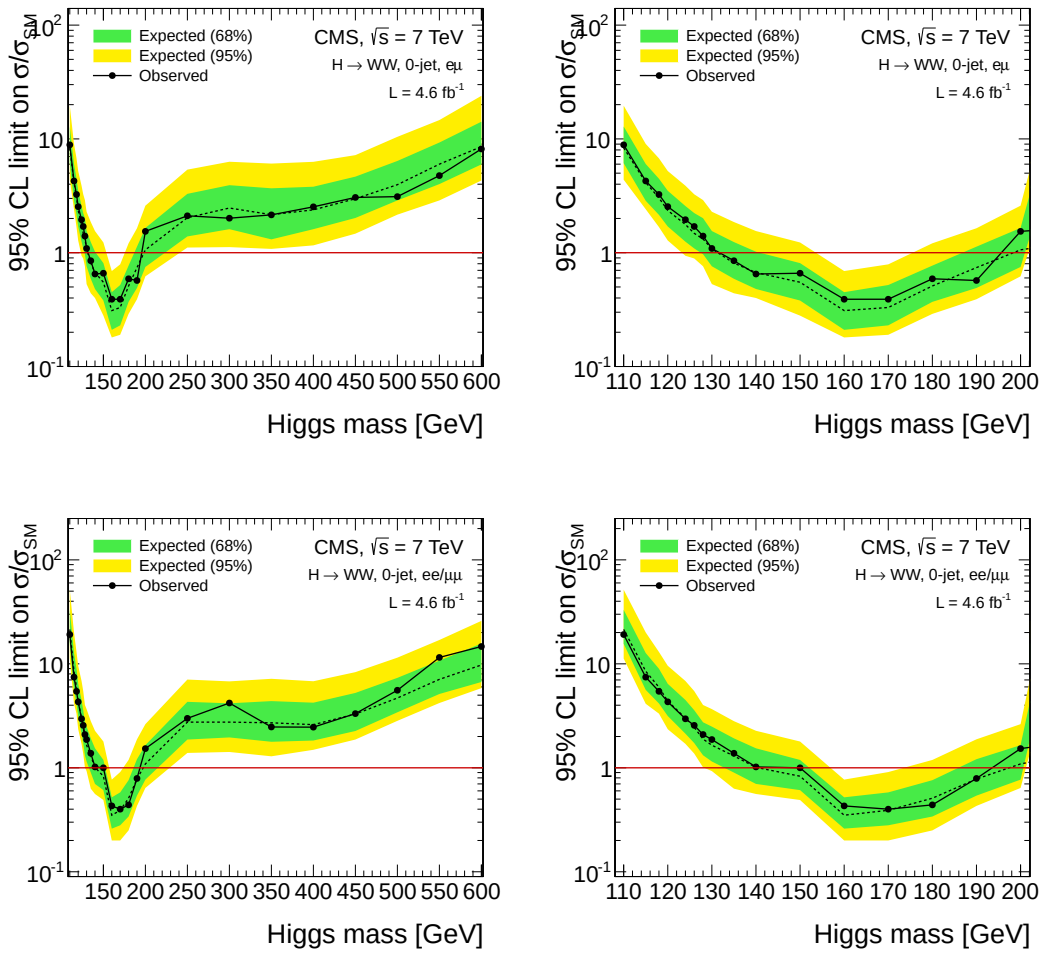

Figure B.1: 95% CL in the 0-jet category for the opposite flavor channel (top) and the same flavor channel (bottom). The plots on the left display the results over the full Higgs boson mass range while the plots on the right display the results up to $m_{\mathrm{H}} = 200$ GeV.

Table B.1: Expected and observed 95% C.L. upper limits and uncertainty band for opposite flavour events in the 0-jet category.

m_H [GeV]	observed (CLs)	observed (Bayesian)	median expected (CLs)	expected range for 68%	expected range for 95%
110	9.0	8.7	8.7	[5.3 , 13.0]	[3.9 , 20.4]
115	4.2	4.1	4.0	[2.9 , 6.0]	[1.9 , 9.2]
120	2.6	2.5	2.4	[1.7 , 3.6]	[1.3 , 5.3]
130	1.1	1.1	1.1	[0.8 , 1.6]	[0.5 , 2.3]
140	0.6	0.7	0.7	[0.4 , 1.0]	[0.3 , 1.6]
150	0.7	0.7	0.6	[0.4 , 0.8]	[0.3 , 1.2]
160	0.4	0.4	0.3	[0.2 , 0.4]	[0.2 , 0.6]
170	0.4	0.4	0.3	[0.2 , 0.5]	[0.2 , 0.8]
180	0.6	0.6	0.5	[0.3 , 0.8]	[0.3 , 1.2]
190	0.6	0.6	0.8	[0.5 , 1.1]	[0.3 , 1.7]
200	1.6	1.6	1.1	[0.8 , 1.7]	[0.6 , 2.6]
250	2.0	2.2	2.0	[1.5 , 3.3]	[1.4 , 4.9]
300	2.1	2.2	2.5	[1.6 , 4.0]	[1.2 , 6.1]
350	2.2	2.3	2.2	[1.4 , 3.5]	[1.0 , 5.7]
400	2.5	2.6	2.4	[1.6 , 3.7]	[1.4 , 6.1]
450	3.1	3.2	3.0	[1.9 , 4.7]	[1.3 , 6.9]
500	3.1	3.3	3.9	[2.9 , 6.8]	[2.0 , 9.4]
550	4.6	5.1	5.7	[3.8 , 9.3]	[2.2 , 14.9]
600	8.4	9.1	9.0	[5.9 , 14.2]	[5.4 , 23.0]

Table B.2: Expected and observed 95% C.L. upper limits and uncertainty band for same flavour events in the 0-jet category.

m_H [GeV]	observed (CLs)	observed (Bayesian)	median expected (CLs)	expected range for 68%	expected range for 95%
110	19.1	19.6	21.3	[14.6 , 33.2]	[11.4 , 52.2]
115	7.3	7.4	8.2	[5.9 , 12.1]	[4.2 , 18.9]
120	4.4	4.2	4.4	[3.0 , 6.6]	[2.2 , 9.8]
130	1.9	1.8	1.7	[1.2 , 2.5]	[1.0 , 3.6]
140	1.0	1.0	1.0	[0.7 , 1.5]	[0.6 , 2.2]
150	1.0	0.9	0.9	[0.6 , 1.2]	[0.5 , 1.7]
160	0.4	0.4	0.4	[0.2 , 0.5]	[0.2 , 0.8]
170	0.4	0.4	0.4	[0.3 , 0.6]	[0.2 , 1.0]
180	0.4	0.5	0.5	[0.3 , 0.8]	[0.3 , 1.2]
190	0.8	0.8	0.8	[0.6 , 1.2]	[0.4 , 1.8]
200	1.6	1.5	1.1	[0.8 , 1.8]	[0.6 , 2.8]
250	3.0	3.1	2.8	[1.9 , 4.3]	[1.3 , 7.1]
300	4.2	4.2	2.6	[1.9 , 4.2]	[1.5 , 6.9]
350	2.5	2.5	2.7	[1.8 , 4.4]	[1.4 , 7.1]
400	2.5	2.6	2.6	[1.9 , 4.2]	[1.3 , 6.9]
450	3.4	3.5	3.4	[2.3 , 5.2]	[1.6 , 8.1]
500	5.6	5.7	4.8	[3.3 , 7.4]	[2.7 , 11.2]
550	11.8	11.9	7.1	[5.2 , 11.1]	[4.0 , 17.3]
600	14.6	15.4	10.3	[7.8 , 15.6]	[5.7 , 26.1]

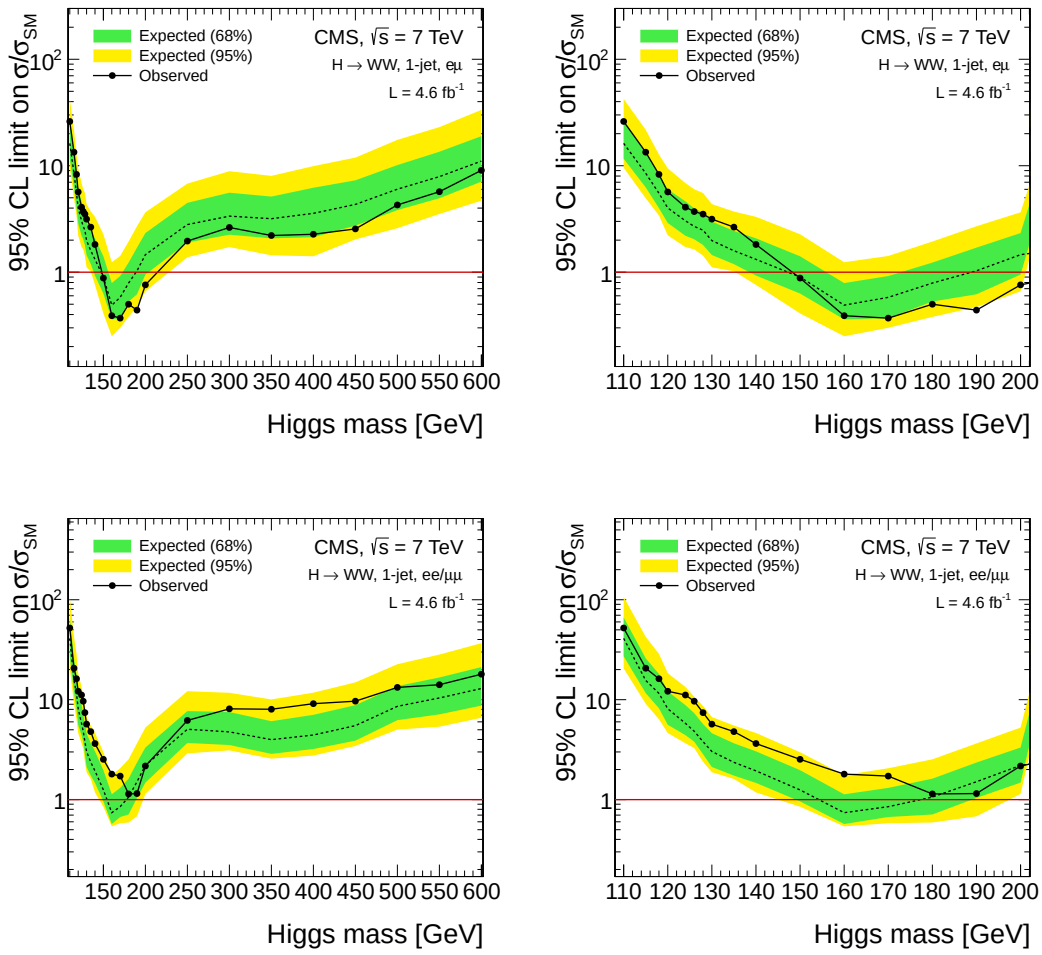

Figure B.2: 95% CL in the 0-jet category for the opposite flavor channel (top) and the same flavor channel (bottom). The plots on the left display the results over the full Higgs boson mass range while the plots on the right display the results up to $m_{\mathrm{H}} = 200$ GeV.

Table B.3: Expected and observed 95% C.L. upper limits and uncertainty band for opposite flavour events in the 1-jet category.

m_H [GeV]	observed (CLs)	observed (Bayesian)	median expected (CLs)	expected range for 68%	expected range for 95%
110	25.8	25.4	16.0	[11.4 , 25.8]	[8.9 , 42.2]
115	13.6	13.0	8.4	[6.1 , 13.8]	[4.7 , 21.4]
120	6.1	5.7	4.3	[2.9 , 6.5]	[2.1 , 9.7]
130	3.3	3.1	2.0	[1.5 , 3.1]	[1.1 , 4.8]
140	1.9	1.9	1.4	[1.0 , 2.2]	[0.8 , 3.5]
150	0.9	1.0	0.9	[0.6 , 1.5]	[0.5 , 2.3]
160	0.4	0.4	0.5	[0.3 , 0.8]	[0.3 , 1.3]
170	0.4	0.4	0.6	[0.4 , 0.9]	[0.3 , 1.4]
180	0.5	0.6	0.8	[0.5 , 1.3]	[0.4 , 2.0]
190	0.5	0.6	1.0	[0.7 , 1.8]	[0.5 , 2.7]
200	0.7	0.9	1.5	[0.9 , 2.4]	[0.6 , 3.9]
250	2.0	2.1	2.9	[2.0 , 4.5]	[1.5 , 7.2]
300	2.7	2.8	3.5	[2.2 , 5.7]	[1.7 , 8.8]
350	2.1	2.3	3.1	[2.0 , 5.1]	[1.3 , 7.8]
400	2.3	2.5	3.5	[2.2 , 6.0]	[1.6 , 9.9]
450	2.6	2.9	4.2	[2.8 , 7.3]	[2.0 , 12.0]
500	4.2	4.7	6.0	[3.7 , 10.1]	[2.6 , 16.9]
550	5.7	6.5	7.7	[5.1 , 13.6]	[3.0 , 25.1]
600	9.1	9.9	10.9	[7.0 , 19.2]	[4.7 , 34.5]

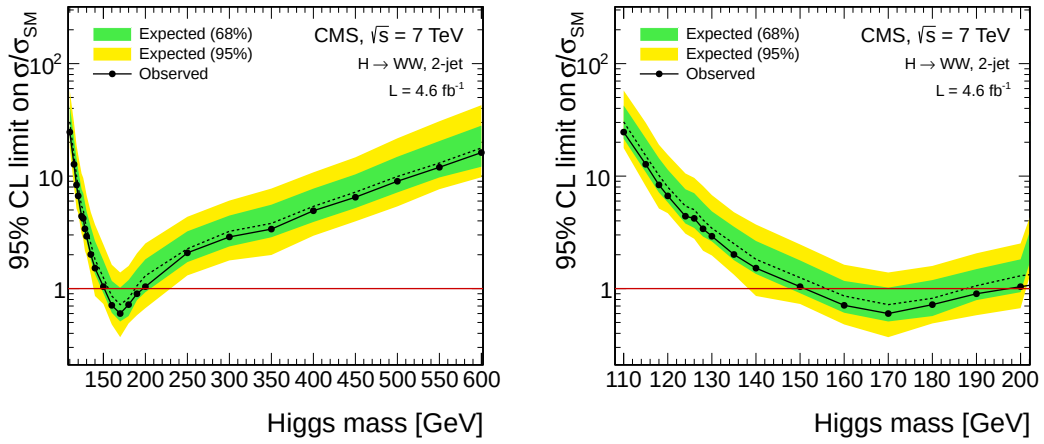

Figure B.3: 95% CL in the 2-jet category. The plot on the left displays the results over the full Higgs boson mass range while the plot on the right displays the results up to $m_H = 200$ GeV.

Table B.4: Expected and observed 95% C.L. upper limits and uncertainty band for same flavour events in the 1-jet category.

m_H [GeV]	observed (CLs)	observed (Bayesian)	median expected (CLs)	expected range for 68%	expected range for 95%
110	51.0	54.8	39.5	[26.8 , 64.8]	[20.8 , 106.9]
115	20.8	21.5	15.8	[12.0 , 24.9]	[7.8 , 42.3]
120	13.1	13.0	8.5	[6.2 , 13.0]	[3.9 , 19.9]
130	5.9	5.9	3.2	[2.3 , 4.7]	[2.2 , 7.0]
140	3.8	3.9	2.1	[1.5 , 3.2]	[1.2 , 5.2]
150	2.7	2.6	1.3	[1.0 , 2.0]	[0.8 , 3.2]
160	1.9	1.9	0.8	[0.6 , 1.2]	[0.5 , 1.8]
170	1.8	1.8	0.9	[0.6 , 1.3]	[0.5 , 2.1]
180	1.2	1.2	1.1	[0.8 , 1.7]	[0.6 , 2.6]
190	1.2	1.3	1.4	[1.1 , 2.5]	[0.7 , 3.8]
200	2.2	2.2	2.2	[1.5 , 3.5]	[1.1 , 5.3]
250	6.3	6.1	5.2	[3.5 , 7.9]	[2.7 , 12.7]
300	8.1	8.1	5.0	[3.5 , 7.5]	[2.4 , 11.4]
350	8.3	8.3	3.9	[3.0 , 6.4]	[2.3 , 10.1]
400	9.2	9.4	4.5	[3.3 , 7.0]	[3.0 , 11.4]
450	9.6	9.8	5.5	[3.9 , 8.8]	[3.7 , 14.9]
500	13.1	13.2	8.5	[5.8 , 13.1]	[4.6 , 23.3]
550	13.8	14.3	9.9	[6.7 , 16.5]	[5.9 , 27.6]
600	18.3	19.0	13.2	[8.8 , 21.9]	[7.4 , 37.5]

Table B.5: Expected and observed 95% C.L. upper limits and uncertainty band for events in the 2-jet category.

m_H [GeV]	observed (CLs)	observed (Bayesian)	median expected (CLs)	expected range for 68%	expected range for 95%
110	24.5	23.7	30.0	[21.0 , 43.1]	[16.8 , 57.6]
115	12.4	12.1	15.1	[10.1 , 21.2]	[8.8 , 30.9]
120	6.5	6.3	7.9	[5.8 , 11.3]	[3.9 , 15.8]
130	3.0	2.8	3.5	[2.5 , 5.0]	[1.8 , 6.6]
140	1.5	1.5	1.9	[1.4 , 2.7]	[1.1 , 3.6]
150	1.1	1.0	1.3	[0.9 , 1.8]	[0.7 , 2.4]
160	0.7	0.7	0.9	[0.6 , 1.2]	[0.4 , 1.6]
170	0.6	0.6	0.7	[0.5 , 1.0]	[0.4 , 1.4]
180	0.7	0.7	0.8	[0.6 , 1.2]	[0.5 , 1.6]
190	0.9	0.9	1.1	[0.8 , 1.5]	[0.6 , 2.1]
200	1.0	1.0	1.3	[0.9 , 1.8]	[0.8 , 2.5]
250	2.1	2.0	2.2	[1.6 , 3.2]	[1.3 , 4.3]
300	2.9	2.7	3.1	[2.3 , 4.5]	[2.0 , 6.2]
350	3.6	3.3	3.9	[2.8 , 5.6]	[1.8 , 7.7]
400	4.9	4.5	5.4	[4.0 , 7.8]	[3.1 , 10.7]
450	6.4	6.0	7.0	[4.9 , 10.3]	[4.1 , 14.5]
500	9.1	8.6	10.4	[7.2 , 15.0]	[5.1 , 21.2]
550	11.7	11.3	13.3	[8.7 , 19.9]	[6.8 , 29.6]
600	16.2	15.5	17.9	[12.1 , 28.3]	[8.3 , 43.6]

Appendix C

Fake Rates

The following tables give a detailed account of the fake rates in each of the categories dicussed in Sec. 5.4.1.

Table C.1: Measured prompt rate for muons in bins of η, p_{T} and number of primary vertices. Errors are statistical only.

$N_{vtx} < 10$		
p_{T} range [GeV]	$0 < \eta \leq 1.5$	$1.5 < \eta \leq 2.5$
$10 < p_{\mathrm{T}} \leq 15$	0.723 ± 0.006	0.741 ± 0.006
$15 < p_{\mathrm{T}} \leq 20$	0.777 ± 0.003	0.770 ± 0.004
$20 < p_{\mathrm{T}} \leq 25$	0.948 ± 0.001	0.913 ± 0.002
$25 < p_{\mathrm{T}} \leq 50$	0.984 ± 0.000	0.965 ± 0.000
$50 < p_{\mathrm{T}}$	0.995 ± 0.000	0.987 ± 0.000
$N_{vtx} \geq 10$		
p_{T} range [GeV]	$0 < \eta \leq 1.5$	$1.5 < \eta \leq 2.5$
$10 < p_{\mathrm{T}} \leq 15$	0.667 ± 0.011	0.654 ± 0.012
$15 < p_{\mathrm{T}} \leq 20$	0.715 ± 0.007	0.682 ± 0.009
$20 < p_{\mathrm{T}} \leq 25$	0.923 ± 0.003	0.863 ± 0.004
$25 < p_{\mathrm{T}} \leq 50$	0.976 ± 0.000	0.938 ± 0.001
$50 < p_{\mathrm{T}}$	0.992 ± 0.000	0.981 ± 0.002

Table C.2: Measured prompt rate for electrons in bins of η, p_{T} and number of primary vertices. Errors are statistical only.

$N_{vtx} < 10$			
p_{T} range [GeV]	$0 < \eta \leq 1.4442$	$1.4442 < \eta \leq 1.566$	$1.566 < \eta$
$10 < p_{\mathrm{T}} \leq 15$	0.589 ± 0.010	0.465 ± 0.043	0.371 ± 0.193
$15 < p_{\mathrm{T}} \leq 20$	0.673 ± 0.006	0.541 ± 0.043	0.449 ± 0.009
$20 < p_{\mathrm{T}} \leq 25$	0.778 ± 0.003	0.712 ± 0.017	0.675 ± 0.006
$25 < p_{\mathrm{T}} \leq 50$	0.874 ± 0.063	0.823 ± 0.090	0.779 ± 0.001
$50 < p_{\mathrm{T}}$	0.906 ± 0.001	0.967 ± 0.070	0.838 ± 0.002
$N_{vtx} \geq 10$			
p_{T} range [GeV]	$0 < \eta \leq 1.4442$	$1.4442 < \eta \leq 1.566$	$1.566 < \eta$
$10 < p_{\mathrm{T}} \leq 15$	0.528 ± 0.046	0.271 ± 0.081	0.305 ± 0.042
$15 < p_{\mathrm{T}} \leq 20$	0.616 ± 0.014	0.479 ± 0.089	0.351 ± 0.022
$20 < p_{\mathrm{T}} \leq 25$	0.739 ± 0.008	0.658 ± 0.045	0.588 ± 0.015
$25 < p_{\mathrm{T}} \leq 50$	0.862 ± 0.001	0.790 ± 0.000	0.722 ± 0.003
$50 < p_{\mathrm{T}}$	0.901 ± 0.002	0.863 ± 0.018	0.793 ± 0.009

Table C.3: Measured fake rates in bins of η and p_{T}. Errors are statistical only.

electron fake rate				
p_{T} range [GeV]	$0 < \eta \leq 1$	$1 < \eta \leq 1.479$	$1.479 < \eta \leq 2$	$2 < \eta \leq 2.5$
$10 < p_{\mathrm{T}} \leq 15$	0.066 ± 0.015	0.040 ± 0.012	0.016 ± 0.009	0.023 ± 0.013
$15 < p_{\mathrm{T}} \leq 20$	0.057 ± 0.009	0.054 ± 0.010	0.018 ± 0.007	0.041 ± 0.013
$20 < p_{\mathrm{T}} \leq 25$	0.085 ± 0.009	0.064 ± 0.011	0.057 ± 0.010	0.046 ± 0.009
$25 < p_{\mathrm{T}} \leq 30$	0.085 ± 0.012	0.067 ± 0.015	0.052 ± 0.012	0.070 ± 0.015
$30 < p_{\mathrm{T}} \leq 35$	0.085 ± 0.017	0.059 ± 0.019	0.072 ± 0.019	0.068 ± 0.019
muon fake rate				
p_{T} range [GeV]	$0 < \eta \leq 1$	$1 < \eta \leq 1.479$	$1.479 < \eta \leq 2$	$2 < \eta \leq 2.5$
$10 < p_{\mathrm{T}} \leq 15$	0.194 ± 0.003	0.221 ± 0.005	0.247 ± 0.006	0.289 ± 0.010
$15 < p_{\mathrm{T}} \leq 20$	0.127 ± 0.007	0.151 ± 0.011	0.161 ± 0.013	0.188 ± 0.022
$20 < p_{\mathrm{T}} \leq 25$	0.238 ± 0.003	0.283 ± 0.005	0.251 ± 0.006	0.285 ± 0.010
$25 < p_{\mathrm{T}} \leq 30$	0.194 ± 0.007	0.262 ± 0.010	0.250 ± 0.011	0.280 ± 0.020
$30 < p_{\mathrm{T}} \leq 35$	0.180 ± 0.005	0.240 ± 0.0075	0.256 ± 0.008	0.328 ± 0.016

Table C.4: W+jets yields in the 0-jet bin. Errors are statistical only.

fake lepton bin	ee channel	μe channel
barrel, $10 \leq p_{\mathrm{T}} < 20$ GeV	1.3 ± 0.4	5.5 ± 1.0
barrel, $p_{\mathrm{T}} \geq 20$ GeV	7.3 ± 1.1	9.3 ± 1.4
endcap, $10 \leq p_{\mathrm{T}} < 20$ GeV	0.2 ± 0.2	1.3 ± 0.2
endcap, $p_{\mathrm{T}} \geq 20$ GeV	2.9 ± 0.7	6.8 ± 1.3
total	11.4 ± 1.4	22.9 ± 2.2
fake lepton bin	eμ channel	$\mu\mu$ channel
barrel, $10 \leq p_{\mathrm{T}} < 20$ GeV	13.8 ± 2.5	2.2 ± 0.9
barrel, $p_{\mathrm{T}} \geq 20$ GeV	16.3 ± 1.9	5.6 ± 1.6
endcap, $10 \leq p_{\mathrm{T}} < 20$ GeV	11.1 ± 2.5	0.6 ± 0.6
endcap, $p_{\mathrm{T}} \geq 20$ GeV	10.7 ± 1.8	0.5 ± 1.0
total	52.0 ± 4.5	8.2 ± 2.1

Table C.5: W+jets yields in the 1-jet bin. Errors are statistical only.

fake lepton bin	ee channel	μe channel
barrel, $10 \leq p_{\mathrm{T}} < 20$ GeV	0.4 ± 0.3	4.4 ± 1.0
barrel, $p_{\mathrm{T}} \geq 20$ GeV	3.1 ± 0.8	9.4 ± 1.4
endcap, $10 \leq p_{\mathrm{T}} < 20$ GeV	0.1 ± 0.1	1.3 ± 0.2
endcap, $p_{\mathrm{T}} \geq 20$ GeV	1.6 ± 0.5	3.2 ± 0.7
total	5.1 ± 1.0	18.3 ± 1.9
fake lepton bin	eμ channel	$\mu\mu$ channel
barrel, $10 \leq p_{\mathrm{T}} < 20$ GeV	9.9 ± 2.2	0.9 ± 0.8
barrel, $p_{\mathrm{T}} \geq 20$ GeV	15.5 ± 2.0	2.8 ± 1.1
endcap, $10 \leq p_{\mathrm{T}} < 20$ GeV	2.7 ± 1.8	1.1 ± 0.7
endcap, $p_{\mathrm{T}} \geq 20$ GeV	7.4 ± 1.6	3.6 ± 1.4
total	35.6 ± 3.8	8.3 ± 2.1

Table C.6: W+jets yields in the 2-jet bin. Errors are statistical only.

fake lepton bin	ee channel	μe channel
barrel, $10 \leq p_{\mathrm{T}} < 20$ GeV	0.3 ± 0.3	1.5 ± 0.6
barrel, $p_{\mathrm{T}} \geq 20$ GeV	1.4 ± 0.6	3.9 ± 0.9
endcap, $10 \leq p_{\mathrm{T}} < 20$ GeV	0.1 ± 0.1	0.3 ± 0.1
endcap, $p_{\mathrm{T}} \geq 20$ GeV	0.2 ± 0.2	1.6 ± 0.7
total	1.8 ± 0.7	7.3 ± 1.3
fake lepton bin	eμ channel	$\mu\mu$ channel
barrel, $10 \leq p_{\mathrm{T}} < 20$ GeV	3.2 ± 1.5	0.3 ± 0.5
barrel, $p_{\mathrm{T}} \geq 20$ GeV	4.9 ± 1.1	0.2 ± 0.8
endcap, $10 \leq p_{\mathrm{T}} < 20$ GeV	3.1 ± 1.4	0.4 ± 0.4
endcap, $p_{\mathrm{T}} \geq 20$ GeV	3.2 ± 1.2	0.3 ± 0.6
total	14.5 ± 2.6	0.8 ± 1.1